STUDIES OF Ni-RICH POSITIVE ELECTRODE MATERIALS FOR LITHIUM ION BATTERIES

by

Hongyang Li

Submitted in partial fulfilment of the requirements

for the degree of Doctor of Philosophy

at

Dalhousie University

Halifax, Nova Scotia

November 2019

To my daughter, my wife and my parents,

TABLE OF CONTENT

LIST OF TABLES

LIST OF FIGURES

ABSTRACT

Ni-rich layered Li transition metal oxides are some of the most promising positive electrode materials for Li-ion batteries due to low cost and high energy density. Increasing the Ni content is one important approach to further increase the energy density and lower the cost. However, it is conventionally believed that high Ni content brings about challenges like poor cycling stability and thermal stability. This thesis focuses on fundamental studies of Ni-rich positive electrode materials, development of novel materials with enhanced properties, and investigations of failure mechanisms.

The thesis begins with a study of $LiNiO_2$, the "grandfather" of Ni-rich positive electrode materials. The multiple phase transitions which occur as x varies in Li_xNiO_2 ($0 \leq x \leq 1$) were thoroughly investigated by X-ray diffraction, neutron diffraction, and electrochemical measurements. Based on this work, a study on how dopants, M, affect $LiNi_{1-x}M_xO_2$ was performed. The effects of dopants on structural, electrochemical, and thermal properties were comprehensively studied. It was concluded that Co, commonly believed to be an essential dopant in Ni-rich materials, is actually not required.

The development of single crystal $LiNi_{1-x-y}Mn_xCo_yO_2$ (NMC) and $LiNi_{1-x-y}Co_xAl_yO_2$ (NCA) is another focus of this thesis. Optimal synthesis conditions were developed for single crystal NMC622, and a two-step synthesis method was invented for impurity-free single crystal NCA preparation. Preliminary electrochemical studies of materials made at Dalhousie are included.

The last part of this thesis presents an unavoidable challenge for Ni-rich positive electrode materials. On the basis of a large volume of data collected from Ni-rich positive electrode materials having various compositions, a failure mechanism, which relates the cycling stability to the universal structural changes of Ni-rich materials, was proposed. It is hoped that this work can effectively guide further research to overcome this unavoidable challenge.

LIST OF ABBREVIATIONS AND SYMBOLS USED

(h k l)	Miller indices
(u_n, k_n, w_n)	fractional atomic coordinates of individual atom n
θ_i	scattering angle at the i^{th} calculation step
θ_k	Bragg angle
β	angle
λ	wavelength
a,b,c	unit cell lattice constants
AG	artificial graphite
A_k	absorption correction factor
ALD	atomic layer deposition
ARC	accelerating rate calorimetry
BC	band contrast
BET	Brunauer-Emmett-Teller
BMF	blown microfiber separator
BSE	backscattered electron
C	C as in C-rate, constant
CSTR	continuously stirred tank reactor
CT	computer tomography
d	atomic plane distance
DEC	diethyl carbonate
DI	de-ionized
DMC	dimethyl carbonate
DTD	ethylene sulfate
e^+	electron
EBSD	electron backscattering diffraction
EBSP	EBSD pattern
EC	ethylene carbonate
E_k	extinction correction factor

EMC	ethyl methyl carbonate
EV	electric vehicle
f	atomic scattering factor
FCC	face centered cubic
FEC	fluoroethylene carbonate
F_{hkl}	geometrical structure factor
G_{ik}	normalized peak profile function
H_k	full width half maximum
HWS	heat-wait-search
I	intensity, current
IRC	irreversible capacity
LCO	$LiCoO_2$
LCV	lower cutoff voltage
LDH	layered double hydroxide
LFO	lithium difluorophosphate
LFP	$LiFePO_4$
LiBOB	lithium bisoxalato borate
LiDFOB	lithium difluorooxalatoborate
LiFSi	lithium bis(fluorosulfonyl)imide
$LiMO_2$	layered lithium metal oxide
LiTFSi	lithium bis(trifluoromethanesufonyl)imide
L_k	Lorentz-polarization factor
LMO	$LiMn_2O_4$
LNO	$LiNiO_2$
LTO	$Li_{4/3}Ti_{5/3}O_4$
MA	methyl acetate
MCMB	mesocarbon microbeads
M_k	multiplicity
n	molar amount
N_A	the Avogadro’s number
NCA	Li-Ni-Co-Al oxide

NG	natural graphite
NMC/NMCxyz	Li-Ni-Mn-Co oxide/$LiNi_xMn_yCo_zO_2$
NMP	N-methyl-2-pyrrolidone
NMR	nuclear magnetic resonance
P	fraction of adjacent parallel misaligned layers in graphite
p	pressure
PC	polycrystalline
PE	polyethylene
P_k	preferred orientation parameter
PPE	polypropylene
PSD	particle size distribution
PVDF	polyvinylidene fluoride
Q	capacity
R_B	Bragg R factor
S	scale factor, total surface area
SBC	soluble base content
SBR	styrene-butadiene rubber
SC	single crystal
SE	secondary electron
SEI	solid state electrolyte interface
SEM	scanning electron microscopy
SHR	self-heating rate
SOC	state of charge
T	temperature
TM	transition metal
U, V, W	refinable parameters for the peak width
UVB	upper cutoff voltage
V	voltage, volume
VC	vinylene carbonate
XAS	X-ray absorption spectroscopy
XRD	X-ray diffraction

Z	atomic number

ACKNOWLEDGEMENTS

I would like to give my special thanks to my supervisor, Dr. Jeff Dahn, for his extensive support, patience and guidance, not only in research, but in life as well. I would also like to thank my committee members, Dr. Mita Dasog and Dr. Kevin Hewitt for their continuous help and advice.

I am also very grateful to all the Dahn lab members for their support during my Ph.D. work. Thanks to Robbie Sanderson, Simon Trussler and Michel Johnson for help with operating and repairing facilities. Thanks to Dr. Jing Li, Ning Zhang, Marc Cormier, Aaron Liu, and Xiaowei Ma for their great contribution to my experiments throughout the years. I am also very grateful for help from Lin Ma, Deijung Xiong, Remi Petibon, Stephen Glazier and many others who generously shared their experience with me.

I am thankful to the *Natural Sciences and Engineering Research Council* (NSERC) and to then Nova Scotia Graduate Scholarship for their financial support, along with Tesla Canada for the partial funding of this work.

CHAPTER 1 INTRODUCTION

Since first commercialized by SONY almost three decades ago, Li-ion batteries have been ubiquitous in people's life powering consumer electronic devices such as laptops, cell phones, wearable electronics, etc. In the face of global climate change, the transition from fossil fuel energy to sustainable energy becomes imminent and important. This energy revolution is contingent on not only clean energy generation, but also the effective and efficient energy storage. As crucial parts of the energy revolution, vehicle electrification and the prevalence of the smart grid greatly relies on the development of batteries. Compared with lead acid batteries, NiCd batteries, and NiMH batteries, Li-ion batteries possess several advantages like high energy density, long cycle life and low self-discharge rate.[1] These advantages of Li-ion batteries make them promising solutions for both stationary energy storage and electric vehicle (EV) applications.

Conventional Li–ion batteries used for portable electronic devices have layered $LiCoO_2$ (LCO) as the positive electrode material. LCO has a theoretical capacity of 272 mAh/g, but limited by its intrinsic structure stability, the accessible capacity is only ~160 mAh/g.[1] Another issue for LCO is the high price of Co (13.38 USD/lb as of June 27, 2019) and humanitarian concerns about the Co mining industry in the Congo. Thus, LCO is not a promising positive electrode material candidate for the new generation of Li-ion batteries. Another layered transition metal oxide material, $LiNiO_2$ (LNO) was initially developed at the similar time as LCO. LNO is isostructural with LCO and has a relative low cost and a similar theoretical capacity of 275 mAh/g. However, LNO has issues of rapid capacity fade due to structural instability during cycling, as well as safety concerns at high state of charge (SOC).[2–5]

Derived from LNO and LCO, a series of solid solution materials,[6] $LiNi_xMn_yCo_{1-x-y}O_2$ (NMC) and $LiNi_xCo_yAl_{1-x-y}O_2$ (NCA), have been successfully developed and utilized during the past two decades. NCA was selected by Panasonic as the positive electrode materials for their 18650 cylindrical Li-ion cells used in Tesla EVs.[7] NMC materials with various Ni-Mn-Co compositions are used by CATL and others in their EV batteries supplied to EV manufacturers. NCA and NMC materials were developed on the basis of LNO and LCO with cycling performance and safety greatly improved. With the increasing demand for Li-ion batteries with higher energy, longer life time, and lower cost, many efforts are being made in both industry and academia to make better NCA and NMC materials. One important approach is to increase the Ni content because with the same upper cut-off voltage, Ni-rich NCA and NMC materials can deliver more capacity.[8] As demonstrated in Figure. 1.1, challenges coming along with increasing the Ni content are cycling stability issues and safety problems. Therefore, improving Ni-rich positive electrode materials is important and a lot of contributions have been made by both industry and academia. Another widely acknowledged trend in positive electrode material development is "Co free" to eliminate costly Co and the child labor issues associated with Co mining. As Co has been used in both NCA and NMC for decades, and has been claimed to play important roles,[9–12] a systematic investigation is needed to fully understand how Co, as well as other elements work in the Ni-rich positive electrode materials.

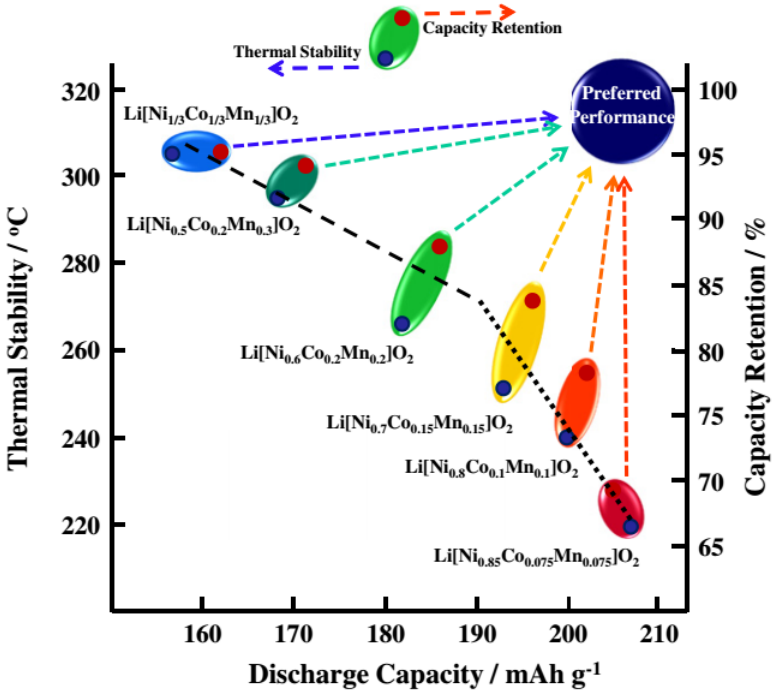

Figure 1.1 Relationship between discharge capacity, thermal stability and capacity retention of Li/Li[Ni$_x$Co$_y$Mn$_z$]O$_2$ (x= 1/3, 0.5, 0.6, 0.7, 0.8 and 0.85) Reprinted with permission from Journal of Power Sources.[8] Copyright (2016) Elsevier.

This thesis is focused on understanding and improving Ni-rich positive electrode materials for Li-ion batteries. As an outline of this thesis, Chapter 1 gives a brief introduction to Li-ion cells covering the cell configuration and three major components (positive electrode, negative electrode, and electrolyte) in a Li-ion cell. Chapter 2 gives a more detailed review of Ni-rich positive electrode materials. Chapter 3 elaborates the experimental methods and theories used throughout works included in this thesis. Chapter 4 presents a study where LiNiO$_2$ is revisited. As Ni content in NMC and NCA materials is increased toward 100%, eventually these materials approach LNO.[9] So it is worthwhile to revisit LNO with modern synthesis and analysis methods for a better understanding of Ni-rich positive electrode materials. Following the studies on LNO, Chapter 5 gives systematic work on the derivatives of LNO. Motivated by the need to eliminate Co in positive electrode materials, the impacts of single cation substitution in LNO was studied with both experiments and calculations. Chapter 5 shows that Co is not needed in Ni-rich positive electrode materials, and the mechanisms for the function of cation substitutions including Co, Mg, Al, and Mn are proposed in this chapter. Chapter 6 and Chapter 7 focus on the synthesis of single crystal NMC and NCA materials. Single crystal NMC positive electrode materials newly developed by industry have been shown to be superior to the conventional polycrystalline counterparts.[13] Chapter 6 discloses the synthesis method for single crystal NMC622 materials and Chapter 7 presents a novel two-step lithiation method for impurity free single crystal NCA materials. Chapter 8 demonstrates an unavoidable challenge for Ni-rich positive electrode materials. A set of data collected with different positive electrode material chemistries shows that there is a universal relationship between capacity retention and accessible capacity. Chapter 9 summarizes the thesis and provides suggestions for the future work.

1.1 Lithium-Ion Batteries

A Li-ion battery is a collection of cells or cell assemblies, with a housing, electrical connections, and possibly electronics for control and protection.[14,15] A Li-ion cell is the basic electrochemical unit in a Li-ion battery, and Figure 1.2 shows that it typically consists of a positive electrode (cathode), a negative electrode (anode), a separator and electrolyte. Li-ion batteries work by shuttling Li ions back and forth inside between the positive and negative electrodes through the electrolyte while transferring electrons in the external circuit simultaneously.

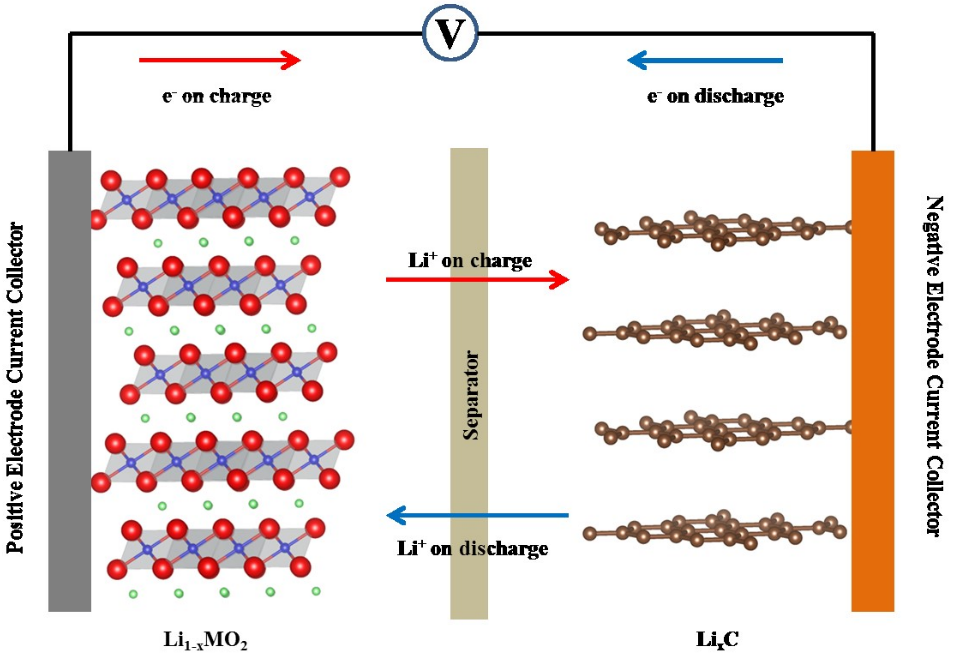

Figure 1.2 A schematic of how a Li-ion cell works during charge and discharge

Choices of positive electrode materials include layered lithium transition metal oxide ($LiMO_2$), spinel lithium transition metal oxide (LiM_2O_4), and lithium metal phosphate ($LiMPO_4$).[1] In Figure 1.2, a layered lithium transition metal oxide is used as an example of a positive electrode. Commercial choices of negative electrode materials typically include carbonaceous materials and silicon-graphite composite materials.[16–18] Both positive and negative electrode materials need to be mixed with a binder, typically polyvinylidene fluoride (PVDF), carboxymethylcellulose, and/or styrene-butadiene rubber (SBR), and a conductive additive, typically a carbon black or graphite. The positive electrode and negative electrode material mixtures are coated onto an Al current collector or a Cu current collector, respectively. The positive electrode and negative electrode are electrically insulated by a separator, typically a microporous polyethylene (PE) or a polypropylene (PPE) film, which can be coated on one or both sides by a thin layer of ceramic particles. In conventional Li-ion cells, liquid electrolyte is used to ionically connect the positive and negative electrodes. The most common electrolyte formulation is a solution of a lithium salt, typically $LiPF_6$, in a blend of organic solvents, typically carbonates.[1,19,20]

Li-ion cells work by shuttling Li ions between the positive and negative electrodes back and forth. During charge, driven by the external power supply, Li ions de-intercalate from the positive electrode material with the same number of electrons transferred through the external circuit. On the negative electrode side, Li ions intercalate between the graphite layers with the same number of electrons added from the external circuit. During discharge, driven by the electrochemical potential difference, Li ion and electron movement is reversed compared to charge. [21–23]

The two half reactions which take place on the positive electrode ($LiMO_2$, layered lithium metal oxide as an example) and the negative electrode (C, graphite as an example) can be represented by the following equations:[1]

$$LiMO_2 \leftrightarrow x\,Li^+ + xe^- + Li_{1-x}MO_2 \qquad (1.1)$$

$$yC + xLi^{+} + xe^{-} \leftrightarrow yLi_{x/y}C \qquad (1.2)$$

The overall reaction can be written as:

$$LiMO_2 + yC \leftrightarrow Li_{1-x}MO_2 + yLi_{x/y}C. \qquad (1.3)$$

In the charge and discharge process, the value of x is determined by the positive electrode material and the upper cut-off voltage (vs. Li). For NMC materials, with the same upper cut-off voltage of 4.3V (vs. Li), NMC811 has an x value of ~0.23, while NMC111 has a value of ~0.36. On the negative electrode side, the value of y or x/y depends on the balance of positive electrode materials and negative electrode materials in the cell.

Li-ion cells using graphite or other negative electrode materials other than metallic Li are referred to as “full cells”. The operation voltage of a full cell is determined by the potentials of both the positive and negative electrodes:

$$V_{cell} = V_{pos.} - V_{neg.} \qquad (1.4)$$

where V_{cell} is the cell voltage, $V_{pos.}$ is the potential of positive electrode, and $V_{neg.}$ is the potential of negative electrode both measured with reference to Li metal. $V_{pos.}$ and $V_{neg.}$ are determined by the chemical potential of the positive and negative electrode materials, respectively. For a half-cell, which has a Li metal disc as the negative electrode, $V_{neg.}$ is fixed at 0 V (vs. Li) and $V_{\mathrm{cell}} = V_{pos.}$ Most commercial Li-ion cells are full cells because of safety issues and poor cycling performance when Li metal is used as the negative electrode material.[24–26] In scientific research, half-cells are extensively used to study the electrochemical properties of positive electrode materials, which can be directly reflected by the cell voltage – composition curve, specific capacity, differential capacity, etc.

1.2 Positive Electrode Materials

Commercial positive electrode materials typically include layered lithium metal oxide, spinel lithium metal oxide and lithium metal phosphate. Among those, layered lithium metal oxide is the most successful positive electrode material. The first Li-ion batteries marketed by Sony in the early 1990's used $LiCoO_2$ as the positive electrode materials, and after almost 30 years, $LiCoO_2$ is still being utilized in batteries for consumer electronic devices. NMC and NCA materials are another family of layered lithium metal oxide materials derived from $LiNiO_2$, and have been drawing great attention in both industry and academia due to high energy density. Both LCO and NMC/NCA have an O3-type layered structure, which can be described in the $R\bar{3}m$ space group (α-$NaFeO_2$-type structure). The oxygen anions are on the 6c sites and adopt an FCC close packing structure with an A-B-C stacking sequence as shown in Figure 1.3. Li atoms are on the 3a sites and transition metals are on the 3b sites forming Li layers and transition metal layers stacked alternatively.[6] The structure is referred as the O3 structure because the unit cell has three transition metal oxide (MO_2) slabs and the transition metals occupy the octahedral sites. In between the MO_2 slabs, Li atoms occupy the octahedral sites. Figure 1.3 shows the layer stacking sequence, a Greek letter indicates the Li plane, a small letter indicates the transition metal plane, and a capital letter indicates the oxygen plane.

The layered structure can be greatly affected by Li content. For LCO, the removal of Li atoms causes a relative shift between the CoO_2 slabs, and it goes through the O3-O6-O1 phase transitions.[27–30] LNO shows the H1-M-H2-H3 multiple phase transitions during the course of Li atom de-intercalation, and the multiple phase transitions in LNO will be discussed in detail in Chapter 4. Although no phase transitions exist in NMC and NCA materials during Li atom de-intercalation and intercalation,[31–33] the structure and stability of materials are highly related to the Li content, and this will be elaborated in Chapter 7.

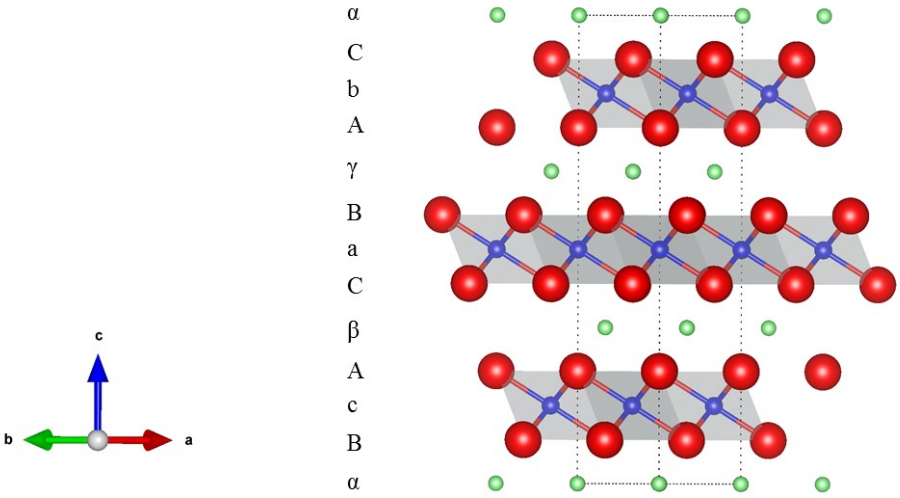

Figure 1.3 Crystallite structure of layered $LiMO_2$ (O3-type). The symbols which align with either a transition metal atom layer (small letter), oxygen atom layer (capital letter) or Li atom layer (Greek letter) show the stacking sequence. The blue, red and green balls show the M, O and Li atoms respectively.

$LiMn_2O_4$ (LMO) is a typical spinel lithium metal oxide positive electrode material with a specific capacity of 100-120 mAh/g. It has good thermal stability and lower cost because of the abundance of Mn.[34,35] $LiMn_2O_4$ adopts a spinel structure with a three-dimensional framework. Li atoms fill one-eighth of the tetrahedral sites within the λ-MnO_2 frame and Mn-centered oxygen octahedral fill one-half of the octahedral sites.[1] The wide application of $LiMn_2O_4$ is limited by its low energy density and poor cycling performance, especially at elevated temperatures. [36–39]

$LiFePO_4$ (LFP) is another commercial positive electrode material with a specific capacity of about 160 mAh/g. It adopts an olivine structure and a three-dimensional framework built by PO_4 tetrahedra and FeO_6 octahedra enables Li atoms to move along one-dimensional tunnels. Due to the poor Li ion conductivity, the particle size of commercial LFP materials is small, generally on the scale of 100 nm. [1] LFP is unreactive with electrolyte even at elevated temperature, which makes it advantageous over NMC and NCA from a safety perspective. However, the low capacity, low voltage, and low packing efficiency due to low tap density make it difficult for LFP to meet the requirement of high energy density in EV applications. [1]

Table 1.1 summarizes the properties and market share of these positive electrode materials.[1,41,] In 2017, the total volume of positive electrode materials was greater than 275,000 tons and the sum of NMC and NCA market share was 42%. It is forecasted that in 2025, the total volume will be larger than 870,000 tons, in which the NMC and NCA material will account for about 78%. The prediction of a huge increase in NMC and NCA market volume is made based on the continuing trend of vehicle electrification and the fact that Ni-rich positive electrode materials are promising candidates for EV battery applications due to the overall advantages in energy density, cycle life and cost. Due to the importance of Ni-rich positive electrode materials in EV industry and battery community, this thesis focuses on the studies of Ni-rich positive electrode materials including fundamental studies, failure mechanism, and novel material development. Chapter 2 presents a detailed literature review of the state of art Ni-rich positive electrode materials.

Table 1.1 Summary of properties of the most common commercial positive electrode materials.

	Specific capacity (mAh/g)	Midpoint V vs. Li at C/20	Theoretical energy density (Wh/kg)	Major OEM users	Market share in 2017	Predicted market share in 2025
NCA	200-220	3.7-3.73	740-820	Tesla	9%	8%
NMC	140-190	~3.8-3.9	532-741	Nissan, Honda	33%	70%
LCO	155-185	3.9-3.95	590-730	Apple, Samsung	14%	6%
LFP	160	3.45	552	BYD	38%	15%
LMO	100-120	4.05	405-486	Nissan	6%	1%

1.3 Negative Electrode Materials

Common negative electrode materials include carbon materials, lithium titanate ($Li_{4/3}Ti_{5/3}O_4$, LTO), silicon-containing materials, and Li metal. Among those, carbon materials are the most commercially successful products widely used in state-of-the-art Li-ion cells. Coke-based material was initially used as the negative electrode material in commercial Li-ion batteries by Sony, and was able to deliver a capacity of 180 mAh/g stably in propylene carbonate containing electrolyte.[1,42] Mesocarbon microbeads (MCMB) were used in the mid-1990s, and can offer a specific capacity of 300-350 mAh/g with low irreversible capacity and good safety properties. Recently, artificial (synthetic) graphite and natural graphite materials have become the negative electrode materials most widely used.

Graphite is built by stacking graphene, which is a planar sheet of carbon atoms arranged in a hexagonal structure. The stacking sequence of graphene sheets can be either ABABAB (2H) type or ABCABC (3R) type.[43] Both types of graphite have the same in-plane carbon-carbon distance of 1.42 Å and the same inter-plane spacing of 3.36 Å.[44] Graphite materials can have both 2H (more common) and 3R stacking, as well as random stacking with shifts or rotation between parallel layers, as well as nonparallel stacking. The term turbostratic misalignment is used to describe the random stacking,[45] and P, the fraction of adjacent parallel misaligned layers, is used to characterize the disorder. The theoretical specific capacity of graphite material can be written as

$$Q = 372(1-P) \text{ mAh/g} \qquad (1.5)$$

where 372 mAh/g is the theoretical specific capacity of graphite. The value of P and the resulting specific capacity of graphite material is affected by heat treatment.[46]

Natural graphite (NG) and artificial graphite (AG) are the most common negative electrode materials in Li-ion battery industry. In 2016, the market share of AG was 46% and the share of NG was 54%. Compared with AG, NG has a lower price, but NG is known to have poor performance reportedly due to surface exfoliation and cracking of particles.[47–50] It is projected by AVICENNE ENERGY that with improved process efficiency and new processes, the price of AG and NG will both decrease.[41] The demand for AG will increase rapidly because of the demand for high performance graphite in the EV market. It is predicted that in 2025, the share of AG will increase to 73%.

Spinel LTO is featured with low reactivity with electrolyte and better rate capability due to higher operating voltage compared with graphite.[51–53] The high operating voltage makes it uncompetitive for EV applications due to low energy density. Silicon-containing materials can provide a higher specific capacity, but Si, Si-O, and Si alloys all suffer from large volumetric change and irreversible structural change during charge and discharge, which makes it challenging to work as a negative electrode material.[16] However, when blended with graphite, Si-O materials have been successfully utilized in commercial Li-ion cells.[16,54,55] The use of Li metal as a negative electrode and the realization of “anode-free” cells have been an important effort aiming to boost the energy density of Li-ion cells.[56–59] However, more work is still needed to overcome many existing challenges like cycling stability and safety issues.

1.4 Electrolyte Systems.

Commercial Li-ion cells typically use non-aqueous liquid electrolytes, which are solutions of lithium salts in organic solvents. Electrolyte additives, which are typically added into electrolytes at less than 5% by weight, play significant roles in the electrolyte systems providing benefits in cell safety, cycle lifetime, etc.[1]

Ideal lithium salts should be able to completely dissolve and dissociate in solvents, be stable against oxidative decomposition, be inert to electrolyte and cell components, and be able to move with high mobility.[19] Taking all the factors into consideration, lithium hexafluorophosphate ($LiPF_6$) becomes the most appropriate lithium salt to be used in Li-ion cells due to its well-balanced properties: high ionic conductivity (10^{-2} S/cm)[60] in carbonate solvents, high Li^+ transference number (~0.35), and acceptable safety properties. Some borates and imide salts heavily investigated by academia include lithium tetrafluoroborate ($LiBF_4$),[61] lithium bisoxalato borate (LiBOB),[62] lithium difluorooxalatoborate (LiDFOB),[63] lithium bis(fluorosulfonyl)imide (LiFSi),[64–66] and lithium bis(trifluoromethanesufonyl)imide (LiTFSi).[67] These salts have shown advantages in some specific aspects like high temperature stability, better solid state electrolyte interface (SEI) formation, improved stability against electrode, etc. [63,68–73] However, compared with $LiPF_6$, these salts provide improvements with significant sacrifice of other important properties, which makes them not able to challenge the dominance of $LiPF_6$.

The solvents are usually a mixture of organic carbonates, typically the cyclic structured ethylene carbonate (EC) which has a high dielectric constant to dissociate salts, in combination with linear structured dimethyl carbonate (DMC) and/or ethyl methyl carbonate (EMC), which have low viscosity to enable fast ion transport.[19] Other organic solvents such as methyl acetate (MA) and fluorinated solvents like fluoroethylene carbonate (FEC) are also used to yield improvements in transport properties and SEI formation quality.

Electrolyte additives play important roles in improving cell performance. Studies show that additives can improve SEI stability, mitigate gassing, scavenge HF or water, form protective layers on the positive electrode, control impedance growth and improve cell safety.[20,74,75] Among those, vinylene carbonate (VC), FEC, $LiPF_2O_2$ (LFO) and ethylene sulfate are common additives used to improve cell cycle life by forming high quality SEI layers. [76–80]

Studies have shown that the development of positive electrode and negative electrode materials cannot be isolated from the electrolyte systems, thus comprehensive consideration and investigation of each part of a Li-ion cell is necessary to make improvements.

CHAPTER 2 Ni-RICH POSITIVE ELECTRODE MATERIALS

2.1 Background

Layered lithium transition metal oxide materials, which include $LiCoO_2$ and NMC/NCA materials, are currently the most dominant positive electrode materials used in Li-ion cells for consumer electronic devices and EVs. Chapter 1 presented a brief introduction of $LiCoO_2$ and NMC/NCA materials, which have the same crystal structure. As high Ni content positive electrode materials have drawn great attentions due to advantages in cost and energy density, this chapter focuses on the basics of Ni-rich positive electrode materials. Although $LiCoO_2$ and $LiNiO_2$ have the identical R-3m structure and Ni is adjacent to Co in the periodic table, the two materials behave differently during charge and discharge as mentioned in Chapter 1. Derived from $LiNiO_2$, NMC and NCA materials adopt the same layered hexagonal crystal structure as $LiNiO_2$, but the addition of Mn, Co and Al cations change the electronic structures. This first half of this chapter will present background information about the crystallography and electronic structures of NMC and NCA materials. As the Ni content is increased to higher levels, more challenges in cycling stability and safety start emerging.[81] The second part of this chapter presents a brief review of recent developments aiming to overcome these challenges.

2.1.1 Crystallography

Figure 1.3 shows the crystal structure of $LiMO_2$ and the stacking sequence of transition metal, lithium and oxygen atoms are noted by small, Greek and capital letters. Figure 2.1 shows an FCC (face centered cubic) close packed structure that the oxygen atoms adopt. Li and M atoms fill the planes marked by red triangles alternatively, and the sites for Li and M atoms are equivalent. A rhombohedral space group, R-3m, is appropriate to characterize the structure and symmetry of $LiNiO_2$. Figure 1.3 shows the structure and unit cell marked by dashed lines, in which Ni atoms are at 3b (or 3a) sites marked by blue balls in; and for NMC/NCA materials, the Ni, Mn, and Co cations or Ni, Co, and Al cations are randomly distributed on the 3b (or 3a) sites marked by blue balls.

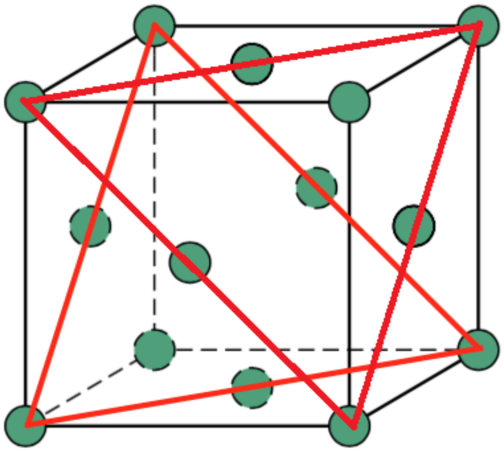

Figure 2.1 Face centered cubic (FCC) close packing structure.

An ideal stoichiometric $LiNiO_2$ or NMC/NCA material should have no inter layer cation mixing. However, real materials have Ni/Li mixing, and it is found that Ni^{2+} is prone to move to the lithium layers due to the similar size of Ni^{2+} and Li^+ ions.[82,83] Studies show that the inter layer mixing originates from the nature of $LiNiO_2$, which is one composition within the solid solution series of $Li_{1-x}Ni_{1+x}O_2$.[84,85] For an ideal LNO, x=0, all the Ni atoms are in the form of Ni^{+3}, a layered hexagonal structure forms due to steric effects, which accommodate the large size difference between Ni^{+3} (0.56 Å) and Li^+ (0.76 Å). [86–88] As the x increases, more Ni^{2+} (0.69 Å) ions exist. When x is greater than 0.38, a phase transition from layered hexagonal structure (R-3m space group) to a disordered rock salt structure (Fm-3m space group) takes place.[89,90] In practice, it is hard to oxidize all the Ni atoms to Ni^{+3} during synthesis. Even LNO and NCA materials made with modern synthesis methods have at least ~1-2% of Ni atoms in the Li layers.[9,91] For NMC materials, the Mn^{4+} ions make it inevitable to have Ni^{+2} ions to compensate the charge. Studies show that without Co, more Mn substitution results in a higher degree of Ni/Li mixing, while adding Co can reduce the Ni/Li mixing.[10,11,32,88,92]

2.1.2 Electronic Structure

The electronic structure of Ni-rich positive electrode materials has a significant influence on both the structural properties and electrochemical properties. During charge and discharge, Li ion intercalation is accompanied by redox reactions. Electrons are added to/removed from the 3d orbitals of the transition metal atoms, which are hybridized with oxygen 2p orbitals to some degree. The configuration that one transition metal is coordinated by six oxygen atoms creates a crystal field, which splits the 3d orbital of the transition metal into two sets labeled as e_g and t_{2g} bands.[93–96] For NMC materials, in-situ

X-ray absorption spectroscopy (XAS) studies show that the oxidation states of Ni and Co cations change between 2+/3+ to 4+ and 3+ to 4+, respectively, during charge and discharge, while the Mn cations remain unchanged at 4+.[97] Compared with NMC, the difference is that Al atoms in NCA materials are believed to be electrochemically inactive.

Figure 2.2(a) shows electron probability distribution of the five 3d orbitals of a transition metal in octahedral coordination and Figure 2.2(b) shows common electronic energy level positions of the 3d orbitals for cationic Ni, Co, and Mn species. The black arrows indicate electrons with different spins. In octahedral coordination, the interaction between orbitals that lie on x, y, and z axes and ligands are stronger. The stronger interaction results in splitting of the levels into the e_g ($d_z{}^2$ and $d_{(x^2-y^2)}$ levels) and t_{2g} (the other three orbitals) levels. The e_g band of Ni^{3+} and Mn^{3+} cations have one electron. This configuration makes the MO_2 octahedra susceptible to a Jahn-Teller distortion, an elongation or compression of the bonds along one of the octahedra axes, which lowers the overall energy of the solid by breaking the degeneracy between the two e_g orbitals, and the lower-energy orbital is occupied by the electron.[98] Some studies suggest that the Jahn-Teller distortion is partially responsible for the hexagonal to monoclinic phase transition observed in $LiNiO_2$.[99,100]

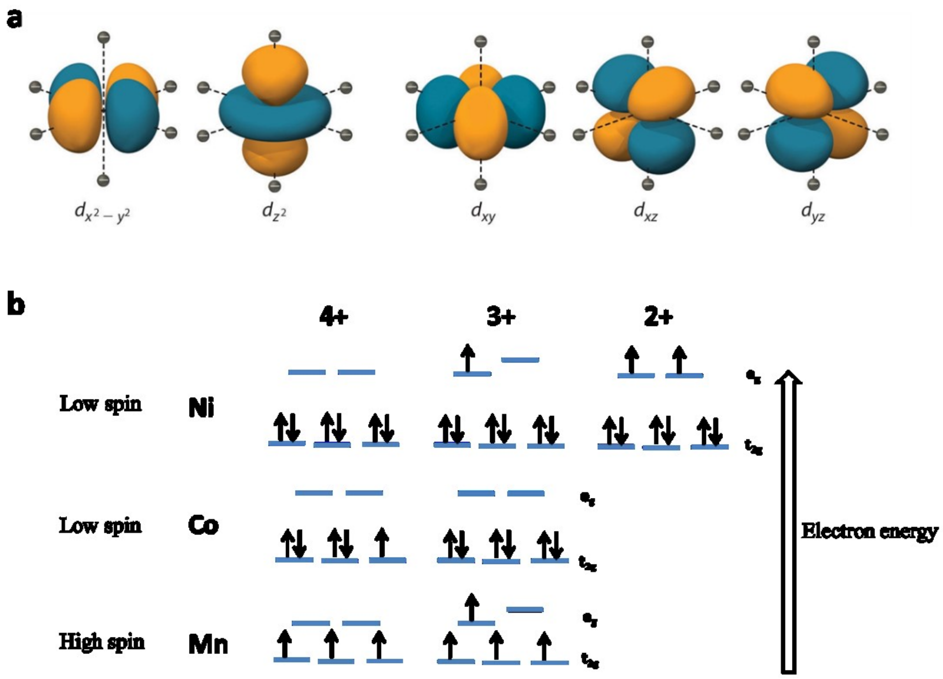

Figure 2.2 (a) Electron probability distributions for the five d orbitals for a transition metal in octahedral coordination; (b) common electronic energy level positions of the 3d orbitals for cationic Ni, Co, and Mn species.

As Li intercalation/de-intercalation is associated with electron transfer to and from transition metal cations, the electrochemical properties are related to the electronic structure. Figure 2.3 shows an oversimplified relative electron energy alignment for the 3d bands of Ni, Mn, Co, and the 2p band of oxygen. Lower electron energy means higher stability, which corresponds to higher Li intercalation/de-intercalation voltage. Figure 2.3 shows that the Co^{3+}/Co^{4+} level is the lowest among Ni, Mn, and Co because it involves the electron on the more stable t_{2g} band. The Mn^{3+}/Mn^{4+} couple has the highest electron energy, which makes the electron transfer from Mn^{3+} to Ni^{3+} spontaneous, yields Mn^{4+} and Ni^{2+} in common NMC materials.[101–103] For NMC materials with a Mn content lower than or equal to the Ni content, the Mn^{4+} cations stay electrochemically inactive during charge and discharge. In the simplest possible picture, where the hybridization of the 3d orbital with oxygen 2p orbital is neglected, during the course of Li de-intercalation, electrons are first removed from Ni^{2+} followed by further oxidation of Ni^{3+}, and then finally Co^{3+} to Co^{4+} occurs. This explains the fact that in the NMC series, materials with higher Ni content can deliver more specific capacity to the same upper cutoff voltage. This model is oversimplified to illustrate the impacts of electronic structure on electrochemical properties. For real NMC materials, the oxidation of different cations is not a discrete process, and the electronic structure is also dynamic during Li (de)intercalation.[93]

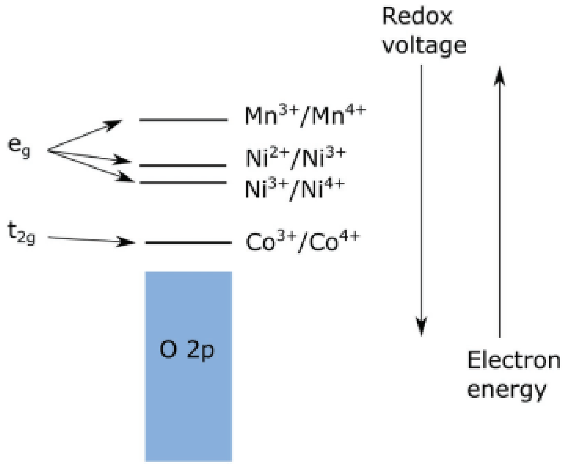

Figure 2.3 An oversimplified relative electron energy alignment for 3d band of Ni, Mn, Co, and the 2p band of oxygen. Reprinted with permission from Advanced Energy Materials.[93] Copyright (2017) John Wiley and Sons.

2.2 Challenges for Ni-Rich Positive Electrode Materials

Figure 1.1 shows that pushing Ni content to a higher level enables more accessible capacity, while the tradeoff is a compromise in cycling and thermal stability. For Ni-rich positive electrode materials, there are some existing challenges spanning from material synthesis, material handling, to cell performance and safety.

2.2.1 Surface Soluble Base Content Control

The use of an excess of Li source during synthesis is usually necessary to compensate for Li loss at high heating temperature. Due to this, a challenge in Ni-rich positive electrode material synthesis and handling is the control of residual soluble base content (SBC), typically lithium compounds, on the surface of synthesized materials. Jens Paulsen et al. showed that material with higher Ni content tends to form more SBC during synthesis, and the gas flow, heating temperature, and heating time are critical parameters to optimize the SBC formation.[104] Faenza et al.[105] proposed a mechanism for lithium impurity formation on NCA materials during storage, and pointed out the importance of moisture control. Work from Sicklinger and Jung et al.[106,107] revealed that high Ni content NMC is more susceptible to reactions with ambient air forming basic products, as well as transition metal hydroxides/carbonates.

In Li-ion cells, the undesired SBC on the surface of positive electrode materials can lead to side reactions with electrolyte during cycling, and further result in gas [108,109] and poor cycling stability.[107] In the positive electrode material industry, a washing-drying process is generally applied to eliminate the residual lithium compounds after heating.[110]

However, besides the additional cost of adding a washing-drying step, studies show that washing process can make the material more sensitive to moisture, and further gives rise to sever capacity fading issues.[111]

2.2.2 Material Degradation

Another challenge for Ni-rich positive electrode materials is poor capacity retention during charge-discharge cycling, which worsens as the Ni content increases. The structural reconstruction from layered structure to spinel and rock salt structure, mainly on the surface of positive electrode material particles, is a failure mechanism that numerous studies propose.[112–117] The mechanism is not well understood yet. Some studies show that in the delithiated state, Ni-rich materials have more the tetravalent Ni ions, which increase the covalent nature of Ni-O bonding, and oxygen is less reduced resulting in the formation of oxygen-containing compounds.[112,118,119] The destabilized oxygen atoms and further oxygen evolution provide a strong thermodynamic driving force for the phase transition from layered structure to spinel structure, and finally to the rock-salt structure. The phase transition in the bulk is kinetically hindered by poor oxygen diffusivity, while it easily occurs on the surface.

The positive electrode/electrolyte interfacial reaction is another cause of capacity fading. The side reactions include spontaneous chemical reactions occurring upon the contact of positive electrode materials with electrolyte,[120,121] and electrochemical reactions, which proceed during cycling.[19,122] The reactions can consume the lithium inventory[123–125] and also form a film like layer containing species like lithium carbonate, lithium fluoride, and alkyl carbonates on the positive electrode materials which can impede Li ion transport.[54,126,127]

For layered lithium transition metal oxide cathode materials, many failure mechanism studies attribute some portion of cell degradation to micro-cracks which form in the secondary particles causing impedance growth and active material loss. [128–134] As a result of cracking, electrolyte infiltration into the particle interior can further worsen the cell performance. Such cracking issues were identified in studies of NCA materials by Y. Makimura et al.[132] It is believed that the secondary particle cracking issue is highly related to the anisotropic volume change during charge and discharge, which has been observed in both NCA and NMC materials.[31,32] H. Ryu et al.[135] showed that in the NMC series, the problem of micro-crack generation during cycling becomes more severe as the Ni content increases.

2.2.3 Safety

The safety of Li-ion batteries is a big concern for EV manufacturers and consumers. In the case of an internal short circuit, a large amount of heat will be generated. If the heat cannot be dissipated out efficiently, the internal temperature of the cell rises and triggers several reactions.[136–141] On the positive electrode side, the delithiated positive electrode material decomposes when heated sufficiently. This exothermic reaction releases oxygen, which reacts further with the electrolyte to release more heat and trigger more positive electrode material decomposition. This positive feedback loop is known as a thermal runaway and the temperature of the cell rises uncontrollably. Studies have shown that charged $LiNiO_2$ and its Ni-rich derivatives are less thermally stable than other materials.[137–146] Similar to Figure 1.1, the thermal instability has been correlated to the Ni content by many studies.[81,137,143,146–150] In addition, the state of charge, or degree of delithiation, also affects the decomposition temperature. [137,142,144,150–152]

2.3 Recent Developments

As discussed in the previous section, the degradation mechanisms of Ni-rich materials are complex and interrelated with each other. To fulfill the need for higher energy density, efforts to overcome the challenges for Ni-rich positive electrode materials are being continuously made by both industry and academia. This section briefly reviews some major state-of-art approaches applied to make improvements from various perspectives, including bulk structural stabilization, morphology and surface modification.

2.3.1 Cation Substitution

Cation substitution is the most successful approach in the development of NMC and NCA materials. On the basis of $LiNiO_2$, NMC and NCA materials were developed by partially replacing Ni with Mn/Co, and Co/Al, respectively. H. Arai et al.[153] reported that Mn substitution could enhance the thermal stability of the material in the delithiated state. Substitution of Al for Ni was shown to improve the thermal stability and safety.[154,155] Partial replacement of Ni with Co was thought to be effective to the structure stabilization by hindering the cation mixing between Ni^{2+} and Li^{+} [10,11], and suppressing the multiple phase transitions during charge and discharge.[12] Facing the existing challenges for Ni-rich NMC and NCA materials, researchers proposed a quaternary material, NCMA, which combines NMC and NCA and shows improvements in many aspects as shown in a work by U.H. Kim et al.[156]

Other substituents were also explored. Work by the group of Y. Ukyo et al. on Mg substituted into NCA[157–159] showed that Mg substitutions helped to eliminate particle cracking and hence improved charge-discharge capacity retention. Q. Xieet al. also shows the benefits of adding Mg into $LiNi_{0.94}Co_{0.06}O_2$.[160] K. Park et al.[161] showed that doping $LiNi_{0.9}Mn_{0.05}Co_{0.05}O_2$ with boron can alter the orientation of primary particles and form a well aligned radial close packed geometry, which reduces the negative effect of particle anisotropic volume change during cycling and can alleviate cracking issues. Ti, Fe, and W dopants were also studied by researchers over the years, and were shown to be beneficial in structural stabilization upon cycling.[162–165]

2.3.2 Core-Shell and Concentration Gradient

As previously discussed, one tradeoff of Ni-rich positive electrode materials is increased cycling capacity fade, which is shown to be related to the high Ni content. It is demonstrated that the degradation generally starts from the surface of particles due to the contact with electrolyte and facile oxygen loss. A concept of core-shell particle structure design was initially proposed by the group of Y.K. Sun,[166–169] and has been adopted by many researchers.[170,171] The design is to encapsulate a Ni-rich core with a Mn-rich shell. The Ni-rich core can deliver the desired high specific capacity, and the Mn-rich shell, which is more stable against electrolyte, can protect the core. Studies show that the core-shell structure renders an improvement in both cycling stability and thermal stability.[166,169]

To overcome issues with core-shell materials, concentration gradient materials were proposed. Core-shell materials were found to have several problems such as a large sacrifice in capacity due to the low capacity of Mn-rich shell, and strains caused by lattice mismatch between core and shell during charge and discharge.[172] Figure 2.4 shows a schematic of core-shell design and two concentration gradient designs. [143] Compared to Gen 1, the shell of Gen 2 has a concentration gradient within the shell, in which the Mn concentration decreases linearly from the outer layer to the inner layer of the shell. For Gen 3, the full concentration gradient design has a continuous compositional change from the center of the particle to the surface.

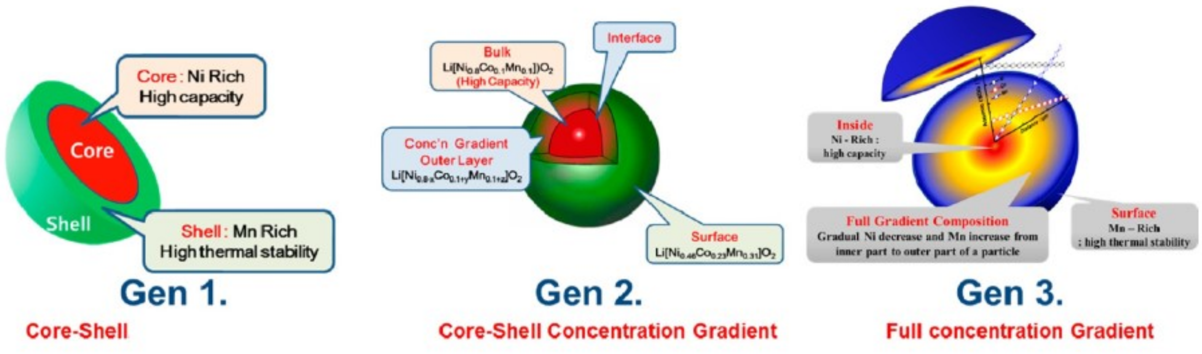

Figure 2.4 A schematic of core-shell, core-shell concentration gradient, and full concentration gradient positive electrode materials.[143] Reprinted with permission from ACS Energy Letters.[143] Copyright 2017 American Chemical Society

2.3.3 Single Crystal

Many studies have shown that the generation of micro-cracks in Ni-rich positive electrode materials during cycling is partially responsible for the cell failure.[128–135] Micro-cracks in the secondary particles are believed to be triggered by anisotropic volume changes (during charge and discharge) of the primary particles which make up the secondaries. Therefore, a simple strategy to eliminate micro-cracks is to use single crystal positive electrode materials. Figure 2.5 shows a comparison between conventional polycrystalline NMC532 (UC-532) and single crystal NMC532 (SC-532). Conventional polycrystalline materials typically have spherical secondary particles of 10-18 µm, consisting of small primary grains of 100-300 nm in size. In comparison, single crystal materials have monolithic primary particles, each of which is a single crystal of 3-5 µm in size. The term “single crystal” used in this thesis refers to ideally monolithic particles of 2- 5 µm in size that have no grain boundaries.

Single crystal positive electrode materials are believed to maintain particle integrity during cycling.[173] The advantages of commercially available single crystal $LiNi_{0.5}Mn_{0.3}Co_{0.2}O_2$ (NMC532) has been reported by J. Li et al.[174]. Their work showed that when appropriate electrolyte systems were used, cells using single crystal NMC532 had much longer cycle life and calendar life than cells using polycrystalline NMC532.

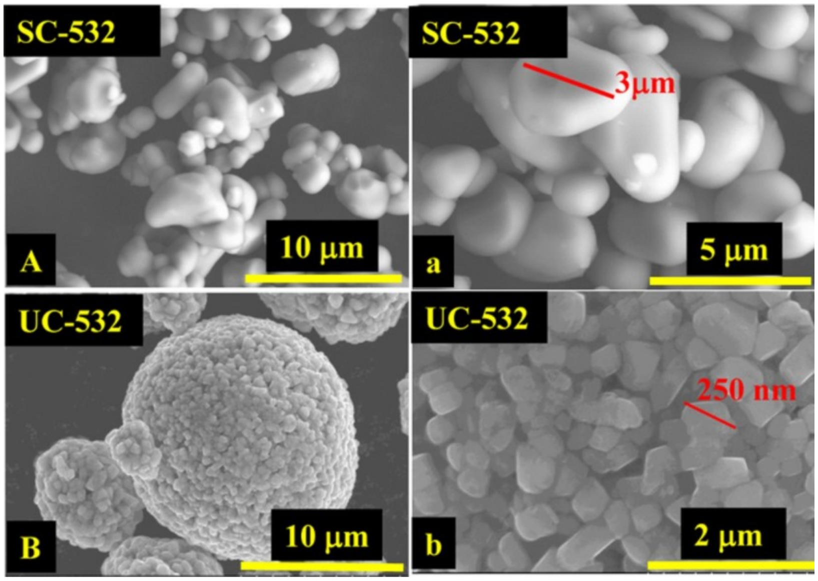

Figure 2.5 SEM images of a commercial single-crystal $Li[Ni_{0.5}Mn_{0.3}Co_{0.2}]O_2$ (NMC532) (called SC-532) material with large grain size of ~3 µm (A, a), SEM images of commercial polycrystalline (NMC532) without coating (UC-532) (B, b).[174] Reproduced with permission from *J. Electrochem. Soc.*, 164.7 (2017): A1534-A1544. Copyright 2017, The Electrochemical Society.

2.3.4 Coatings

Surface coating is another important approach to improve the electrochemical performance of Ni-rich materials. The idea is to artificially create a SEI-like layer between the positive electrode materials and the electrolyte. An ideal coating layer should have several critical properties: 1. uniform distribution on particle surface; 2. good Li ion conductivity; 3. chemical and electrochemical stability; 4. good mechanical strength.[93] Typical coating materials include oxides (ZrO_2, TiO_2 CeO_2, Al_2O_3, ZnO, Sb_2O_3 and CuO), fluorides (AlF_3, LaF_3, and ZrF), and phosphates ($FePO_4$ and $AlPO_4$).[93] Among those, Al_2O_3 has been the most commonly used coating candidate, but the mechanism of how oxide materials conduct Li ions is still unclear. Besides serving as a protection layer for positive electrode materials, some synergic effects may also offer benefits.[175,176] Some Li-ion conductors are proposed as coating materials, such as lithium lanthanum titanium oxide, lithium aluminum titanium oxide, $LiFePO_4$, Li_3PO_4, and Li_3VO_4.

Common coating methods include wet chemistry methods, atomic layer deposition (ALD), and mechanofusion. Wet chemistry is widely used due to process simplicity and low cost. However, the use of aqueous solutions makes it an issue for Ni-rich positive electrode materials, which are highly sensitive to moisture. ALD is able to make the desired homogenous thin coating layers,[177] but the high cost and limited chemical choices are the major problems. Mechanofusion is a coating method which uses mechanical force to fuse the coating materials on the surface of particles.[178,179] In principle, it is capable of coating anything on anything with a low cost and easy control of coating thickness.

The above mentioned coating methods are generally used to coat the secondary particles when applied to the conventional polycrystalline positive electrode materials. Recently, researchers introduced a method of coating the primary particles by a novel wet chemical approach. H. Kim et al. [180] showed that a spinel structured coating on primary particles can serve as a "glue layer", and leads to improved particle integrity after cycling in $LiNi_{0.6}Mn_{0.2}Co_{0.2}O_2$ (NMC622) cells. A similar work by K. Min et al.[181] showed that the coating on primary particles improved the cycling of $LiNi_{0.91}Co_{0.06}Mn_{0.03}O_2$ by suppressing particle cracking.

CHAPTER 3 EXPERIMENTAL TECHNIQUES

3.1 Material Synthesis

The synthesis of lithium transition metal oxide positive electrode materials includes the preparation of metal hydroxide precursors and a following heating or lithiation process. The state-of-art precursor synthesis approach is the co-precipitation method. The lithiation step is done by heating a precursor with a lithium source at high temperature.

3.1.1 Co-Precipitation Method for the Synthesis of Precursors

Metal hydroxide precursors were prepared by co-precipitation using a continuously stirred tank reactor (CSTR). Compared to solid-state synthesis, the advantages of the CSTR co-precipitation method includes high tap density of synthesized materials, more homogeneous cation distribution, and facile control of particle size.[182–186] Figure 3.1 shows a schematic of the CSTR co-precipitation system used and Figure 3.2 shows a photo of the CSTR system (Brunswick Scientific/Eppendorf BioFlo 310). A typical CSTR setup includes a jacketed glass vessel, an airtight metal lid with gas/solution inlets and outlets, an overhead stirrer, a pH probe and a temperature probe. The co-precipitation process is controlled by a computer which controls the digital peristaltic pumps based on the pH and temperature readings.

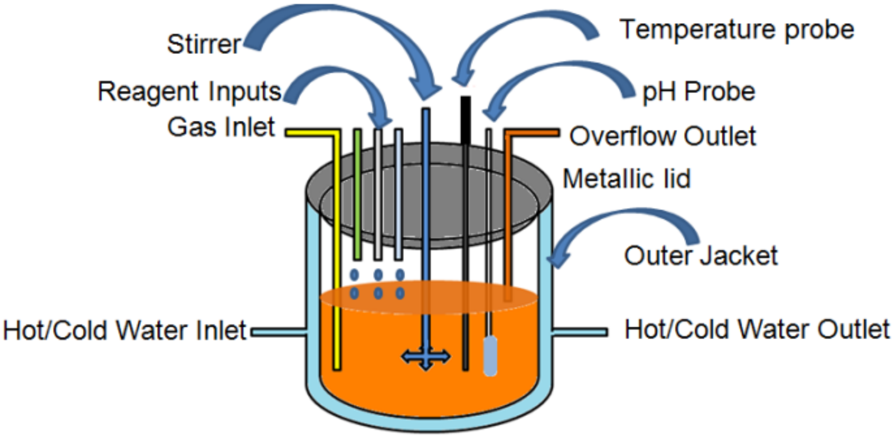

Figure 3.1 Schematic of a typical CSTR co-precipitation system

Figure 3.2 Photo of the operating CSTR co-precipitation system used in this work

For typical NMC precursor synthesis, $Ni_xMn_yCo_zSO_4$ solutions are prepared by dissolving nickel (II) sulfate hexahydrate ($NiSO_4 \cdot 6H_2O$, 98%, Alfa Aesar), manganese sulfate monohydrate ($MnSO_4 \cdot H_2O$, 98%, Alfa Aesar), and cobalt sulfate heptahydrate ($CoSO_4 \cdot 7H_2O$, 98%, Alfa Aesar) into deaerated deionized (DI) water with Ni:Mn:Co molar ratios of x:y:z. The use of dearated DI water is to avoid oxidizing divalent cations. The total metal ion concentration of each solution is 2.0 M. A volume of 1 L of 1.0 M ammonium hydroxide solution ($NH_4OH_{(aq)}$, 28.0–30.0%, Sigma-Aldrich) is added into the vessel and heated to 60°C before the reaction starts. During the reaction, a solution of 5.0 M $NH_4OH_{(aq)}$ and the mixed metal sulfate (MSO_4) solutions are constantly added into the vessel using digital peristaltic pumps at a rate of 0.14 ml/min and 0.5 ml/min, respectively. A 10.0 M sodium hydroxide (NaOH, 98%, Alfa Aesar) solution is added to the vessel as the source of base by a pump controlled by the pH probe and the computer to maintain a desired pH value. The reaction temperature is kept at 60°C by a hot water jacket, N_2 gas flows through the vessel constantly at a rate of 60 sccm (standard cubic centimeter per minute), and the contents of the reactor are stirred by an overhead stirrer at 800-1000 rpm.

The properties of the synthesised precursors are highly correlated to the experimental conditions of the co-precipitation. Studies have shown that NH_4OH works as a chelating agent, which increases the solubility of metal hydroxides and promotes the growth of spherical dense particles by a dissolution-recrystallization process.[183] The pH value is another critical experimental parameter. Van Bommel et al.[183] have shown that the particle size and tap density of the synthesized materials are highly dependent on the pH value. They also showed that the concentrations of Ni^{2+}-NH_3, Co^{2+}-NH_3 and Mn^{2+}-NH_3

change differently with pH value, therefore, different NMC compositions require different optimal pH values to obtain the desired dense spherical particles. For Ni-rich precursors, the pH range is typically 10-11. The use of deaerated DI water and N_2 gas flow is to protect the divalent metal cations from getting oxidized during co-precipitation. Zhou et al.[182] reported that air exposure during synthesis cause the formation of a layered double hydroxide (LDH) phase and a spinel phase if Mn ions exist. The LDH phase can cause low tap density and the formation of the spinel phase effects the uniform cation distribution. Reaction time also has influence on precursor qualities. Insufficient reaction time leads to small and irregular shaped particles. The reaction time was typically set to 12-24 hours.

For NCA and other Al containing layered positive electrode materials, precursor synthesis is slightly different because trivalent Al ions are present. Because ammonia does not complex well with Al cations, conventional co-precipitation method is not applicable. Liu et al.[187] and other researchers[188–190] reported a method of NCA precursor synthesis. The mixed solutions of $NiSO_4$ and $CoSO_4$ were prepared as described previously, while a solution of $[Al(OH)_x]^{3-x}$ solution was prepared and added into the reaction vessel separately and simultaneously with other reagents. Due to the presence of Al^{3+}, the formation of an LDH phase is expected. To remove or partially remove the LDH phase, a method of washing with hot concentrated NaOH solution was reported by Liu et al. [187]

The products of co-precipitation were filtered and rinsed with 4 L of DI water. Then the wet precipitates were dried in an oven at 100-120°C for about 12 hours.

3.1.2 Lithiation of Precursors

The precursors were mixed thoroughly with a stoichiometric equivalent of Li_2CO_3 (from Chemetall > 99%) or $LiOH \cdot H_2O$ (purity > 99.8%, FMC Corporation) by ball milling or hand milling using a mortar and a pestle. Samples with a desired lithium/transition metal molar ratio (Li/TM ratio) were prepared. **In this thesis, with respect to the Li/TM ratio, all metals other than Li are classified as transition metals, even though Al and Mg are not transition metals.** This convention is used because these metals are targeted to occupy the same positions in the crystal structure, i.e. the Ni sites in $LiNiO_2$ which are the transition metal sites. The mixed powders were preheated in oxygen in a tube furnace at 485ºC ($LiOH \cdot H_2O$) or 800ºC (Li_2CO_3)for 3 hours. A heating rate of 10ºC/min was used to increase the temperature to the set point. The preheated powders were taken out of the furnace and ground again by hand milling to minimize areas of local Li compound excess. The ground powders were then heated in the tube furnace (⌀ 5 cm) under an oxygen flow of 60 sccm at 485ºC for 2 hours, and then at designated temperature for 12-20 hours. A heating rate of 10 ºC/min was used to change temperatures. The first three hours of heat treatment is to melt, decompose and mix the lithium source uniformly with the precursor. During this step, initial reactions like dehydration and oxidation of the lithium source and the precursor also occurs. The mass of material synthesized in each batch was 5 g - 7.5 g.

3.2 Material Characterizations

3.2.1 X-Ray Diffraction (XRD)

X-ray diffraction was used to understand the structural properties of synthesized materials. The elastic scattering of X-ray photons by electrons of atoms enables the observation of diffraction patterns caused by the constructive interference according to Bragg's law. The diffraction patterns can be used for material phase identification, and with Rietveld refinements, more detailed structural information can be extracted.

3.2.1.1 Bragg's Law

Figure 3.3 shows the diffraction of X-rays by the atoms of a crystal. As an oversimplified model, it illustrates how constructive interference happens. The two red parallel beams represent the incident X-ray, and the two blue beams represent the X-ray diffracted by two atoms. The red and blue dashed lines represent the wave front. This diagram shows that the path difference between the two paths, diffracted by the two atoms, is $AB+BC=2d\sin\theta$. If the scattered waves are to be in phase and interfere constructively, then

$$2d\sin\theta=n\lambda \qquad (3.1)$$

Where n is an integer and λ is the wavelength. Equation 3.1 is referred to Bragg's law.[191]

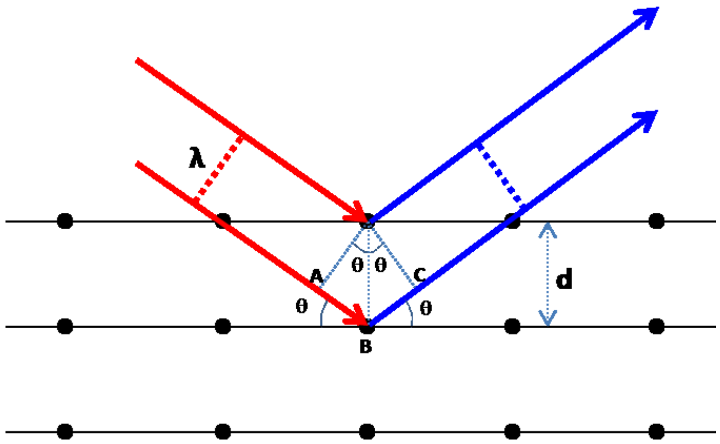

Figure 3.3 Diffraction of X-rays by a crystal.

3.2.1.2 Intensity of Diffraction

The intensity of scattered beams is affected by the crystal on three scales, electrons, atoms, and unit cell. In a classical picture, electrons can be driven to oscillate by an incident X-ray beam, which is an electromagnetic wave. The oscillation of an electron results in the radiation of X-ray beams with the same wavelength and frequency as the incident beam, and this is how X-rays are scattered by electrons. The scattered X-rays are emitted in all directions, and the intensity of the scattered beam depends on the scattering angle by the Thompson equation:

$$I = I_O \frac{K}{r^2}\left(\frac{1+\cos^2 2\theta}{2}\right) \qquad (3.2)$$

where I_O is intensity of the incident beam, K is a constant ($7.94*10^{-30}$ m^2), r is the distance from the electron to the detector, and 2θ is the scattering angle. The Thompson equation gives the absolute intensity of X-rays scattered by a single electron.

At the level of atoms, which have Z electrons in each atom with an atomic number of Z, the overall scattering intensity by all the electrons in one atom is dependent on the atomic number Z, the scattering angle, and the wave length of the incident beam. The atomic scattering factor f is defined as the ratio of the amplitude of the wave scattered by an atom to the scattering amplitude of an electron. When the scattering is in the forward direction ($\theta=0^{o}$), the overall scattering intensity from an atom is the sum of the waves scattered by its component electrons, and f is equal to Z. If the scattering is in other directions, the wave path difference between different electrons can cause partial interference, and f is therefore less than Z. The value of f decreases with the increase of $\frac{\sin\theta}{\lambda}$ (larger diffraction angle and shorter wavelength lead to greater interference).[191]

At the scale of a unit cell, the scattered beams from different atoms interact with each other, which makes destructive interference possible even when Bragg's law is satisfied. The geometrical structure factor F_{hkl} is introduced to take the interference of individual atoms in the unit cell into account, and it is given by:

$$F_{hkl} = \sum_{1}^{N} f_n e^{2\pi i(hu_n + kv_n + lw_n)} \qquad (3.3)$$

where the summation extends over all N atoms of the unit cell, hkl are the Miller indices for lattice planes, (u_n, k_n, w_n) are the fractional atomic coordinates of individual atom n, and f_n is the atomic scattering factor of atom n The diffraction intensity of X-rays scattered from the (hkl) planes is proportional to $|F_{hkl}|^2$. [191]

3.2.1.3 XRD Data Collection

In this thesis, powder X-ray diffraction (XRD) was conducted to study the structure of the materials using a Siemens D5000 diffractometer equipped with a Cu target X-ray tube and a diffracted beam monochromator. Figure 3.4 shows a schematic of the Bragg-Brentano diffractometer. The X-ray beams generated by the X-ray tube first pass through the divergence slit and then reach the sample and get scattered. The focusing circle in Figure 3.4 changes with the scattering angle 2θ, and the use of a flat specimen keeps the changing sampling arc within the specimen during testing, but also causes broadening in diffraction peaks. [191] The scattered beams pass an anti-scattering slit, which screens beams scattered by air, and a receiving slit, which improves the resolution. Then the beams go through a monochromator to filter out Cu K_β and fluorescence radiation before striking the detector. [191] Most diffraction patterns in this thesis were collected in the scattering angle (2θ) range of 15–70^o at 0.02^o intervals with a dwell time of 3 s. A 1^o divergence slit, 1^o anti-scattering slit and 0.2 mm receiving slit were used for the measurements. The collected XRD patterns were refined (Rietveld method) using "Rietica".[192]

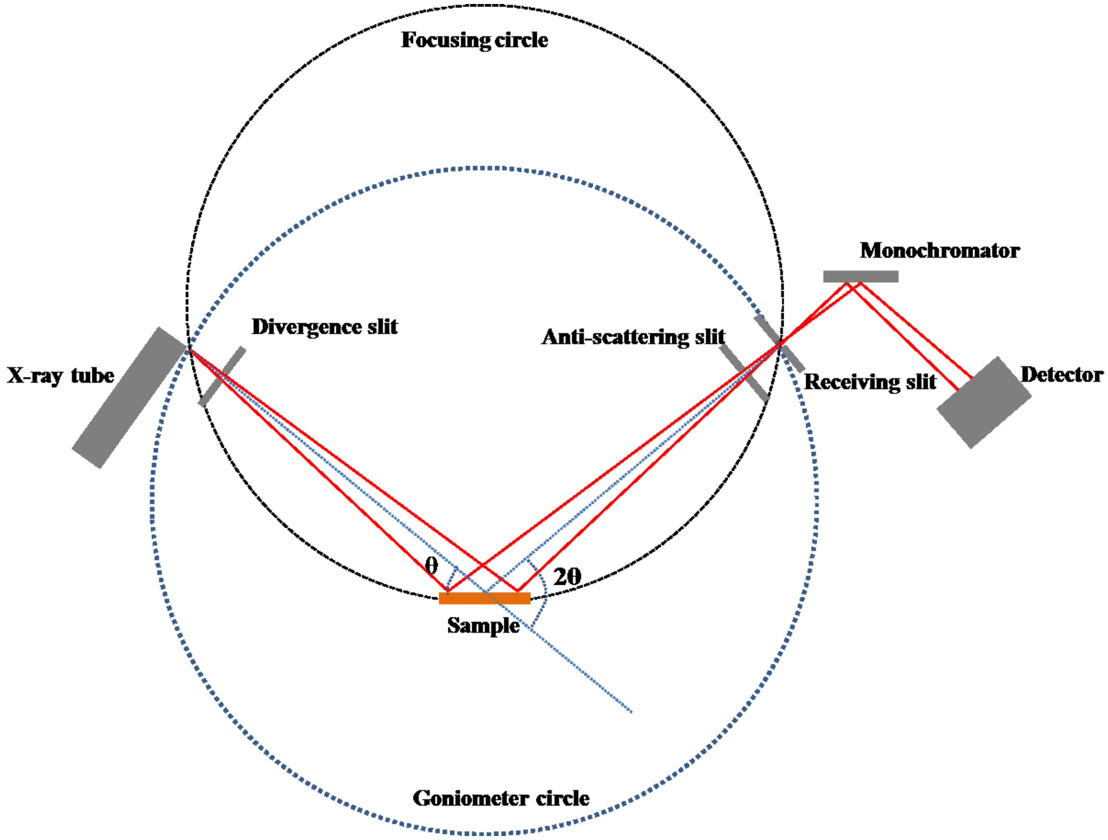

Figure 3.4 Schematic of the Bragg-Brentano diffractometer.

The In-situ X-ray diffraction experiment was carried out with a Bruker D8 diffractometer equipped with a Cu target X-ray source and a diffracted beam monochromator. Measurements were conducted with a step size of 0.05° and a 10 second dwell time per step. The scattering angle (2θ) range was 17.5 - 68°. Each scan took 2.803 hours, and the corresponding change of x value in $Li_{1-x}MO_2$ (M: metal) is about 0.025. A 1 mm divergence slit, 1 mm anti-scattering slit and 0.2 mm receiving slit were used for the measurements. Diffraction patterns were refined (Rietveld method) using “GSAS”.

3.2.2 Rietveld Refinements

The X-ray diffraction patterns can be refined with the Rietveld method, which fits the experimental patterns to a calculated diffraction pattern with various parameters optimized by the least square method. Information about the crystal structure of measured samples such as lattice parameters, fractional atomic coordinates, site occupancies, phase content, etc. can be extracted by comparing calculated peak position, shape, and intensity with experimental data. In this thesis, the Rietveld refinements were performed with the following function that calculates the intensity at point i as:

$$I_{ic} = I_{ib} + \sum_{k=k_1}^{k_2} G_{ik} I_k \qquad (3.4)$$

where I_{ic} is the net calculated intensity, I_{ib} is the calculated background intensity, G_{ik} is a normalized peak profile function, I_k is the intensity of the k^th^ Bragg reflection, and k_1 and k_2 represent reflections contributing the intensity.[193] I_k is given by the expression:

$$I_k = S M_k L_k |F_{hkl}|^2 P_k A_k E_k \qquad (3.5)$$

where S is the scale factor, M_k is the multiplicity, L_k is the Lorentz-polarization factor, F_{hkl} is the geometrical structure factor, P_k is the preferred orientation parameter, A_k is the absorption correction factor, and E_k is the extinction correction factor. G_{ik} is calculated with the Pseudo-Voigt peak profile function, which linearly combines Lorentzian and Gaussian functions as follows:

$$G_{ik} = \gamma L(\theta_i, \theta_k, H_k) + (1-\gamma) G(\theta_i, \theta_k, H_k) \qquad (3.6)$$

where $L(\theta_i, \theta_k, H_k)$ and $G(\theta_i, \theta_k, H_k)$ are Lorentzian and Gaussian contributions as functions of θ_i (the scattering angle at the ith calculation step), θ_k (the Bragg angle) and H_k (the full width half maximum). The value of γ is refinable and the value of H_k can be refined by tuning the value of U, V, W shown in the following expression:

$$H_k = (Utan^2\theta + Vtan\theta + W)^{1/2} \qquad (3.7).$$

In this thesis, Rietveld refinements were performed on the full XRD data assuming a hexagonal layered phase in the R-3m space group (α-$NaFeO_2$-type structure) to obtain the structural information. It was assumed that Li ions were on the 3a sites (Li layer), transition metals were on the 3b sites (transition metal layer), and oxygen ions were on the 6c sites. The exchange of Ni and Li atoms between 3a and 3b sites was allowed with constraints such that the stoichiometry of the phase was fixed to the value of specified composition.

The quality of the refinements is assessed by comparing calculated and observed data, and a parameter to measure the quality is the Bragg R factor (R_B) defined as:

$$R_B = \frac{\sum\left|I_k^{obs} - I_k^{cal}\right|}{\sum I_k^{obs}} \qquad (3.8)$$

where I_k^{obs} and I_k^{cal} are the observed and calculated integrated intensity of Bragg peak k respectively.

3.2.3 Scanning Electron Microscopy (SEM)

Scanning electron microscopy (SEM) is applied to study the surface morphology of materials. In an SEM system, accelerated electrons generated by a thermionic electron gun or a field emission gun are focused onto the specimen by electromagnetic lenses and apertures, and the interactions between the electrons and the specimen can generate a variety of signals. When the incident electrons are elastically scattered by the nucleus, the backscattered electrons (BSEs) can be collected by the detector. Because atoms with higher atomic number scatter more electrons, the image produced from BSEs can show compositional contrast, and typically compounds containing lighter elements appear dark in the image. Besides the BSEs, secondary electrons (SEs) are another commonly used imaging signal. The SEs are generated by inelastic interaction, during which atoms of the specimen are excited by the incident beam, and electrons from outer shells are emitted. The contrast of a SE image typically reflects the topographic properties of the specimen such as surface texture and roughness. Other electrons and photon signals such as Auger electrons and characteristic X-rays are also of great value for material characterization.[194–196]

In this thesis, SEM imaging was conducted using a Nanosciences Phenom Pro G2 Desktop Scanning Electron Microscope with a backscattered electron detector. Samples were prepared by mounting the powders onto adhesive carbon tape. The images of samples were taken with an accelerating voltage of 5 kV and a current of 0.6 nA.

3.2.4 Electron Backscattering Diffraction (EBSD)

As discussed in the section 3.3.2, the BSEs come from the elastic interactions between incident electron beams and the specimen, and the scattered electrons are channeled and are subject to path differences which lead to constructive and destructive interference. The interference forms an EBSD pattern (EBSP) which is also referred to as a Kikuchi pattern, and this pattern is uniquely defined by the lattice parameters of the particular crystal under the beam, crystal orientation in space, wavelength of incident electron beam, and the proximity of the detector to the sample. Figure 3.5 shows a schematic of how Kikuchi patterns form. The software analyzed the Kikuchi patterns, and determined all possible orientations with each phase and reports the best fit as the identified phase and orientation.[197]

Band contrast (BC) is an EBSP quality factor that characterizes the average intensity of the Kikuchi bands with respect to the overall intensity within the EBSP, and the values are scaled from 0 to 255. A mapping image plotted with BC value is able to show the grain boundaries, which show poor BC due to less diffraction intensity and therefore appear dark in the map. [197]

EBSD Euler color mapping is used to show the crystal orientations of grains. Euler angles are a set of three angles used to describe the crystallographic orientation of a grain with respect to a reference coordinate system. Angle φ1, Φ, and φ2 represent a series of rotations about the z, x, and rotated z axes. Normally, the values of three Euler angles are set to three color scales, red, green, and blue, and the three colors are combined into a single RGB color for each grain. Thus, grains with similar colors have similar crystal orientations. [197]

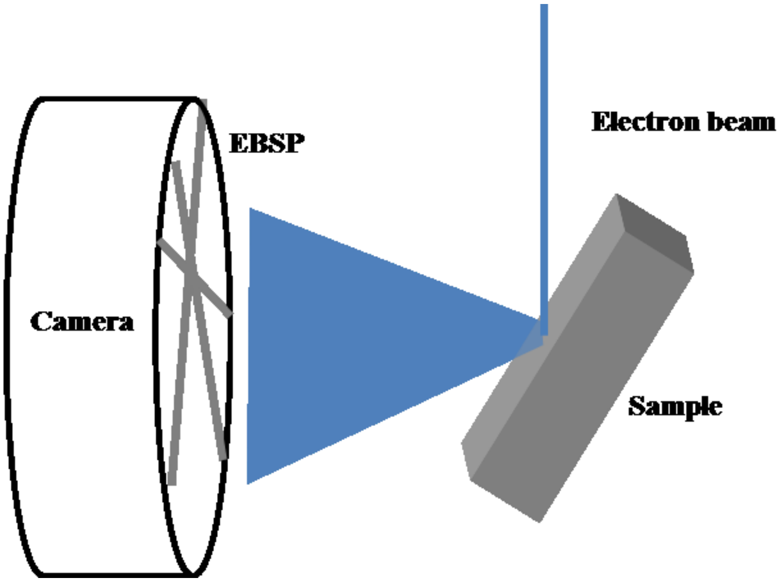

Figure 3.5 A schematic of how EBSD patterns form.[197]

Samples used for cross-sectional analysis were prepared by an ion beam cross-section polisher (JEOL IB09010CP) at the Canadian Centre for Electron Microscopy (CCEM). The powder sample was first mixed with carbon paste (amorphous carbon powder) and propanol to make a paste. The paste was then embedded in a graphite block and then the cross-section of the block was created by a cross-section polisher with an Ar ion beam (5 KV for 10 hours). Electron backscatter diffraction (EBSD) mapping was carried out using a JEOL JSM-7000F SEM at CCEM. The step size of the EBSD maps was 200 nm (each pixel is 200 nm × 200 nm).

3.2.5 Brunauer-Emmett-Teller (BET) Surface Area Measurements

The BET method is applied to measure the surface area of powder samples from the adsorption and desorption of gas molecules (adsorbates) on the solid surface of samples (adsorbent). A mixture of adsorptive gas (nitrogen) and non-adsorptive gas (helium) with known concentrations is admitted to the sample that is in a cooling bath. As a result of adsorption on the sample, the concentration of adsorptive gas decreases. The decrease in concentration in comparison to that of the initial mixture leads to a change in thermal conductivity of the mixture. After removing the cooling bath, desorption happens and similar to adsorption, the concentration of adsorptive gas changes. The ensuing change in thermal conductivity can be recorded. From the signal of thermal conductivity change during either adsorption or desorption, the amount of adsorbed gas, n_a (molar amount), can be calculated. The monolayer gas adsorption amount, n_m (molar amount), can be correlated to n_a by the BET equation:

$$\frac{p/p_0}{n_a(1-\frac{p}{p_0})} = \frac{1}{n_m C} + \frac{C-1}{n_m C}\frac{p}{p_0} \qquad (3.9)$$

where p and p_0 are the equilibrium and the saturation pressure of adsorbates at the temperature of adsorption, and C is a constant derived from energy of adsorption. The total surface area of measured samples, S, can be calculated as follows:

$$S = n_m N_A A \qquad (3.10)$$

where N_A is the Avogadro's number, A is the cross-sectional area of each adsorbed molecule, and V_m is the molar volume of gas.[198–201]

The surface area measurements were carried out using the single point BET method. A Micromeritics FlowSorb II 2300 was used with a nitrogen/helium flow (28.6% N_2). Samples were degassed at 150°C for 0.5h to remove moisture before the measurement.

3.2.6 Particle Size Distribution (PSD) Measurements

Particle size distribution analysis was carried out using laser scattering. When a beam of light is scattered by a group of dispersed particles, large particles scatter light at small angles relative to the laser beam and small particles scatter light at large angles. The angular scattering intensity data is then analyzed to calculate the size of the particles responsible for creating the scattering pattern, using the Mie theory of light scattering. Using Mie theory, the relative refractive index of samples and dispersant is required.

A Partica LA-950V2 laser scattering particle size distribution analyzer (Horiba) was used. Synthesized powders were added into DI water and sonicated for 30 mins before analyzing. The refractive index (adopted from a patent) of positive electrode materials tested in this work in water is about 1.24.[202] Because the PSD tests in this work were performed on the same materials before and after processing for comparison, it is considered fair to adopt this value for the refractive index although it may not be the true value of the materials tested in this work.

3.3 Cell Construction

3.3.1 Half Coin Cell, Full Coin Cell, and Pellet Coin Cell

Synthesized positive electrode materials were mixed with polyvinylidene difluoride (PVDF) and Super-S carbon black having a mass ratio of 92:4:4 in N-methyl-2-pyrrolidone (NMP) to make a slurry. Single side coated electrodes were made by casting the slurry onto Al foil with a 150 µm notch bar spreader. The electrodes were dried in an oven at 120°C for 3 hours. Dried electrodes were then calendared at a pressure of 2000 atm. The loading of electrode material was ~12 mg/cm^2. Coin cell electrodes were punched (1.2 cm in diameter) and further dried under vacuum at 120°C for 14 hours before coin cell fabrication. Figure 3.6 shows a schematic of a standard 2325 coin cell.

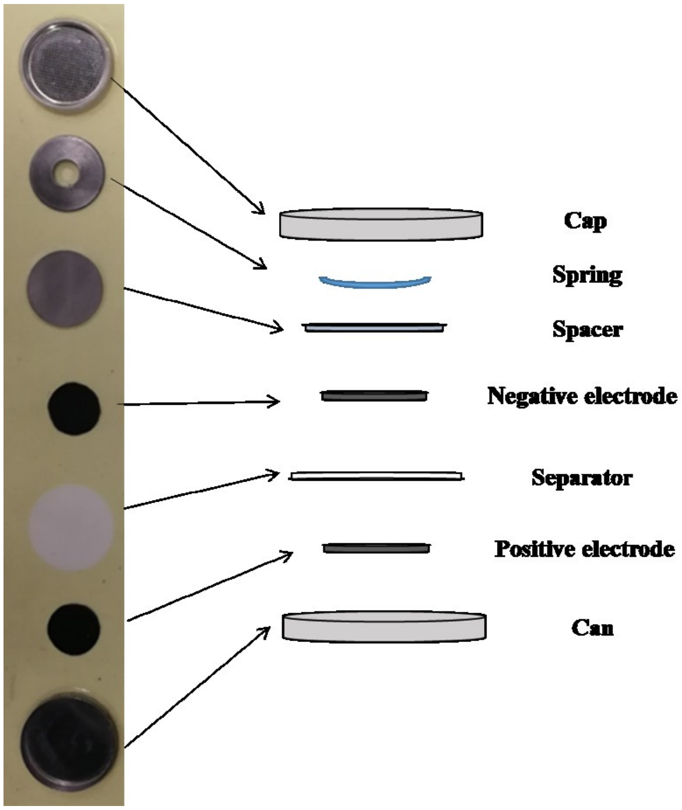

Figure 3.6 Schematic of a typical coin cell.

For half coin cell, a Li foil is used as the negative electrode, and two layers of separators (Celgard #2300) are placed in between the positive electrode and the negative electrode. A full coin cell had a graphite negative electrode and one layer of polypropylene blown microfiber separator (BMF – obtained from 3M Co., 0.275 mm thickness, 3.2 mg/cm^2). A pellet cell has a positive electrode pellet as the positive electrode. The positive electrode slurry was prepared the same as a regular slurry, and the slurry was dried under vacuum to evaporate the NMP solvent. The dried slurry was ground into fine powder and was pressed into a pellet with a mold under a pressure of 2000 psi. Each pellet is about 200-300 mg, and the pellet was dried under vacuum at 120ºC for 14 hours before coin cell fabrication. A pellet cell typically has no spring and negative electrode. Coin cells were assembled in an argon-filled glovebox.

Electrolytes used in this thesis typically include carbonate solvents such as ethylene carbonate (EC, BASF, purity 99.99%), diethyl carbonate (DEC, BASF, purity 99.99%), fluoroethylene carbonate (FEC. BASF, purity 99.94%), ethyl methyl carbonate (EMC, BASF, purity 99.99%), and dimethyl carbonate (DMC, Shenzhen Capchem Technology Co., Ltd.). Lithium hexafluorophosphate ($LiPF_6$, BASF, purity 99.9%) was used as the lithium salt. Electrolyte additives used in this thesis include vinylene carbonate (VC, BASF, purity 99.97%) and ethylene sulfate (DTD, Sigma Aldrich, purity 98%). Exact electrolyte formulations used in different tests will be specified in each chapter.

3.3.2 In-situ XRD Half Coin Cell

The coin cell used for in-situ XRD used a beryllium x-ray window as the positive electrode current collector. Positive electrode material slurry was made as described above but less NMP was used to increase the slurry viscosity. The slurry was coated onto a 2 cm diameter beryllium disc with a 660 μm notch bar spreader and dried at 120°C for 2 hours. The coated beryllium disc was pressed at a pressure of 2000 kPa, and further dried under vacuum at 120°C for 14 hours before coin cell fabrication. The loading of the electrode material was 20 - 25 mg/cm^2. The relatively higher loading was used to better signal to noise in the in-situ XRD experiments. The coated beryllium disc was attached using Roscobond^{TM} pressure sensitive adhesive to the positive electrode side of the cell case that had a pre-cut 1.5 cm diameter hole. After this, assembly of the in-situ coin cell was the same as described above for regular half coin cells. The cell was cycled at a rate of ~C/100 (discharge or charge was set to complete in 100 hours) with an E-one Moli charger system, while diffraction patterns were collected. Using a rate of C/100, the variation of x in Li_xMO_2 across each XRD data collection (2.803 hours) is limited to only ~0.028. The slow rate also ensures enough time for Li diffusion in the thick electrode. Electrolyte with 1.0 M $LiPF_6$ in EC:DEC (1:2 v/v) was used in in-situ XRD half coin cells.

3.4 Electrochemical Measurements

Galvanostatic charge and discharge cycling was used to analyze coin cells. The cells were charged and discharged with a constant current determined by the electrode loading and designated current density. An upper cut-off voltage and lower cut-off voltage were set as the end points of charge and discharge. Specific capacity was typically measured at 30ºC with a specific current of 10 mA/g (~C/20), and the cycling performance was measured at 30ºC with a current density of 40 mA/g (~C/5). Differential capacity vs. voltage (dQ/dV vs. V) analysis was used to study the electrochemical and structural properties. Material degradation, impedance growth, and structural evolution of positive electrode materials during charge/discharge can be extracted accompanied by other characterization methods. Figure 3.7 shows an example of how dQ/dV vs. V evolves during cycling. During cycling, impedance growth can be discerned from the peak shift and voltage drop at the top of discharge. Figure 3.7b plots a magnified view of the top of discharge, which shows the peak shift and increased voltage drop during cycling.

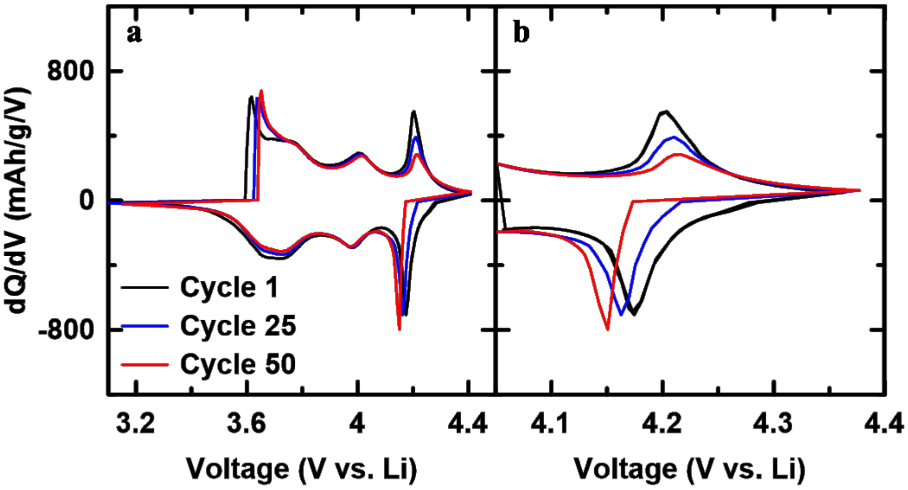

Figure 3.7 An example of how dQ/dV vs. V evolves during cycling.

3.5 Accelerating Rate Calorimetry

Accelerating rate calorimetry (ARC) is an adiabatic calorimetry, and Figure 3.7 shows a simplified schematic of the calorimeter.[203] A sample is attached to a thermocouple in a chamber encapsulated by a heating jacket. When an exothermic reaction happens in the sample, the temperature of the sample increases due to heat generation. The heating jackets then maintain the same temperature as the sample, and thus the heat flow between sample and the jackets is negligible and near-adiabatic conditions are maintained. The temperature of sample (T) is measured as a function of time (t) and the self-heating rate (dT/dt) vs. T is monitored. Typical ARC measurements are operated in a heat-wait-search (HWS) mode. In the HWS mode, the jacket is heated up to an initial temperature and then waits for the sample to reach the same temperature. Once thermal equilibrium between the sample and jacket is achieved, the system starts to search for the self-heating rate of the sample. If the self-heating rate is lower than the set threshold (0.02ºC/min), the ARC will proceed to the next temperature step and another round of HWS is performed. If the self-heating rate is greater than the threshold, the system considers the reaction in the sample as an exothermic reaction. In this case, the ARC will track the exotherm by maintaining adiabatic conditions until the measured self-heating rate reaches the safety limit or the set end point temperature is reached.

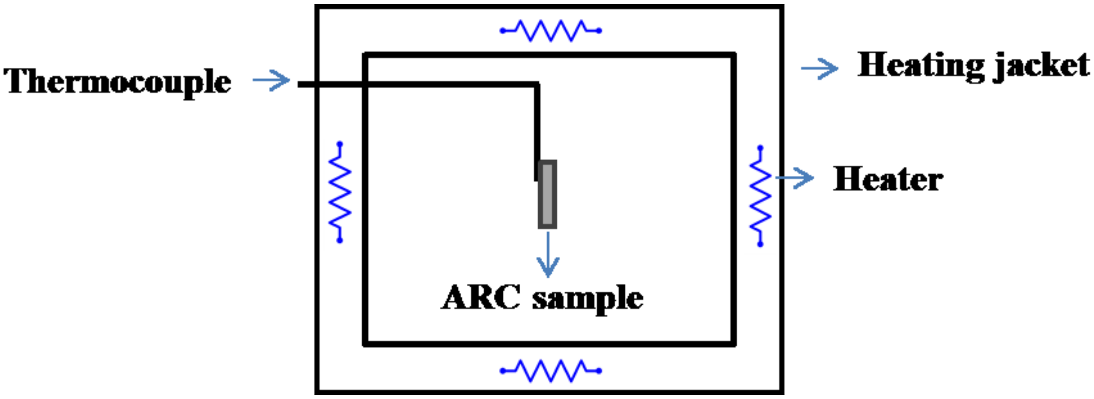

Figure 3.8 Schematic of the accelerating rate calorimeter (ARC)

ARC samples used in this thesis are a mixture of charged positive electrode powders with electrolyte encapsulated in a stainless steel tube. Pellet coin cells with pellet-type positive electrodes were made using the method described in previous sections.[204] 1.2 M $LiPF_6$ in EC:EMC (v/v 3:7) electrolyte was used for consistency to better compare with past results. Cells were charged to the same specific charge capacity of 230 mAh/g. After charging, the pellet cells were transferred to and opened in an Ar filled glove box carefully without shorting. The delithiated positive electrode powder was ground and then rinsed with DMC 4 times to remove the residual electrolyte. The rinsing process does not change the bulk structure or the reactivity of the delithiated electrode as reported by D.D. MacNeil et al.[205] The powder was dried in vacuum for 24 h before being put into a stainless steel ARC tube along with fresh electrolyte (1.2 M $LiPF_6$ in EC:EMC 3:7). For better comparison, the capacity of the charged positive electrode material in each ARC tube was fixed at 10 mAh and the amount of electrolyte included was around 28 mg. The starting temperature of the ARC experiment was set to 120^{o}C and all the samples were tested under adiabatic conditions. Experiments ceased when the self-heating rate

(SHR) exceeded 20ºC/min or the temperature reached 250ºC. Duplicate experiments were made to confirm the repeatability of the data.

CHAPTER 4 STUDIES OF THE STRUCTURE AND ELECTROCHEMISTRY OF Li_xNiO_2 FOR $0 \leq X \leq 1$

Many derivatives of $LiNiO_2$, such as $LiNi_{1-x-y}Mn_xCo_yO_2$(NMC) and $LiNi_{1-x-y}Co_xAl_yO_2$ (NCA) have been of great interest in both industry and academia.[81,206,207] As the trend continues to reduce the Co, Mn and Al content in these materials, a careful, modern study of $LiNiO_2$, the end member of the NMC and NCA series when x = y = 0, is required as a solid reference for workers in the field.

For Ni-rich NMC and NCA materials, although Ni is partially substituted by other transition metal atoms such as Co, Mn and Al to improve structural and electrochemical stability,[103,155,208] the substituted materials still have many properties that originate from $LiNiO_2$. Without an in-depth understanding of the structural and electrochemical behavior of $LiNiO_2$, it is hard to effectively solve existing problems.

$LiNiO_2$ was initially reported about sixty five years ago, and numerous studies have been made to investigate the structural and electrochemical properties[209,210] Now with modern synthesis methods, $LiNiO_2$ with superior quality can be made. Figure 4.1 shows a comparison of voltage (vs. Li/Li^+) versus x in $Li_{1-x}NiO_2$ for a sample made in 1993 by W. Li et al.[209] and modern $LiNiO_2$ made by the author. Black lines and red lines show the cell voltage as a function of x in $Li_{1-x}NiO_2$ of the old and modern $LiNiO_2$ materials respectively. The value of x is calculated assuming $LiNiO_2$ has a theoretical first charge capacity of 274 mAh/g. The old $LiNiO_2$ was made by lithiating $Ni(OH)_2$ at 700°C for 2 hours in air, while the modern $LiNiO_2$ was made with better control as described in the experimental section. Figure 4.1 shows that modern $LiNiO_2$ has a first charge capacity close to the theoretical capacity and a very small irreversible capacity. Many researchers refer to reference 209 to interpret the structural changes in Li_xNiO_2. It is clear that the structural information needs to be updated based on the superior quality of the modern $LiNiO_2$.

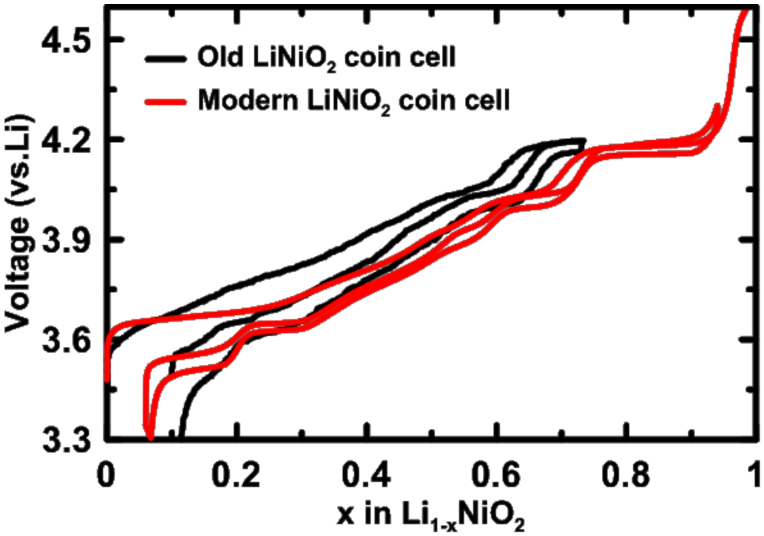

Figure 4.1 A comparison of voltage-specific capacity data between old and modern $LiNiO_2$. Black lines and red lines are the cell voltage as a function of x in $Li_{1-x}NiO_2$ of old and modern $LiNiO_2$ materials respectively. The data was collected both at room temperature. The data for òld`$LiNiO_2$ was taken from reference [209].

In this chapter, Li_xNiO_2 ($0 \leq x \leq 1$) is studied with in-situ X-ray diffraction and the unit cell parameters and unit cell volume are carefully measured versus x. Multiple phase transitions are clearly demonstrated and analyzed in detail. The H1 single phase region is found to demonstrate severe kinetic hindrance presumably due to very slow Li diffusion and that the kinetic hindrance gets more severe in the H1 phase, but not in the other phases, with charge discharge cycling. Neutron diffraction on de-lithiated Li_xNiO_2

powders was performed to explore the origin of the monoclinic distortion. The majority of this chapter was published in Journal of The Electrochemical Society.[9] H. Li conducted the XRD measurements, the electrochemical tests and the data analysis, N. Zhang and J. Li contributed to the in-situ XRD measurements. Reproduced with permission from *J. Electrochem. Soc.*, 165.13 (2018): A2985-A2993. Copyright 2018, The Electrochemical Society. The authors thank N. Sharma, M. Avdeev, and D. Goonetilleke from University of New South Wales and Australian Nuclear Science and Technology Organisation for carrying out the experiments.

4.1 Experimental Design

The nickel hydroxide ($Ni(OH)_2$) precursor used for $LiNiO_2$ synthesis was provided by Guizhou Zoomwe Zhengyuan Advanced Material Co., Ltd. and $LiOH▪H_2O$ (purity > 99.8%, FMC Corporation) was used as the lithium source. The $Ni(OH)_2$ precursor was mixed thoroughly with a stoichiometric equivalent of $LiOH•H_2O$ by hand milling using a mortar and a pestle with a Li/TM ratio of 1.02. The mixed powders were preheated in oxygen in a tube furnace at 485ºC for 3 hours. A heating rate of 10ºC/min was used to increase the temperature to the set point. The preheated powders were taken out of the furnace and ground again by hand milling to minimize areas of local LiOH excess. The ground powders were then heated in oxygen in the tube furnace at 485ºC for 2 hours, and then at 700ºC for 20 hours. A heating rate of 10 ºC/min was used to change temperatures.

SEM and powder XRD characterizations were performed as described in Chapter 3. The experimental details about coin cell assembly, electrochemical tests, and in-situ XRD measurements were described in Chapter 3. The in-situ XRD coin cell had a material loading of 24.01 mg/cm^2. The in-situ XRD coin cell was cycled at a rate of ~C/100 between 3.0 - 4.3 V for one cycle and 3.0 – 4.6 V for the second charge using an E-one Moli charger system, while diffraction patterns were collected. Electrolyte used for coin cell testing and for in-situ XRD coin cells was 1.0 M $LiPF_6$ in EC:DEC (1:2 v/v).

Neutron diffraction measurements was carried out at the Australian Centre for Neutron Scattering at Australian Nuclear Science and Technology Organisation (ANSTO). The wavelength of the neutrons used was 2.4395Å and the experiments were conducted at 300K. Rietveld refinements were done with Rietica. The charged Li_xNiO_2 samples were prepared by charging $LiNiO_2$-Li pellet half coin cells to 3.83V (vs. Li) as described in Chapter 3. The charged cells were opened in a glove box to recover the Li_xNiO_2 positive electrode materials. The recovered material was rinsed with DMC for 4 times, and vacuum dried and then sealed in a glove box before being shipped to Australia. The value of x for Li_xNiO_2/Li cells charged to 3.83V (vs. Li) is about 0.5 based on the in-situ XRD data.

4.2 Results and Discussion

4.2.1 Material Characterizations of $LiNiO_2$

Figures 4.2A and 4.2B show SEM images of the synthesized $LiNiO_2$ materials. The synthesized materials have ~18 μm diameter spherical secondary particles and each secondary particle consists of dense small-size (about 200 nm) primary particles. Panels C1, C2 and C3 in Figure 4.2 show the full X-ray diffraction patterns and two expanded views of the (104) and (108)/(110) Bragg peaks of the synthesized $LiNiO_2$. The black dots are the measured diffraction data, and the solid red lines show the calculated pattern from Rietveld refinement. The green lines show the differences between the measured and calculated patterns. Rietveld refinements were performed on the full XRD data (15 - 70°) assuming a hexagonal layered phase in the R-3m space group (α-$NaFeO_2$-type structure) to obtain the structural information. Li ions were assumed to be on the 3a sites (Li layer), Ni ions were on the 3b sites (transition metal layer), and oxygen ions were on the 6c sites. The exchange of Ni and Li atoms between 3a and 3b sites was allowed with constraints such that the stoichiometry of the phase was fixed to the values assumed from the target composition. Figure 4.2C4 shows that the synthesized $LiNiO_2$ has no appreciable impurity phase. The refinement results show that cation mixing between Li ions and Ni ions is 1.81(4)%, lattice constants a and c are 2.8751(1)Å and 14.2000(3) Å, respectively, and the z value of the oxygen fractional atomic coordinate is 0.2424(1). The refinement has a Bragg R factor (R_B) of the refinement was 1.87. An estimate for the Li content of the synthesized $LiNiO_2$ can be made using an empirical relationship between unit cell volume and x in $Li_{1-x}Ni_{1+x}O_2$.[211] Using the fitted relationship in reference [211], x for the synthesized $Li_{1-x}Ni_{1+x}O_2$ is about 0.996.

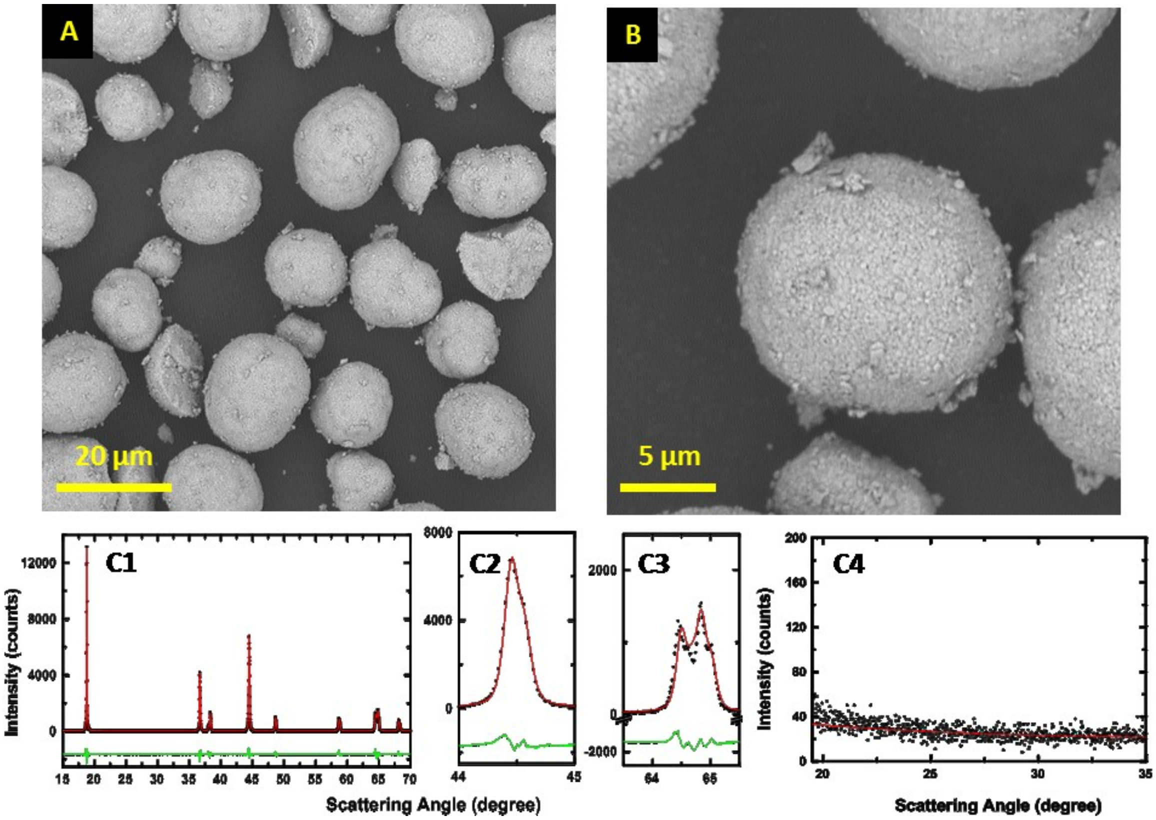

Figure 4.2 SEM images of synthesized $LiNiO_2$ (A),(B); XRD patterns of $LiNiO_2$ (C1), expanded view of the (104) Bragg peak of $LiNiO_2$ (C2), expanded view of (108)/(110) Bragg peaks of $LiNiO_2$ (C3), impurity regions in the XRD patterns of $LiNiO_2$ where Li_2CO_3, if present, can be observed (C4). Black circles are experimental XRD data, solid red lines are calculated patterns from Rietveld refinement, green lines show the differences between the measured and calculated patterns.

4.2.2 Crystallography of $LiNiO_2$

Figure 4.3 shows the crystal structure of $LiNiO_2$. Blue balls are Li, red balls are oxygen, and black balls are Ni. In this figure, two choices of unit cell are shown. The unit cell drawn with solid black lines is the conventional choice of unit cell for hexagonal structured $LiNiO_2$.

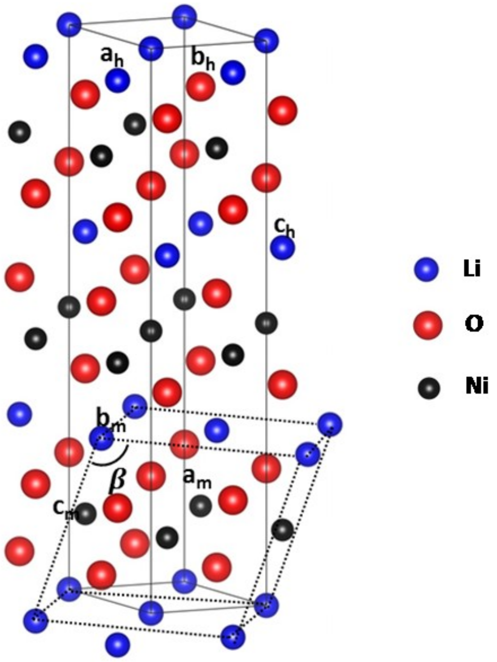

Figure 4.3 Crystal structure of $LiNiO_2$. Blue balls represent Li atoms, red balls represent O atoms, and black balls represent Ni atoms. Solid black lines depict a hexagonal unit cell of $LiNiO_2$. The dashed lines depict a monoclinic unit cell of $LiNiO_2$.

Vector $\mathbf{a_h}$ is equal to vector $\mathbf{b_h}$ in magnitude and the angle between them is 120°. Vector $\mathbf{c_h}$ is perpendicular to both $\mathbf{a_h}$ and $\mathbf{b_h}$. The dashed lines depict a monoclinic unit cell, in which vector $\mathbf{b_m}$ is perpendicular to $\mathbf{a_m}$ and $\mathbf{c_m}$, and the angle between $\mathbf{a_m}$ and $\mathbf{c_m}$ is β ($\neq$ 90°). When there is no distortion in crystal structure, the transformation between the hexagonal unit cell vectors and the monoclinic unit cell vectors can be described by:

$$\begin{bmatrix} a_m \\ b_m \\ c_m \end{bmatrix} = \begin{bmatrix} -1 & 1 & 0 \\ 1 & 1 & 0 \\ 1/3 & -1/3 & -1/3 \end{bmatrix} \begin{bmatrix} a_h \\ b_h \\ c_h \end{bmatrix} \qquad (4.1)$$

and the transformation of the Miller indices of the Bragg peaks can be described by:

$$\begin{bmatrix} h_m \\ k_m \\ l_m \end{bmatrix} = \begin{bmatrix} -1 & 1 & 0 \\ 1 & 1 & 0 \\ 1/3 & -1/3 & -1/3 \end{bmatrix} \begin{bmatrix} h_h \\ k_h \\ l_h \end{bmatrix} \qquad (4.2)$$

In the non-distorted structure, $b_m = a_h = b_h$, $a_m = \sqrt{3}b_m$, and $c_m = 1/3*\sin\beta*c_h$.

4.2.3 In-situ XRD Measurements

Figure 4.4 shows the in-situ X-ray diffraction patterns, with a sequential offset in intensity for clarity, accompanied by the in-situ coin cell cycling profile in which voltage was plotted as a function of cell running time. Figure 4.4a is aligned with the diffraction patterns. Figures 4.4b – 4.4e show the in-situ XRD patterns of selected scattering angle regions, and the initial diffraction peaks were indexed in a R-3m space group. A peak from beryllium oxide was observed at 46°. Figure 4.4a shows that the cell was first charged and discharged between 3.0 - 4.3 V for 1 cycle at a rate of ~C/100, and then the cell was charged to 4.6 V at the same rate. Each XRD scan took exactly 2.803 hours. Figure 4.4b shows that during the first charge, the (003) peak shifted continuously until two peaks coexisted at a high state of charge. Figures 4.4c and 4.4d show that for the (101) and (104) peaks, clear peak splitting was observed at certain states of charge. This observed peak coexistence and peak splitting were reported by W. Li et al.[209], and are caused by a two-phase region at the top of charge and a monoclinic distortion, respectively. The in-situ XRD patterns were analyzed using the LeBail refinement method with Rietica. For refinements, a hexagonal R-3m space group was assumed in the single or two hexagonal phase regions, and a monoclinic c2/m space group was assumed in the single monoclinic phase region, and a mixture of the two space groups was assumed in the hexagonal-monoclinic two-phase regions.

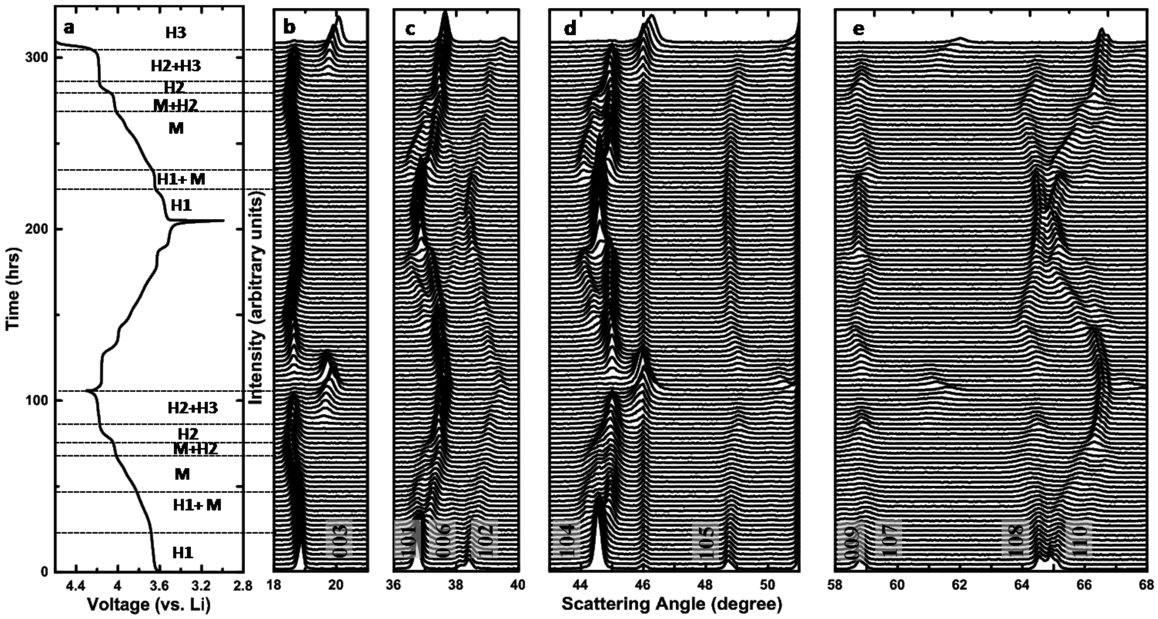

Figure 4.4 Diffraction patterns from the in-situ XRD experiment. Cell voltage as a function of time, which is aligned with the diffraction patterns (a). In-situ XRD patterns of selected scattering angle regions: 18 - 21° (b), 36 - 40° (c), 43 - 51° (d), 58 - 68° (d). The cell was charged and discharged between 3.0 – 4.3 V at a rate of ~C/100 for 1 cycle, and charged to 4.6 V at a rate of ~C/100.

Figure 4.4 shows the in-situ X-ray diffraction patterns, with a sequential offset in intensity for clarity, accompanied by the in-situ coin cell cycling profile in which voltage was plotted as a function of cell running time. Figure 4.4a is aligned with the diffraction patterns. Figures 4.4b – 4.4e show the in-situ XRD patterns of selected scattering angle regions, and the initial diffraction peaks were indexed in a R-3m space group. A peak from beryllium oxide was observed at 46°. Figure 4.4a shows that the cell was first charged and discharged between 3.0 - 4.3 V for 1 cycle at a rate of ~C/100, and then the cell was charged to 4.6 V at the same rate. Each XRD scan took exactly 2.803 hours. Figure 4.4b shows that during the first charge, the (003) peak shifted continuously until two peaks coexisted at a high state of charge. Figures 4.4c and 4.4d show that for the (101) and (104) peaks, clear peak splitting was observed at certain states of charge. This observed peak coexistence and peak splitting were reported by W. Li et al.[209], and are caused by a two-phase region at the top of charge and a monoclinic distortion, respectively. The in-situ XRD patterns were analyzed using the LeBail refinement method with Rietica. For refinements, a hexagonal R-3m space group was assumed in the single or two hexagonal phase regions, and a monoclinic c2/m space group was assumed in the single monoclinic phase region, and a mixture of the two space groups was assumed in the hexagonal-monoclinic two-phase regions.

By combining the in-situ XRD refinement results with the in-situ cell cycling data, phase transitions can be correlated with the voltage profile during charge and discharge. Figure 4.4a shows that during the first charge, the $LiNiO_2$ went through multiple phase transitions including H1 (1st hexagonal) phase to M (monoclinic) phase, M phase to H2 (2nd hexagonal) phase, and H2 phase to H3 (3rd hexagonal) phase, and this is consistent with results shown by W. Li et al. [209] During the 2nd charge, phase transitions followed the same manner, but a faster H1-M phase transition was observed, accompanied by a flatter voltage plateau at 3.65 V. The phase transitions during the first discharge mirror those during the 2nd charge and will not be discussed in detail.

Figure 4.5 shows selected regions of the in-situ XRD patterns during the 1st charge accompanied by the corresponding in-situ coin cell cycling profile. Three regions were selected to discuss the phase transitions. Figure 4.5a shows that the (003) peak started shifting to lower angle as Li ions were de-intercalated. When the voltage reached about 4.0 V, the peak began to shift back to higher angle and then a Bragg peak from another phase started to evolve at higher angle when the cell was charged to about 4.19 V. This two-peak region indicates the existence of two phases at high state of charge. Figure 4.5b shows the evolution of the Bragg peaks between 36°-40°. At the beginning of the 1st charge, the $(101)_{H1}$, $(006)_{H1}$ and $(012)_{H1}$ peaks were observed. As Li ions were de-intercalated, the $(101)_{H1}$ peak started to diminish until it disappeared, and two peaks close to the initial $(101)_{H1}$ peak started to emerge. In a hexagonal structure, the $(101)_{H1}$ peak has a multiplicity of 12 including the $\pm(01\pm1)_{H1}$, $\pm(10\pm1)_{H1}$ and $\pm(1\text{-}1\pm1)_{H1}$ peaks. In the case of the R-3m space group only 6 of these peaks have non-zero geometrical structure factor. Table 4.1 shows the six peaks with non-zero structure factor and the corresponding monoclinic Miller indices calculated using Eq.(4.2). When the structure is not distorted, the $(110)_M$ and $(20\bar{1})_M$ planes have the same plane spacing as the $(101)_H$ planes, and a single diffraction peak appears at a certain scattering angle. When the basal plane distortion occurs and the monoclinic phase forms, the inter-plane distance of the $(110)_M$ planes is no longer equal to that of $(20\bar{1})_M$ planes, thus two corresponding diffraction peaks will emerge. Table 4.1 also shows that in the monoclinic phase, the $(110)_M$ peak has a multiplicity of four, while the $(20\bar{1})_M$ has a multiplicity of two. Due to the factor of two difference in multiplicity, the intensity of the $(20\bar{1})_M$ peak is expected to be half of the intensity of the $(110)_M$ peak as observed in Figure 4.5b. As the charge continued, the $(110)_M$ peak and the $(20\bar{1})_M$ peak shifted smoothly until they merged forming a single peak at higher state of charge, and the distorted monoclinic phase transformed back to the hexagonal, H2 phase.

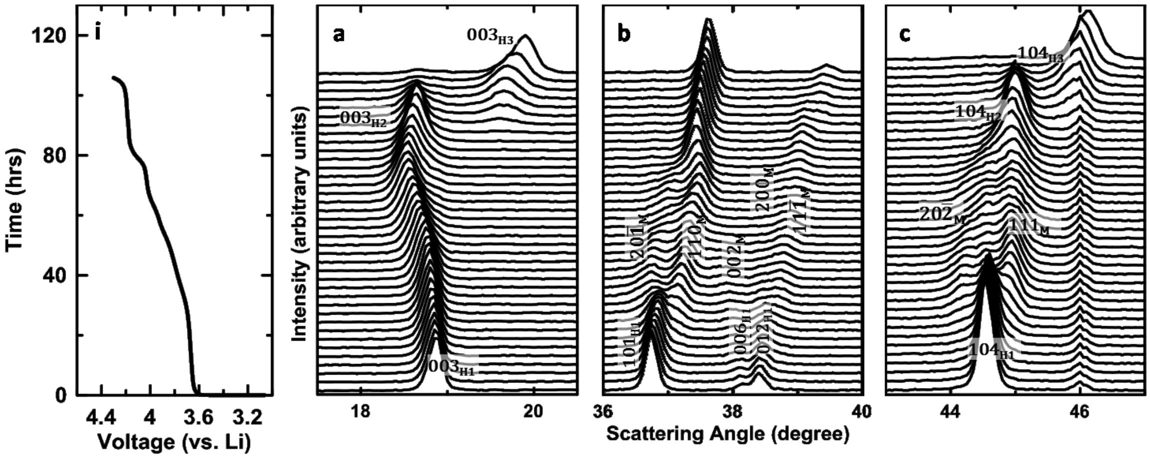

Figure 4.5 In-situ coin cell cycling profile in which voltage was plotted as a function of cell running time (i). In-situ XRD scans during 1st charge of selected scattering angle regions. 18 - 21° (a), 36 - 40° (b), 43 - 47° (c). Miller indices of the diffraction peaks are labeled according to XRD profile refinement. Voltages are labeled according to the cell voltage profile.

The mechanism of the monoclinic phase formation was proposed by H. Arai et al.[84] Some studies attribute the monoclinic distortion to an ordering of Li in alternating rows of mostly full and mostly empty sites in the Li layer which breaks the hexagonal symmetry.[212,213] An analogous ordering was also observed in Li_xCoO_2 ($0 \leq x \leq 1$) when x is near 0.5 and can be explained by a lattice gas model.[27] Driven by further de-intercalation of Li, a transition from the H2 phase to the H3 phase started near the end of the 1st charge, which can be clearly observed in Figure 4.5a.

Table 4.1 lists the transformations of the Miller indices of selected diffraction peaks of the hexagonal phase and the monoclinic phase. Using Table 4.1 the Miller indices of the other peaks shown in Figures 4.5b and 4.5c can be determined and they are labeled in the Figures. The $(006)_{H1}$ peak did not split, as expected in the monoclinic phase region, while the $(012)_{H1}$ and $(104)_{H1}$ peaks split into two peaks when the distorted monoclinic phase formed. The observed intensity ratios of the split peaks agree well with calculated diffraction multiplicity listed in Table 4.1.

Table 4.1 Hexagonal-monoclinic Miller indices transformation list.

Hexagonal Indices	Monoclinic Indices	Multiplicity
003	00-1	2
00-3	001	
101	-110	4
01-1	110	
-10-1	1-10	
0-11	-1-10	
-111	20-1	2
1-1-1	-201	
006	00-2	2
00-6	002	
-11-2	200	2
1-12	-200	
10-2	-111	4
012	11-1	
-102	1-1-1	
0-1-2	-1-11	
104	-11-1	4
-10-4	1-11	
01-4	111	
0-14	-1-1-1	
-114	20-2	2
1-1-4	-202	

Figure 4.6 shows the in-situ XRD patterns measured during the 2nd charge accompanied by the corresponding in-situ coin cell cycling profile. All the peaks changed in a similar manner as during the 1st charge shown in Figure 4.5. However, during the second charge, the phase transition from the H1 phase to the M phase occurred more quickly than the same transition during the first charge. Figure 4.6b shows that in the monoclinic phase region, the $(110)_M$ peaks and $(20\bar{1})_M$ peaks appear to be much sharper compared with the same peaks shown in Figure 4.5. Figure 4.4a shows that during the first charging process, the phase transition from the H1 phase to M phase was accompanied by a sloping voltage region from about 3.65 – 3.8 V. By comparison, during the second charge (see Figure 4.4a), the voltage plateau at 3.65 V was flat and short, indicating a rapid phase transition from H1 phase to M phase. A similar phenomenon was also observed during the first discharge. After the first charge, apparently the transition between the H1 phase and the M phase became kinetically easier, and there was a smaller Li concentration gradient in the $LiNiO_2$ particles. As a result, diffraction peaks were sharper, and the voltage plateau was flatter.

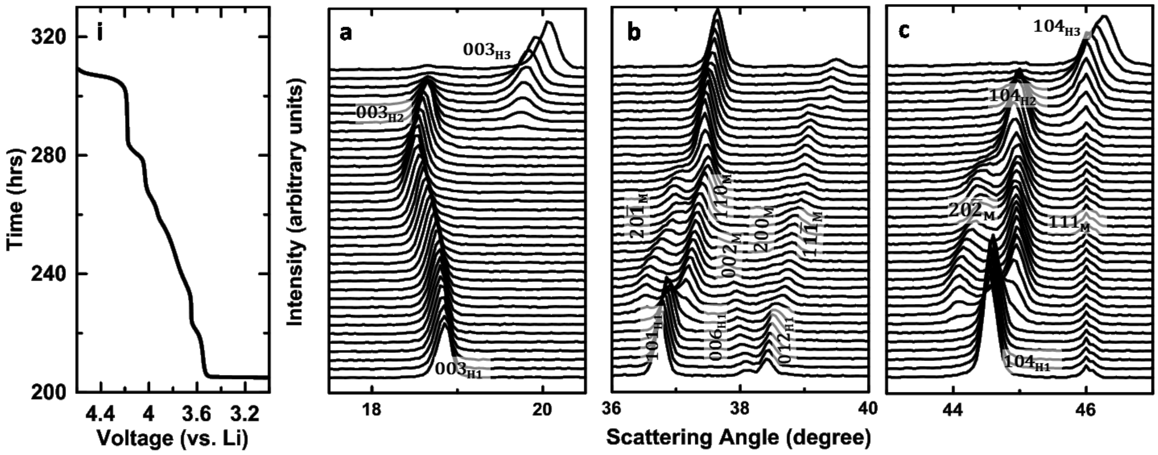

Figure 4.6 In-situ coin cell cycling profile in which voltage was plotted as a function of cell running time (i). In-situ XRD scans during 2nd charge of selected scattering angle regions. 18 - 21° (a), 36 - 40° (b), 43 - 47° (c). Miller indices of the diffraction peaks are labeled according to XRD profile refinement. Voltages are labeled according to the cell voltage profile

4.2.4 Rietveld Refinements of In-situ XRD Patterns

Figure 4.7 shows refinement results of the in-situ XRD patterns accompanied by cell charge and discharge profiles. Figure 4.7A(1) shows the in-situ cell voltage as a function of specific capacity during the first charge; Figure 4.7A(2) shows the unit cell constants a_{H}, b_{M}, and $a_{M}/\sqrt{3}$ as a function of specific capacity during the first charge; Figure 4.7A(3) shows the unit cell constants c_{H} and $3c_{M}\sin\beta$ as a function of specific capacity during the first charge and Figure 4.7A(4) shows the angle β as a function of specific capacity during the first charge. Panels B(1) - B(4) and C(1) - C(4) in Figure 4.7 show the same parameters as a function of specific capacity during first discharge and second charge, respectively.

Panels A(2), B(2) and C(2) in Figure 4.7 show that a_H, b_M and a_M generally decrease as Li is extracted from Li_xNiO_2. In the figures, $a_M/\sqrt{3}$ and b_M were plotted in order to show the magnitude of the distortion. Figure 4.3 shows that in the undistorted monoclinic cell, $a_M/\sqrt{3}$ is equal to b_M. Figure 4.7 clearly shows that in the hexagonal-monoclinic phase transition region and in the monoclinic single phase region, a distortion in the basal plane exists.

In panels A(3), B(3), and C(3) in Figure 4.7, $3c_M\sin\beta$ was plotted in order to show the changes along the c_H axis in a consistent way. In an undistorted monoclinic cell, $3c_M\sin\beta$ is equal to c_H. Panels A(3), B(3), and C(3) show that unit cell expanded along c_H axis initially as Li ions get extracted until the H3 phase with small c_H forms. Panels A(4), B(4), and C(4) in Figure 4.7 show that after the first charge, the angle β in the monoclinic cell changed in a more reversible manner during the following discharge and charge.

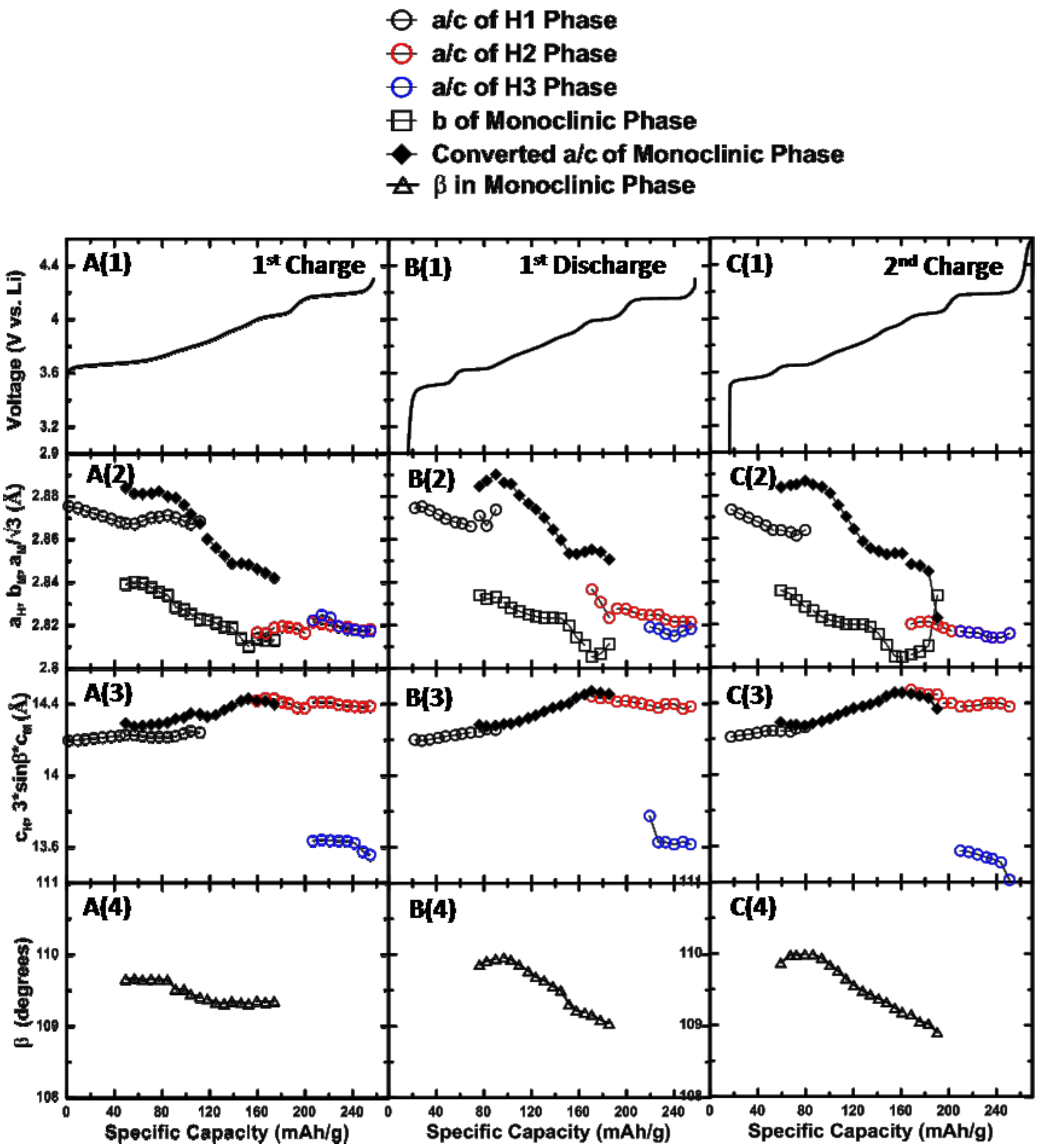

Figure 4.7 Cell voltage as a function of specific capacity during the 1st charge (A(1)), 1st discharge (B(1)), and 2nd charge (C(1)). Lattice parameters and β values of Li_xNiO_2 ($0 \leq x \leq 1$) as a function of specific capacity during 1st charge (A(2)-A(4)), 1st discharge (B(2)-B(4)), and 2nd charge (C(2)-C(4)).

Figure 4.8 shows the volumes of the hexagonal unit cells and 3/2 the volume of the monoclinic unit cell accompanied by the in-situ cell voltage profiles. Figure 4.8A(1), shows the in-situ cell voltage as a function of specific capacity during the first charge, and Figure 4.8A(2) shows the corresponding unit cell volumes during the first charge. The volume of monoclinic unit cell is multiplied by 3/2 and shown in the figure to observe the unit cell volume changes in a consistent way. Figure 4.3 shows that the unit cell volume of the undistorted monoclinic phase is equal to 2/3 of the hexagonal unit cell volume. Panels B(1)-B(2) and C(1)-C(2) in Figure 4.8 show the same parameters as a function of specific capacity during first discharge and second charge, respectively. Panels A(2), B(2) and (C)2 in Figure 4.8 show that as Li was de-intercalated, the unit cell volume decreased continuously until the H3 phase formed. From the H2 phase to the H3 phase, the unit cell volume decreases dramatically. The volume contraction at high states of charge observed is consistent with many studies on $LiNiO_2$ derivatives such as NMC and NCA positive electrode materials.[31,214] However the NMC and NCA samples do not show a two-phase region at top of charge; instead the materials contract as a single phase.[31,214]

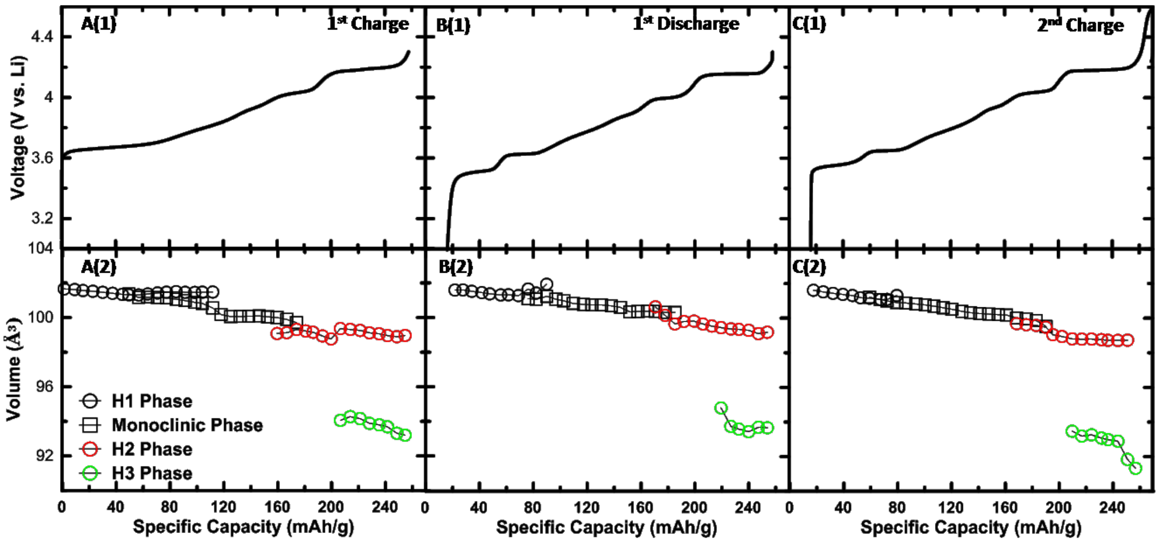

Figure 4.8 Cell voltage as a function of specific capacity during the 1st charge (A(1)), 1st discharge (B(1)), and 2nd charge (C(1)). Unit cell volumes as a function of specific capacity during 1st charge (A(2)), 1st discharge (B(2)), and 2nd charge (C(2)).

In order to assist possible theoretical efforts on Li_xNiO_2 ($0 \le x \le 1$), Table 4.2 lists the structural parameters versus x in $Li_{1-x}NiO_2$ as determined during the second charge of the in-situ cell. Based on the work of Mueller-Neuhaus et al.[164], and M. Winter et al.,[215] it is assumed that all the Li atoms did not re-insert into the material at the bottom of the first discharge, i.e. the measured irreversible capacity represents Li that cannot be re-inserted at the applied specific current. The values of x in Table 4.2 have been derived based on this assumption.

Table 4.2 Structural parameters versus x in $Li_{1-x}NiO_2$ as determined during the second charge of the in-situ cell.

	$Li_{1-x}NiO_2$	**H1/H2 Phase**			**M Phase**					**H3 Phase**		
Phase	x	a/b (Å)	c(Å)	Volume($Å^3$)	a(Å)	b(Å)	c(Å)	β (°)	Volume($Å^3$)	a/b (Å)	c(Å)	Volume($Å^3$)
H1	0.0636	2.8734	14.211	101.6126								
	0.0900	2.8714	14.218	101.5212								
	0.1166	2.8696	14.224	101.4367								
	0.1433	2.8678	14.233	101.3736								
	0.1694	2.8659	14.243	101.3104								
	0.1910	2.8639	14.245	101.1833								
H1-M	0.2158	2.8637	14.243	101.1550	4.9948	2.8357	5.0655	109.87	101.2127			
	0.2453	2.8628	14.241	101.0772	4.9965	2.8341	5.0635	109.98	101.0797			
	0.2631	2.8613	14.257	101.0847	4.9972	2.8312	5.0639	109.98	100.9984			
	0.2897	2.8638	14.264	101.3112	4.9999	2.8281	5.0623	109.99	100.9041			
M	0.3140				4.997	2.8263	5.0672	109.99	100.8789			
	0.3412				4.9951	2.8234	5.0698	109.94	100.8207			
	0.3663				4.99	2.8218	5.0722	109.84	100.7720			
	0.3906				4.9804	2.8211	5.0767	109.76	100.6930			
	0.4154				4.9712	2.82	5.0801	109.65	100.6042			
	0.4391				4.9611	2.8199	5.0833	109.56	100.5157			
	0.4664				4.9512	2.82	5.0846	109.48	100.3940			
	0.4895				4.9457	2.8187	5.0872	109.43	100.3184			
	0.5149				4.9432	2.8154	5.0911	109.37	100.2641			
	0.5392				4.9407	2.8104	5.0997	109.32	100.2351			
	0.5648				4.9416	2.805	5.1045	109.24	100.2038			
	0.5869				4.9414	2.8047	5.1022	109.18	100.1805			
M-H2	0.6144	2.8201	14.473	99.6823	4.9328	2.8059	5.0994	109.15	100.0122			
	0.6407	2.821	14.455	99.6219	4.9315	2.8071	5.0926	109.05	99.9556			
	0.6674	2.8212	14.447	99.5809	4.927	2.8099	5.0868	109.02	99.8682			
	0.6940	2.8197	14.447	99.4750	4.8894	2.8334	5.062	108.9	99.5193			
H2	0.7126	2.8183	14.399	99.0461								
	0.7374	2.8168	14.399	98.9407								
H2-H3	0.7652	2.8167	14.38	98.8031						2.8198	13.574	93.4706
	0.7911	2.8162	14.383	98.7887						2.8162	13.567	93.1840
	0.8178	2.8159	14.387	98.7951						2.8188	13.553	93.2598
	0.8444	2.8142	14.399	98.7581						2.8176	13.537	93.0704
	0.8622	2.8138	14.398	98.7232						2.8171	13.529	92.9824
	0.8889	2.8137	14.398	98.7162						2.8178	13.509	92.8911
	0.9150	2.8157	14.379	98.7261						2.812	13.411	91.8380
H3	0.9369									2.8118	13.338	91.3251

4.2.5 Electrochemical Testing Results

Figure 4.9 shows the differential capacity as a function of cell voltage (dQ/dV vs. V) of the in-situ cell (black solid lines) and of a regular coin cell (red dotted lines). Figure 4.9a shows dQ/dV vs. V during the first charge and Figure 4.9b shows dQ/dV vs. V during the following discharge and charge. The regular coin cell was tested with a specific current of 10 mA/g (~C/20) at 30ºC and the in-situ cell was tested with a specific current of 2 mA/g(~C/100) at room temperature (~25ºC). The good match between in-situ cell data and the coin cell data indicates the exceptional quality of the in-situ cell. Figures 4.9a and 4.9b show the phase evolution labeled according to the in-situ XRD refinements and analysis. Figure 4.9a shows that starting from a fresh cell, $LiNiO_2$ had a relatively large H1-M phase transition peak, which overlaps with the H1 single phase capacity. This is consistent with the previous discussions of the in-situ XRD refinement results, which showed that during the first charge, the H1-M phase transition was much slower. However during the following discharge and charge, the H1-M phase transition peak was sharp and narrow. This also agrees well with the in-situ XRD refinement results, which show that after the first charge, $LiNiO_2$ had a more rapid H1-M phase transition. Figure 4.9c shows the dQ/dV vs. V between 3.45 V to 3.75 V during the 1st charge (black line) and 2nd charge (blue line). It is likely that during the 1st charge, because of slow kinetics, the two peaks that appeared in the 2nd charge were shifted to higher potential and overlapped with each other.

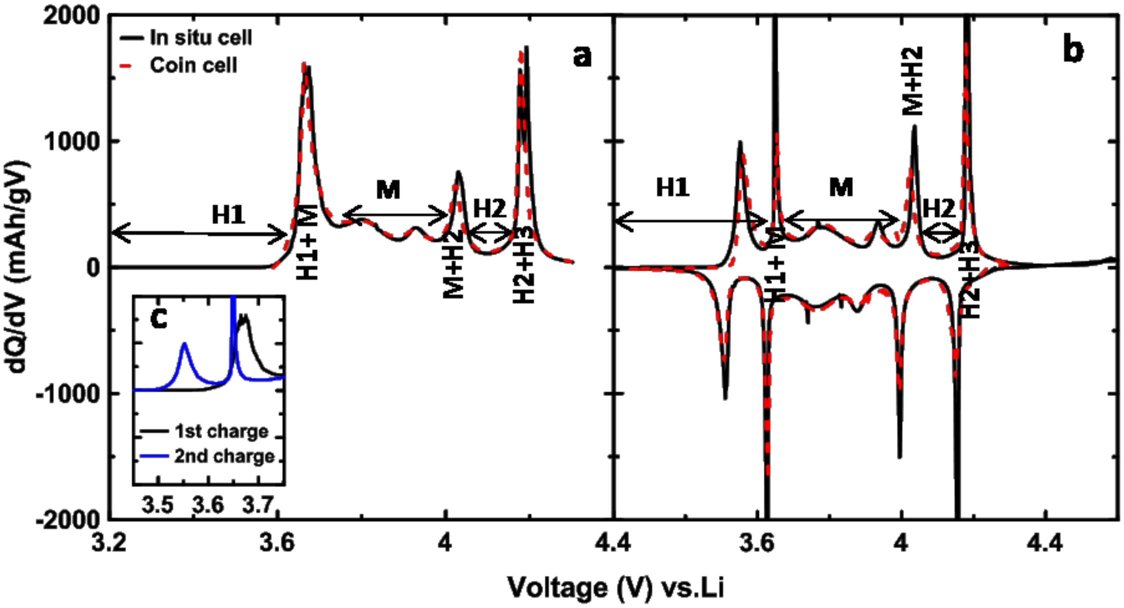

Figure 4.9 Differential capacity as a function of cell voltage (dQ/dV vs. V) of a Li/$LiNiO_2$ half coin cell and in-situ cell during 1st charge (a) and 1st discharge and 2nd charge (b). Black solid lines show the curves of the in-situ cell, and the red dotted lines show the curves of the regular coin cell. The inset (c) shows dQ/dV vs. V between 3.45 V to 3.75 V during the 1st charge (black line) and 2nd charge (blue line)

Figure 4.9b shows that after the first charge, there was a new peak at ~3.5 V in the H1 phase region. Figure 4.4 clearly shows that there is no two phase co-existence in the region between 3 - 3.6 V at least at the resolution of the x-ray diffractometer used. It may be that this peak is related to a transition between states where Li ions are ordered and disordered, respectively[93], and that the lattice constants of the two phases are very similar. The significant "step" in the voltage curve near 3.6 V and the corresponding minimum in dQ/dV vs. V is a strong signature of a composition where Li atoms are ordered.[216] If there is an ordered state at x = 1/4 or x = 1/7 in $Li_{1-x}NiO_2$ [217] on the triangular lattice of sites within each Li layer then unoccupied sites will have no unoccupied neighboring sites and diffusion will be very slow according to the work of A. Ven der Ven et al.[218]

They reported that Li ions diffuse from one octahedral site to an adjacent octahedral vacant site by passing through a tetragonal site. Figure 4.10 shows how aLi atom hops into an isolated vacancy in the presence or absence of a divacancy (circles are Li, squares are vacancies, and triangles are tetrahedral sites within the Li layer) as it moves from octahedral site to octahedral site. Based on their calculation, the diffusivity of Li ions is dependent on the number of nearest vacancies in the Li layer. When a di-vacancy exists, the energy barrier to pass through the tetragonal site is much lower.

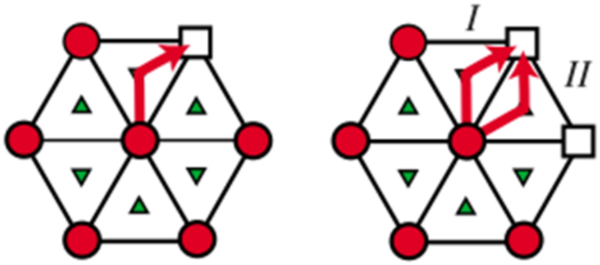

Figure 4.10 Li hops into an isolated vacancy (left) or in the presence of a divacancy (right) (circles are Li, squares are vacancies, and triangles are tetrahedral sites within the Li layer). Reprinted with permission from APS Physics Review B.[218] Copyright 2008 American Physical Society

Figure 4.11a shows the specific capacity versus cycle number of Li/$LiNiO_2$ coin cells made with the same $LiNiO_2$ studied in the in-situ XRD studies. Coin cells were first cycled at 30°C between 3.0 and 4.3 V with a specific current of 10 mA/g (~C/20) for two cycles, and then were cycled with a specific current of 40 mA/g (~C/5) for 20 cycles. After the cycling, coin cells were cycled with a specific current of 10 mA/g (~C/20) for one more cycle. Figure 4.11b shows dQ/dV vs. V of the C/20 cycle (black curves) of the fresh cell and the 1st C/5 cycle (blue curves). Figure 4.11c shows the 20th C/5 cycle (green curves) and the C/20 cycle (red curves) after the cycling tests. The 1st C/5 cycle dQ/dV vs. V is also shown in Figure 4.11c for comparison. Figure 4.11b shows that compared with the C/20 cycle, the C/5 cycle has the same peak shape as the preceding C/20 cycle except for the peak at ~3.5 V, which diminished with the increase in rate. Figure 4.11c shows that after the 20 C/5 cycles, the 3.5 V peak shrank dramatically while other peaks in dQ/dV were virtually the same. The post cycling C/20 cycle shows that with a relatively low rate, the diminished 3.5 V peak can be partially recovered. The origin of the increased kinetic hindrance is still unclear although there are some works about Li kinetics in literature. The group of C. Delmas et al. [219] showed that for Li deficient $Li_{1-x}Ni_{1+x}O_2$, there were more Ni atoms in the Li layer, and cells showed huge impedance and irreversible capacity, which can be attributed to a poorer Li diffusion.[164] It is likely that the Ni atoms between the transition metal oxide slabs can hinder the Li diffusion by reducing the number of divacancies, and also increase the local Li diffusion activation energy by decreasing inter slab distance in the vicinity of cationic mixing Ni atoms.[219] This region of kinetic hindrance near 3.5 V was recently highlighted in a study of NCA by J. Li. et al.[220] It may be that developing a complete understanding of the kinetic hindrance region in the model system $LiNiO_2$ will enable greater understanding of the commercially relevant NCA materials as well.

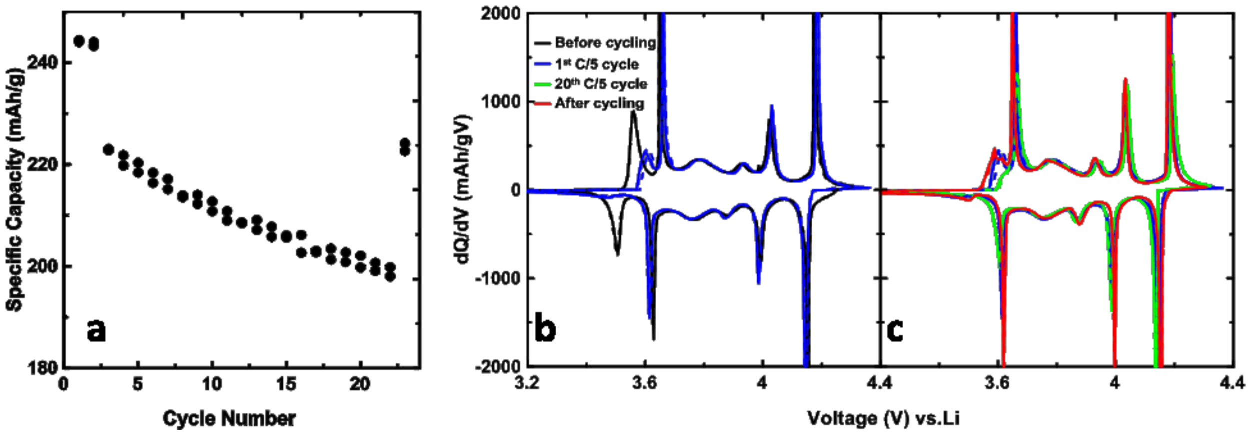

Figure 4.11 Specific capacity as a function of cycle number for two duplicate Li/LiNiO$_2$ coin cells (a). dQ/dV vs. V curves of C/20 cycle (black curves) before C/5 cycling tests, and dQ/dV vs. V curves of the 1st C/5 cycle (blue curves) (b). dQ/dV vs. V curves of the 20th C/5 cycle (green curves) and dQ/dV vs. V curves of the C/20 cycle (red curves) after the C/5 cycling tests (c). The 1st C/5 cycle dQ/dV vs. V is also shown in (c) for comparison.

4.2.6 Neutron Diffraction Measurements

To further explore the origin of the multiple phase transitions in LiNiO$_2$ during charge/discharge, neutron diffraction measurements were performed on charged LiNiO$_2$ powders. The advantage of neutron diffraction over XRD is the ability of detecting light elements like Li. XRD relies on the interaction between electrons with incident X-ray beams, and light elements have small atomic scattering factors *f* as discussed in Chapter 3. Neutrons are scattered primarily by atomic nuclei, so neutron scattering lengths vary "randomly" with atomic number.[221] Table 4.3 shows the X-ray atomic scattering factors and neutron scattering lengths for Li, Ni and O atoms acquired from the data base of NIST.[223] The small value of atomic scattering factor of Li indicates a weak interaction between X-ray and Li atoms. While in the case of neutron scattering, a negative scattering length of Li nuclei results in a phase shift on scattering, and helps makes the scattering from Li nuclei non-negligible.

Table 4.3 X-ray atomic scattering factors and neutron scattering lengths for Li, Ni and O atoms.

	X-ray (8.04 keV) atomic form factor (*e* atom^{-1})	Neutron scattering lengths (fm)
Li	3.00	-1.90
Ni	24.5-25.4	10.3
O	8.04-8.05	5.803

The hexagonal-monoclinic phase transition in $LiNiO_2$ was correlated to the Li-vacancy ordering by works from C. Delmas et al.[212,213] It was reported that similar to $LiCoO_2$,[223] at the 50% de-lithiation degree ($Li_{0.5}NiO_2$), the structure has alternately fully occupied Li sites and vacancies in rows. To verify whether this row-by-row Li/vacancy ordering exists, neutron diffraction was performed on $Li_{0.5}NiO_2$ powders, which was prepared by charging ~20 $LiNiO_2$-Li pellet half coin cells to 3.83V (vs. Li), and recovering about 5 g of positive electrode powders. Figure 4.12 shows the XRD patterns (black circles) and calculated profile (red line) of $LiNiO_2$ pellet materials charged to 3.83 V, and the XRD patterns of Li_xNiO_2 (x=~0.5) (blue line) taken from the in-situ XRD data in Figure 4.4. Figure 4.12 shows that XRD patterns of the pellet materials charged to 3.83 V match the in-situ XRD data of $Li_{0.5}NiO_2$. The samples were sealed in Al pouches in an Ar filled glove box before shipping to ANSTO. The authors thank N. Sharma, M. Avdeev, and D. Goonetilleke for carrying out the experiments.

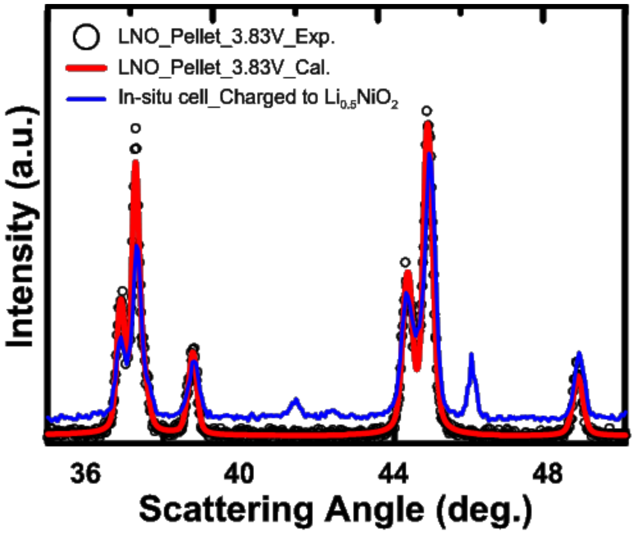

Figure 4.12 The XRD patterns (back circles) and Rietveld refinement calculation profile (red line) of $LiNiO_2$ pellet materials charged to 3.83 V; the XRD patterns of Li_xNiO_2 (x=~0.5) (blue line) taken from the in-situ XRD data in Figure 4.4.

Rietveld refinements were performed on the experimental neutron diffraction patterns with two different unit cell configurations. Figure 4.13a shows a unit cell built in a c2/m space group with a random distribution of 50% of Li atoms in Li layers. Figure 4.13b shows the unit cell built in a P2 space group with 50% of Li atoms occupying alternative rows. Table 4.4 shows the atom site information used for Rietveld refinements. Figures 4.14a and 4.14b show the neutron diffraction patterns and two refinements results based on the two Li distribution assumptions.

Table 4.4 Atomic site information of two unit cells with different Li distribution assumptions.

Unit cell	Space group	Atom	Atomic coordinates	Occupancy
Random Li distribution	C2/m	Li	(0, 0, 0)	0.5
		Ni	(0, 0.5, 0.5)	1
		O	(0.76657, 0, 0.28941)	2
Ordered Li distribution	P2	Li	(0, 0, 0)	1
		Vacancy	(0.5, 0.5, 0)	NA
		Ni_1	(0, 0.5, 0.5)	1
		Ni_2	(0.5, 0, 0.5)	1
		O_1	(0.2388, 0, 0.7153)	2
		O_2	(0.2388, 0.5, 0.2847)	2

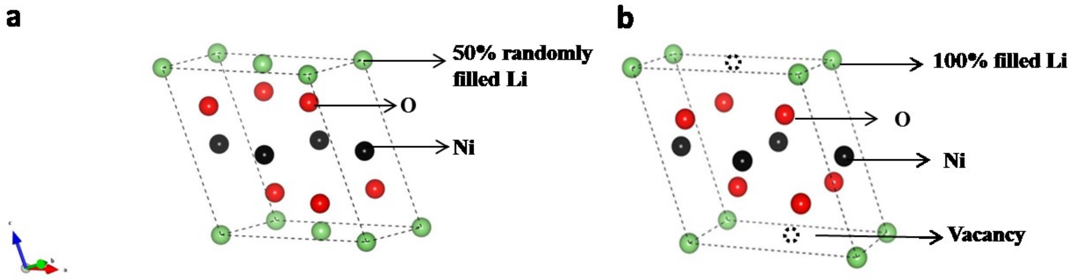

Figure 4.13 Unit cells of $Li_{0.5}NiO_2$ with random Li distribution (a) and ordered Li-vacancy configuration (b).

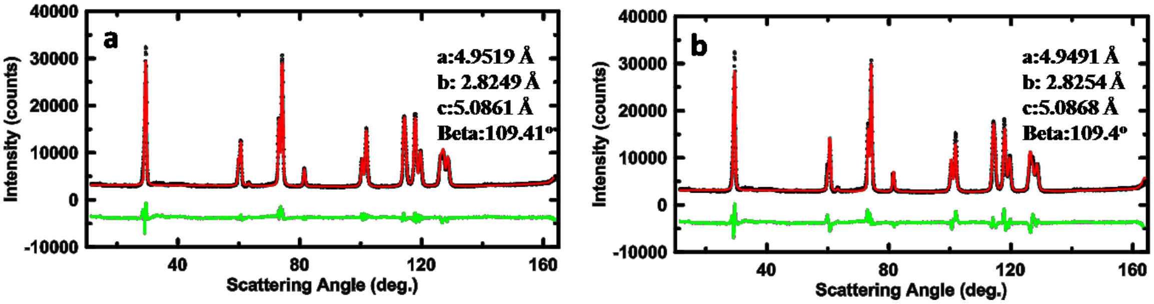

Figure 4.14 Neutron diffraction patterns of Li_xNiO_2 (x=~0.5, 3.83V vs Li) and Rietveld refinements with random Li distribution (a) and Li-vacancy ordering (b). Black circles are experimental data, solid red lines are calculated patterns from Rietveld refinement, green lines show the differences between the measured and calculated patterns.

The refinement performed with the random Li distribution assumption has a $R_{Bragg} = 2.98$, and the refinements performed with the ordered Li distribution assumption has $R_{Bragg} = 4.93$. Figure 4.15 shows expanded views of neutron diffraction patterns and two calculated profiles made with the two Li distribution assumptions. Figure 4.15a shows that the row-by-row Li/vacancy ordering assumption calculated profile has a poor agreement in relative intensity with the experimental data, and Figure 4.15b shows that with the row-by-row Li/vacancy ordering assumption, a (21-1) superlattice Bragg peak should be expected at ~82.7°. Refinement performed based on the random Li distribution assumption has a better agreement with the experimental data. This indicates that the row-by-row Li/vacancy ordering may not exist in the monoclinic phase of Li_xNiO_2 (x=~0.5).

G. Ceder et al. proposed that based on a first principle calculation, the monoclinic distortion arises due to a synergetic effect between Jahn-Teller distortion and Li/vacancy ordering.[99,100] In their work, they predicted several complex Li-vacancy ordering distributions at different compositions. However, there has been no experimental data to back the proposed hypothesis. Neutron diffraction measurements were also performed on another three sets of samples charged to 3.54 V, 3.67 V, and 4.07 V, respectively. No superlattice Bragg peaks were observed.

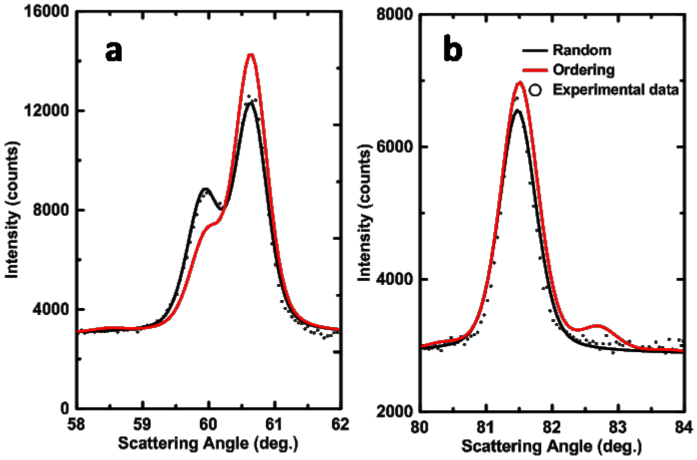

Figure 4.15 Expanded views of neutron diffraction patterns and two refinements calculation profiles made with two Li distribution assumptions.

4.3 Conclusions

With commercial $Ni(OH)_2$ precursors and an improved synthesis method, modern $LiNiO_2$ with high capacity and low irreversible capacity was made. Using this high quality $LiNiO_2$, this work systematically measured the electrochemical and structural properties of $LiNiO_2$ with in-situ XRD and careful electrochemical measurements. Multiple phase transitions during charge and discharge were carefully observed and analyzed. A distinct slow H1-M phase transition behavior during first charge and the development of kinetic hindrance, most likely due to slow Li diffusion, in the H1 phase region during extended charge-discharge cycling was observed. For $LiNiO_2$ and other high Ni content positive electrode materials like NCA, an understanding of the kinetic hindrance is essential in order to eliminate it. The neutron diffraction measurement on distorted monoclinic Li_xNiO_2 (x=~0.5) shows that an ordering of Li/vacancy in alternating rows may not exist based on the Rietveld refinement results.

CHAPTER 5 STUDIES OF CATION SUBSTITUTION IN $LiNi_{1-X}M_XO_2$ (M= Al, Co, Mn OR Mg) : IS COBALT NEEDED IN Ni-RICH POSITIVE ELECTRODE MATERIALS FOR LITHIUM ION BATTERIES?

Partial replacement of Ni in $LiNiO_2$ with other cations has been adopted as an effective approach to make improved positive electrode materials. As one of the derivatives of $LiNiO_2$, NCA ($LiNi_{1-x-y}Co_xAl_yO_2$) is widely used in the EV industry because of its high energy density.[81,206,207] It is thought that Co and Al both play important roles in enhancing NCA material properties such as thermal stability, structure stability and cation interlayer mixing.[10–12,154,155] S. Myung et al., C. Delmas et al. and A. Ueda et. al showed that partial replacement of Ni with Co reduced the cation mixing between Ni^{2+} and Li^{+} [10,11], and suppressed the multiple phase transitions during charge and discharge.[12] However, there is no solid evidence in the literature that clearly shows that Co is required in NCA with high Ni (e.g. when 1-x-y > 0.9) content. Besides Co and Al, other cation substituents such as Mn, Mg, Ti, and Fe have been investigated by different researchers showing improvements in thermal stability, structure stability, and cycling performance. [153,157–159,162–164,224,225] However it is hard to make a head to head comparison among the different substituents because of different synthesis conditions and analysis procedures chosen by different researchers. With the increasing demand to reduce Co content and increase Ni content, it becomes important for researchers to go "back to basics" and systematically study the impact of different cation substitutions.

Following the work on $LiNiO_2$ discussed in Chapter 4, a systematic study on the effects of cation substitutions was made. Early on in this work, it was found that the electrochemical properties of NCA with a composition of $LiNi_{0.90}Co_{0.05}Al_{0.05}O_2$, which were studied and reported in detail in a recent paper by J. Li et al.,[91] were very close to those of $LiNi_{0.95}Al_{0.05}O_2$ and $LiNi_{0.95}Mn_{0.05}O_2$. Figure 5.1 shows the differential capacity versus voltage for $Li/LiNi_{0.90}Co_{0.05}Al_{0.05}O_2$, $Li/LiNi_{0.95}Al_{0.05}O_2$ and $Li/LiNi_{0.95}Mn_{0.05}O_2$ cells. Figure 5.1 suggests that at least the electrochemical properties of NCA ($LiNi_{0.90}Co_{0.05}Al_{0.05}O_2$) can be matched by materials without Co. If so, then why include Co? Figure 5.1 provided much of the motivation for this work and will hopefully serve to motivate readers to study this work with care.

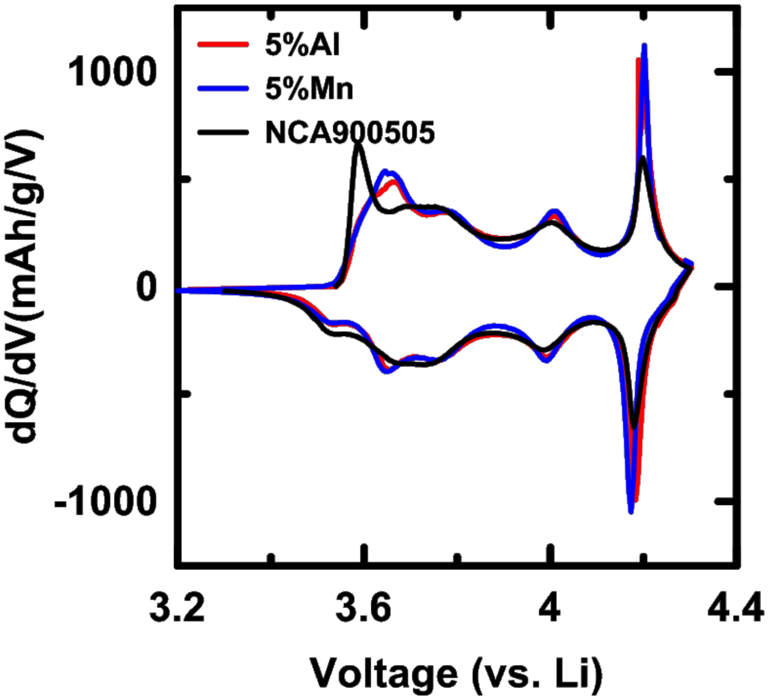

Figure 5.1 Differential capacity as a function of cell voltage (dQ/dV vs. V) for Li/$LiNi_{0.90}Co_{0.05}Al_{0.05}O_2$, Li/$LiNi_{0.95}Al_{0.05}O_2$ and Li/$LiNi_{0.95}Mn_{0.05}O_2$ cells. The cells were tested at C/20 and at 30ºC.

In this work, metals including Al, Co, Mn, and Mg, which are of great interest, were selected for investigation. Samples of $LiNi_{1-n}M_nO_2$ (M = Al, Co, Mn or Mg, n=0.05 or 0.1), as well as $LiNi_{0.90}Co_{0.05}Al_{0.05}O_2$, were synthesized and studied with differential capacity versus voltage (dQ/dV vs. V) methods. In-situ X-ray diffraction measurements were carried out on selected samples and the unit cell parameters and unit cell volume were carefully measured versus x in $Li_xNi_{1-n}M_nO_2$ ($0 \leq x \leq 1$). The impacts of selected substituents were studied and a simple model describing their function was proposed. Accelerating rate calorimetry testing was performed to evaluate the impact of different substituents on the thermal stability of charged positive electrode materials in electrolyte. The majority of this Chapter was published in Journal of The Electrochemical Society.[32] H. Li conducted the material synthesis, ex/in-situ XRD measurements, and electrochemical tests; M. Cormier performed the first-principle calculation; N. Zhang performed the ARC tests, J. Inglis and J. Li contributed to the electrochemical tests. Reproduced with permission from *J. Electrochem. Soc.*, 166.4 (2019): A429-A439. Copyright 2019, The Electrochemical Society.

5.1 Experimental Design

$Ni_{1-n}M_n(OH)_2$ (M = Co, Mn, or Mg, n=0.05 or 0.1) and $Ni_{0.9}Al_{0.1}(OH)_2$ precursors were made using co-precipitation as described in Chapter 3. $Ni_{0.95}Al_{0.05}(OH)_2$ and $Ni_{0.9}Co_{0.05}Al_{0.05}(OH)_2$ precursors were provided by Zoomwe Zhengyuan Advanced

Material Co., Ltd. The lithiation process was carried out as described in Chapter 3. Mixed precursors and $LiOH•H_2O$ with a Li/TM ratio of 1.02 were prepared and heated at 700°C for 20 hours for $LiNi_{0.95}M_{0.05}O_2$ samples and at 735°C for 20 hours for $LiNi_{0.9}M_{0.1}O_2$ and $LiNi_{0.9}Co_{0.05}Al_{0.05}O_2$ samples.

SEM and powder XRD characterizations were performed as described in Chapter 3. The experimental details about coin cell assembly, electrochemical tests, in-situ XRD measurements were described in Chapter 3. Electrolyte with 1.0 M $LiPF_6$ in EC:DEC (1:2 v/v) was used for collecting coin cell voltage vs. specific capacity profiles, dQ/dV vs. V measurements and in-situ X-ray diffraction experiment. Electrolyte with 1.0 M $LiPF_6$ in FEC:DMC (1:4 v/v) was used for the half coin cell cycling tests as this electrolyte gives better long-term Li metal cycling. ARC tests were conducted as described in Chapter 3 to assess the reactivity between charged positive electrode materials and electrolyte.

5.2 Results and Discussion

5.2.1 Material Characterization

To demonstrate that high quality samples were synthesized at Dalhousie, Figures 5.2 to 5.3 show the original x-ray diffraction patterns of the samples studied here. Of particular note is the expanded view of the diffraction patterns between 20° and 35° where the strongest diffraction peaks from typical impurities such as Li_2CO_3 and Li_5AlO_4 appear. Figures 5.2 to 5.3 show that all samples are single phase and impurity-free except for

$LiNi_{0.9}Al_{0.1}O_2$, which has a small amount of Li_5AlO_4. As reported by J. Li et al.,[226] the formation of Li_5AlO_4 is dependent on NCA elemental composition and it is prone to form in high Al content compositions. Figures 5.4a to 5.4e show SEM images of some of the synthesized materials as representatives of all the samples studied in this work. The SEM images show that all the samples made from precursors prepared at Dalhousie are spherical and dense with a typical secondary particle size of 10 μm. The samples of $LiNi_{0.95}Al_{0.05}O_2$ and $LiNi_{0.9}Co_{0.05}Al_{0.05}O_2$ prepared from the commercial $Ni_{0.95}Al_{0.05}(OH)_2$ and $Ni_{0.9}Co_{0.05}Al_{0.05}(OH)_2$ precursors, have a secondary particle size of 17 μm.

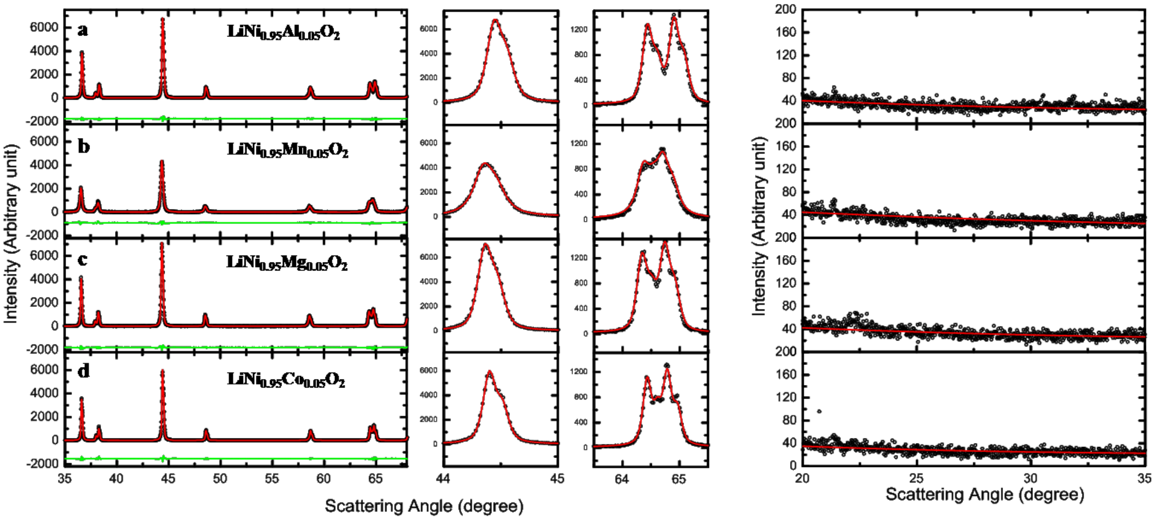

Figure 5.2 XRD patterns of $LiNi_{0.95}Al_{0.05}O_2$ (a), $LiNi_{0.95}Mn_{0.05}O_2$ (b), $LiNi_{0.95}Mg_{0.05}O_2$ (c), and $LiNi_{0.95}Co_{0.05}O_2$ (d). Expanded view of the (104) Bragg peak, (108)/(110) Bragg peaks, and impurity regions were shown. Black circles are experimental XRD data, solid red lines are calculated patterns from Rietveld refinement, and green lines show the differences between the measured and calculated patterns.

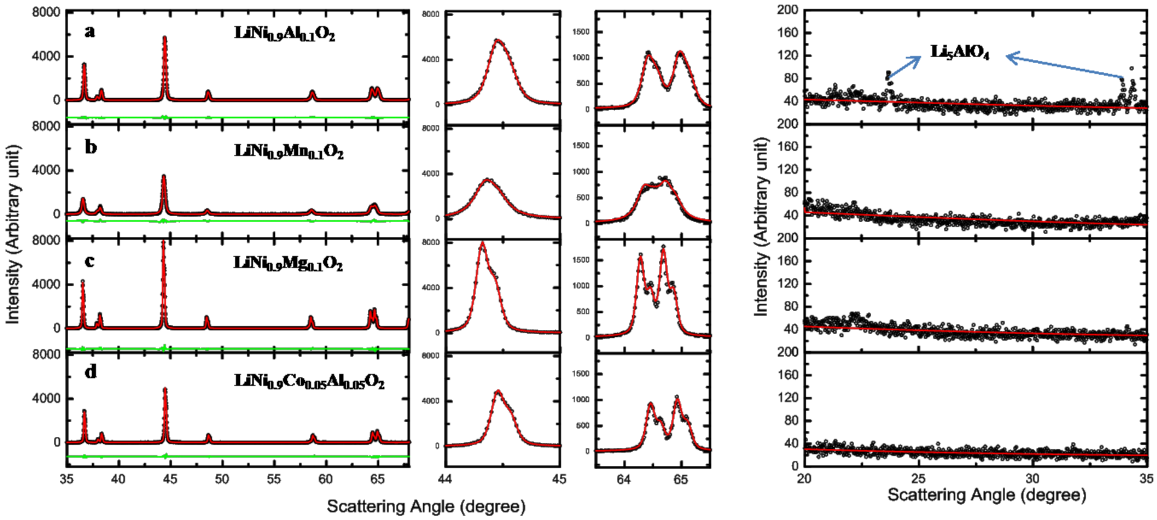

Figure 5.3 XRD patterns of $LiNi_{0.9}Al_{0.1}O_2$ (a), $LiNi_{0.9}Mn_{0.1}O_2$ (b), $LiNi_{0.9}Mg_{0.1}O_2$ (c), and $LiNi_{0.95}Co_{0.05}Al_{0.05}O_2$ (d). Expanded view of the (104) Bragg peak, (108)/(110) Bragg peaks, and impurity regions were shown. Black circles are experimental XRD data, solid red lines are calculated patterns from Rietveld refinement, and green lines show the differences between the measured and calculated patterns.

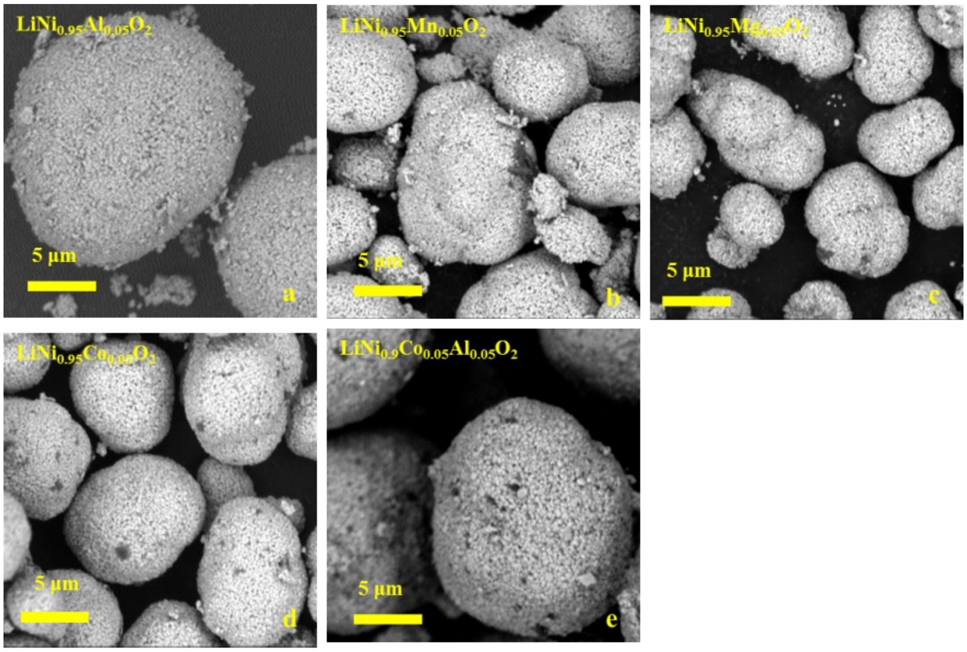

Figure 5.4 SEM images of synthesized $LiNi_{0.95}Al_{0.05}O_2$ (a), $LiNi_{0.95}Mn_{0.05}O_2$ (b), $LiNi_{0.95}Mg_{0.05}O_2$ (c), $LiNi_{0.95}Co_{0.05}O_2$ (d), and $LiNi_{0.9}Co_{0.05}Al_{0.05}O_2$ (e).

5.2.2 Effects of Cation Substitution on Structure Parameters and Irreversible Capacity

It has been thought that Co-doping reduces the Ni/Li interlayer mixing[7,8]. But analysis of XRD patterns suggests that for Mn-free materials Co provides no benefit in reducing Ni/Li interlayer mixing. Figures 5.5a and 5.5b show the lattice constants, a and c, as a function the percent of Al, Mn and Mg substituents added. Samples with 2.5% Al, 2.5% Mg, 2.5 Mn, and 7.5% Al content were made for other studies but are included here for completeness. Table 5.1 shows the structural results from the x-ray profile refinements. Table 5.1 shows that for the three different substituents, the *c* lattice constant increased continuously with the amount of substituent. The *a* lattice constants of the Mn and Mg series increased as the substituent content increased, while for the Al series, the *a* lattice constant continuously decreased as the substituent content increased. Figure 5.5c shows the percentage of Ni atoms in the Li layers. It is not surprising that with more Mn substituent, there were more Ni atoms in the Li layers because of the presence of more Ni^{2+} to compensate Mn^{4+}. Figure 5.5c and Table 5.1 show that even without Co, both the Al and Mg series demonstrated very low interlayer mixing, suggesting that Co is not required to eliminate Ni/Li mixing when there is no Mn in the structure.

Table 5.1 Rietveld refinement results of cation doped $LiNiO_2$

	a/b (Å) (within ± 0.0001 Å)	c (Å) (within ± 0.001 Å)	Ni in Li layer (within 0.3%)	R_{Bragg}
$LiNi_{0.95}Co_{0.05}O_2$	2.8752	14.189	0.83%	1.57
$LiNi_{0.95}Al_{0.05}O_2$	2.8711	14.202	1.22%	1.65
$LiNi_{0.95}Mn_{0.05}O_2$	2.8778	14.200	5.79%	3.78
$LiNi_{0.95}Mg_{0.05}O_2$	2.8774	14.215	1.66%	1.51
$LiNi_{0.9}Co_{0.05}Al_{0.05}O_2$	2.8697	14.197	1.10%	1.76
$LiNi_{0.9}Al_{0.1}O_2$	2.8679	14.212	1.03%	1.45
$LiNi_{0.9}Mn_{0.1}O_2$	2.8773	14.208	7.45%	4.0
$LiNi_{0.9}Mg_{0.1}O_2$	2.8795	14.266	2.00%	1.75

Figure 5.5d shows the irreversible capacity (IRC) of coin cells cycled at 30°C with a current density of 10 mA/g (~C/20) between 3.0 - 4.3V. The IRC increases as the dopant content increases. The black dotted line shows the IRC of $LiNi_{0.90}Co_{0.05}Al_{0.05}O_2$ synthesized in this work, indicating that the $LiNi_{0.95}M_{0.05}O_2$ (M = Al, Mn, Mg) materials do not have significantly different irreversible capacity compared to a typical NCA material with 5% Al content. **(What is the purpose of the Co?)** Table 5.2 summarizes the data for coin cells tested at 30°C and 55°C with a current density of 10 mA/g (~C/20) between 3.0 and 4.3V. $LiNi_{0.9}Co_{0.05}Al_{0.05}O_2$ and $LiNi_{0.9}M_{0.1}O_2$ (M = Al, Mn, or Mg) cells were cycled at both 30°C and 55°C. Table 5.2 shows that at elevated temperature, the IRC was reduced significantly. This suggests that the increase in IRC observed in

Figure 5.5d is not due to irreversible structural changes during the 1st charge/discharge caused by the introduction of substituents, and is presumably related to a Li diffusion hindrance.[164]

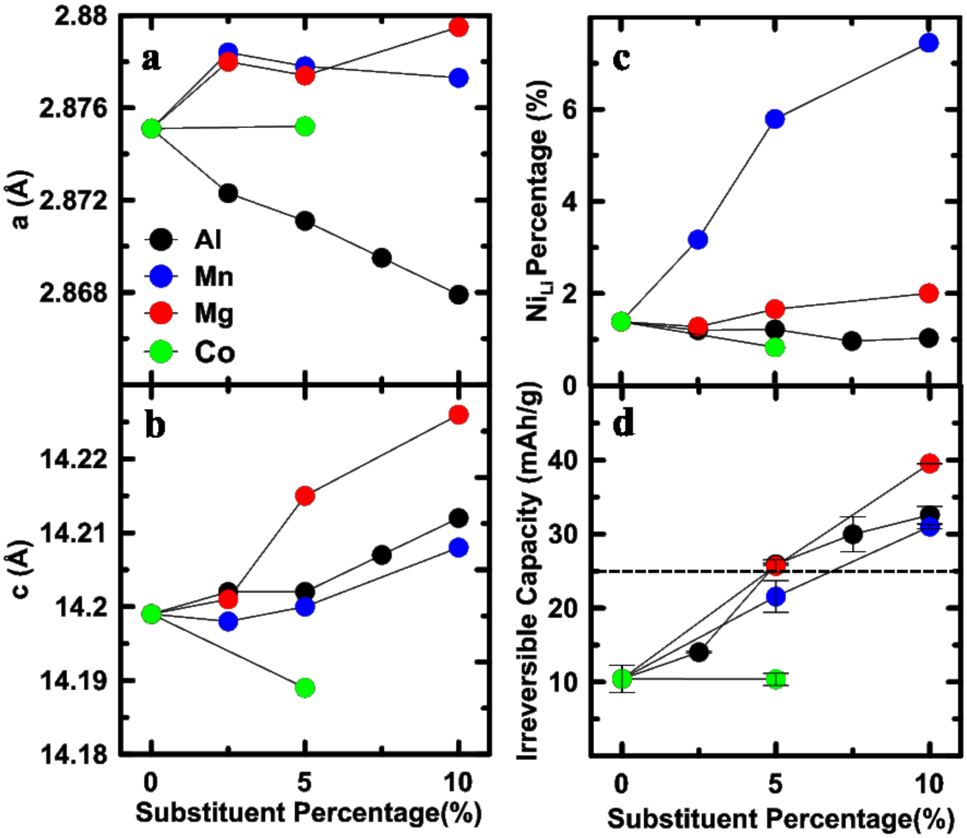

Figure 5.5 Unit cell constants a (a) and c (b) as a function of substituent percentage; the percentage of Ni/Li interlayer mixing as a function substituent percentage (c); the irreversible capacity (IRC) as a function of substituent percentage (d). The horizontal dashed line in Figure 5.5d shows the irreversible capacity of $LiNi_{0.95}Co_{0.05}Al_{0.05}O_2$.

Table 5.2 Half coin cell testing results of cation doped $LiNiO_2$. Cells were tested between 3.0 and 4.3 V at C/20 and at 30°C. The errors indicate the difference between duplicate cells and the value reported is the average from duplicate cells.

	Testing Temperature (°C)	Average first Charge Capacity (mAh/g)	Average Discharge Capacity (mAh/g)	IRC (mAh/g)	IRC Percentage (%)
$LiNiO_2$	30	254(2)	244.2(2)	10(2)	4.1(6)%
$LiNi_{0.95}Co_{0.05}O_2$	30	246.7(7)	236.4(1)	10.3(8)	4.2(3)%
$LiNi_{0.95}Al_{0.05}O_2$	30	244.6(8)	218.6(9)	25.9(1)	10.60(9)%
$LiNi_{0.95}Mn_{0.05}O_2$	30	238.8(9)	217(1)	21(2)	9.0(9)%
$LiNi_{0.95}Mg_{0.05}O_2$	30	228.3(9)	203(2)	25.7(8)	11.3(4)%
$LiNi_{0.9}Co_{0.05}Al_{0.05}O_2$	30	240(3)	215(1)	25(4)	11 (1)%
$LiNi_{0.9}Al_{0.1}O_2$	30	215.4(1)	183(1)	32(1)	15.1(5)%
$LiNi_{0.9}Mn_{0.1}O_2$	30	219.6(3)	188.6(1)	31.0(3)	14.1(1)%
$LiNi_{0.9}Mg_{0.1}O_2$	30	202(2)	162(2)	39.53(4)	19.6(2)%
$LiNi_{0.9}Co_{0.05}Al_{0.05}O_2$	55	242(1)	233(1)	18(2)	7.5(9)%
$LiNi_{0.9}Al_{0.1}O_2$	55	226(2)	212(1)	14(4)	6(1)%
$LiNi_{0.9}Mn_{0.1}O_2$	55	221(1)	210(1)	11.2(1)	5.05(1)%
$LiNi_{0.9}Mg_{0.1}O_2$	55	213(2)	197.0(2)	16(2)	8(1)%

5.2.3 dQ/dV vs. V Studies on $LiNi_{1-n}M_nO_2$ (M = Al, Co, Mn or Mg, n=0.05 or 0.1)

The following discussion addresses the possibility that Co doping may suppress the multiple phase transitions observed in $LiNiO_2$ during charge and discharge[10]. It is found that Co content up to at least 5% does not effectively suppress phase transitions during charge and discharge. Figures 5.6A – 5.6E show the cell voltage as a function of specific capacity (V vs. Q) for $LiNiO_2$, $LiNi_{0.95}Al_{0.05}O_2$, $LiNi_{0.95}Mn_{0.05}O_2$, $LiNi_{0.95}Mg_{0.05}O_2$, and $LiNi_{0.95}Co_{0.05}O_2$, respectively. Figures 5.6a – 5.6e show the corresponding differential capacity as a function of cell voltage (dQ/dV vs. V) for the 2nd charge and discharge. Solid and dashed lines represent two duplicate cells. The data in Figures 5.6A and 5.6a were reported by H. Li et al.[9] and discussed in Chapter 4, where the multiple phase transitions of $LiNiO_2$ during charge and discharge were discussed in detail. Four pairs of peaks have been circled in Figure 5.6a, and peaks i-iv represent the kinetic hindrance peak in the H1 phase, the H1-M phase transition peaks, the M-H2 phase transition peaks, and the H2-H3 phase transition peaks, respectively.[9] Figures 5.6a and 5.6e show that both $LiNiO_2$ and $LiNi_{0.95}Co_{0.05}O_2$ have clear and intense dQ/dV peaks, while Figures 5.6b – 5.6d show that with 5% Al, 5% Mn or 5% Mg substitutions, the peaks were diminished significantly, suggesting an effective suppression of the phase transitions observed in $LiNiO_2$, as will be proved by in-situ XRD experiments discussed below. The insets in Figures 5.6b – 5.6d show the dQ/dV vs. V curves with an expanded scale.

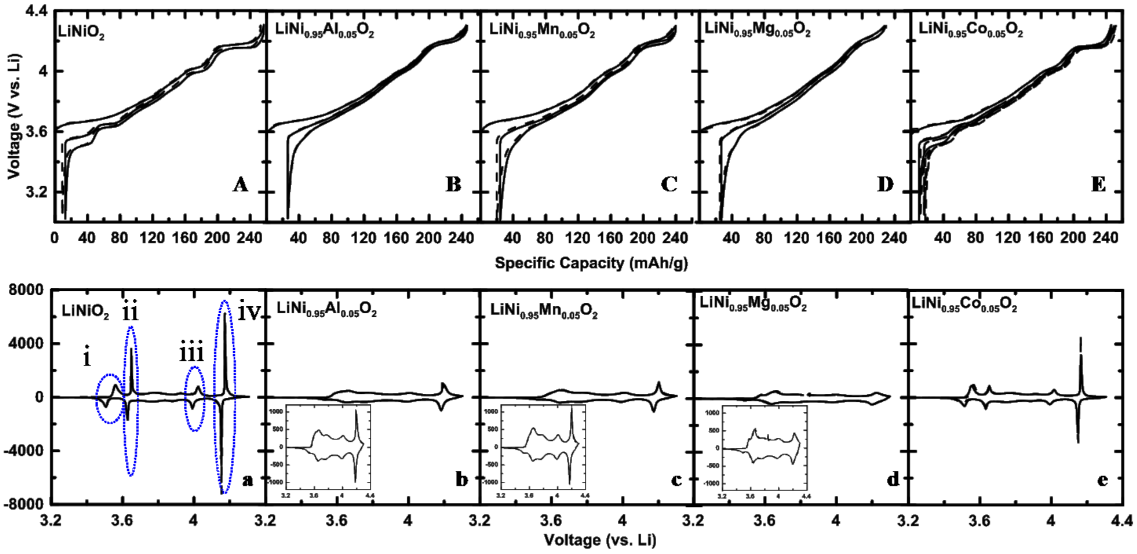

Figure 5.6 Cell voltage as a function of specific capacity (V vs. Q) of $LiNiO_2$ (A), $LiNi_{0.95}Al_{0.05}O_2$ (B), $LiNi_{0.95}Mn_{0.05}O_2$ (C), $LiNi_{0.95}Mg_{0.05}O_2$ (D), and $LiNi_{0.95}Co_{0.05}O_2$ (E); Differential capacity as a function of cell voltage (dQ/dV vs. V) of 2nd charge and discharge of $LiNiO_2$ (a), $LiNi_{0.95}Al_{0.05}O_2$ (b), $LiNi_{0.95}Mn_{0.05}O_2$ (c), $LiNi_{0.95}Mg_{0.05}O_2$ (d), and $LiNi_{0.95}Co_{0.05}O_2$ (e).

For $LiNiO_2$, the kinetic hindrance peaks, which fall in the H1 single phase region, and the other three pairs of phase transition peaks are believed to be related to Li ion ordering and disordering.[9,84] The significant "steps" in the voltage curve and the corresponding minima in dQ/dV vs. V are strong signatures of a composition where Li atoms are ordered.[216] However, as shown by the neutron diffraction experiments in Chapter 3, no evidence of the Li/vacancy row-by-row ordering could be found in the monoclinic phase It is believed that with 5% Al, 5% Mn or 5% Mg substitutions, the Li ordering can be suppressed. Figure 5.6e shows that compared with $LiNiO_2$, the addition of 5% Co cations resulted in attenuated dQ/dV vs. V peaks, but the features associated with Li ordering and ensuing phase transitions during charge and discharge are still quite distinct. Previous studies have shown that $LiNi_{0.5}Co_{0.5}O_2$,[12] $LiNi_{0.8}Co_{0.2}O_2$,[92] and $LiNi_{0.7}Co_{0.3}O_2$[11] have smooth V vs. Q curves, and no phase transitions were observed. This suggests that unlike Al, Mn and Mg, Co does not effectively suppress phase transitions during charge/discharge until the content of Co is higher than at least 5% and probably higher. To further understand these observed phenomena, first-principles computations were performed by M. Cormier and discussed in detail in the paper published based on this the work of this Chapter.[32]

Figures 5.7A – 5.7D show the V vs. Q curves of $LiNi_{0.9}Al_{0.1}O_2$, $LiNi_{0.9}Mn_{0.1}O_2$, $LiNi_{0.9}Mg_{0.1}O_2$, and $LiNi_{0.9}Co_{0.05}Al_{0.05}O_2$, respectively. Figures 5.7a – 5.7d show the corresponding dQ/dV vs. V curves of the 2nd charge and discharge in black lines. In Figures 5.7a and 5.7b, red lines show the dQ/dV vs. V curves of $LiNi_{0.95}Mg_{0.05}O_2$. Solid and dashed lines represent two duplicate cells. Figures 5.7a, 5.7b, and 5.7c show that with 10% cation substitution, dQ/dV vs. V peaks were further attenuated compared to samples with 5% of substituent (see Figure 5.6). Especially in Figure 5.7c, for $LiNi_{0.9}Mg_{0.1}O_2$, all the peaks that corresponded to phase transitions in $LiNiO_2$ virtually disappeared. Figure 5.7d shows that with both 5% Co and 5% Al substituents, $LiNi_{0.9}Co_{0.05}Al_{0.05}O_2$ showed different dQ/dV vs. V features compared to $LiNi_{0.95}Co_{0.05}O_2$, and that the distinct phase transition peaks diminish significantly due to the presence of Al, not Co. Figures 5.7a and 5.7b include the dQ/dV vs. V curves of $LiNi_{0.95}Mg_{0.05}O_2$ in red, to illustrate that dQ/dV for a 5% Mg substitution is very similar to materials with 10% Al or 10% Mn. This is presumably due to a similar degree of Li ion/vacancy ordering suppression and a similar amount of capacity reduction.

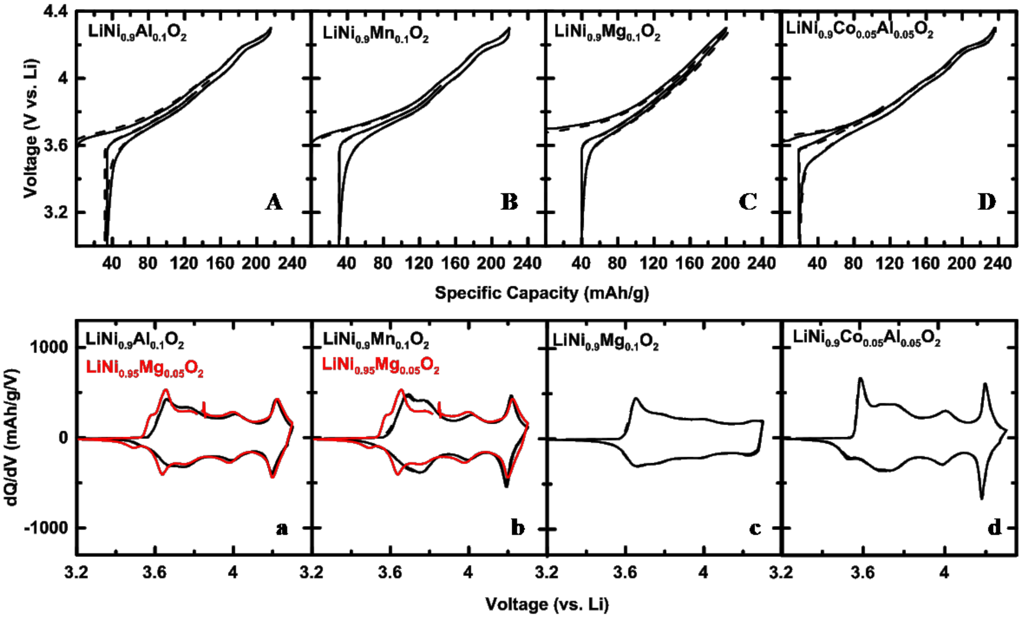

Figure 5.7 V vs. Q curves of $LiNi_{0.9}Al_{0.1}O_2$ (A), $LiNi_{0.9}Mn_{0.1}O_2$ (B), $LiNi_{0.9}Mg_{0.1}O_2$ (C), and $LiNi_{0.95}Co_{0.05}Al_{0.05}O_2$ (D); dQ/dV vs. V curves of 2nd charge and discharge of $LiNi_{0.9}Al_{0.1}O_2$ (a), $LiNi_{0.9}Mn_{0.1}O_2$ (b), $LiNi_{0.9}Mg_{0.1}O_2$ (c), and $LiNi_{0.95}Co_{0.05}Al_{0.05}O_2$ (d). The dQ/dV vs. V curve of $LiNi_{0.95}Mg_{0.05}O_2$ was plotted in Figures (a) and (b) in red for comparison.

5.2.4 In-situ XRD Measurements and Analysis

Figure 5.8 shows the results of in-situ X-ray diffraction experiments on $LiNi_{0.95}Al_{0.05}O_2$, $LiNi_{0.95}Mn_{0.05}O_2$, $LiNi_{0.95}Mg_{0.05}O_2$, and $LiNi_{0.9}Co_{0.05}Al_{0.05}O_2$ cells. The XRD patterns are sequentially offset for clarity and are accompanied by the in-situ coin cell voltage-time profile which has been scaled so that each XRD pattern appears at the time, voltage and cycle number when it was collected. Figures 5.8a1, 5.8b1, 5.8c1, and 5.8d1 are aligned with the corresponding diffraction patterns and show that the cell was first charged and discharged between 3.0 - 4.3 V for 1 cycle at a rate of ~C/100, and then the cell was charged to 4.6 V at the same rate. Each XRD scan took exactly 2.803 hours. In the four sets of in situ XRD patterns, four selected scattering angle regions were shown. A peak from beryllium oxide was observed at 46°. Chapter 4 shows that the in situ XRD patterns of $LiNiO_2$ have very distinct features signaling multiple phase transitions during charge and discharge, which include the splitting of (101) and (104) Bragg peaks at ~3.7V and the coexistence of two (003) Bragg peaks at high states of charge. Figure 5.8a2 shows that during charge, the (003) Bragg peaks continuously shifted to lower angle first, and then shifted to higher angle at the end of charge. Figures 5.8a3, 5.8a4, and 5.8a5 also show continuous peak shifting, and no splitting of peaks was observed. This suggests that for $LiNi_{0.95}Al_{0.05}O_2$, a single phase structure was maintained during charge and discharge. Similar phenomena were also observed in the case of $LiNi_{0.95}Mn_{0.05}O_2$, $LiNi_{0.95}Mg_{0.05}O_2$, and $LiNi_{0.9}Co_{0.05}Al_{0.05}O_2$, and no phase transitions were observed during either charge or discharge.

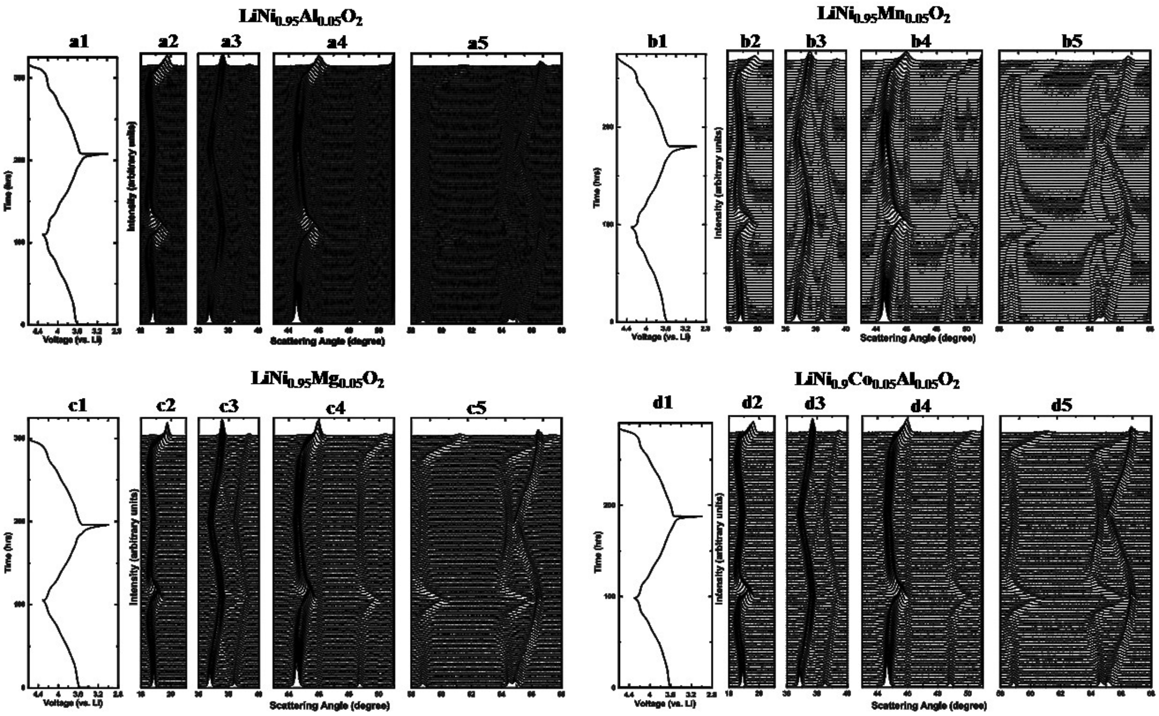

Figure 5.8 In-situ XRD patterns and cell cycling profiles of $LiNi_{0.95}Al_{0.05}O_2$ (a1 - a5), $LiNi_{0.95}Mn_{0.05}O_2$ (b1 – b5), $LiNi_{0.95}Mg_{0.05}O_2$ (c1 – c5), and $LiNi_{0.9}Co_{0.05}Al_{0.05}O_2$ (d1 – d5). In-situ XRD patterns of selected scattering angle regions of 18 - 21°, 36 - 40°, 43 - 51°, and 58 - 68° are shown. The cells were charged and discharged between 3.0 – 4.3 V at a rate of ~C/100 for 1 cycle, and charged to 4.6 V at a rate of ~C/100.

Figure 5.9 shows the results of in-situ XRD measurements on a $LiNi_{0.95}Co_{0.05}O_2$ cell. The cell was charged from 3.0 V to 4.3 V at a rate of ~C/100. Figure 5.9 shows that $Li_xNi_{0.95}Co_{0.05}O_2$ has a very similar phase evolution behavior as Li_xNiO_2 $(0 \le x \le 1)$.[9] The splitting of the (101) and (104) Bragg peaks indicates the existence of the monoclinic distortion, and the phase transition from the H2 phase to H3 phase at the high state of charge was also captured. These in-situ XRD measurements correspond well to the dQ/dV vs. V measurements, and confirm that 5% Al, 5% Mn or 5% Mg can suppress the phase transitions exactly as in $LiNi_{0.9}Co_{0.05}Al_{0.05}O_2$, while 5% Co cannot eliminate the phase transitions.

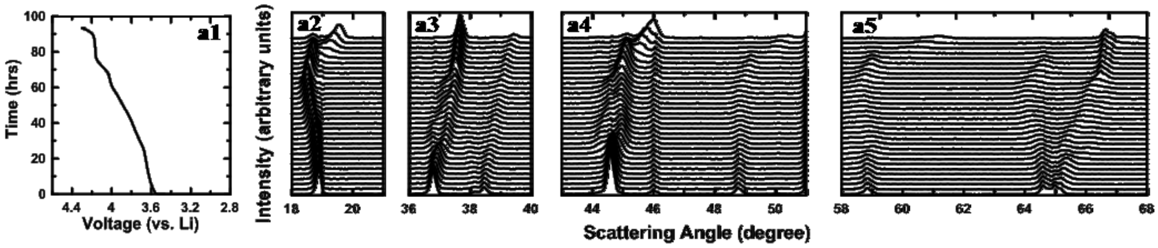

Figure 5.9 In-situ XRD patterns and cell cycling profiles of $LiNi_{0.95}Co_{0.05}O_2$ (a1 - a5). In-situ XRD patterns of selected scattering angle regions of 18 - 21°, 36 - 40°, 43 - 51°, and 58 - 68° are shown. The cell was charged from 3.0 V to 4.3 V at a rate of ~C/100.

The question of whether the presence of Co in small concentrations brings any structural stabilization during charge and discharge cycles is now addressed. Figure 5.10 shows the profile refinement results of the in-situ XRD patterns accompanied by cell charge and discharge profiles. Figure 5.10a(1) shows the $LiNi_{0.9}Co_{0.05}Al_{0.05}O_2$ in-situ cell voltage as a function of specific capacity during the 1st charge (black line), 1st discharge (blue line), and 2nd charge (red line). Figure 5.10 a(2) - a(4) show the corresponding unit cell constant *a*, *c*, and unit cell volume as a function of specific capacity, respectively. Figures 5.10b, 5.10c, and 5.10d show the same sets of refinement results for $LiNi_{0.95}Al_{0.05}O_2$, $LiNi_{0.95}Mn_{0.05}O_2$, and $LiNi_{0.95}Mg_{0.05}O_2$, respectively. Figures 5.10a(2) - 5.10d(2) show a similar phenomenon that the lattice constant, *a*, decreased continuously as Li ions were deintercalated, and increased reversibly during Li intercalation. Figures 5.10a(3) - 5.10d(3) show that for all the four samples, the *c* lattice constant increased initially as Li ions were de-intercalated, and decreased dramatically at high state of charge. During the process of lithiation, the *c* lattice constant followed the same trend reversely. Figures 5.10a(4) - 5.10d(4) show that the unit cell volumes of the four samples also changed in a similar manner. The unit cell volumes decreased slowly during Li de-intercalation and then shrank dramatically at highly state of charge because of the sudden decrease in the *c* lattice constant.

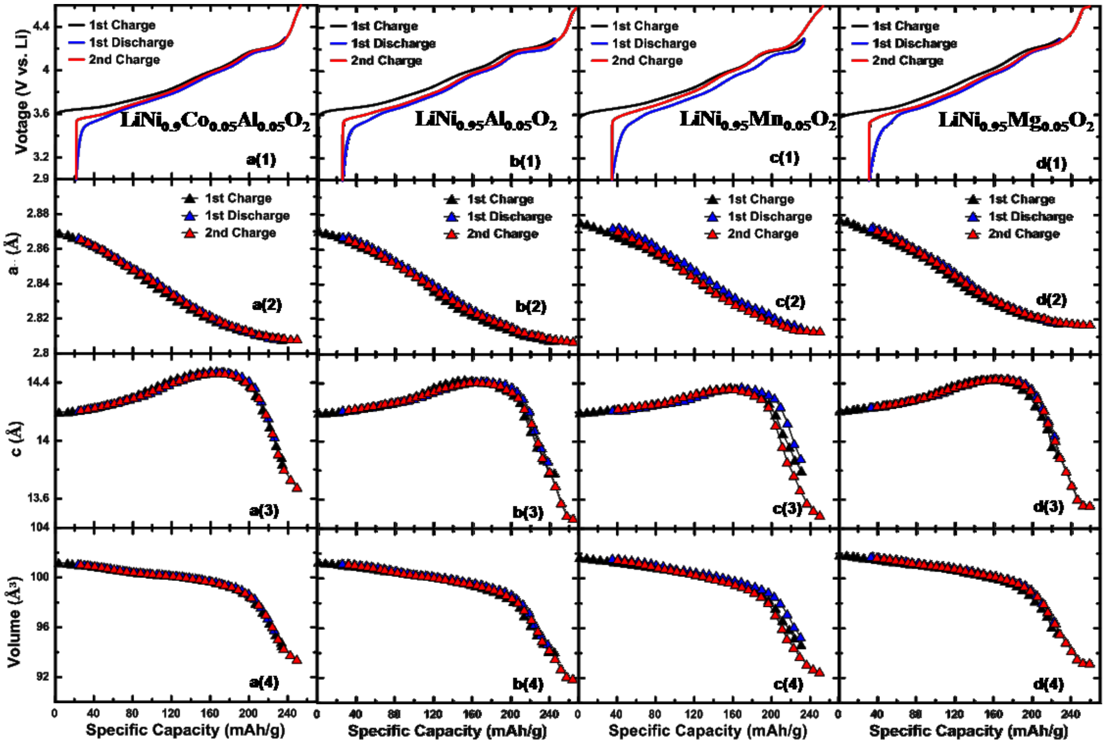

Figure 5.10 $LiNi_{0.9}Co_{0.05}Al_{0.05}O_2$ cell voltage (a(1)), unit cell lattice constants a (a(2)), c (a(3)), and volume (a(4)) as a function of specific capacity; $LiNi_{0.95}Al_{0.05}O_2$ cell voltage (b(1)), unit cell lattice constants a (b(2)), c (b(3)), and volume (b(4)) as a function of specific capacity; $LiNi_{0.95}Mn_{0.05}O_2$ cell voltage (c(1)), unit cell lattice constants a (c(2)), c (c(3)), and volume (c(4)) as a function of specific capacity; $LiNi_{0.95}Mg_{0.05}O_2$ cell voltage (d(1)), unit cell lattice constants a (d(2)), c (d(3)), and volume (d(4)) as a function of specific capacity.

Figure 5.11 shows the normalized unit cell volumes of $LiNiO_2$, $LiNi_{0.95}Al_{0.05}O_2$, $LiNi_{0.95}Mn_{0.05}O_2$, $LiNi_{0.95}Mg_{0.05}O_2$ and $LiNi_{0.90}Co_{0.05}Al_{0.05}O_2$ plotted as a function of x in $Li_{1-x}MO_2$. The unit cell volume of $Li_{1-x}NiO_2$ was included from Chapter 4.[9] The volume changes versus Li content for the $Li_{1-x}Ni_{0.95}M_{0.05}O_2$ samples are almost exactly the same **and** match that of $Li_{1-x}Ni_{0.90}Co_{0.05}Al_{0.05}O_2$ suggesting there is nothing "special" that Co brings to the table in terms of "structural stabilization". The dashed line marks the place where the H3 phase, which has a smaller unit cell volume, forms in $Li_{1-x}NiO_{2.}$ This place is also the onset of the abrupt unit cell volume decrease for the substituted samples. Unlike $Li_{1-x}NiO_2$, which shows the formation of the H3 phase at high states of charge due to complete removal of Li atoms from Li layers, the substituted samples experienced a more homogeneous Li de-intercalation. This suppresses the formation of the H3 phase, and results in a continuous rapid contraction along the *c*-axis, instead. A single phase region with lattice constants that vary with Li content is more resistant to particle cracking than a two phase region where the phases have quite different lattice constants.[130]

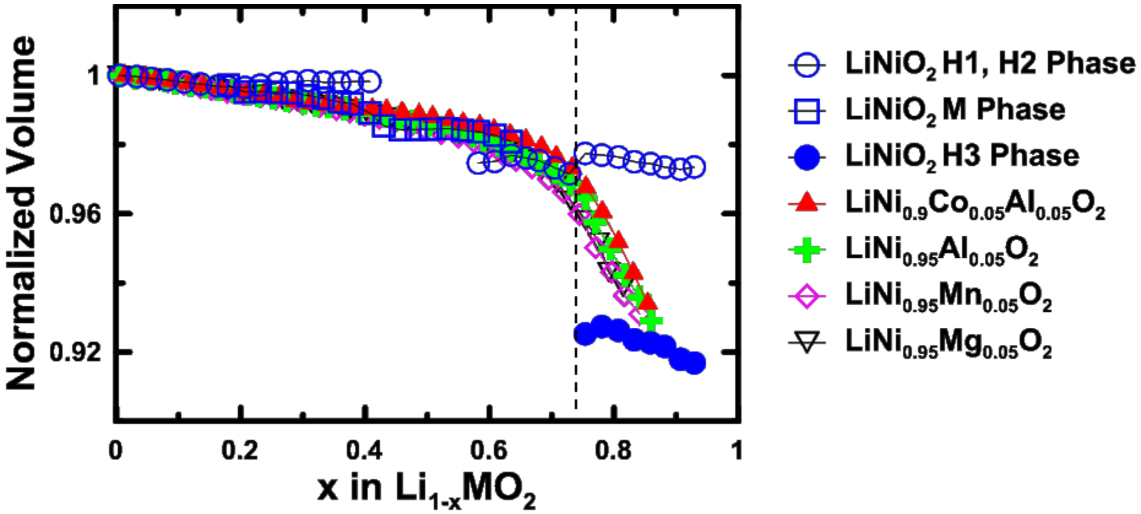

Figure 5.11 Normalized unit cell volumes of $LiNiO_2$, $LiNi_{0.9}Co_{0.05}Al_{0.05}O_2$, $LiNi_{0.95}Al_{0.05}O_2$, $LiNi_{0.95}Mn_{0.05}O_2$, and $LiNi_{0.95}Mg_{0.05}O_2$ as a function of Li content x in $Li_{1-x}MO_2$

5.2.5 A Simple Model to Explain How Substituents Work

Figures 5.7a and 5.7b show that the dQ/dV vs. V curves of the 5% Mg substitution is very similar to the curves of materials with 10% Al or 10% Mn. Besides, Figure 5.1 shows that $LiNi_{0.90}Co_{0.05}Al_{0.05}O_2$, $LiNi_{0.95}Al_{0.05}O_2$ and $LiNi_{0.95}Mn_{0.05}O_2$ have similar dQ/dV vs. V features. The similarities in dQ/dV vs. V curves can be addressed by a simple "Li site locking" model proposed in this work. In the case of $LiNiO_2$, during Li de-/intercalation, along with the redox reaction of $Ni^{3+/4+}$, all the Li atoms in Li layers are mobile and can be removed from the structure. While with cation substitution, the mobility of Li sites is changed. In the case of small amounts of Al and Mg substitutions, simple oxidation state arguments can be used to also explain how the Li sites are deactivated. Randomly distributed Al substituents exist in the form of Al^{3+} and cannot be oxidized to Al^{4+}, so each Al atom deactivates one Li atom; Mg substituents are divalent and cannot be oxidized during delithiation. Thus similarly, each Mg atom deactivates two Li sites. In the case of Mn substitutions, it is the Ni in the Li layer that causes inactive Li sites. It is very interesting that a 5% Mn substitution leads to approximately an additional 5% Ni in the Li layer compared to $LiNiO_2$, while a 10% Mn substitution leads to only about 7% Ni in the Li layer. (See Figure 5.5c). Further work is needed to explain this non-linear behavior.

It is believed that the deactivation of Li sites results in a disturbance in Li ordering during charge/discharge, and further supress multiple phase transitions. For Co substitutions, Co is electrochemically active and can be oxidized and reduced during lithiation and delithiation, which makes it not effective in "locking" Li and supressing the phase transitions. Besides the simple model proposed above, first-principles computations were performed by M.Cormier to study how cation substitutions deactivate Li sites. The calculation demonstrates that for Al doping, one of the Li sites near the Al atom shows a tendency of keeping one Li atom at delithiated status, and thus one Li atom will be rendered inactive. For Mg doping, two Li sites near the Mg atom show the similar tendency of holding Li atoms at delithiated state, and thus two Li atoms will be rendered inactive. The inactive Li sites play a role of disturbing the Li ordering during delithiation and suppressing the phase transitions. The Mn-substituted case exhibits similar behavior to the $LiNiO_2$ case, which supports the proposed model that Mn substitution suppresses the phase transitions by introducing Ni atoms into Li layers. Calculation shows that with Co substitution, a Li atom in the vicinity of a Co atom has two sites available without a large thermodynamic penalty. So at a low doping level, Co cannot disturb the Li ordering effectively. This calculation is consistent with previous experimental studies, which have shown that with 20% Co substitution, $LiNi_{0.8}Co_{0.2}O_2$ shows no phase transition features in dQ/dV vs V.[92] It suggests that a relatively large amount of Co substitution is required to block the Li ordering in the Li layer during charge and discharge. These arguments do not consider "oxygen redox",[227] which would occur at higher potentials. Thus, it is appropriate to neglect oxygen redox in these simple oxidation state based arguments for cells charged to 4.3 V. The calculation details are not included in this thesis and can be found in the reference 32.

Figure 5.12a plots the 1st charge/discharge specific capacity as a function of substituent percentage. Coin cells were cycled at 30ºC with a current density of 10 mA/g between 3.0 and 4.3 V. Black symbols, blue symbols, and red symbols represent the Al series, Mn series, and Mg series, respectively. Solid circles represent the 1st charge capacity, and triangular symbols represent the 1st discharge capacity. The black, blue and red solid lines are the predicted first charge capacity for the Al series, Mn series, and Mg series, respectively. Based on the simple model discussed above, Al substitution results in a corresponding amount of inactive Li atoms that cannot de-intercalate. Thus the 1st charge capacity of $LiNi_{1-n}Al_nO_2$ (Q_{Al}) between 3.0 and 4.3 V should follow the equation:

$$Q_{Al} = Q_{LNO}*(1-n) \qquad (5.1)$$

where Q_{LNO} is the 1st charge capacity of $LiNiO_2$ between 3.0 and 4.3 V. Similarly, in $LiNi_{1-n}Mg_nO_2$, each Mg doping atom can "lock" two Li atoms, so

$$Q_{Mg} = Q_{LNO}*(1-2n) \qquad (5.2)$$

For $LiNi_{1-n}Mn_nO_2$, the interlayer mixing between Ni and Li is thought to be the origin of capacity loss. Based on this,

$$Q_{Mn} = Q_{LNO}*(1-Ni_{Li}) \qquad (5.3)$$

where Ni_{Li}% is the fraction of Ni/Li cation mixing. Figure 5.12a shows that the theoretical lines agree well with the experimental data when the substituent percentage is relatively low, but deviations can be observed when more than 5% of substituents were added. This indicates that the theoretical models proposed here are too simple. For example, these simple models do not take into account the changes to the delithiation/lithiation potential caused by the substituents. Figures 5.12b – 5.12d show the 1st charge/discharge V vs. Q profiles of $Li/LiNi_{0.95}M_{0.05}O_2$ (black lines) and $Li/LiNi_{0.9}M_{0.1}O_2$ (red lines) cells. Solid and dashed lines in the same color represent two duplicate cells. It is clear that with more substituent, the lithiation and delithiation potential increases. More sophisticated models are needed to consider this.

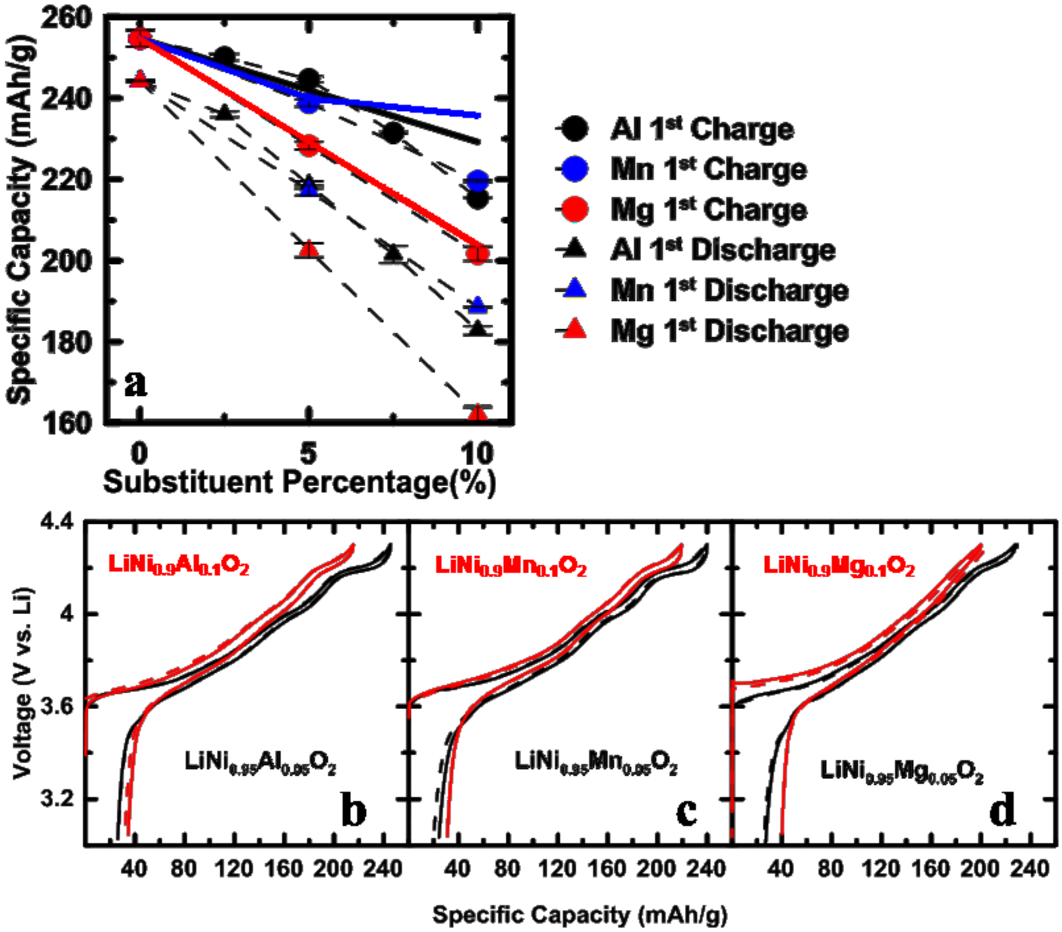

Figure 5.12 Specific 1st charge/discharge capacity as a function of substituent percentage of Al, Mn, and Mg series (a); 1st charge/discharge V vs Q curves of $LiNi_{0.95}Al_{0.05}O_2$ and $LiNi_{0.9}Al_{0.1}O_2$ (b), $LiNi_{0.95}Mn_{0.05}O_2$ and $LiNi_{0.9}Mn_{0.1}O_2$ (c), and $LiNi_{0.95}Mg_{0.05}O_2$ and $LiNi_{0.9}Mg_{0.1}O_2$ (d).

Figure 5.13 shows the dQ/dV vs. V curves of $LiNi_{0.95}M_{0.05}O_2$ and $LiNi_{0.9}M_{0.1}O_2$ (M= Al, Mn or Mg) measured at different temperatures and C rates between 3.0 - 4.3 V. Data represented by black lines were measured at 30°C with a current density of 10 mA/g (~C/20), data represented by red lines were measured at 30°C with a current density of 5 mA/g (~C/40) and data represented by blue lines were measured at 55°C with a current density of 5 mA/g (~C/40). Solid and dashed lines in the same color represent two duplicate cells. For all of the six compositions, the dQ/dV vs. V features between 3.6 V and 4.3 V remained unchanged at lower rates and higher temperature. However, the pair (charge and discharge) of diminished kinetic hindrance peaks in the region of 3.4 - 3.6 V could be recovered at lower rates and higher temperature, and these peaks are marked with black circles in Figure 5.13. Figures 5.13b and 5.13e show that compared with Mg and Al, Mn substituted samples had a much more moderate recovery of kinetic hindrance peaks at slower rates and higher temperature. This is presumably because unlike Mg and Al, which have Li atoms in the Li layers "bound" to substituent atoms in the transition metal layers, Mn substituted samples have inactive Ni atoms in Li layers which will impede diffusion greatly. According to Van der Ven's divacancy model[218], diffusion will slow when there are no divacancies in the Li layer which will occur when the Li layer is almost full and also when states with ordered vacancies are formed. Even though the Al and Mg substituents suppress long range order, it is unlikely they suppress short range order and hence if the H1 phase in $LiNiO_2$ is one where vacancies are ordered, one expects a similar degree of kinetic hindrance in the Al and Mg substituted samples.

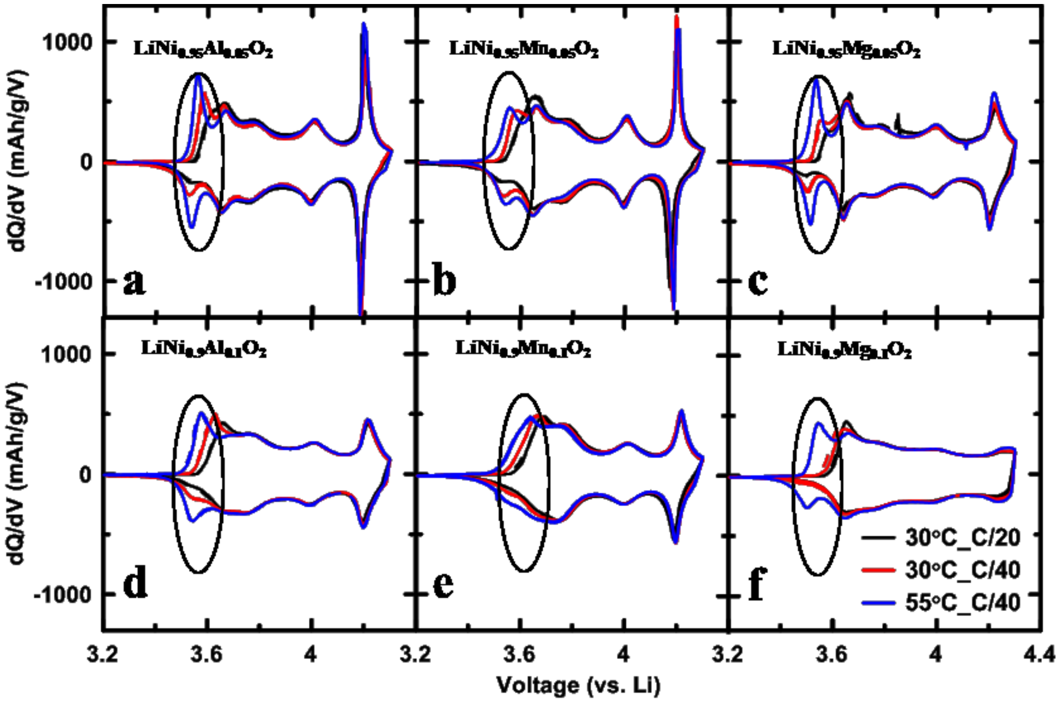

Figure 5.13 dQ/dV vs. V curves measured at different C rates and temperatures: $LiNi_{0.95}Al_{0.05}O_2$ (a), $LiNi_{0.95}Mn_{0.05}O_2$ (b), $LiNi_{0.95}Mg_{0.05}O_2$ (c), $LiNi_{0.9}Al_{0.1}O_2$ (d), $LiNi_{0.9}Mn_{0.1}O_2$ (e), and $LiNi_{0.9}Mg_{0.1}O_2$ (f).

5.2.6 ARC and Cycling Tests

ARC results show that Co-doping brings negligible contribution to thermal stability while Al, Mg, and Mn -doping demonstrate substantial benefit. Figure 5.14 shows the ARC results for selected samples. Results for Li_xNiO_2 (LNO), $Li_xNi_{0.95}Co_{0.05}O_2$, (NiCo95/05), $Li_xNi_{0.95}Mg_{0.05}O_2$ (NiMg95/05), $Li_xNi_{0.95}Al_{0.05}O_2$ (NiAl95/05), and $Li_xNi_{0.95}Mn_{0.05}O_2$ (NiMn95/05) are represented by black lines, green lines, magenta lines, blue lines and red lines, respectively. All positive electrode samples were delithiated to 230 mAh/g specific capacity before the ARC testing. It is clear that the self-heating rates of (SHR) of $LiNiO_2$ and $LiNi_{0.95}Co_{0.05}O_2$ increased rapidly above about 160ºC, and the samples went into thermal runaway. However, the $LiNi_{0.95}Mg_{0.05}O_2$, $LiNi_{0.95}Al_{0.05}O_2$, and $LiNi_{0.95}Mn_{0.05}O_2$ samples did not reach the ARC maximum SHR threshold of 20ºC/min over the entire testing temperature range. ARC results strongly indicate that 5% Mg, 5% Al, or 5% Mn substitutions can effectively lower the reactivity of charged positive electrode powders with electrolyte, while the 5% Co substituent has little to no effect on the thermal stability of LNO.

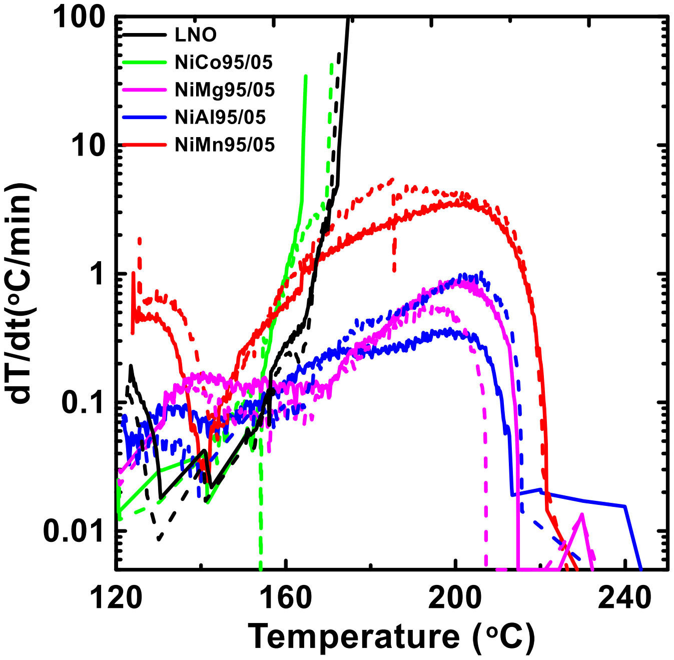

Figure 5.14 Self-heating rate as a function of temperature for delithiated $LiNiO_2$ and $LiNi_{0.95}M_{0.05}O_2$ (M= Co, Mg, Al or Mn) electrode samples reacting with electrolyte in accelerating rate calorimeter experiments. All samples were delithiated to a delithiation specific capacity of 230 mAh/g.

Figure 5.15 shows specific capacity (a) and normalized capacity (b) as a function of cycle number for NCA 80/15/05 ($LiNi_{0.8}Co_{0.15}Al_{0.05}O_2$, obtained from Ecopro) and two selected "Co-free" samples, NA 95/05 ($LiNi_{0.95}Al_{0.05}O_2$) and NMg 95/05

($LiNi_{0.95}Mg_{0.05}O_2$). Coin cells were cycled with a current density of 10 mA/g (~C/20) for 2 cycles and then with a current density of 40 mA/g (~C/5) for 50 cycles. NCA 80/15/05 was cycled between 3.0 – 4.4 V. NA 95/05 and NMg 95/05 were cycled between 3.0 - 4.3 V for 52 cycles, followed by another 52 cycles between 3.0 – 4.4 V. The comparison between NCA 80/15/05 and NA 95/05 shows that for the same specific capacity delivered, the additional 15% of Co provides little benefit to the capacity retention. With 5% Mg substitution, which as discussed above results in more inactive Li atoms, less specific capacity was accessed with a 4.3 V upper cut-off voltage and this material shows the best capacity retention. Figure 5.15 strongly suggests that Co is not required in materials with high Ni content (> 90% Ni in the transition metal layer) in order to obtain acceptable capacity retention during cycling.

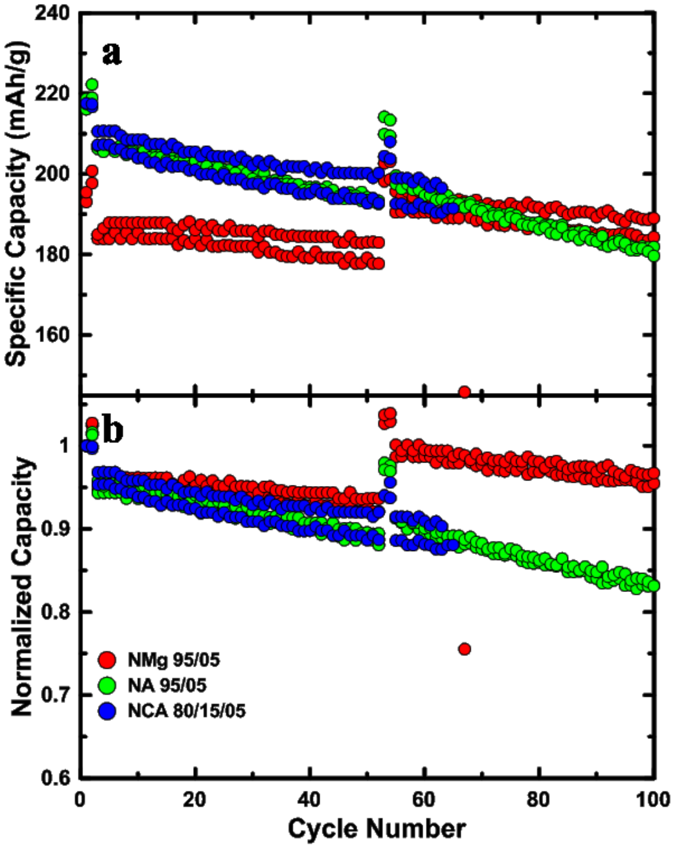

Figure 5.15 Specific capacity (a) and normalized capacity (b) as a function of cycle number for NCA 80/15/05 ($LiNi_{0.8}Co_{0.15}Al_{0.05}O_2$, obtained from Ecopro) and two selected "Co-free" samples, NA 95/05 ($LiNi_{0.95}Al_{0.05}O_2$) and NMg 95/05 ($LiNi_{0.95}Mg_{0.05}O_2$). Coin cells were cycled with a current density of 10 mA/g (~C/20) for 2 cycles and with a current density of 40 mA/g (~C/5) for 50 cycles. NCA 80/15/05 was cycled between 3.0 – 4.4 V. NA 95/05 and NMg 95/05 were cycled between 3.0 - 4.3 V for 52 cycles, followed by another 52 cycles between 3.0 – 4.4 V.

5.3 Conclusions

In this work, positive electrode materials made by doping $LiNiO_2$ with various amounts of Al, Mn, Mg, or Co were systematically investigated and compared to $LiNi_{0.9}Co_{0.05}Al_{0.05}O_2$ with electrochemical characterization, in-situ XRD, dQ/dV analysis and accelerating rate calorimetry. It was found that $LiNi_{0.95}Al_{0.05}O_2$, $LiNi_{0.95}Mg_{0.05}O_2$,

$LiNi_{0.95}Co_{0.05}O_2$ and $LiNi_{0.9}Co_{0.05}Al_{0.05}O_2$ all had very similar amounts of Ni in the Li layer (Table 5.1) suggesting Co is not required when the substituents Al and Mg are used. Just as in $LiNi_{0.9}Co_{0.05}Al_{0.05}O_2$, 5% Al, 5% Mn or 5% Mg cation substitutions in $LiNi_{0.95}M_{0.05}O_2$ were found to suppress the multiple phase transitions observed in $LiNiO_2$ during charge and discharge, while 5% Co in $LiNi_{0.95}Co_{0.05}O_2$ did not. This suggests Co is unnecessary in these materials. 5% Al, 5% Mn or 5% Mg cation substitutions in $LiNi_{0.95}M_{0.05}O_2$ reduced the reactivity of the charged electrode material with electrolyte. By contrast, 5% Co substitution did not significantly reduce reactivity with electrolyte at elevated temperature also suggesting Co is unnecessary in these materials.

The dQ/dV vs. V curves of $Li/LiNi_{0.9}Co_{0.05}Al_{0.05}O_2$ cells can be well matched by $LiNi_{0.95}Al_{0.05}O_2$, $LiNi_{0.95}Mn_{0.05}O_2$ and presumably by $LiNi_{1-x}Mg_xO_2$ with x near 0.025. The reversible and irreversible specific capacities of $Li/LiNi_{0.9}Co_{0.05}Al_{0.05}O_2$ cells can be well matched by $LiNi_{0.95}Al_{0.05}O_2$, $LiNi_{0.95}Mn_{0.05}O_2$ and presumably by $LiNi_{1-x}Mg_xO_2$ with x near 0.025. The structural changes in $Li_{1-x}Ni_{0.9}Co_{0.05}Al_{0.05}O_2$, $Li_{1-x}Ni_{0.95}Al_{0.05}O_2$ and $Li_{1-x}Ni_{0.95}Mn_{0.05}O_2$ and $Li_{1-x}Ni_{0.95}Mg_{0.05}O_2$ with x are all virtually identical. **All the relevant properties of NCA with high Ni content can be matched by materials with no Co.**

Cycling tests for $LiNi_{0.95}Al_{0.05}O_2$, $LiNi_{0.95}Mg_{0.05}O_2$, and commercial $LiNi_{0.8}Co_{0.15}Al_{0.05}O_2$ showed that the 15% Co substitution in commercial NCA material did not improve capacity retention compared with Co-free $LiNi_{0.95}Al_{0.05}O_2$. Long term charge-discharge cycle testing of commercial grade pouch cells was not included in the results presented here. Recent work by others has shown the strong impact of coatings and dopants on the capacity retention of Ni-rich materials.[165,181] We are optimistic that with appropriate coatings or low levels of dopants at the surface, that $LiNi_{1-x}M_xO_2$ materials of the type discussed here can be matched or exceeded by materials without Co.

A mechanism for how substituents function in $LiNiO_2$ was proposed and shows good agreement with the experimental results. It is hoped that this work can help both industry and academia to understand how substituents work and why Co may not be necessary for Ni-rich positive electrode materials.

Chapters 4 and 5 presented work on the basics of Ni-rich positive electrode materials. In the following two chapters, the focus switches to the development of methods for synthesizing a novel type of positive electrode material, that is, single crystal material.

CHAPTER 6 SYNTHESIS OF SINGLE CRYSTAL $LINi_{0.6}Mn_{0.2}Co_{0.2}O_2$ WITH ENHANCED ELECTROCHEMICAL PERFORMANCE FOR LITHIUM ION BATTERIES

Chapter 2 briefly introduced single crystal positive electrode materials and their advantages. Li et al. showed that single crystal NMC532 materials in NMC532/artificial graphite cells have superior performance compared to their polycrystalline counterparts.[174] In terms of single crystal positive electrode material synthesis, molten salt synthesis is an approach adopted in references 2 and 3 but the cost and handling challenges render it unacceptable for mass production. Li et al.[230] introduced a method to synthesize single crystal NMC532 and found that the lithium/transition metal molar ratio and sintering temperature played important roles in the synthesis. Excess Li can provide a self-flux environment which facilitates particle growth.[173] High sintering temperatures also assist the particle growth significantly.

NMC622 has higher specific capacity and better rate capability compared to NMC532 at the same upper cutoff voltage voltage,[81] which makes it very attractive. In this work, the synthesis of single crystal NMC622 is explored with the goal of attaining optimized electrochemical performance. There were no publications about single crystal NMC622 synthesis that had been reported in the scientific literature at the time we started this work. Although Wang et al.[231] reported the synthesis of single crystal NMC622, their synthesized materials were made up of agglomerates with individual grain size less than

1 μm. In our view, single crystal materials should be individual grains of greater than 2 μm. The electrochemical properties of single crystal NMC622 (SC622) were compared with polycrystalline NMC622 (PC622) made with conventional methods. The impact of some electrolyte additives on the charge-discharge cycling performance of the materials synthesized was also investigated. This work will be of interest to both industrial and academic researchers developing single crystal NMC materials for long lifetime Li-ion batteries. The majority of this Chapter was published in Journal of The Electrochemical Society.[232] H.Li performed the material synthesis, material characterizations, and electrochemical tests; J. Li contributed to the material synthesis; X. Ma contributed to the BET measurement. Reproduced with permission from *J. Electrochem. Soc.*, 165.5 (2018): A1038-A1045. Copyright 2018, The Electrochemical Society.

6.1 Experimental Design

$Ni_{0.6}Mn_{0.2}Co_{0.2}(OH)_2$ precursors were made using the co-precipitation method as described in Chapter 3. The dried precursors were mixed with a stoichiometric equivalent of Li_2CO_3 (from Chemetall > 99%) by ball milling using a mixer miller (SPEX Certi Prep 8000-D), which had been modified to mix at low speed, for 30 minutes with a beads/material mass ratio of 1.5. Samples with Li/TM ratios of 1.05, 1.1 and 1.15 were prepared. The mixed powders were sintered in alumina crucibles in air in a box furnace at 800ºC for 3 hours, and further at 900, 925, 940 or 955ºC for 6 hours, with the same heating and cooling rate of 10 ºC/min. After sintering, single crystal materials in the alumina crucibles were “brick”-like chunks that needed to be ground and sieved.

Selected synthesized single crystal NMC622 materials were washed with deionized (DI) water to remove the excess lithium carbonate residue. 2 g of synthesized powders were added to 8 ml of DI water and centrifuged for ten minutes, three times. The washed powders were dried at 80ºC for 12 hours and were further heated in an oxygen environment at 550ºC for 3 hours. The heating after washing was done based on the work reported by Chen and Dahn,[233] who showed that $LiCoO_2$ exposed to water could be "repaired" by a heat treatment to 550ºC.

SEM, powder XRD, and BET measurements were carried out as described in Chapter 3. Control electrolyte used for coin cell testing was 1.0 M $LiPF_6$ in EC:DEC (1:2 v/v). Electrolyte containing additives (2FEC-1DTD electrolyte) was formulated by adding 2 wt% of FEC and 1 wt% of DTD to control electrolyte. The experimental details about coin cell assembly and electrochemical tests were described in Chapter 3.

6.2 Results and Discussions

6.2.1 Exploration of Synthesis Conditions

Figure 6.1 shows SEM images of the precursors and lithiated samples. Figures 6.1A and 6.1B show the $Ni_{0.6}Co_{0.2}Mn_{0.2}(OH)_2$ precursors made by the co-precipitation method. By tuning the pH value in the co-precipitation process, precursors with different sizes could be made.[183] In this study, large sized precursor 1 (Figure 6.1A) was used to make conventional polycrystalline NMC622 (PC622) because conventional PC622 generally has particles about of 10 - 15 μm in size. Precursor 2 (Figure 6.1B) was used for single crystal NMC622 (SC622) synthesis because according to the previous work by Li et al,[230] smaller sized precursors can alleviate primary particle agglomeration after sintering. The morphology differences between precursor 1 and precursor 2 originate from the difference in pH during synthesis. In a lower pH environment, denser and more spherical particles were formed due to slower transition metal–ammonia dissolution.[183] PC622 was made using a conventional method with a 1.05 Li/TM ratio and a 900°C sintering temperature.[81] Figure 6.1C shows an SEM image of PC622. Figure 6.1C shows that the lithiated particles preserved the spherical morphology, and each secondary particle consisted of nano-sized small grains. According to a previous study of single crystal NMC532,[230] it was found that an excess amount of lithium carbonate and a high sintering temperature play important roles in single crystal NMC synthesis. Figures 6.1D to 6.1I show a 3*3 matrix of SEM pictures of samples sintered with different Li/TM ratios and temperatures. From left to right, each column of samples was sintered at 925°C, 940°C, and 955°C respectively, and from top to bottom, each row of samples were lithiated with Li/TM ratios of 1.05, 1.10 and 1.15 respectively. Figures 6.1D to 6.1L show that at certain sintering temperatures, an increase in Li content caused an increase in grain size. For example, in the 940°C sample series, the sample sintered with a 1.05 Li/TM ratio had grains mostly ranging from 1-2 μm, and as the Li/TM ratio increased to 1.10 and 1.15, most grains had a size of 3 - 4 μm and above 6 μm, respectively. Figure 6.1 shows that with a fixed Li/TM ratio, an increase in sintering temperature assists with particle growth, even though high temperature sintering leads to more Li loss. Compared to the reported SC532 synthesis[230], which requires a sintering temperature of 970°C and a Li/TM ratio of 1.20. SC622 can be made at a lower temperature and with a smaller Li/TM ratio. SEM images were taken with a backscattering electron detector, and thus compounds containing lighter elements appear dark in the image. Figure 6.1 shows that samples made with Li/TM ratios of 1.10 and 1.15 have a considerable number of dark spots, which are due to residual lithium carbonate.

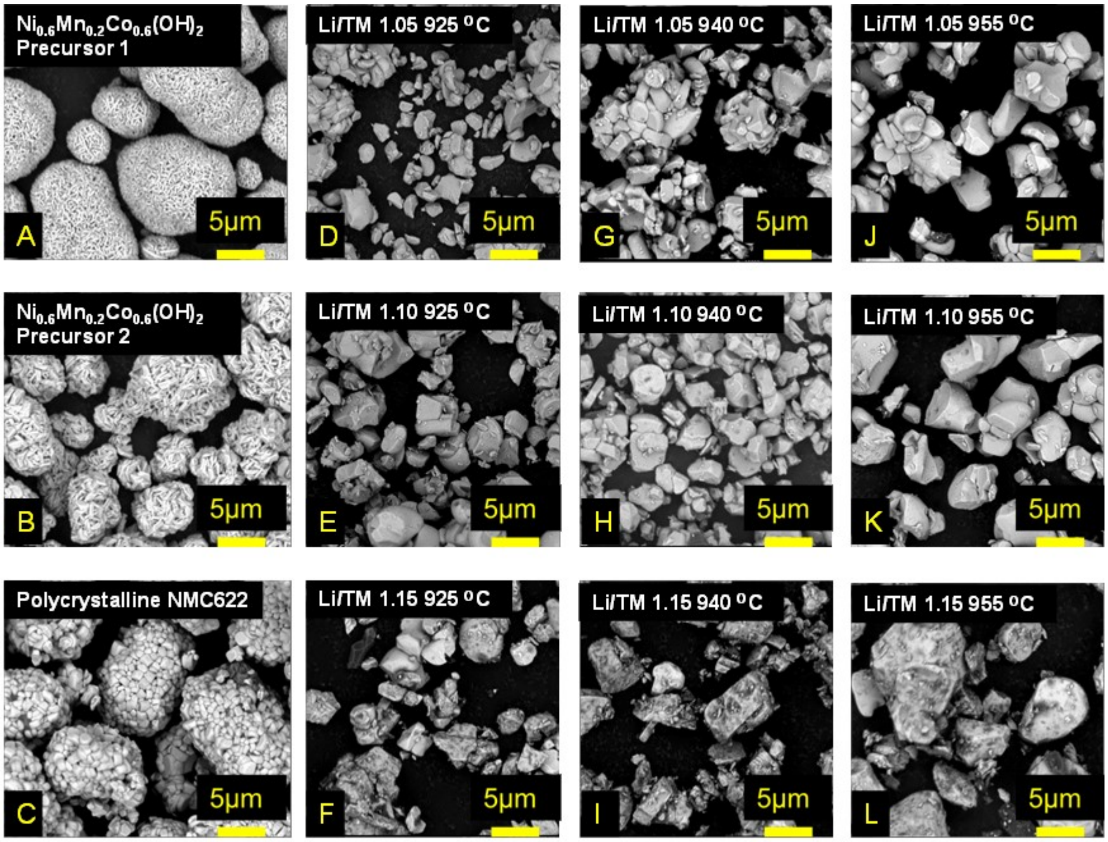

Figure 6.1 SEM images of $Ni_{0.6}Mn_{0.2}Co_{0.2}(OH)_2$ precursors: (A) was used for polycrystalline NMC synthesis and (B) was used for single crystal NMC synthesis. SEM images of polycrystalline NMC622 (C). SEM images of SC622 samples made with Li/TM ratios of 1.05 (D), 1.10 (E) and 1.15 (F) at 925ºC. SEM images of SC622 samples with Li/TM ratios of 1.05 (G), 1.10 (H) and 1.15 (I) made at 940ºC. SEM images of SC622 samples with Li/TM ratios of 1.05 (J), 1.10 (K) and 1.15 (L) made at 955ºC.

Figure 6.2 shows X-ray diffraction patterns of the sintered SC622 samples. Only the (104) Bragg peaks have been selected for display here. Rietveld refinements were performed on the full XRD data (15 - 70º) assuming a hexagonal layered phase in the R-3m space group (α-NaFeO$_2$-type structure) to obtain the structural information. It was assumed that Li ions were on the 3a sites (Li layer), transition metals were on the 3b sites (transition metal layer), and oxygen ions were on the 6c sites. The exchange of Ni and Li atoms between 3a and 3b sites was allowed with constraints such that the stoichiometry of the phase was fixed to the values assumed from the target composition. The black circles are the collected experimental data and the solid black lines are the calculated pattern. In the samples with a Li/TM ratio of 1.05 and 1.10, the splitting of the $K_{\alpha1}$ and $K_{\alpha2}$ peaks in the (104) peak region is an indication of good crystallinity. The peak splitting is less pronounced in the sample with a Li/TM ratio of 1.15 perhaps because these samples were very firmly agglomerated and needed aggressive grinding to be reduced back to powder. The degree of agglomeration increased as the excess Li content increased. Another possible explanation for the peak broadening is that excess Li will result in non-uniform stress induced by the existence of Li ions in the transition metal layer.[234] Table 6.1 summarizes the refinement results. J. Li et al.[235] and E. McCalla et al.[236] have extensively studied the pseudo-ternary phase diagrams of Ni-Mn-Li oxide materials, and their works show that the lattice constants decrease with increasing Li/TM ratio. In this work, the lattice constants change in a way consistent with the previous studies. The percentage of Ni in the Li layer drops as the amount of excess Li increases.

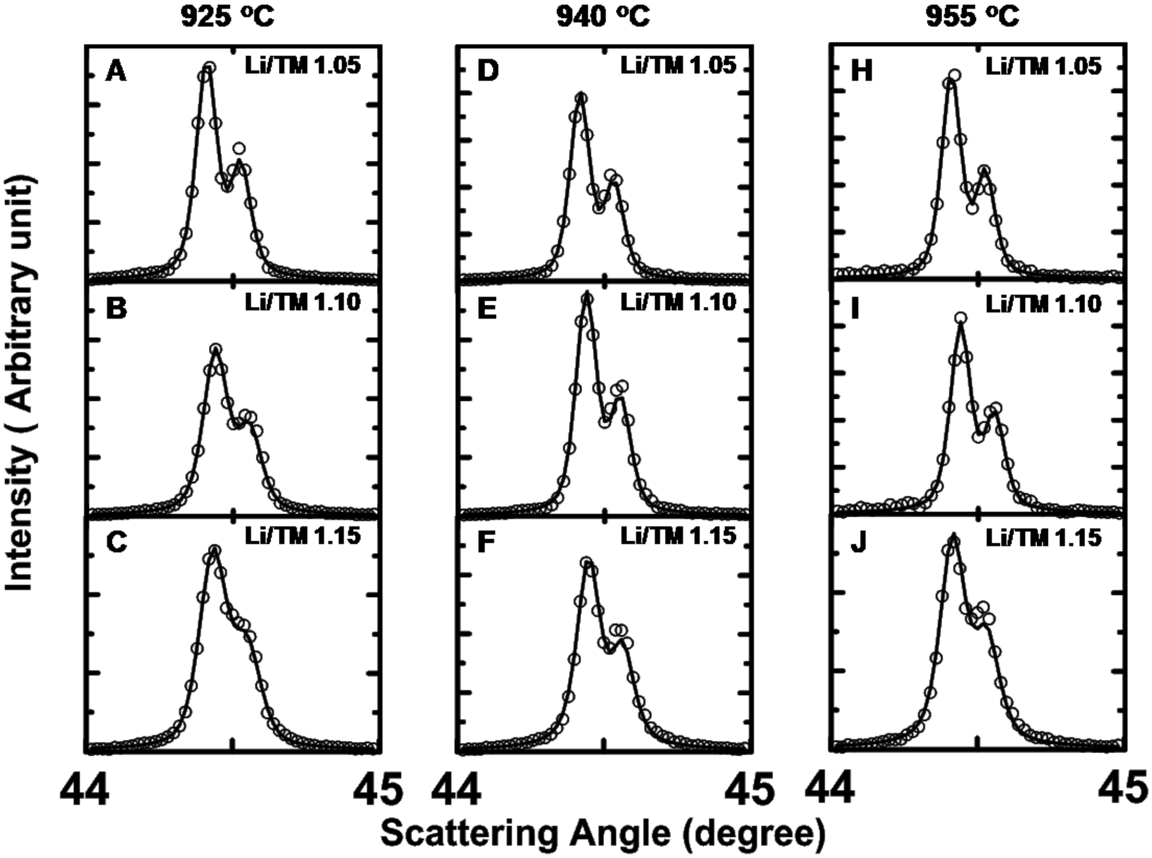

Figure 6.2 XRD patterns of the (104) Bragg peaks of SC622 samples made with Li/TM ratios of 1.05 (A), 1.10 (B) and 1.15 (C) at 925°C. XRD patterns of (104) Bragg peaks of SC622 samples made with Li/TM ratios of 1.05 (D), 1.10 (E) and 1.15 (F) at 940°C. XRD patterns of (104) Bragg peaks of SC622 samples made with Li/TM ratios of 1.05 (H), 1.10 (I) and 1.15 (J) at 955°C. Black circles are experimental XRD data and solid black lines are calculated patterns from Rietveld refinement.

Table 6.1 Crystallographic data for the SC622 samples produced.

Sintering Temp.	**Li/TM**	**a/b (Å) (within ±0.001 Å)**	**c (Å) (within ±0.001 Å)**	**Ni at Li site (%) (within ±0.1%)**	**c/3a**	**R_B**
925	1.05	2.869	14.216	2.41	1.6519	2.04
	1.10	2.867	14.214	1.39	1.6527	2.03
	1.15	2.866	14.214	2.17	1.6528	2.38
940	1.05	2.870	14.217	3.43	1.6514	2.21
	1.10	2.869	14.214	2.96	1.6516	2.47
	1.15	2.867	14.213	1.67	1.6525	3.54
955	1.05	2.871	14.220	3.26	1.6509	1.63
	1.10	2.869	14.216	2.54	1.6515	2.38
	1.15	2.869	14.215	1.26	1.6516	3.12

Figure 6.3 shows the c/3a value plotted versus temperature for samples with the three Li/TM ratios. The c/3a ratio has been reported to be an indication of cation ordering. For a pure cubic close packed rock salt structure, in which Ni and Li atoms are fully disordered, the value of c/3a is 1.633, and greater c/3a values suggests a more ordered structure.[237] Figure 6.3 shows that the c/3a value decreases at higher temperature, due to

the Li loss at high temperature, and these results are consistent with the studies reported by J. Li et al.[230]

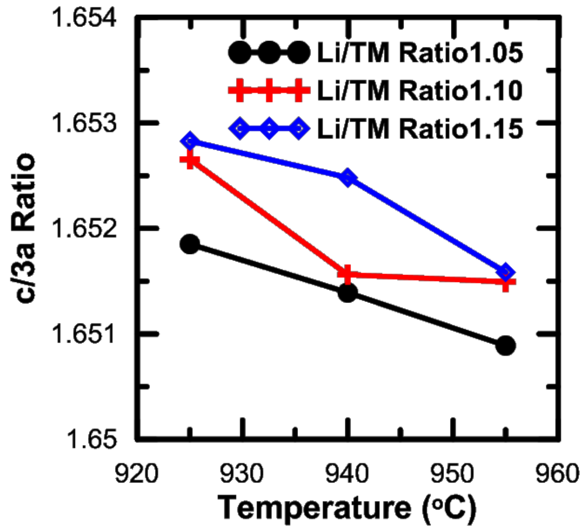

Figure 6.3 The c/3a ratio of SC622 samples as a function of sintering temperature. Black dots are data for samples made with a Li/TM ratio of 1.05, red crosses are for samples made with a Li/TM ratio of 1.10, and blue diamonds are for samples made with a Li/TM ratio of 1.15.

6.2.2 Effects of Synthesis Conditions on Electrochemistry

Figure 6.4 shows the cell voltage as function of specific capacity (V vs. Q) for samples prepared with Li/TM ratios of 1.05, 1.10, and 1.15, and at sintering temperatures of 925°C, 940°C, and 955°C, respectively. Figures 6.5a – 6.5i show the corresponding differential capacity as a function of cell voltage (dQ/dV vs. V), and the blue circles mark the voltage change at the beginning of discharge. All the cells were cycled at 30ºC with a specific current of 10 mA/g between 3.0 to 4.3 V or 3.0 to 4.4 V. The shift between the charge and discharge curves and the voltage change at the beginning of discharge can be used to compare the cell impedance. Figures 6.4A/6.5a, 6.4D/6.5d and 6.4G/6.5g show that the impedance increases as the Li/TM ratio increases from 1.05 to 1.15 at 925ºC, and similar trends can also be observed in the cases of 940 ºC and 955ºC sintering temperature. The trend observed from the perspective of sintering temperature is more complex. Figures 6.4A/6.5a, 6.4B/6.5b and 6.4C/6.5c show that the sample made at 940ºC has the least impedance among the samples with a Li/TM ratio = 1.05. Similarly, in the case of a Li/TM ratio of 1.10, the sample shown in Figures 6.4E/6.5e, made at 940ºC has the least impedance. When the Li/TM ratio is 1.15, the sample shown in Figures 6.4I/6.5i, made at 955ºC has the smallest impedance. A possible explanation for the observed trends is that both excess Li and increased particle size can contribute to cell impedance. At a fixed Li/TM ratio, on the one hand, temperature increase can reduce Li excess due to Li loss at high temperature; while on the other hand, the increased temperature will assist particle growth, which results in longer Li diffusion length. It is likely that for Li/TM ratios of 1.05 and 1.10, the "sweet temperature spot" is 940ºC, where particle growth and Li loss balance well. For a Li/TM ratio of 1.15, 955ºC sintering results in the least impedance even though the particles appear to be very large in Figure 6.1L. This suggests that when the Li/TM ratio is 1.15, excess lithium carbonate residue, which is smallest in the sample heated to 955ºC, is the dominant factor causing impedance. From the results in Figures 6.4 and 6.5 combined with the SEM images in

Figure 6.1, the optimal sintering temperature and the Li/TM ratio are critical for single crystal NMC synthesis.

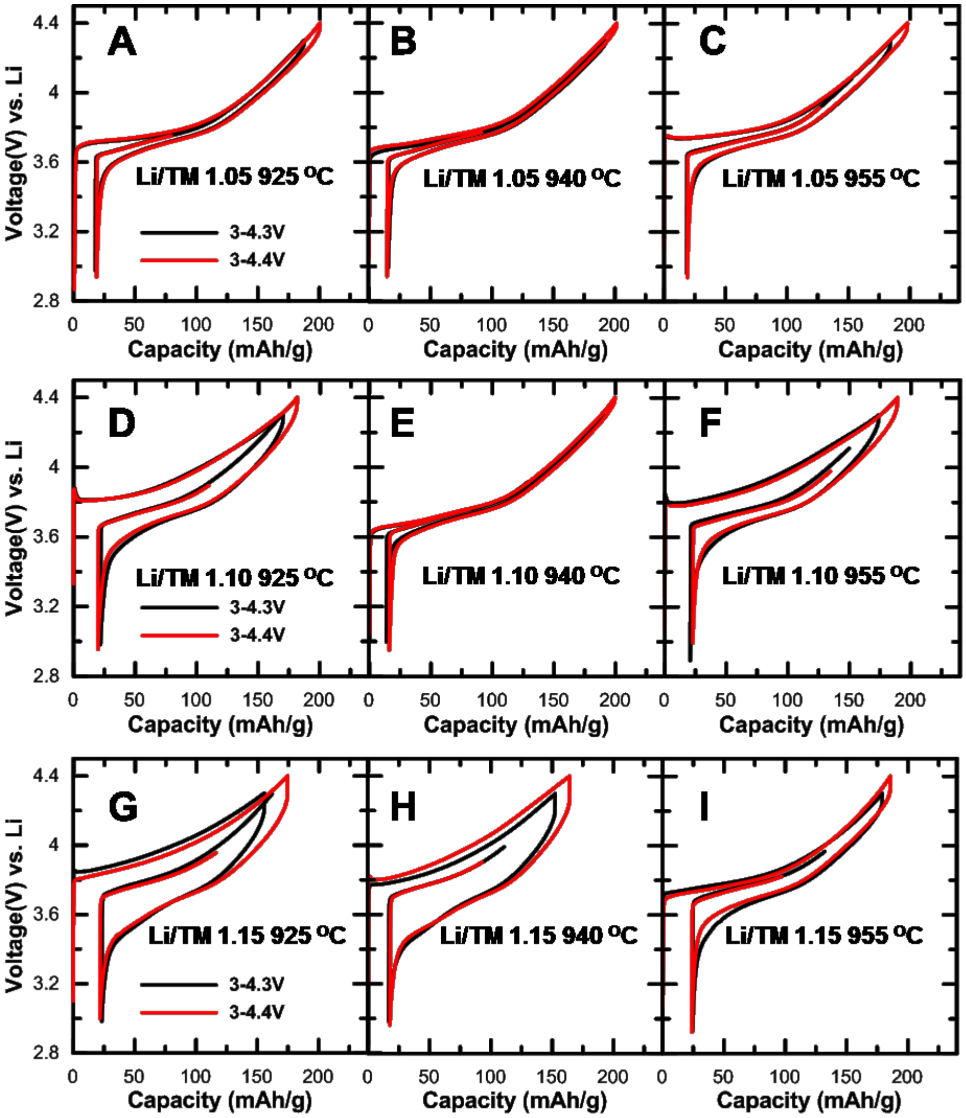

Figure 6.4 The cell voltage as a function of specific capacity for SC622 samples made with Li/TM ratios of 1.05 at 925°C (A), 940°C (B) and 955°C (C); samples made with Li/TM ratios of 1.10 at 925°C (D), 940°C (E) and 955°C (F); and samples made with Li/TM ratios of 1.15 at 925°C (G), 940°C (H) and 955°C (I). Solid black lines show the curves of cells cycled between 3.0 - 4.3 V, and red lines are the curves of cells cycled between 3.0 - 4.4 V.

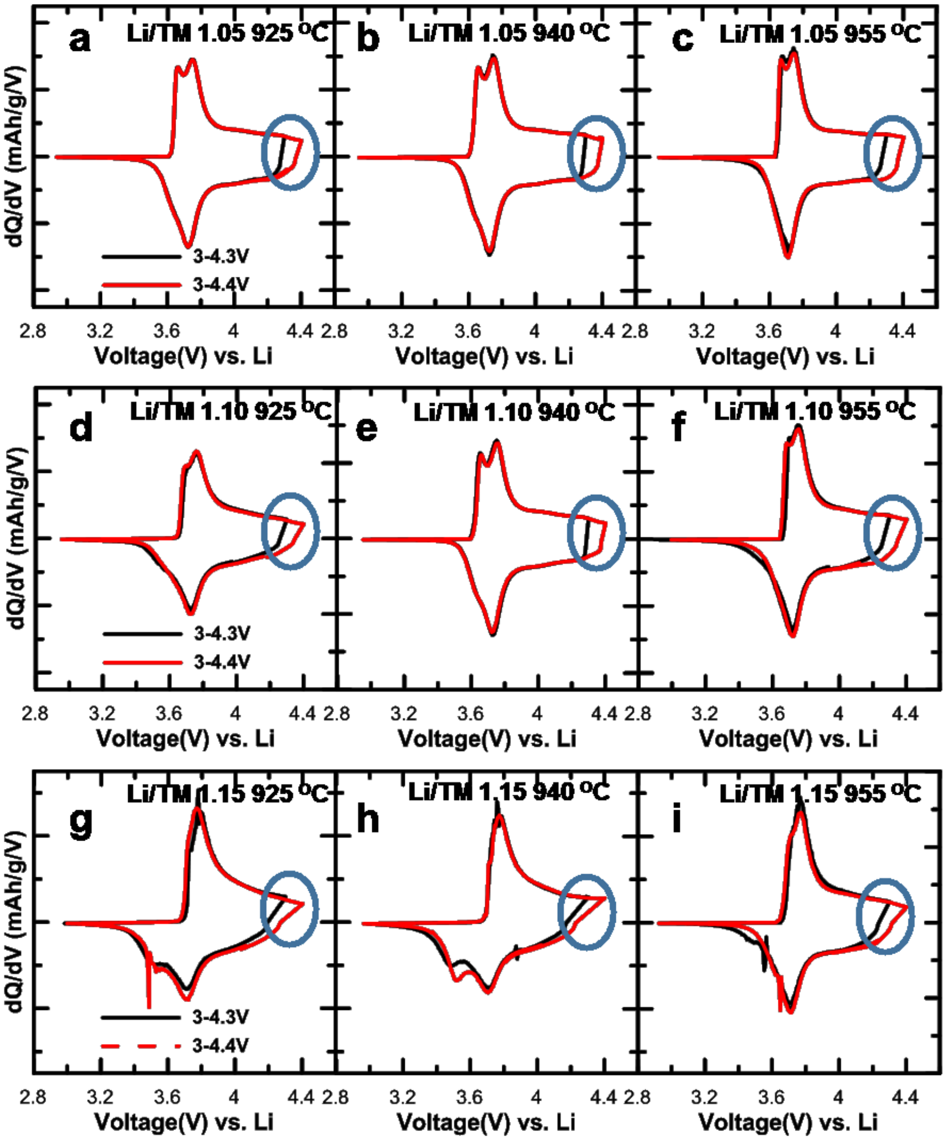

Figure 6.5 The differential capacity as a function of voltage for samples made with Li/TM ratios of 1.05 at 925ºC (a), 940ºC (b) and 955ºC (c); samples made with Li/TM ratios of 1.10 at 925ºC (d), 940ºC (e) and 955ºC (f); and samples made with Li/TM ratios of 1.15 at 925ºC (g), 940ºC (h) and 955ºC (i). The blue circles mark the voltage change at the beginning of discharge. Solid black lines show the curves of cells cycled between 3.0 - 4.3 V, and red lines are the curves of cells cycled between 3.0 - 4.4 V.

Figure 6.6 summarizes the specific reversible discharge capacity (3.0 - 4.4 V) and the irreversible capacity (IRC) as a function of sintering temperature for samples with different Li/TM ratios. Cells were tested at 30°C with a current density of 10 mA/g. Consistent with the work shown by J. Li et al.,[230] Figure 6.6a shows that at a fixed sintering temperature, an increase in excess Li results in a decrease in capacity because there is less available transition metal redox capacity in $Li_{1-x}[NMC]_{1+x}O_2$ when x increases (more Ni^{3+} and less Ni^{2+} ions). Figure 6.6a shows that samples synthesized at 940°C with Li/TM ratios of 1.05 and 1.10 can deliver reversible capacities of 186(2) mAh/g and 185(1) mAh/g respectively. Temperatures far away from 940°C will result in either Li excess (low temperature) or larger particle size (high temperature) and larger amounts of Ni on the Li sites (high temperature), and result in lower capacity samples. Figure 6.6b shows the IRC of the synthesized samples and a similar but inverse trend can be observed, which agrees well with previous discussions. Figure 6.6 shows that to get the best electrochemical performance it is important to find the "sweet spots" of single crystal NMC synthesis, which are determined by both temperature and the amount of Li excess.

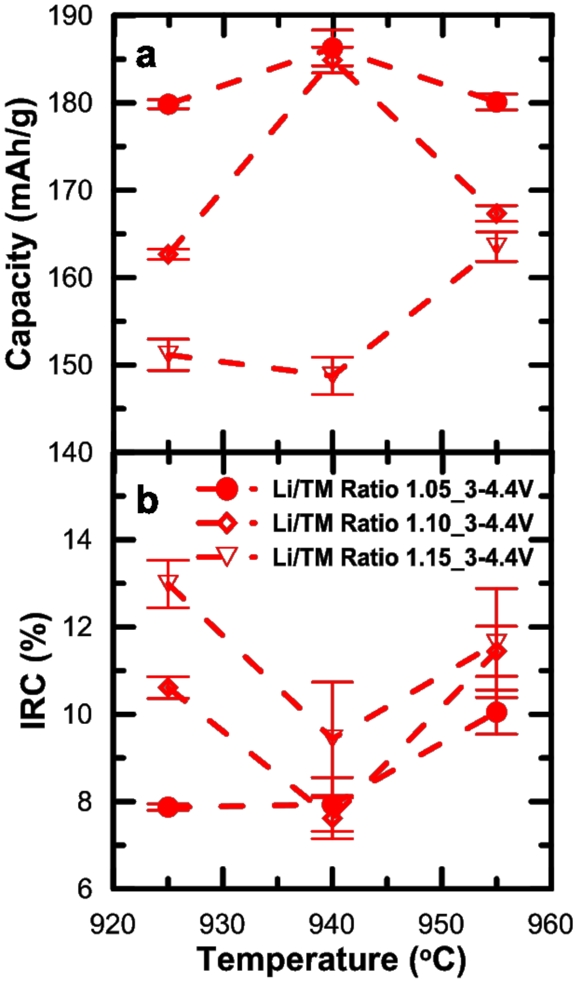

Figure 6.6 Specific capacity (a) and percentage IRC (b) as a function of sintering temperature. Red dots are for samples made with a Li/TM ratio of 1.05, red diamonds are for samples made with a Li/TM ratio of 1.10, and red triangles are for samples made with a Li/TM ratio of 1.15.

6.2.3 Comparisons between Un/washed SC622 and PC622

To further investigate the properties of synthesized single crystal NMC622 samples, the best two candidates prepared at 940ºC with Li/TM ratios of 1.05 and 1.10, were selected. Figure 6.7A shows an SEM image of the sample with a Li/TM ratio of 1.05 (called - SC622A) and Figure 6.7B shows an SEM image of the sample with a Li/TM ratio of 1.10 (called - SC622B). SEM images were taken with a backscatter electron detector, thus the dark spots shown in the images represent compounds made of light elements, mostly lithium carbonate residues. It has been reported that washing with DI water followed by a heat treatment can remove the surface lithium carbonate and recover the materials.[233,238] The two samples were washed with DI water to remove the lithium carbonate residue from the surface, and then reheated at 550ºC in oxygen. Figures 6.7C and 6.7D show the SEM images of the washed and reheated SC622A and SC622B samples, respectively. Figure 6.7 shows that after the washing and reheating treatment, the lithium carbonate residue can be removed without any visible damage to the particle morphology.

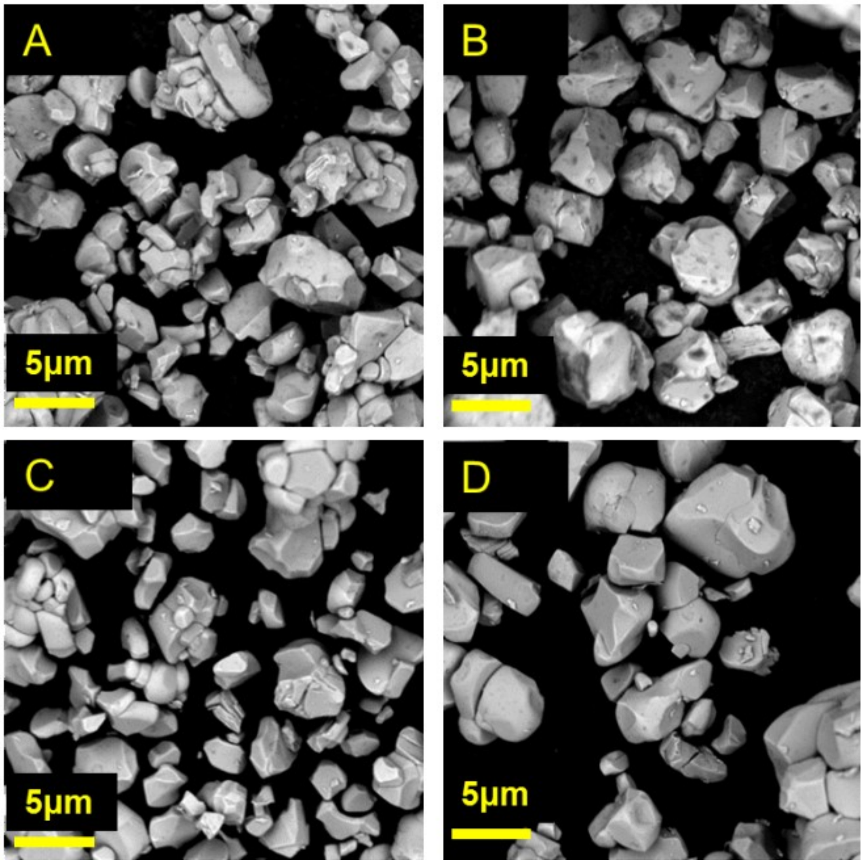

Figure 6.7 SEM images of unwashed SC622A (A), unwashed SC622B (B), washed SC622A (C) and washed SC622B (D).

Figures 6.8A, 6.8B and 6.8C show the XRD patterns of the washed SC622A, washed SC622B, and polycrystalline NMC 622 (PC622) samples, respectively. Figures 6.8a, 6.8b and 6.8c show an expanded view of the (104) Bragg peak in the region of 44° - 45°. The red dots are the measured diffraction data, and the solid black lines show the calculated pattern from Rietveld refinement. The green lines show the differences between the measured and calculated patterns. Figures 6.8a, 6.8b and 6.8c show that compared to PC622, SC622A and SC622B have a clear $K_{\alpha1}$ and $K_{\alpha2}$ peak splitting which is an indication of better crystallinity. Table 6.2 shows the results of Rietveld refinement of

SC622A and SC622B before and after the washing and heating process. Table 6.2 shows that the structures of the materials were unchanged after the washing and reheating treatment and that the cation mixing percentage remained low.

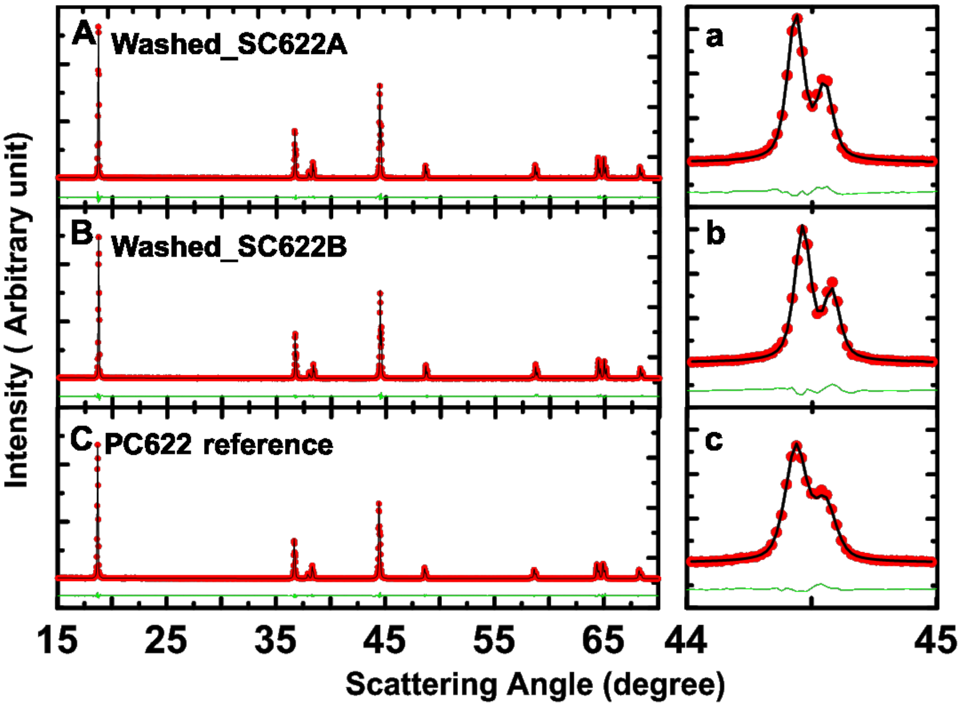

Figure 6.8 XRD patterns of washed SC622A (A), washed SC622B (B), and PC622 (C). Expanded view of (104) Bragg peaks of washed SC622A (a), SC622B (b), and PC622 (c). The red dots are the measured diffraction pattern data, and the solid black lines show the calculated patterns from Rietveld refinement. The green lines show the differences between the measured and calculated patterns.

Table 6.2 Crystallographic parameters of the SC622 samples used for electrochemical testing.

	Sintering Temperature	**Li/TM**	**a/b (Å) (within ±0.001 Å)**	**C (Å) (within ±0.001 Å)**	**Ni at Li site (%) (within ±0.1%)**	**c/3a**	**R_B**
Unwashed	940	1.05	2.8701	14.218	2.98	1.6513	2.93
	940	1.1	2.8682	14.213	1.67	1.6518	2.97
Washed and reheated	940	1.05	2.8706	14.217	2.33	1.6509	1.85
	940	1.1	2.8692	14.214	2.10	1.6513	2.24

Figures 6.9A and 6.9B show V vs. Q curves of the unwashed and washed Li/SC622A and Li/SC622B cells tested at 30ºC with a current density of 10 mA/g (~C/20) in the control electrolyte. Solid and dashed lines of the same color represent duplicate cells. Figures 6.9a and 6.9b show the corresponding dQ/dV vs Q curves. After washing, the specific capacity of SC622A increased from 185(1) mAh/g to 193.1(6) mAh/g, and the capacity of SC622B increased from 184(1) mAh/g to 190.0(4) mAh/g. This is likely due to the removal of excess lithium carbonate.

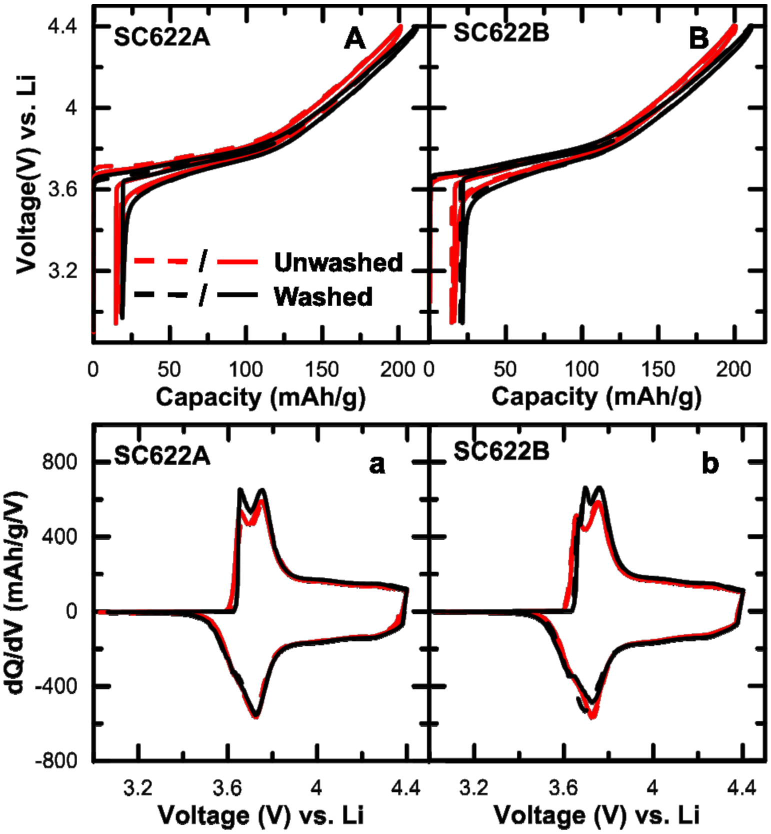

Figure 6.9 The cell voltage as a function of specific capacity for Li/SC622A (A) and Li/SC622B (B) cells. The differential capacity as a function of cell voltage for Li/SC622A (a) and Li/SC622B cells (b). Solid/dashed red lines represent unwashed samples, and solid/dashed black lines represent washed samples.

Figure 6.10 shows the charge-discharge cycling performance of coin cells made with unwashed SC622A, unwashed SC622B, PC622, washed SC622A and washed SC622B samples in control electrolyte and in 2FEC-1DTD electrolyte. Coin cells were cycled with a current density of 40 mA/g (~C/5). Figures 6.10a/6.10b and 6.10c/6.10d show the specific capacity and the normalized capacity as a function of cycle number respectively. Figure 6.10a shows that PC622 has a higher initial capacity than SC622A and SC622B. The washed SC622 samples show higher capacity than the unwashed SC622 samples. This is consistent with expectations because single crystal NMC has a relatively higher Li content, which can be represented by $Li_{1-x}[NMC]_{1+x}O_2$, with $x > 0$,[230] and because the washing-reheating treatment can increase the specific capacity by removing residual lithium compounds. Figures 6.10a and 6.10c show that when control electrolyte is used, cells with washed SC622A and washed SC622B demonstrated inferior capacity retention during cycling compared to cells with unwashed SC622A and unwashed SC622B. It has been reported that the washing process can make Ni-rich positive electrode materials more sensitive to moisture and cause poor cycling performance.[111] Unwashed SC622A and unwashed SC622B demonstrated better capacity retention during cycling than PC622. Figure 10e plots that the normalized delta V for cells. It shows that the impedance of washed SC622 and PC622 samples increased fast, while the unwashed SC622 shows slightly slower impedance increasing rate.

Figures 6.10b and 6.10d show that when 2FEC-1DTD was used, all cells had improved cycling performance, and all the SC622 cells outperformed the PC622 cells. Among the SC622 cells, washed SC622A and washed SC622B cells became comparable with unwashed SC622A and SC622B cells, and higher specific capacity was maintained during cycling. Figure 6.10d shows that washed SC622A and washed SC622B had capacity retentions of 93.5(4)% and 94.7% after 50 cycles at 30°C, while the PC622 only had 88(2)% of its initial capacity remaining. The electrolyte additives 2FEC-1DTD are an effective binary electrolyte additive combination for single crystal NMC532[20]. Figure 10f plots the corresponding normalized delta V for samples cycled with 2FEC-1DTD electrolyte. It shows that with additives, the impedance growth rate of all cells were reduced compared with that in control electrolyte. Both the washed and unwashed SC622 samples show slower impedance growth than the PC622 sample. The use of

2FEC-1DTD can improve the cycling performance of the SC622 samples, and it is likely that the additives form a protective layer on the positive electrode material surfaces and limit degradation during charge-discharge cycling.

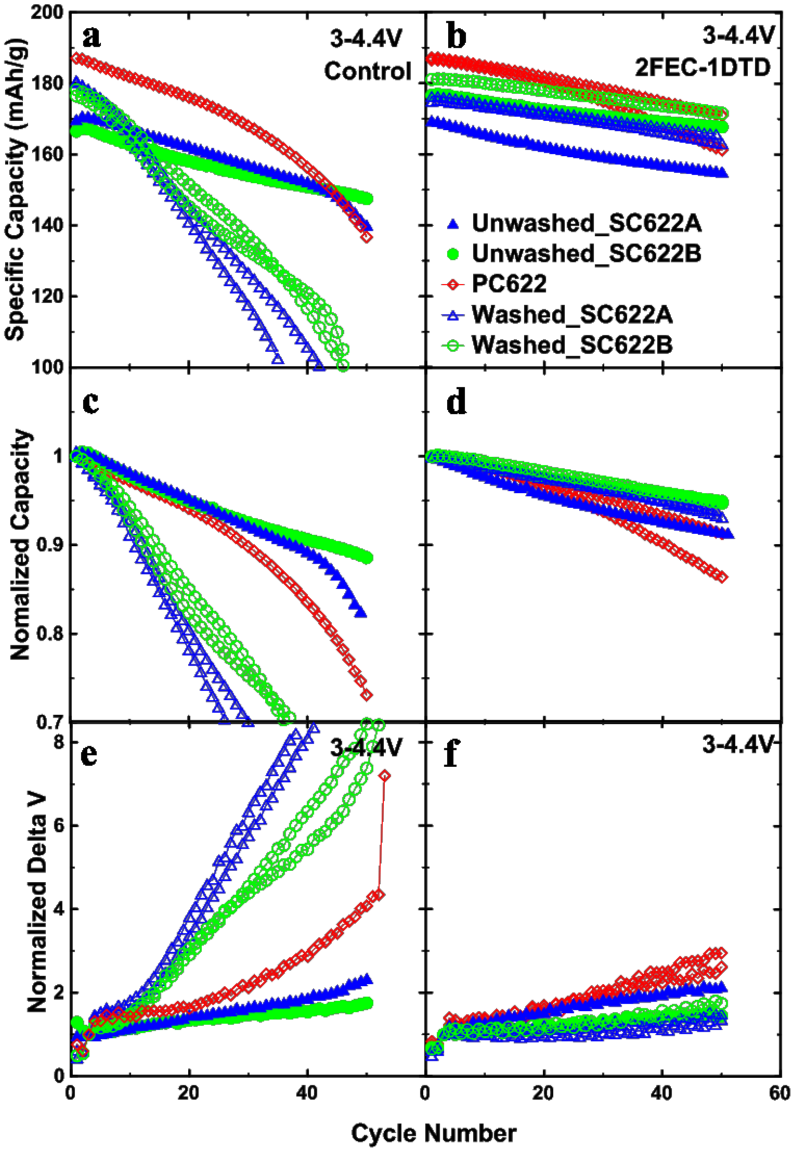

Figure 6.10 Specific capacity (a) (b), corresponding normalized capacity (c) (d), and normalized delta V (e) (f) as a function of cycle number for cells with control electrolyte and 2FEC-1DTD electrolyte. All half cells were cycled at 30 ºC with a current density of 40 mA/g for 50 cycles.

Figure 6.11 shows dQ/dV vs V for the five sets of cells in both control electrolyte and in 2FEC-1DTD electrolyte. In Figures 6.11A-6.11E, the solid black lines show the curves of the 2nd C/5 cycle, and the red lines show the curves of the 23rd or 50th cycle. Figure 6.11 shows that in control electrolyte, washed SC622A and washed SC622B cells develop huge impedance as cells are cycled for 23 cycles. By comparison, PC622, unwashed SC662A and unwashed SC622B cells have moderate impedance after 50 cycles. The PC622 cell shows more capacity loss than the unwashed SC662B cell.

Compared to cells using control electrolyte, cells with 2FEC-1DTD electrolyte performed very differently. In Figures 6.11a-6.11e, the black lines represent the curves of the 2nd cycle, and the red lines are the data for the 50th cycle. When 2FEC-1DTD is used, cells with washed SC622A and washed SC622B show much more moderate impedance compared to cells with control electrolyte and the dQ/dV vs V peak features were well-preserved indicating little material degradation. These results suggest that electrolyte additives play important role in the cathode material protection. Comparing Figures 6.11a, 6.11b, 6.11d and 6.11e with 6.11c, even when 2FEC-1DTD is used, SC622 cells have a larger impedance at the beginning of discharge than PC622 cells. However, SC622 cells still have higher capacity retention after cycling than PC622 cells.

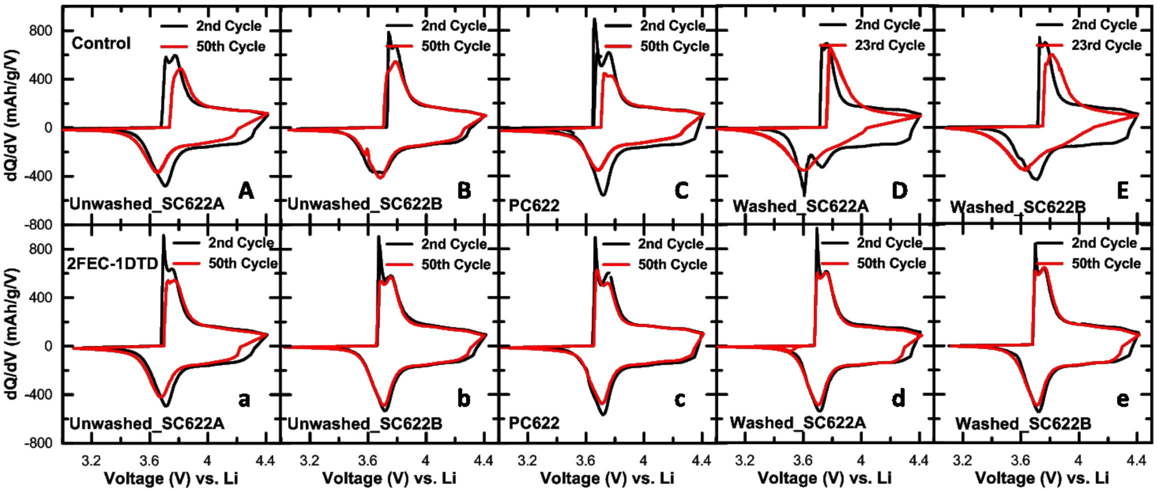

Figure 6.11 Differential capacity as a function of cell voltage of unwashed SC622A (A), unwashed SC622B (B), PC622 (C), washed SC622A (D) and washed SC622B (E) in control electrolyte. Differential capacity as a function of cell voltage of unwashed SC622A (a), unwashed SC622B (b), PC622 (c), washed SC622A (d) and washed SC622B (e) in 2FEC-1DTD electrolyte. The cycle number of the data is indicated in the legends in the figure.

Table 6.3 shows the BET specific surface area measurements of the three samples. Table 6.3 shows that the SC622 samples made here have larger specific surface areas than the PC622 sample. J. Cho et al. have proposed that single crystal materials benefit from lower surface area,[173] but that is not the case here. Figures 6.9 and 6.10 help rule out the possibility that the superior cycling performance of single crystal positive electrode materials is due to lower surface area. A more reasonable explanation is that the superior capacity retention of single crystal cells with charge-discharge cycling originates from better cathode material integrity. For layered lithium transition metal oxide positive electrode materials, many failure mechanism studies attribute some portion of cell degradation to micro-cracks which form in the secondary particles causing impedance growth and active material loss.[128–134,239] By comparison with single crystal positive electrode materials, polycrystalline materials may have micro cracks generated during cycling because of anisotropic volume expansion and contraction of the various crystal grains in one particle. The generated cracks may cause electrical disconnect issues and continuous solid electrolyte interface (SEI) growth on the new surfaces. For single crystal materials, crack formation can be suppressed and more a stable SEI can be preserved.[173]

Table 6.3 Single point BET surface areas of the washed samples used in electrochemical testing.

Sample	**PC622**	**SC622A**	**SC622B**
Specific Surface Area (m^2/g)	0.33(2)	0.50(4)	0.39(2)

A recent work from J. Harlow et al.[240] shows that pouch cells with single crystal NMC532 as the positive electrode material can be stably cycled for more than 5000 cycles with a capacity retention of 97%. The cross-sectional SEM images on the cycled positive electrode show virtually no microcracks. As SC622 is also commercially available, our lab also has ongoing tests on SC622 pouch cells (material provided by EA Spring (China) and pouch cells built at LiFUN Technologies (China)). Figure 6.12 shows the 1C/1C cycling test of SC622/Artificial Graphite pouch cells. The cells were tested at 20ºC using 1C charge and discharge currents between 3-4.3 V with “rate maps” (discharges at C/20, C/2, 1C, 2C, 3C) applied every 100 cycles. For plotting clarity, the rate map data is not fully presented in the figure. The positive electrode material choices include commercial SC622, PC622B (B-type coating, material from Umicore (Korea)), and PC622A (A-type coating, material from Umicore, Korea), and artificial graphite (AG) or natural graphite (NG) were used as negative electrode materials. The same electrolyte system was used in all the cells. Figure 6.12 shows that SC622/AG cells outperformed all the PC622 cells in capacity retention and impedance growth control. Y.Liu et al. showed that even after more than 5000 cycles, no microcracks could be found in cross-sectional SEM images of the SC622 positive electrodes.[241] These works were not done by the author of the thesis but are included in here as supplemental data.

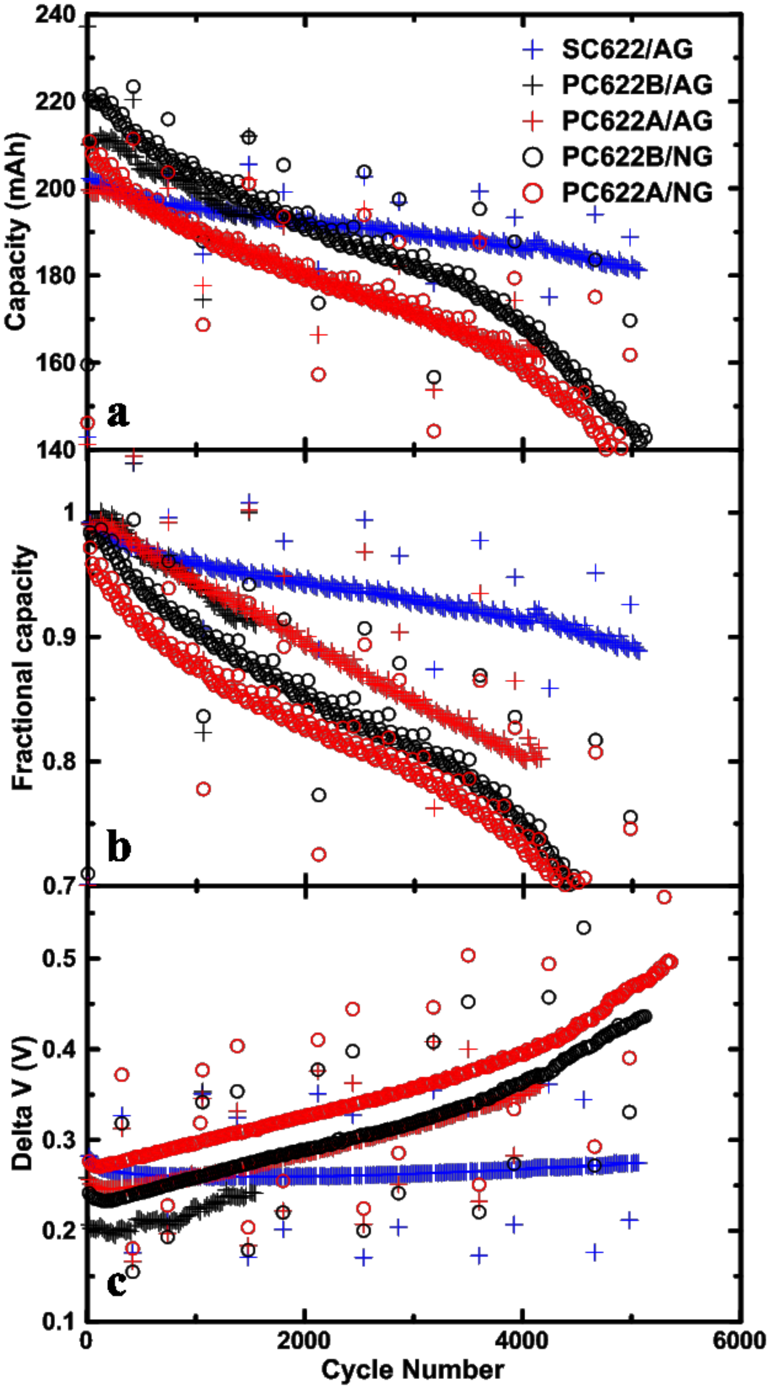

Figure 6.12 Cycling tests of SC622/AG, PC622B/AG, PC622A/AG, PC622B/NG, and PC622A/NG pouch cells. Cells were tested between 3.0 and 4.3 V at 20ºC using currents corresponding to 1C.

Single crystal positive electrode materials have advantages over their conventional polycrystalline counterparts when selected electrolyte additives are used. One may worry whether the rate capability is compromised by increased grain size. Figure 6.13 shows the normalized capacity as a function of discharging rate. Cells were tested at 30ºC. Figure 6.13 shows that for single crystal positive electrode materials, the rate capability is only slightly inferior to the polycrystalline positive electrode material. Many modification methods could be applied in electrode and cell fabrication process to further improve the rate capability.

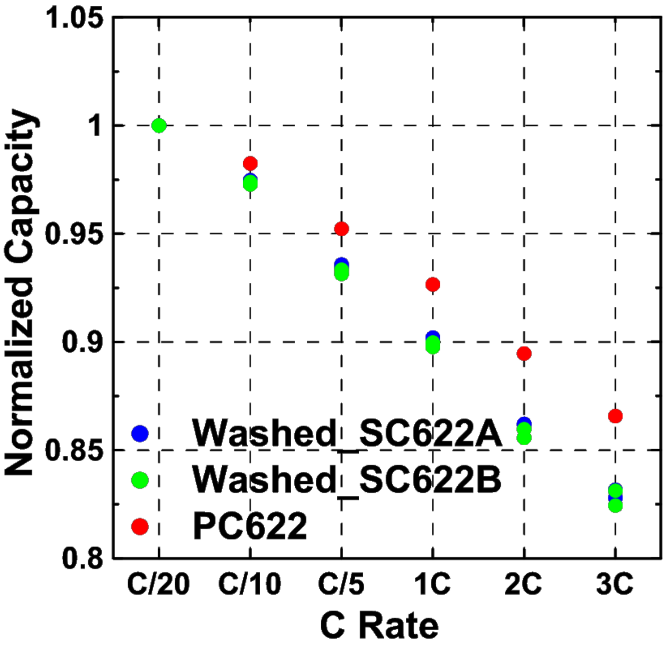

Figure 6.13 Normalized capacity as a function of discharging rate for the samples as indicated in the legend.

6.3 Conclusions

In summary, the synthesis of single crystal NMC622 cathode materials was explored, and consistent with previous work, sintering temperature and the Li/TM ratio during sintering are two critical factors influencing reversible capacity and impedance. From comparative studies, preferred synthesis conditions were found. A washing and reheating treatment was conducted to remove residual lithium carbonate. This treatment increased the specific capacity of the synthesized materials by removing "dead mass" and the structure and morphology of the SC622 samples were preserved. The quality of the synthesized SC622 materials should ideally be characterized by EBSD. In this work, the authors are confident about assessing crystal growth with SEM and XRD based on previous studies on single crystal NMC532, which showed good agreement between EBSD and SEM/XRD results.[230]

Electrochemical studies were also carried out in this work. SC622 has a slightly lower specific capacity than PC622, which agrees well with a previous study on commercial single crystal NMC532.[13] Using control electrolyte, the washed SC622 samples had poor cycling performance compared with the PC622 samples. However, when 2FEC and 1DTD were used as electrolyte additives, washed SC622 outperformed PC622 in charge-discharge capacity retention. These results showed that for single crystal positive electrode materials (without any surface coatings, at least), electrolyte additives have a large impact on performance. The mechanism of enhanced capacity retention for single crystal NMC samples was also discussed. Surface area measurements showed that SC622 did not have less surface area than PC622 which ruled out the possibility that single crystal NMC622 has less side reactions with electrolyte due to less surface area.

The hypothesis that SC622 benefits from particle integrity and SEI stability was considered to be more reasonable.

With larger grain size, SC622 showed slightly worse rate capability and work aiming to improve rate capability could be valuable. Cycling experiments of commercial pouch cells showed that cells with single crystal NMC622 had improved lifetime compared to their polycrystalline counterparts. The cross-sectional SEM images of heavily cycled electrodes showed that single crystal particles are crack-resistant, and this is could be a huge improvement for Ni-rich positive electrode materials.

Other layered transition metal positive electrode materials, like $LiNi_{1-x-y}Co_xAl_yO_2$, which is believed to also have particle cracking problems,[131,132,242] can potentially benefit from the single crystal morphology combined with compatible electrolyte systems, and related work is presented in Chapter 7.

CHAPTER 7 SYNTHESIS OF SINGLE CRYSTAL $LiNi_{0.88}Co_{0.09}Al_{0.03}O_2$ WITH A TWO-STEP LITHIATION METHOD

Micro-cracking is a widely acknowledged contributor to NMC and NCA cell failure. Therefore, single crystal positive electrode materials, which are believed to be advantageous in keeping particle integrity during cycling, become attractive. Single crystal NMC532, NMC622 and now NMC811 materials have been successfully commercialized. The previous chapter presented a study of single crystal NMC622 synthesis. However, single crystal $LiNi_{1-x-y}Co_xAl_yO_2$(NCA) materials have not been reported yet. We showed that using excess lithium carbonate (or hydroxide) and a higher heating temperature during synthesis are two critical factors that promote single crystal formation [230,232]

NCA synthesis studies have shown that the Li_5AlO_4 impurity is prone to form at high temperature (> 850ºC), and using an excess amount of Li source also promotes the formation of Li_5AlO_4.[91] This means that the direct application of a simple method to prepare single crystal NMC to the synthesis of single crystal NCA leads to materials with a significant amount of Li_5AlO_4 impurity. In this work, we introduce a two-step method of synthesizing single crystal $LiNi_{0.88}Co_{0.09}Al_{0.03}O_2$ (NCA880903), by which the formation of Li_5AlO_4 can be avoided. It is believed this method can be applied to the synthesis of other compositions of Al-containing Ni-rich positive electrode materials as well. The majority of this Chapter was published in Journal of The Electrochemical Society.[243] H.Li performed the material synthesis, characterisations, and electrochemical measurements; J. Li and N. Zhang contributed to material synthesis; Nafiseh Zaker contributed to EBSD measurements. Reproduced with permission from *J. Electrochem. Soc.*, 166.10 (2019): A1956-A1963. Copyright 2019, The Electrochemical Society.

7.1 Experimental Design

$Ni_{0.88}Co_{0.09}Al_{0.03}(OH)_2$ precursors (average particle diameter was 3 μm) were provided by Guizhou Zoomwe Zhengyuan Advanced Material Co., Ltd. The $Ni_{0.88}Co_{0.09}Al_{0.03}(OH)_2$ precursor was mixed thoroughly with a stoichiometric equivalent of $LiOH•H_2O$ by hand milling using a mortar and a pestle. In the first step of heating, samples with a lithium/transition metal ratio less than 1 were prepared. The mixed powders were preheated in oxygen in a tube furnace at 485°C for 3 hours under oxygen flow. A heating rate of 10°C/min was used to increase the temperature to the set point. This step causes the LiOH to melt and react initially with the NCA precursor. The preheated powders were taken out of the furnace and ground again by hand milling to eliminate areas of local LiOH excess. The ground powders were then heated in oxygen in the tube furnace at 485°C for 2 hours, and then at a temperature ranging from 850°C to 950°C for 12 hours under oxygen flow. A heating rate of 10 °C/min was used to change temperatures. The entire procedure above is referred to as the “first lithiation step”.

After the samples cooled to room temperature additional $LiOH•H_2O$ was added to obtain an overall Li/TM ratio of 1.01 or 1.02. This added $LiOH•H_2O$ was thoroughly mixed with the product of the first heating using a mortar and pestle. Then the mixed samples were subjected to a second heating cycle in oxygen in the tube furnace at 735ºC for 12 hours under oxygen flow. The addition of the additional $LiOH•H_2O$ followed by heating is referred to as the "second lithiation step".

SEM, powder XRD, EBSD and particle size distribution measurements were carried out as described in Chapter 3. Control electrolyte used for coin cell testing was 1.0 M $LiPF_6$ in EC:DEC (1:2 v/v). Electrolyte containing VC as an additive was formulated by adding 2 wt% of VC to the control electrolyte (2%VC electrolyte). The experimental details about half/full coin cell assembly and electrochemical tests were described in Chapter 3.

7.2 Results and Discussions

7.2.1 First Lithiation Step

In early attempts to make single crystal NCA, we applied the method used in single crystal NMC synthesis, which uses excess $LiOH•H_2O$ and higher sintering temperature. We quickly learned that NCA materials tended to form the Li_5AlO_4 phase when higher Li/TM ratio and higher sintering temperatures were used.[91] Figure 7.1a shows the scanning electron microscopy (SEM) image of a sample made with a Li/TM ratio of 1.04 at 850ºC as representative of samples made in the early attempts. Figure 7.1b shows the full XRD pattern of this selected sample, Figures 7.1c and 7.1d show expanded views of the (104) Bragg peak and the (108)/(110) Bragg peaks. The black circles are the measured diffraction data, and the solid red lines show the calculated pattern from Rietveld refinement. The green lines show the differences between the measured and calculated patterns. Figure 7.1e shows the impurity region of the XRD pattern of the selected sample, and the diffraction pattern matches well with the Li_5AlO_4 reference diffraction pattern plotted in blue, suggesting the formation of Li_5AlO_4 impurities. Similar to single crystal NMC532 and NMC622, the synthesized NCA sample came out of the furnace as a “brick”-like chunk due to the excess Li used and the high sintering temperature.[230,232] The Li_5AlO_4 impurity formation issue and the “bricking” issue demonstrated the need for a new method of single crystal NCA synthesis. Therefore, the two-step lithiation method was developed by the authors.

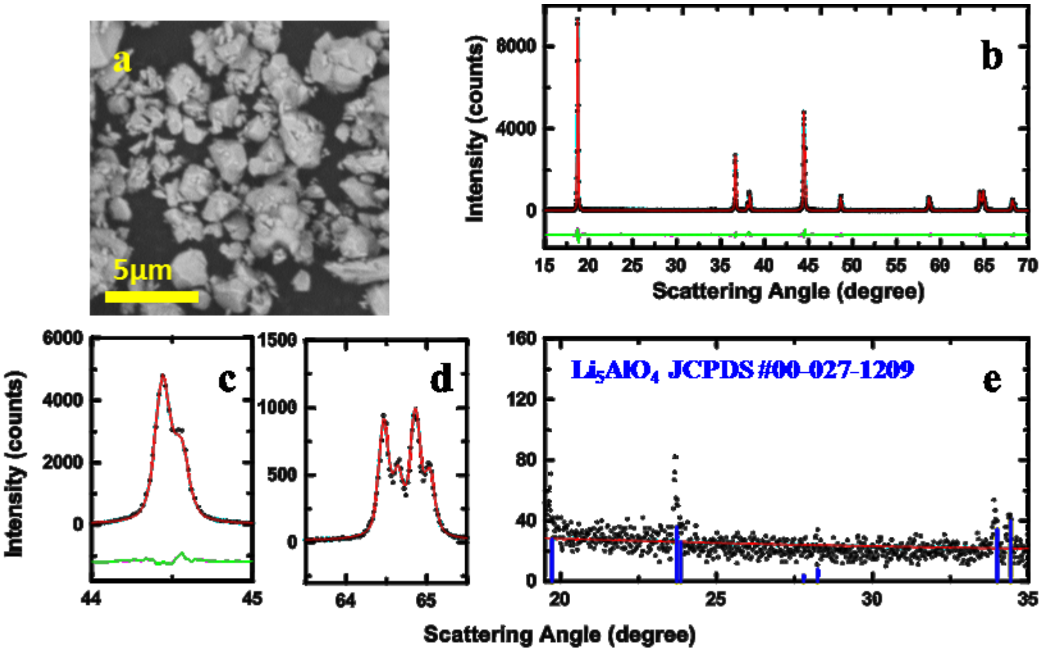

Figure 7.1 SEM image (a) and Full XRD patterns (b) of a sample made with Li/TM ratio of 1.04 at 850°C , expanded view of the (104) Bragg peak (c), expanded view the (108)/(110) Bragg peaks (d), and impurity region in the XRD patterns (e). The reference XRD patterns of Li_5AlO_4 (JCPDS #00-027-1209) are marked with blue lines.

Figures 7.2A and 7.2B show the SEM images of the $Ni_{0.88}Co_{0.09}Al_{0.03}(OH)_2$ precursor. Figures 7.2a – 7.2l show SEM images of the products of a variety of 1st lithiation step reactions with a 5 µm scale bar indicated. Figures 7.2a – 7.2c show samples heated at 950°C with Li/TM ratios of 0.95, 0.90 and 0.80, respectively; Figures 7.2d – 7.2f show samples heated at 900°C with Li/TM ratios of 0.95, 0.925 and 0.90; Figures 7.2g – 7.2i show samples heated at 875°C with Li/TM ratios of 0.95, 0.925 and 0.90; and Figures 7.2j – 7.2l show samples heated at 900°C with Li/TM ratios of 0.975, 0.95 and 0.90. Consistent with previous studies on single crystal NMC material synthesis,[230,232] NCA material synthesized at higher temperature and with higher Li/TM ratio tends to have larger crystallite size. Single crystal NMC532 synthesis succeeds with 20% excess Li and a ~20°C higher sintering temperature compared to polycrystalline NMC532.[14] Single crystal NMC622 synthesis succeeds with 10% excess Li and a ~40°C higher sintering temperature compared to polycrystalline NMC622.[8,232] With a deficient Li source, a much greater sintering temperature increase (~100°C to ~200°C), compared with the conventional polycrystalline NCA synthesis temperature, is needed to promote the grain growth.[226] Samples shown in Figures 7.2c, 7.2f, 7.2g, and 7.2j have the desired single crystal morphology with grain sizes ranging from 2 µm to 5 µm, and these four samples were selected for the second lithiation step.

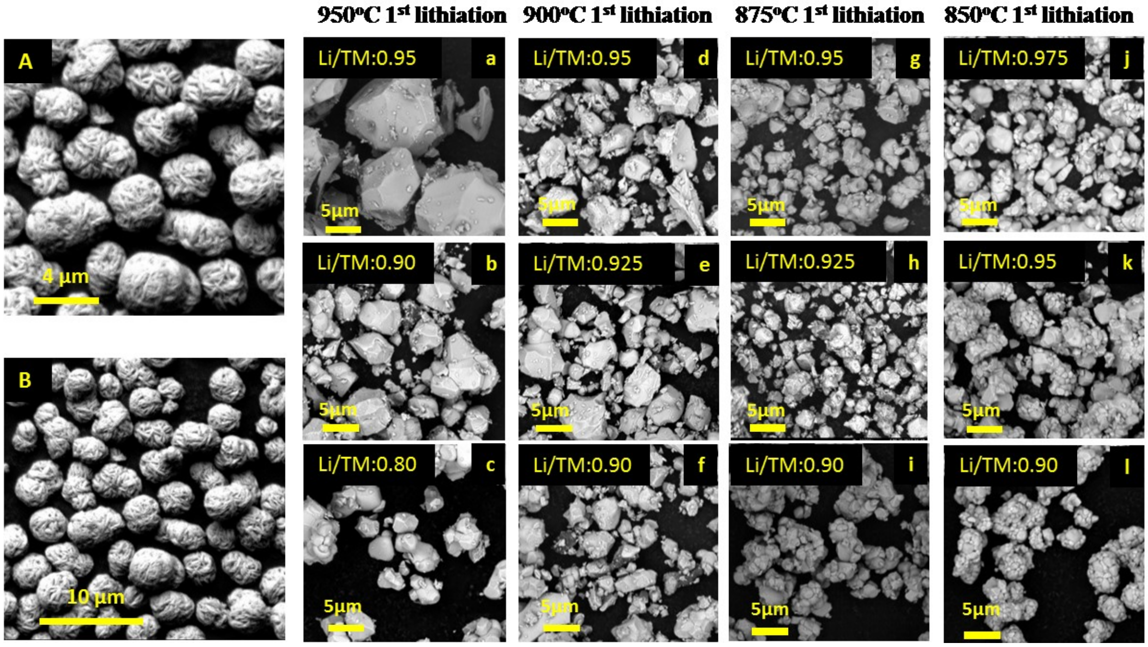

Figure 7.2 SEM images of $Ni_{0.88}Co_{0.09}Al_{0.03}(OH)_2$ precursors (A), (B); SEM images of 1st lithiation step products made at 950°C with Li/TM ratios of 0.95 (a), 0.90 (b), and 0.80 (c); SEM images of 1st lithiation products made at 900°C with Li/TM ratios of 0.95 (d), 0.925 (e), and 0.90 (f); SEM images of 1st lithiation products made at 875°C with Li/TM ratios of 0.95 (g), 0.925 (h), and 0.90 (i); SEM images of 1st lithiation products made at 850°C with Li/TM ratios of 0.975 (j), 0.95 (k) and 0.90 (i).

Figure 7.3 shows the impact of the first step lithiation conditions on the formation of the Li_5AlO_4 impurity. Figures 7.2a – 7.2d show the impurity region between 18–35° in the XRD patterns of samples made at 950°C during the first lithiation step. Diffraction peaks of impurities like Li_2CO_3 and Li_5AlO_4 can be observed within this diffraction angle range. Figure 7.3e shows the the reference XRD pattern of Li_5AlO_4 (JCPDS #00-027-1209). All of the XRD patterns were collected using the same X-ray diffractometer, sample holder, and measuring parameters. Figure 7.3 shows that the peaks from Li_5AlO_4 became more intense as the Li/TM ratio increased from 0.6 to 0.95 at a fixed sintering temperature. To semi-quantify the amount of Li_5AlO_4, the ratio of the diffraction peak height (the overlapping (011) and (101) Bragg peaks) counts at ~23.7° to the average background count rate between 23° – 23.5° is defined as the Li_5AlO_4 impurity relative intensity. XRD patterns of samples made at 900°C, 875°C, and 850°C with different Li/TM ratios were collected in an identical way and the values of the Li_5AlO_4 impurity relative intensity were calculated as described above. Figure 7.3f shows the Li_5AlO_4 impurity relative intensity as a function of sintering temperature and Li/TM ratio. A clear relationship between the amount of Li_5AlO_4 and the synthesis conditions can be observed. As the 1st step lithiation temperature increases, more Li_5AlO_4 can be detected by XRD, and the formation of Li_5AlO_4 is also promoted by adding more $LiOH{\bullet}H_2O$. Figure 7.3f suggests that a two-step lithiation method could be successful. The first step with a deficient amount of Li source and a high sintering temperature can grow the particles to form the desired single crystal morphology with a limited amount of impurity generation. A second lithiation step at lower temperature, to avoid Li_5AlO_4 generation can be used to adjust the Li content to the desired value.

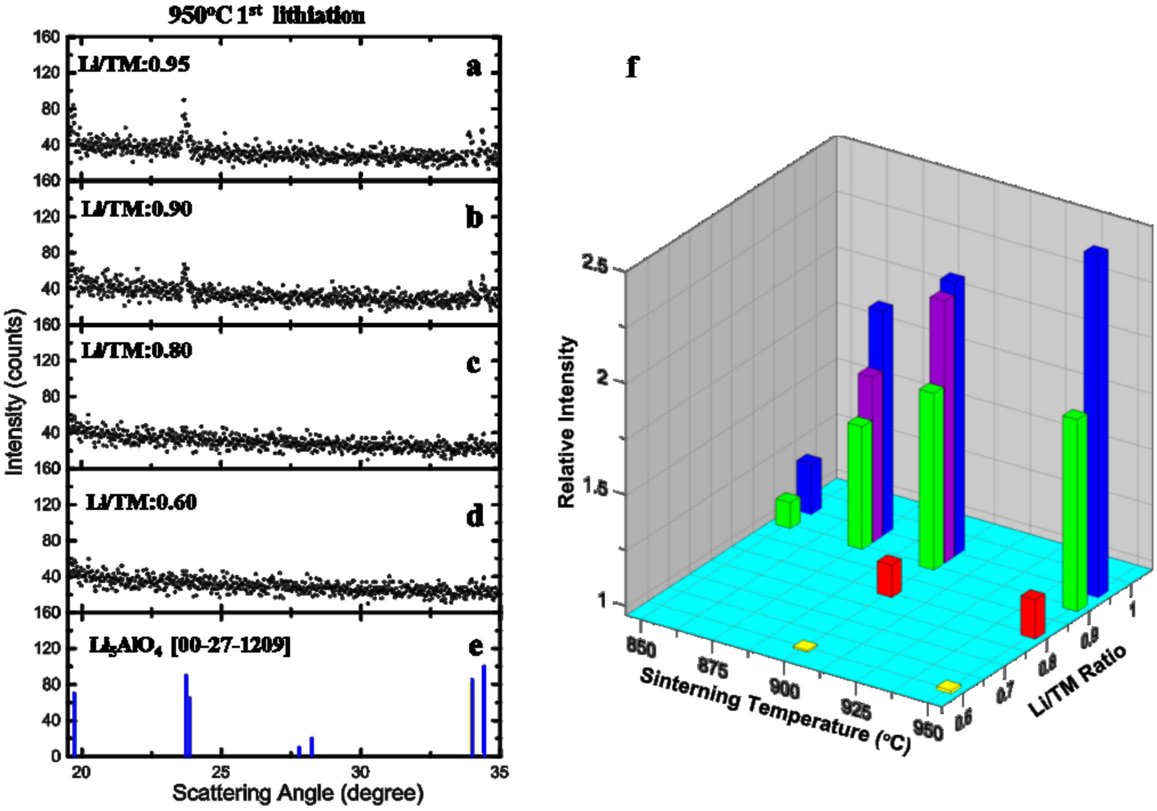

Figure 7.3 Impurity regions in the XRD patterns of 1st lithiation step products made at 950°C with Li/TM ratios of 0.95 (a), 0.90 (b), 0.80 (c), and 0.60 (d). The reference XRD pattern of Li_5AlO_4 (JCPDS #00-027-1209) (e). The relative intensity of the overlapping (011)/(101) Bragg peaks of Li_5AlO_4 as a function of Li/TM ratio and sintering temperature.

7.2.2 Second Lithiation Step

Figures 7.4a – 7.4d show the SEM images of 1st step lithiation products: sample A (made with a Li/TM ratio of 0.8 at 950°C), sample B (made with a Li/TM ratio of 0.9 at 900°C), sample C (made with a Li/TM ratio of 0.95 at 875°C), and sample D (made with a Li/TM ratio of 0.975 at 850ºC), respectively. Panels a1/a2, b1/b2, c1/c2 and d1/d2 in Figure 7.4 show the SEM images of the 2nd lithiation products of samples (A – D) shown in Figures 7.4a – 7.4d. These samples will be called A1/A2, B1/B2, C1/C2, and D1/D2, respectively, in the remaining text. It was assumed that all the Li atoms added in the first-step lithiation were incorporated into the product of the first-step lithiation. In the 2nd step lithiation, the amount of additional $LiOH•H_2O$ to be added was determined by the desired final Li/TM ratio. Two final Li/TM ratios, 1.01 and 1.02, were selected in this work. Figure 7.4 shows that after the 2nd step of heating at a standard lithiation temperature of 735ºC, the particle size was maintained, and no obvious existence of residual lithium compounds (these would be captured as dark spots in images taken by a backscattered electron detector) was observed.

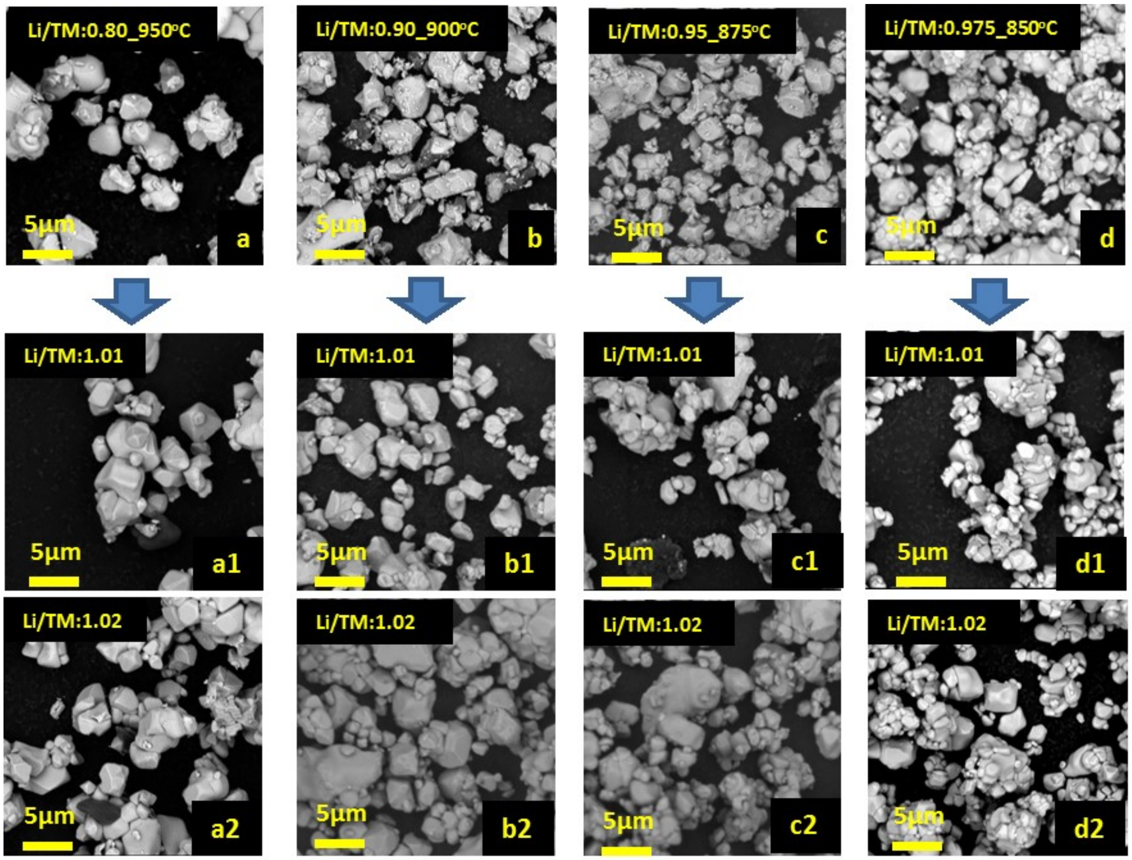

Figure 7.4 SEM images of 1st lithiation step products: sample A (a), sample B (b), sample C (c), and sample D (d). SEM images of 2nd lithiation step products of sample A (a1),(a2); sample B (b1),(b2); sample C (c1),(c2); and sample D (d1),(d2) with overall Li/TM ratios of 1.01 or 1.02.

Figures 7.5a – 7.5d show the XRD patterns of the (104) Bragg peaks of the 1st step lithiation products from samples A, B, C, and D; Panels a1/a2, b1/b2, c1/c2, and 5d1/5d2 in Figure 7.5 show the XRD patterns of the (104) Bragg peaks of the 2nd step lithiation products, samples A1/A2, B1/B2, C1/C2, and D1/D2, respectively. Panels A – A2, B – B2, C – C2, and D – D2 in Figure 7.5 show the impurity region between 18–35° in the XRD patterns of the corresponding samples. Figure 7.5a plots the (104) Bragg peak of sample A with a blue line, and the red dashed line marks the position of the $K_{\alpha1}$ peak.

Figures 7.5a1 and 7.5a2 show that after the 2nd step lithiation, the (104) peaks of samples A1 and A2 moved slightly towards higher angle, which indicates that more Li has been incorporated in the structure.[235] However, a "shoulder" peak can be observed in both Figures 7.5a1 and 7.5a2, and it is at the position marked by the red dashed line. The "shoulder" peaks are believed to be a remaining feature of the 1st step lithiation product. This suggests that the 2nd step lithiation did not fully compensate for the Li deficiency left from the 1st step lithiation. Similar "shoulder" peaks were also observed in Figures 7.5b1 and 7.5b2, and peak broadening can be observed in Figures 7.5c1 and 7.5c2. However, Figures 7.5d1 and 7.5d2 show that samples D1and D2 have more a complete 2nd step lithiation. The change in (104) Bragg peak before and after the second-step lithiation shows that to ensure a fully lithiated final product, the extent of Li deficiency in the 1st step lithiation needs to be relatively small.

As for controlling the amount of Li_5AlO_4, Figure 7.5A shows that there was no Li_5AlO_4 detected by XRD after the 1st lithiation step, while after the 2nd step of lithiation, the Li_5AlO_4 impurity diffraction peak is observed in Figures 7.5A1 and 7.5A2. This is consistent with the previous discussion that the 2nd step lithiation of sample A made at 950°C with a Li/TM ratio of 0.8 was not complete and some Li was in the form of Li_5AlO_4. Figures 7.5B – 7.5D show the existence of the Li_5AlO_4 impurity after the 1st lithiation step, and panels B1/B2, C1/C2, and D1/D2 in Figure 7.5 show that after the 2nd lithiation step at lower temperature, the diffraction peak of Li_5AlO_4 became less intense. This suggests that the amount of Li_5AlO_4 impurity formed during the first lithiation step can possibly be reduced during the 2nd lithiation step at a lower temperature, and that the amount of additional Li source used needs to be carefully controlled.

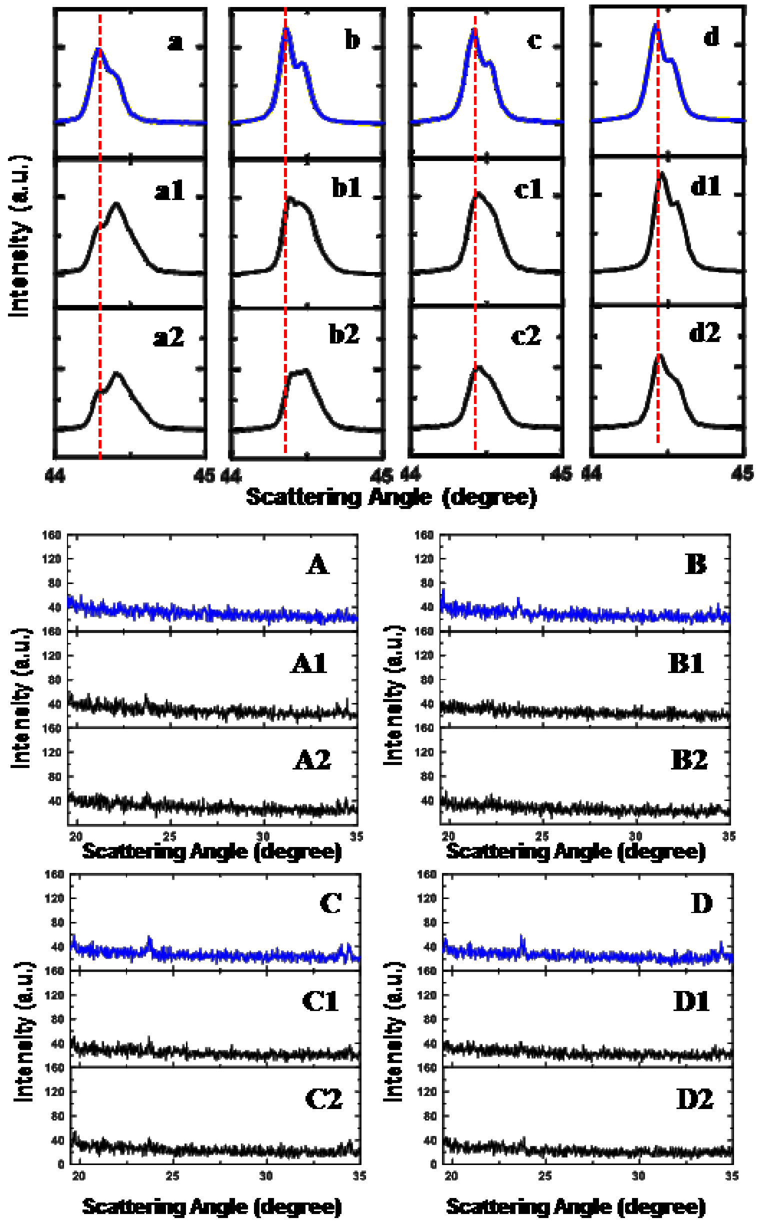

Figure 7.5 XRD patterns of (104) Bragg peaks of 1st lithiation step products: sample A (a), sample B (b), sample C (c), and sample D (d); XRD patterns of (104) Bragg peaks of 2nd lithiation step products of sample A (a1),(a2); sample B (b1),(b2); sample C (c1),(c2); and sample D (d1),(d2) with overall Li/TM ratios of 1.01 or 1.02. Panels A – A2, B – B2, C – C2, and D – D2 show the impurity region between 18–35° in the XRD patterns of the corresponding samples.

To evaluate the outcome of the 2nd lithiation step, Rietveld refinement was performed on the XRD patterns of samples C, C1, C2, D, D1 and D2. The $NaFeO_2$ structure in the R-3m space group was used to describe the structure. For samples C and D, which were made with Li/TM ratios of 0.95 and 0.975 in the 1st lithiation step, respectively, it was assumed that there was no Li loss during the 1st lithiation step. Thus, the refinements on samples C and D were performed with an initial formula of $[Li_{0.974}Ni_{0.026}]_{3a}[Ni_{0.877}Co_{0.092}Al_{0.031}]_{3b}O_2$, and $[Li_{0.987}Ni_{0.013}]_{3a}[Ni_{0.879}Co_{0.091}Al_{0.030}]_{3b}O_2$, respectively. For samples C1/C2 and D1/D2, it was assumed that the final products made after the 2nd lithiation step have a Li/(NiCoAl) ratio of 1 because NCA material cannot accommodate excess Li in its structure, so the refinements were performed with an initial formula of $[Li]_{3a}[Ni_{0.88}Co_{0.09}Al_{0.03}]_{3b}O_2$. In the refinements, exchange of Li and Ni between the predominantly Li layer (3a sites) and the predominantly transition metal layer (3b sites) was allowed subject to the constraint that the overall stoichiometry was fixed. Figure 7.6 shows the percentage of sites in the Li layer occupied by Ni in samples C, C1, C2, and samples D, D1, D2. Figure 7.6 shows that after the 1st lithiation step with a Li/TM ratio smaller than 1, samples C and D have 9.2(1)% and 5.2 (1)% Ni atoms in the Li layer, respectively. After the 2nd lithiation step with Li/TM ratios of 1.01 and 1.02, samples C1/C2 and D1/D2 show that the Ni/Li interlayer mixing was significantly reduced, indicating the effectiveness of 2nd lithiation step.

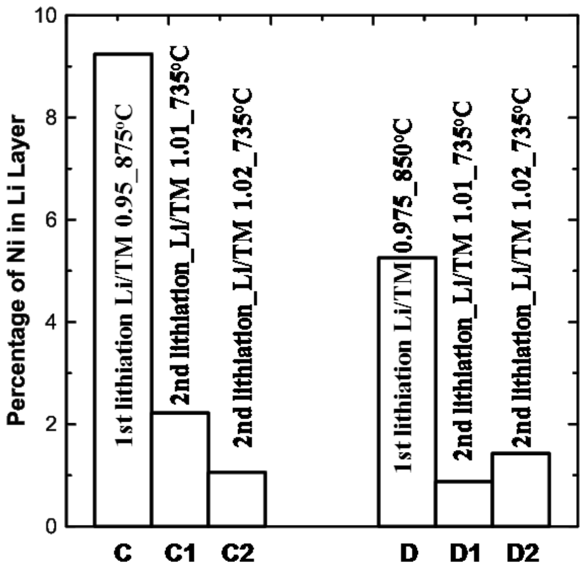

Figure 7.6 Fraction of sites in the Li layer occupied by Ni in the first lithiation step products (samples C/D), and the second lithiation step products (samples C1/C2 and samples D1/D2).

7.2.3 Structural Evaluations of Single Crystal NCA880903

Sample D1, which had the smallest amount of Ni/Li mixing after the 2nd lithiation step was selected as the single crystal sample (SC880903) for further studies. Polycrystalline NCA880903 (PC880903) was made as described in previous work [91] for comparison. Figures 7.7a and 7.7b show the SEM images of PC880903 and SC880903, respectively. The SEM image of PC880903 shows large-size dense spherical secondary particles consisting of primary particles about ~100 nm in size. The image of SC880903 shows 2-5 µm primary particles with some agglomerates. Figure 7.7c shows the particle size distribution plots of sample D and sample D1 (SC880803). Figure 7.7c shows that the desired particle size made in the 1st lithiation step lithiaton was well-preserved after the 2nd lithiation step.

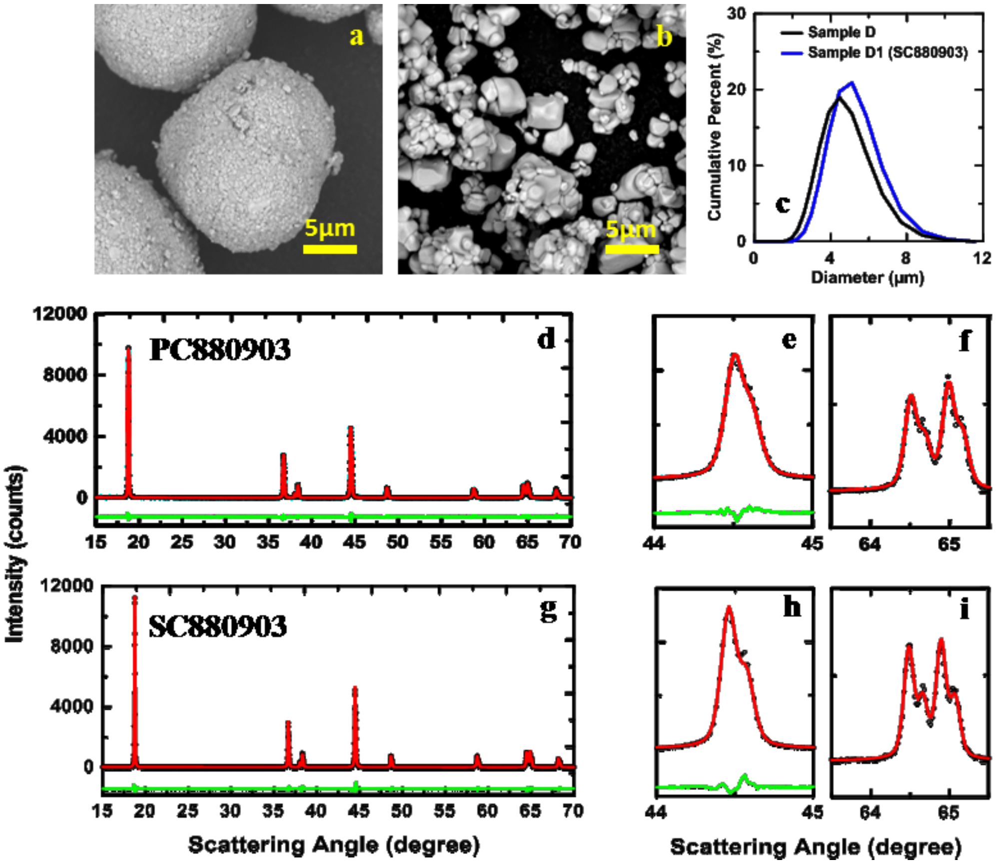

Figure 7.7 SEM images of PC880903 (a) and SC880903 (b). Particle size distribution plot of sample D and D1(SC880903) (c). Full XRD patterns of PC880903 (d), expanded views of the (104) Bragg peak (e), and the (108)/(110) Bragg peaks (f); full XRD patterns of SC880903 (g), expanded views of the (104) Bragg peak (h), and the (108)/(110) Bragg peaks (i).

Figures 7.7d – 7.7f and 7.7g – 7.7i show the XRD patterns of PC880903 and SC880903, respectively. Figures 7.7e and 7.7h show an expanded view of the (104) Bragg peak, and Figures 7.7f and 7.7i show an expanded view of the (108)/(110) Bragg peaks. The black circles are the measured diffraction data, and the solid red lines show the calculated pattern from Rietveld refinement. The green lines show the differences between the measured and calculated patterns. The expanded views of the (104) Bragg peak and the

(108)/(110) Bragg peaks show that SC880903 has less peak broadening and better resolved $K_{\alpha 1}$ and $K_{\alpha 2}$ diffraction peak splitting due to better crystallinity. Table 7.1 summarizes the Rietveld refinement results.

Table 7.1 Rietveld refinement results of PC880903 and SC880903.

	1st Lithiation Condition	2nd lithiation Temperature	Overall Li/TM Ratio	a (Å) (± 0.0001 Å)	c(Å) (± 0.001 Å)	Ni/Li Mixing (%)	R_{Bragg}
PC880903	Li/TM 1.02 735°C	N/A	1.02	2.8690	14.194	0.61(4)	1.86
SC880903	Li/TM 0.975 850°C	735°C	1.01	2.8718	14.189	0.88(5)	2.13

Previously reported synthesis methods for making single crystal NMC532 and NMC622 showed that the sintered materials were "brick"-like chunks that needed to be re-pulverized by grinding aggressively because of the use of excess Li source and high sintering temperature.[230,232] With the two-step lithiation method, which avoids the use of excess Li source in the 1st lithiation step, no "bricking" was observed.

To confirm if the synthesized SC880903 consists of single crystal particles, electron backscatter diffraction (EBSD) was performed on cross sections of SC880903 powders. Figure 7.8A shows a cross-sectional SEM image of the SC880903 sample. Figure 7.8B shows band contrast mapping of the selected region. The white colored grains show a quality of crystallographic match between the material and the R-3m reference lattice, and the grain boundaries can be clearly observed as dark lines due to poor match quality with the reference. Figure 7.8C shows an Euler map of the same region with grains colored based on their Euler angles. The three Euler angles $\varphi1$, Φ, and $\varphi2$ represent a series of rotations about the z, x, and the rotated z axes that needed to be performed on the reference crystal orientation to match the orientation of a grain in the sample. Thus, in Figure 7.8C, grains with different colors have different orientations. Figure 7.8B and 7.8C show that most particles are single crystal grains, while some large sized particles consist of small grains. This indicates the synthesized material consists both mono-dispersed single crystal particles and agglomerates, and this is also observed in commercial single crystal NMC532 materials.[174] More optimization of the heating process or the addition of some post heating processing needs to be considered to improve material quality.

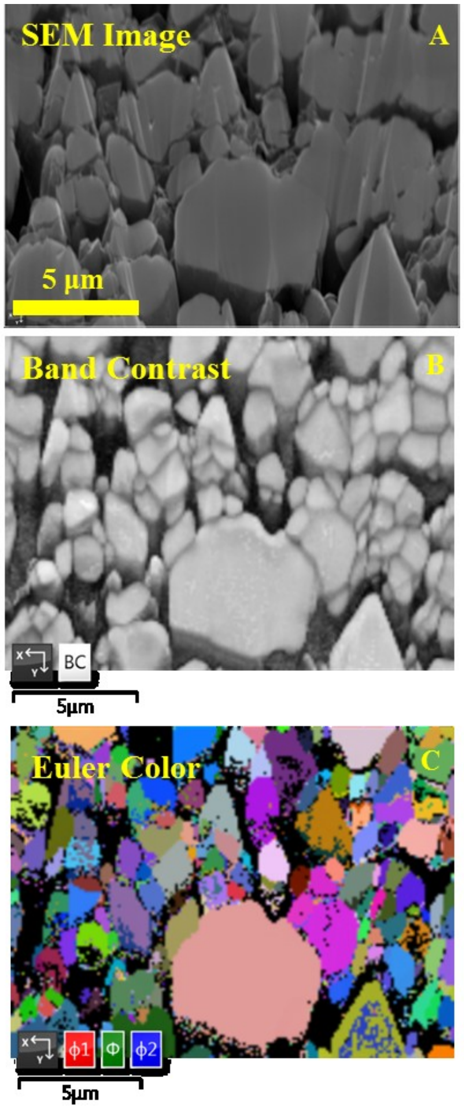

Figure 7.8 Cross-sectional SEM images of SC880903 (A). The band contrast EBSD map (B) and the EBSD Euler Color map (C) of the same region. The three Euler angles φ1, Φ, and φ2 represent a series of rotation about the z, x, and rotated z axes. Each color indicates a specific crystal orientation of the grains.

7.2.4 Electrochemical Evaluations of Single Crystal NCA880903

Figure 7.9 shows some of the electrochemical measurements made on the SC880903 and PC880903 samples. Figure 7.9a shows the cell voltage as a function of specific capacity, and Figure 7.9b shows the corresponding differential capacity versus voltage (dQ/dV vs. V). Cells were cycled with a current density of 10 mA/g (~C/20) at 30°C in control electrolyte, and duplicate cells are represented by solid and dashed lines in the same color. SC880903 shows slightly smaller specific capacity compared with PC880903 presumably due to the longer Li^+ diffusion path in SC880903. The same dQ/dV vs. V features suggest that SC880903 made by two-step lithiation has the same electrochemical features as conventional PC880903. The diminished "kinetic hindrance" peaks at 3.5 - 3.6 V of SC880903 indicates that Li^+ diffusion is kinetically hindered in this voltage range, which is consistent with the larger single crystal grains.

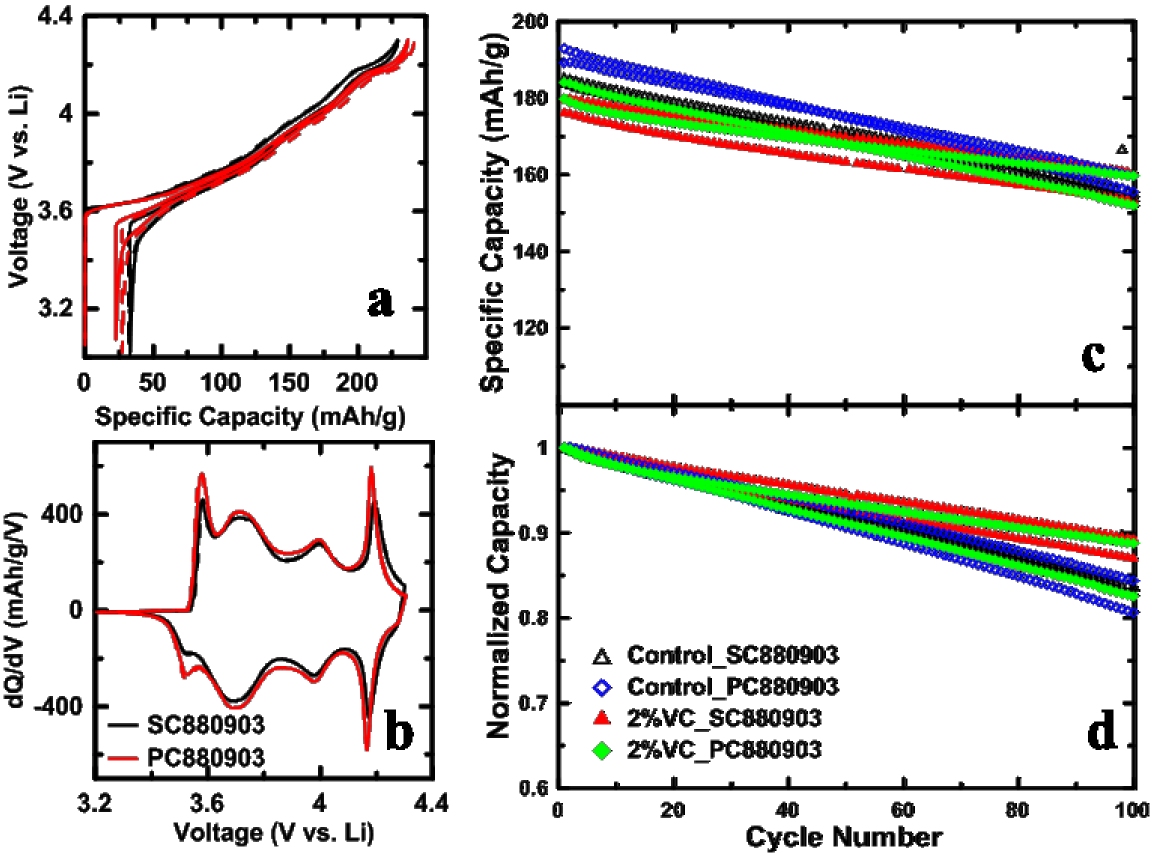

Figure 7.9 Cell voltage as a function of specific capacity for SC880903 and PC880903 samples (a); differential capacity as a function of cell voltage (dQ/dV vs. V) for SC880903 and PC880903 samples (b). The half cells were cycled with a current density of 10 mA/g (~C/20) at 30°C. Specific capacity (c) and normalized capacity (d) as a function of cycle number for SC880903 and PC880903 full coin cells with control electrolyte and 2%VC electrolyte, cells were cycled with a current density of 40 mA/g (~C/5) at 30°C.

Figure 7.9 also shows specific capacity (c) and normalized capacity (d) as a function of cycle number for PC880903 and SC880903 samples in both control electrolyte and 2%VC electrolyte. Full coin cells were cycled with a current density of 40 mA/g (~C/5) at 30°C. This set of cycling data illustrates that the capacity retention for the single crystal sample is at least as good as the polycrystalline sample when 2% VC is used. J.

Li et al.[174,244] have shown that electrolyte additives are critical for single crystal positive electrode materials to demonstrate the benefits of particle integrity preservation. We are optimistic that with appropriate electrolyte additives, single crystal NCA can show many advantages over polycrystalline NCA, but this requires extensive further efforts.

7.3 Conclusions

In summary, this work introduced a two-step lithiation method for single crystal NCA synthesis. When a deficient amount of Li source is used in the 1st lithiation step, the formation of Li_5AlO_4 can be suppressed with particle growth unaffected, and "bricking" of the product can be eliminated as well. The 2nd lithiation step at lower temperature with additional Li source can reduce the Li/Ni interlayer mixing caused in the 1st lithiation step. XRD, EBSD and electrochemical measurements indicate that this method can produce impurity-free single crystal NCA synthesis. It is believed that this method can also be applied in the synthesis of other single crystal positive electrode materials containing Al. The full coin cell cycling shows that the capacity retention of single crystal NCA synthesized with the two-step lithiation method is comparable to conventional polycrystalline NCA samples when 2%VC was used as an electrolyte additive. More efforts focusing on synthesis optimization and post synthesis processing are necessary for material quality improvement. Electrolyte additive development for single crystal NCA will be essential for the single crystal materials to show great advantages over conventional polycrystalline counterparts.

CHAPTER 8 AN UNAVOIDABLE CHALLENGE FOR Ni-RICH POSITIVE ELECTRODE MATERIALS FOR LITHIUM-ION BATTERIES

For layered lithium transition metal oxide cathode materials, many failure mechanism studies attribute some portion of cell degradation to micro-cracks which form in the secondary particles causing impedance growth and active material loss.[128–134] And this is highly related to the anisotropic volume change during charge and discharge, which has been observed in both NCA and NMC materials.[31,32] In this work, from in-situ X-ray diffraction (XRD) measurements on a variety of Ni-rich positive electrode materials, including conventional NMC, NCA, and $LiNiO_2$ materials, it is shown that regardless of the composition, the unit cell volume of $LiNiO_2$ derivative cathode materials change in an almost identical manner with Li content.

From 26 sets of half–cell cycling data collected with different Ni-rich positive electrode materials, an interesting relationship between the capacity retention and accessible capacity cell was found. For materials with a 1st C/20 discharge capacity higher than ~210 mA/g, the capacity retention after 50 cycles dropped rapidly as the accessible capacity increased. This abrupt drop in capacity retention coincides for all materials with a unit cell volume contraction upon delithiation, which shows a sudden drop beyond ~76% of full delithiation or when x = 0.24 in Li_xMO_2. It is tempting to speculate that there is an intrinsic correlation behind the loss in capacity retention and the more severe volume contraction as more capacity is accessed. Recently, Jung et al. [245] have shown that oxygen release from a variety of NMC materials occurs at the point where 81% (very close to 76%) of the Li is removed. It is possible that this increase in oxygen evolution is related to fresh surfaces created by microcracking induced by volume contraction. This work suggests a universal failure mechanism for Ni-rich positive electrode materials which must be overcome and will hopefully help the battery community interpret data sensibly. The majority of this Chapter was published in Chemistry of Materials.[246] H. Li conducted material synthesis, material characterizations, in-situ XRD measurements and electrochemical tests; A. Liu and N. Zhang contributed to material synthesis and electrochemical tests; Y. Wang, S. Yin, and H. Wu contributed to precursor preparation. Reprinted with permission from Chemistry of Materials.[246] Copyright 2019 American Chemical Society.

8.1 Experimental Design

Metal hydroxide precursors used for synthesizing samples 1-16 (listed in Table 7.1) were acquired from Zoomwe Zhengyuan Advanced Material Co., Ltd (China); precursors used for synthesizing samples 17-21 were made at Dalhousie University using co-precipitation as described in Chapter 3. The experimental details of the lithiation (heating) step have been reported in Chapter 3 and references.[32] The NCA material used for sample 22 was provided by Ecopro. Samples 23-26 were extracted as electrodes from dry (no electrolyte) pouch cells provided by reputable suppliers called “vendor” (samples 23-26).

SEM, powder XRD, and in-situ XRD measurements were carried out as described in Chapter 3. EC/DEC electrolyte (1.0 M $LiPF_6$ in EC:DEC (1:2 v/v)), FEC/DMC electrolyte (1.0 M $LiPF_6$ in FEC:DMC (1:4 v/v)), and FEC/DTD-EC:DEC electrolyte (2 wt.% FEC and 1 wt.% DTD in EC/DEC electrolyte) were used for the half coin cell cycling tests. Different electrolytes were used as we learned over time which electrolyte was superior for these tests. Coin cells of samples 23-26 were punched from single side coated regions of electrodes taken from dry (no electrolyte) 402035-size pouch cells provided by Vendor 1. The dry pouch cells had been vacuum sealed in the dry room of Vendor 1 prior to shipping to Canada. The experimental details about coin cell assembly and electrochemical tests were described in Chapter 3.

8.2 Results and Discussions

8.2.1 SEM Images of Selected Samples

Figure 8.1 shows three representative SEM images of the positive electrode materials used in this work. Images are shown of $LiNiO_2$ made starting with a Zoomwe $Ni(OH)_2$ precursor (a), $LiNi_{0.95}Mg_{0.05}O_2$ made starting with a $Ni_{0.95}Mg_{0.05}(OH)_2$ precursor made at Dalhousie Univ. (b), and $LiNi_{0.80}Co_{0.15}Al_{0.05}O_2$ from Ecopro (c).

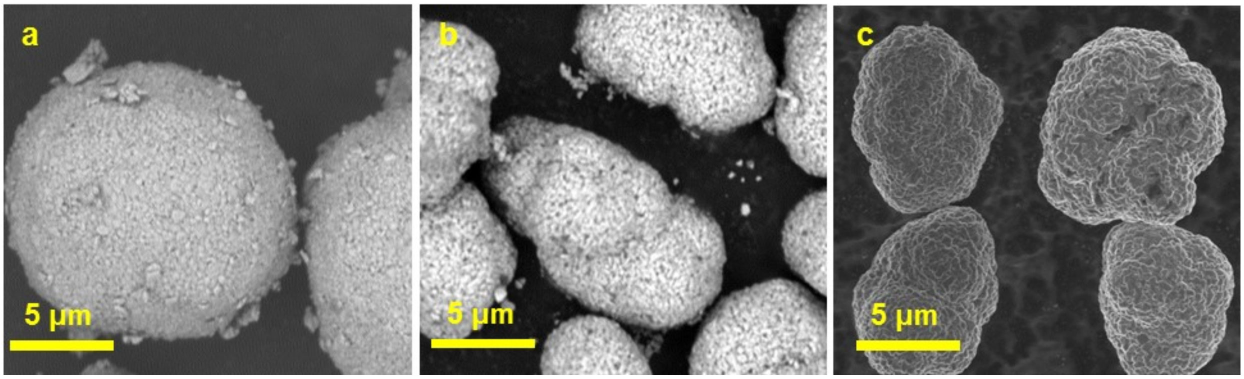

Figure 8.1 SEM images of $LiNiO_2$ (a) made using a $Ni(OH)_2$ precursor from Zoomwe, $LiNi_{0.95}Mg_{0.05}O_2$ (b) made using a $Ni_{0.95}Mg_{0.05}(OH)_2$ precursor made at Dalhousie University, and $LiNi_{0.80}Co_{0.15}Al_{0.05}O_2$ from Ecopro (c).

8.2.2 Cycling of $LiNiO_2$ with Different Cutoff Voltages

As NMC and NCA materials were all developed on the basis of $LiNiO_2$, the failure mechanism of $LiNiO_2$ was first studied in this work. A previous study demonstrated that $LiNiO_2$ goes through a kinetic hindrance region (KH), H1 phase to monoclinic phase (M) transition, single phase M region, M to H2 phase transition, and H2 to H3 phase transition as Li is removed from the material.[9] To investigate the impacts of the phase transitions, five sets of half cells were cycled for 50 cycles at a rate of ~C/5 with different lower cutoff voltages (LCV) and different upper cutoff voltages (UCV). Before and after the cycling, two cycles over a full voltage range (3 - 4.3 V) at a rate of C/20 were performed. FEC/DMC electrolyte (1.0 M $LiPF_6$ in FEC:DMC (1:4 v/v)) was used as the electrolyte. Figure 8.2a shows the specific capacity as a function of cycle number, and Figure 8.2b shows the corresponding normalized capacity retention during cycling. Figure 4.9 in Chapter 4 shows the differential capacity vs. voltage (dQ/dV vs. V) of Li_xNiO_2 with the KH region, and phase transition peaks marked. Figures 8.2c1-8.2c5 show dQ/dV vs. V for the first C/5 cycling of half cells in black. Figure 8.2c shows that cells with a full cycling range have all the KH, H1, M, H2 and H3 regions included, while cells cycled between 3.55-4.3V, 3.65-4.3V, 3-4.1V, and 3.55-4.1V avoid KH, the KH region and the H1-H2 transition, the H2-H3 transition, and both the KH region and the H2-H3 transition, respectively.

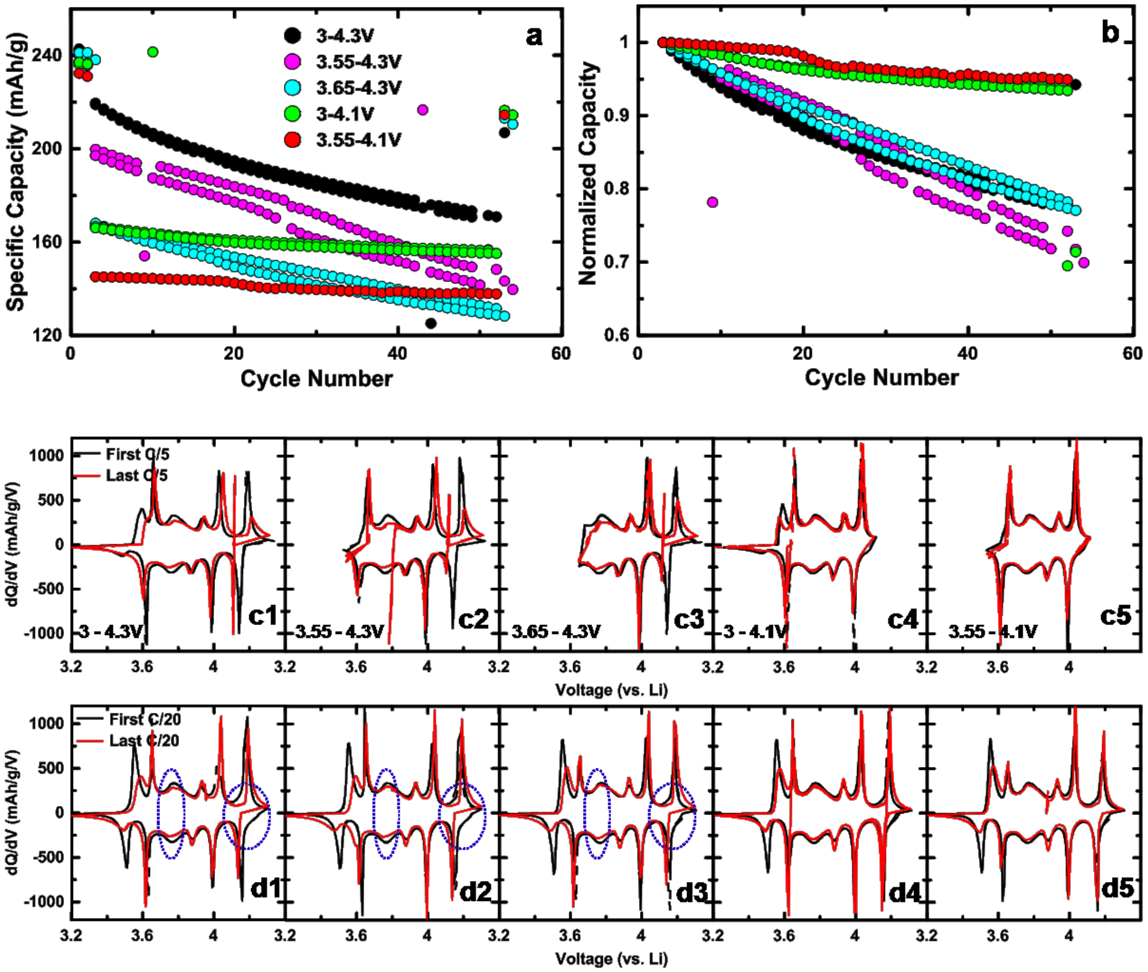

Figure 8.2 Specific capacity (a) and normalized capacity (b) of $LiNiO_2$ with different UCVs and LCVs as a function of cycle number. Differential capacity vs. voltage (dQ/dV vs. V) of first (black) and last (red) C/5 cycles for $LiNiO_2$ half coin cells (c1 – c5). dQ/dV vs. V of first (black) and last (red) C/20 cycles for $LiNiO_2$ half coin cells (d1 – d5). Testing was made at 30°C.

Figure 8.2 shows that cells with an UCV restricted to 4.1 V maintained good capacity retention, while the capacities of cells cycled with an UCV of 4.3 V, regardless of the choice of LCV, lost capacity at a similar rapid rate during cycling. Figure 8.2 shows that traversing the KH region and the H1-M-H2 phase transitions does not result in rapid capacity loss, while the H2-H3 phase transition, which happens between 4.1-4.3 V is highly detrimental to the $LiNiO_2$ cathode material.

Figures 8.2c1-8.2c5 show dQ/dV vs. V of 50th cycle in red. Cells cycled with an UCV of 4.3 V show more changes to the dQ/dV curve after cycling compared to before cycling as shown in Figures 8.2c1-8.2c3 compared to cells with an UCV of 4.1 V as shown in Figures 8.2c4 and 8.2c5. Figures 8.2d1-8.2d5 show dQ/dV vs. V of full voltage range C/20 cycles before and after cycling. For cells that went through the H2-H3 phase transitions during cycling, more polarization at top of discharge, and more reduction of the dQ/dV peaks at ~3.8 V can be observed (marked by blue circles). By contrast, cells cycled with an UCV restricted to 4.1 V have much smaller impedance development and the peaks in dQ/dV vs. V are well preserved after cycling, which indicates less material degradation. The detrimental impact of the H2-H3 phase transition is associated with the abrupt anisotropic unit cell volume contraction,[9] which can cause stress and strain generation due to lattice mismatch. The results presented here are consistent with a study by C. Yoon et al.,[2] which showed the cracking of $LiNiO_2$ particles when cycled to 4.2V and 4.3V.

8.2.3 Cycling of $LiNi_{0.95}Mg_{0.05}O_2$, $LiNi_{0.95}Al_{0.05}O_2$, and $LiNi_{0.9}Co_{0.05}Al_{0.05}O_2$ with Different Cutoff Voltages

In a previous work by the authors and in Chapter 5, it was shown that the phase transitions in Li_xNiO_2 can be effectively suppressed by partially substituting Ni atoms with Al, Mg, or Mn atoms, which can randomly "deactivate" Li sites and thus disturb the Li orderings thought to be responsible for the transitions.[32] The abrupt unit cell volume contraction due to the mismatch between H2 and H3 phases could be suppressed by the elimination of the H2-H3 phase transition, but a continuous rapid unit cell volume change (as a single phase) at high state of charge (SOC) was still observed.[32] To probe the impact of this unit cell volume change, half coin cells made with $LiNi_{0.95}Mg_{0.05}O_2$ (NMg9505), $LiNi_{0.95}Al_{0.05}O_2$ (NA9505), and $LiNi_{0.9}Co_{0.05}Al_{0.05}O_2$ (NCA900505) cathode materials were cycled with different UCVs. Figure 8.3 shows the XRD patterns of $LiNi_{0.95}Mg_{0.05}O_2$, $LiNi_{0.95}Al_{0.05}O_2$, and $LiNi_{0.9}Co_{0.05}Al_{0.05}O_2$. All cells were filled with FEC/DMC electrolyte and cycled at 30°C with a rate of ~C/5 for 50 cycles. Before and after the cycling, two cycles at a rate of C/20 were performed.

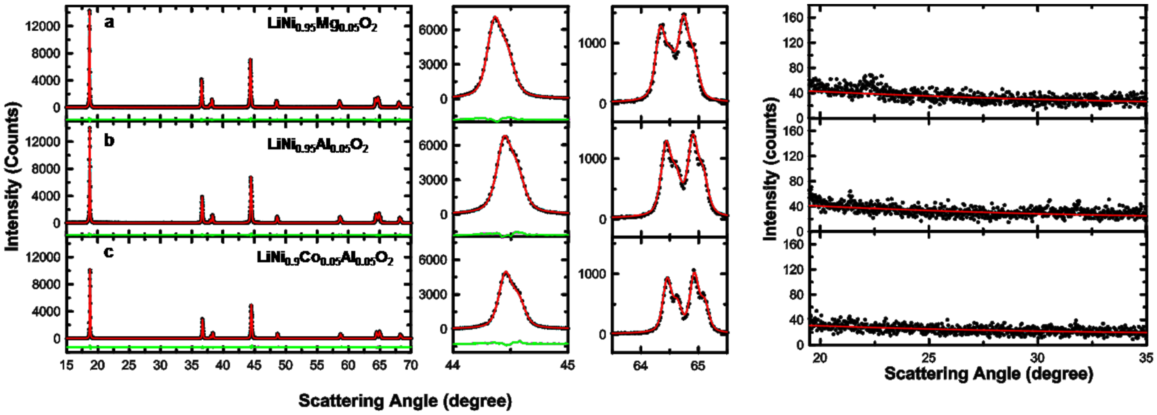

Figure 8.3 XRD patterns of $LiNi_{0.95}Mg_{0.05}O_2$ (a), $LiNi_{0.95}Al_{0.05}O_2$ (b), and $LiNi_{0.9}Co_{0.05}Al_{0.05}O_2$ (c). Expanded view of the (104) Bragg peak, (108)/(110) Bragg peaks, and impurity regions were shown. Black circles are experimental XRD data, solid red lines are calculated patterns from Rietveld refinement, and green lines show the differences between the measured and calculated patterns.

Figures 8.4a – 8.4c show the initial C/20 cycling dQ/dV vs. V of NiMg9505 cells, NA9505 cells, and NCA900505 cells, respectively. The unit cell volume change of each cathode material as a function of cell voltage is plotted in the same corresponding graph, and the data was replotted from previous work.[32] Figure 8.4 shows that cells with an UCV of 4.4 V have a full dQ/dV peak at 4.2 V, which can be considered to be a feature reminiscent of the H2-H3 phase transition peak observed in $LiNiO_2$. Accompanying the 4.2 V peak, there is a continuous sharp drop in unit cell volume. For cells cycled up to 4.3 V, NMg9505 cells have only about 3/4 of the 4.2 V dQ/dV peak accessed, while NA9505 and NCA900505 cells still have most of the 4.2 V dQ/dV peak accessed. For NA9505 and NCA900505 cells, the 3-4.1 V cycling completely excludes the 4.2 V dQ/dV peak. Figures 8.4d – 8.4i show the specific capacity and normalized capacity of half coin cells as a function of cycle number. For all of the three cathode materials, with an increase of UCV, more capacity can be accessed, larger volume changes occur, and the capacity retention becomes worse.

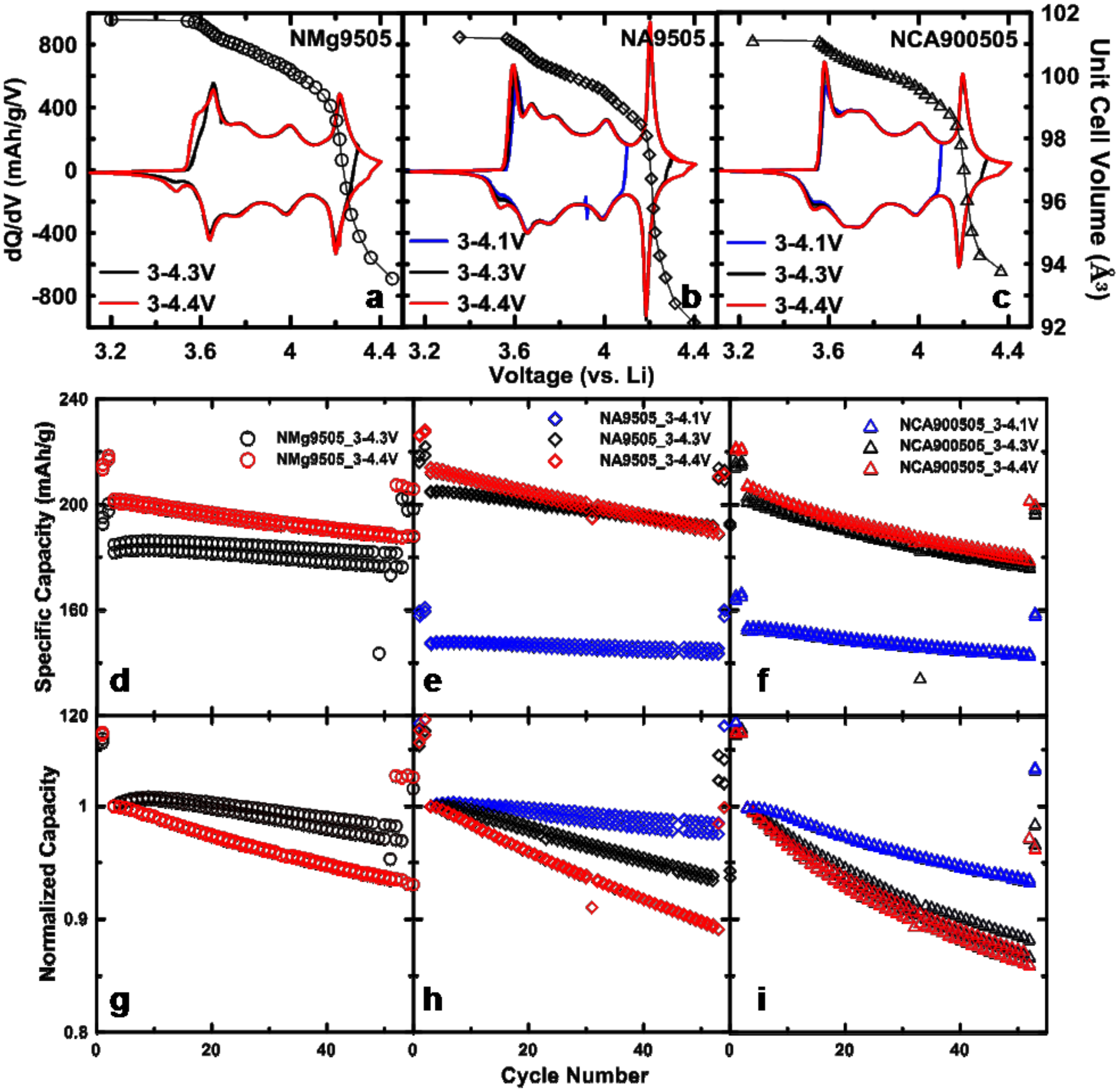

Figure 8.4 dQ/dV vs. V and unit cell volume as a function of cell voltage for NMg9505 (a), NA9505 (b), and NCA900505 (c) cells. Specific capacity (d – f) and normalized capacity (g – i) as a function of cycle number for NMg9505 cells, NA9505 cells, and NCA900505 cells, respectively. All cell testing was made at 30°C.

8.2.4 Capacity Fade Analysis

We plotted the 50-cycle capacity retention of the half coin cells including $LiNiO_2$ as a function of their 1st C/20 discharge capacity in Figure 8.5a. NMg9505 cells, NA9505 cells, and NCA900505 cells are marked by circles, diamonds and triangles, and $LiNiO_2$ (LNO) is marked by a magenta star. Figure 8.5a displays an interesting pattern: the blue ellipse marks a region in which cells show stable capacity retention as C/20 discharge capacity increases, and the red ellipse marks a region in which the capacity retention drops quickly as more C/20 capacity can be accessed. To figure out if this pattern also holds for other cell chemistries, 26 sets of cells were made, and their half-cell testing results listed in Table 8.1 were plotted in the same way shown in Figure 8.5b. The half-cell testing data was collected in the authors' lab. In this table, 16 different cathode materials, including lab made materials and commercial materials, are included. Three types of electrolyte were used due to different original testing purposes. All the cells were cycled at 30°C with the same LCV of 3.0 V and different UCVs ranging from 4.1 V to 4.4 V. Similar to Figure 8.5a, Figure 8.5b demonstrates the same trend of capacity retention change with increase in accessible C/20 discharge capacity. This pattern shows that regardless of the cell chemistry and electrolyte choice, the half-cell cycling capacity retention is mainly governed by the accessible capacity: as more capacity is delivered, an inevitable drop in capacity retention is observed. Figure 8.5 shows a plot adapted from a recent work by J.H Kim et al.[247] In their work, half coin cells made with $LiNi_{0.6}Co_{0.2}Mn_{0.2}O_2$ (NCM-622), $LiNi_{0.8}Co_{0.1}Mn_{0.1}O_2$ (NCM-811), and $LiNi_{0.9}Co_{0.05}Mn_{0.05}O_2$ (NCM-90) were cycled with different upper cut-off voltages. A similar relationship between the capacity retention after 100 cycles (C/2) and the 1st C/2 discharge capacity was observed. This data from the literature about the NMC series is supportive of the pattern shown in Figure 8.5b. It appears that it may be impossible to reach the upper right corner of this graph (our target!) where one would have the highest capacity and also excellent capacity retention. So this represents a real challenge for Ni-rich positive electrode materials.

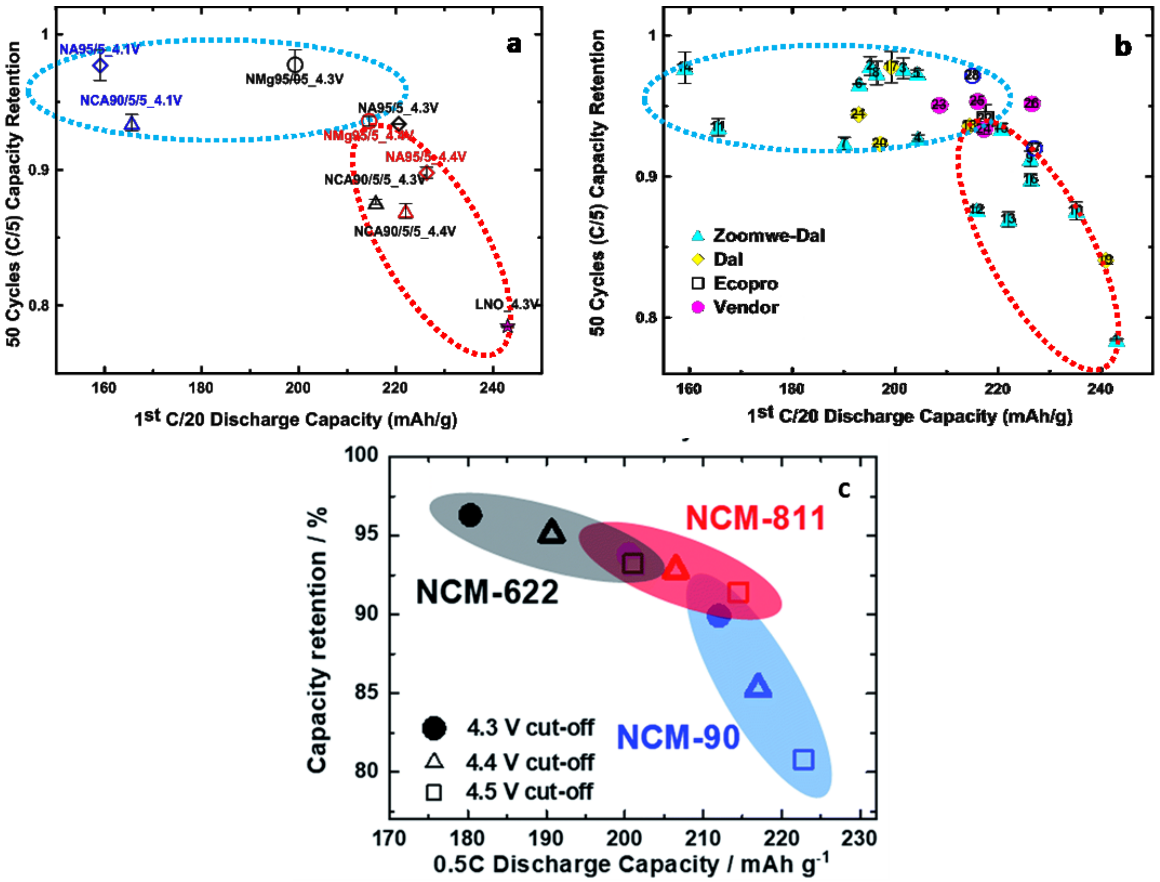

Figure 8.5 Capacity retention after 50 cycles (C/5) as a function of the 1st C/20 discharge capacity for (a) NMg9505, NA9505 and NCA900505 cells, and (b) cells listed in Table 8.1. (c) Capacity retention after 100 cycles (C/2) as a function of the 1st C/2 discharge capacity for NCM-622, NCM811, and NCM-90. Reprinted with permission from Journal of materials chemistry. A.[247] Copyright 2019 Royal Society of Chemistry

To further assess the validity of the curve, we added two sets of half-cell cycling data adopted from the literature as data points 27 and 28.[248] Samples 27 and 28 refer to NCM90 ($LiNi_{0.901}Co_{0.051}Mn_{0.048}O_2$) and NCM80 ($LiNi_{0.796}Co_{0.106}Mn_{0.098}O_2$) in reference [248], respectively. The half-cells in ref. 27 were cycled with a rate of C/2 instead of the C/5 rate used here and the reversible discharge capacity was measured with a rate of C/10 instead of C/20 used here. It is impressive that the data collected from a different research facility with multiple differences in experimental conditions (material synthesis, electrode fabrication, electrolyte formulation, etc.) also falls on the trend shown in Figure 8.5b.

Table 8.1 Summary of half coin cell cycling tests.

Sample	Sample Name	Electrolyte	Compositions (%)					Ni in Li Layer (%)	Capacity (mAh g^{-1})				Retention after 50 cycles	x in $Li_{1-x}NiO_2$***	Material Maker ****	UCV (V)
			Ni	Co	Al	Mg	Mn		C/20 Charge	C/20 Discharge	1st C/5 Discharge	50th C/5 Discharge				
1	LNO	FEC DMC	100					0.973	267.7	243.0	220.9	173.3	0.7844	0.8869	Zoomwe-Dal	4.3
2	NCAMg89/6/3/2	FEC DMC	89	6	3	2		0.714	226.5	195.1	184.5	179.9	0.9751	0.7119	Zoomwe-Dal	4.3
3	NCAMg92/3/3/2	FEC DMC	92	3	3	2		0.9	234.1	201.3	191.7	186.6	0.9735	0.7347	Zoomwe-Dal	4.3
4	NCAMg95/0/3/2	FEC DMC	95		3	2		1.485	236.8	204.1	192.6	178.0	0.9239	0.7450	Zoomwe-Dal	4.3
5	NCAMg89/6/3/2	FEC DMC	89	6	3	2		0.714	233.9	204.3	196.3	191.0	0.9732	0.7454	Zoomwe-Dal	4.4
6	NCAMg92/3/3/2	FEC DMC	92	3	3	2		0.9	226.7	193.3	183.4	175.7	0.9579	0.7055	Zoomwe-Dal	4.25
7	NCAMg95/0/3/2	FEC DMC	95		3	2		1.485	226.5	190.1	178.2	164.6	0.9235	0.6938	Zoomwe-Dal	4.25
8	NMg95/5	EC DEC	95			5		1.36	234.1	196.4	183.5	178.5	0.9733	0.7168	Zoomwe-Dal	4.3
9	NMg97.5/2.5	FEC DMC	97.5			2.5		0.987	242.2	226.3	211.0	192.5	0.9126	0.8258	Zoomwe-Dal	4.3
10	NMg99/1	FEC DMC	99			1		0.788	250.1	235.2	216.7	189.8	0.876	0.858	Zoomwe-Dal	4.3
11	NCA90/5/5	FEC DMC	90	5	5			1.095	185.4	165.6	155.2	145.1	0.9349	0.6044	Zoomwe-Dal	4.1
12	NCA90/5/5	FEC DMC	90	5	5			1.095	235.2	215.9	204.3	179.0	0.8763	0.7878	Zoomwe-Dal	4.3
13	NCA90/5/5	FEC DMC	90	5	5			1.095	241.4	222.0	208.6	181.4	0.8697	0.8103	Zoomwe-Dal	4.4
14	NA95/5	FEC DMC	95		5			1.219	181.7	159.1	149.5	146.1	0.9771	0.5806	Zoomwe-Dal	4.1
15	NA95/5	FEC DMC	95		5			1.219	244.6	218.7	206.6	193.4	0.9362	0.7982	Zoomwe-Dal	4.3
16	NA95/5	FEC DMC	95		5			1.219	244.7	226.3	214.9	192.9	0.8977	0.8260	Zoomwe-Dal	4.4
17	NMg95/05	FEC DMC	95			5		1.658	229.3	203.0	183.4	178.9	0.9759	0.7409	Dal	4.3
18	NMg95/05	FEC DMC	95			5		1.658	238.3	214.5	202.6	189.7	0.9359	0.7828	Dal	4.4
19	NA98.75/1.25	FEC DMC	98.75		1.3			1.5	259.4	240.9	223.2	187.6	0.8407	0.8792	Dal	4.3
20	NMC622 PC	2FEC DTD-ECDEC	60	20			20	2.5	209.5	197.0	187.4	173.0	0.9231	0.7191	Dal	4.4
21	NMC622 SC*	2FEC DTD-ECDEC	60	20			20	2.1	211.2	192.9	183.1	172.8	0.9438	0.7041	Dal	4.4

22	NCA80/15/05	FEC DMC	80	15	5			1.3	224.1	217.5	208.9	196.5	0.9407	0.7937	Ecopro	4.4
23	NMC811 SC*	FEC DMC	80	10			10	N/A	230.0	208.6	199.2	189.4	0.9504	0.7613	Vendor 1	4.3
24	NMC811 SC*	FEC DMC	80	10			10	N/A	238.7	217.3	208.9	195.0	0.9333	0.7929	Vendor 1	4.4
25	NMC811 PC	FEC DMC	80	10			10	N/A	228.0	216.0	205.6	196.0	0.9531	0.7884	Vendor 1	4.3
26	NMC811_PC	FEC DMC	80	10			10	N/A	235.8	226.6	220.5	209.8	0.9515	0.8269	Vendor 1	4.4

* PC: polycrystalline
** SC: single crystal
*** $x = \frac{C/20 \text{ Discharge capacity}}{274 \text{ mAh g}^{-1}}$
**** Zoomwe-Dal: Materials made at Dal with Zoomwe precursors;
Dal: Materials made at Dal with Dal made precursors;
Ecopro: Materials provided by Ecopro;
Vendor 1: Dry pouch cell provided by Vendor

To examine the validity of the trend in Figure 8.5b, studies of the dQ/dV vs. V curves of cells shown in Figure 8.4 were made as examples. Figures 8.6a-8.6h plot dQ/dV vs. V of the 1st C/5 cycles of all the cells in black and the 50th cycles in red. Figures 8.7a-8.7h show expanded views of dQ/dV vs. V of the 1st and 50th cycles. Comparing the dQ/dV vs. V curves before and after cycling shows that NA9505 and NCA900505 cells cycled with an UCV of 4.4 V developed large impedance during cycling, while NMg9505 shows more moderate impedance. With an UCV of 4.3 V, the impedance was smaller in all cases. In the case that the 4.2 V peak was excluded, little impedance was developed in NA9505 and NCA900505 cells.

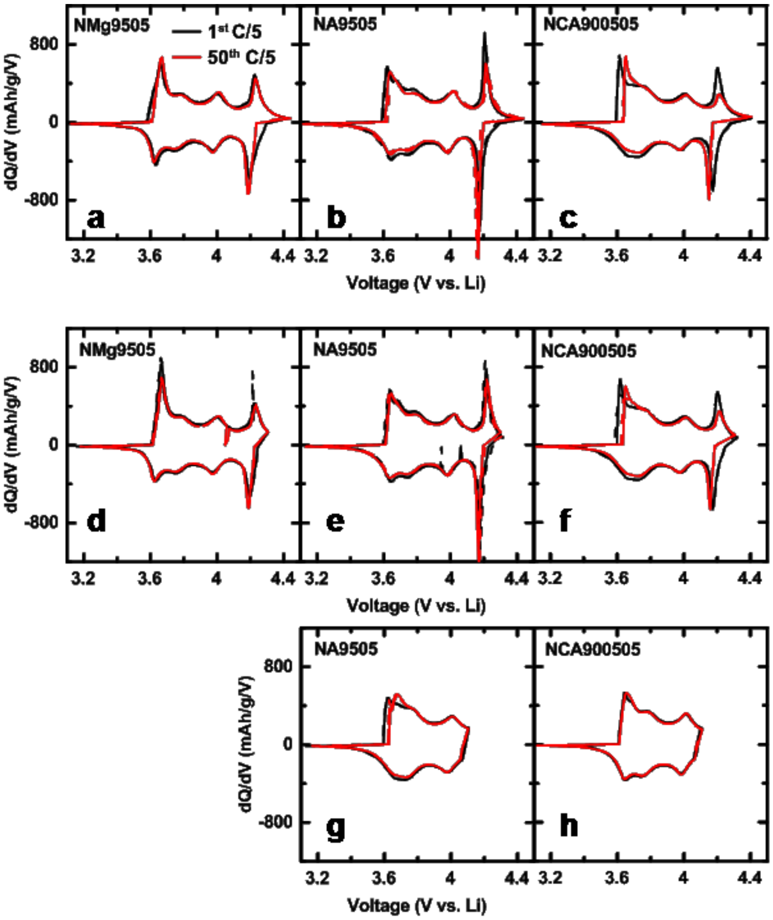

Figure 8.6 dQ/dV vs. V (a – h) of the 1st C/5 cycles in black and the 50th cycles in red for all the cells. Solid and dashed lines in the same color represent pair cells. The testing was all made at 30ºC. In panels a, b and c, the upper cutoff potential as 4.3 V, on panels d, e and f it was 4.2 V while in panels g and h, it was 4.1 V   An expanded view of the 4.2 V peak region is given in Figure 8.7

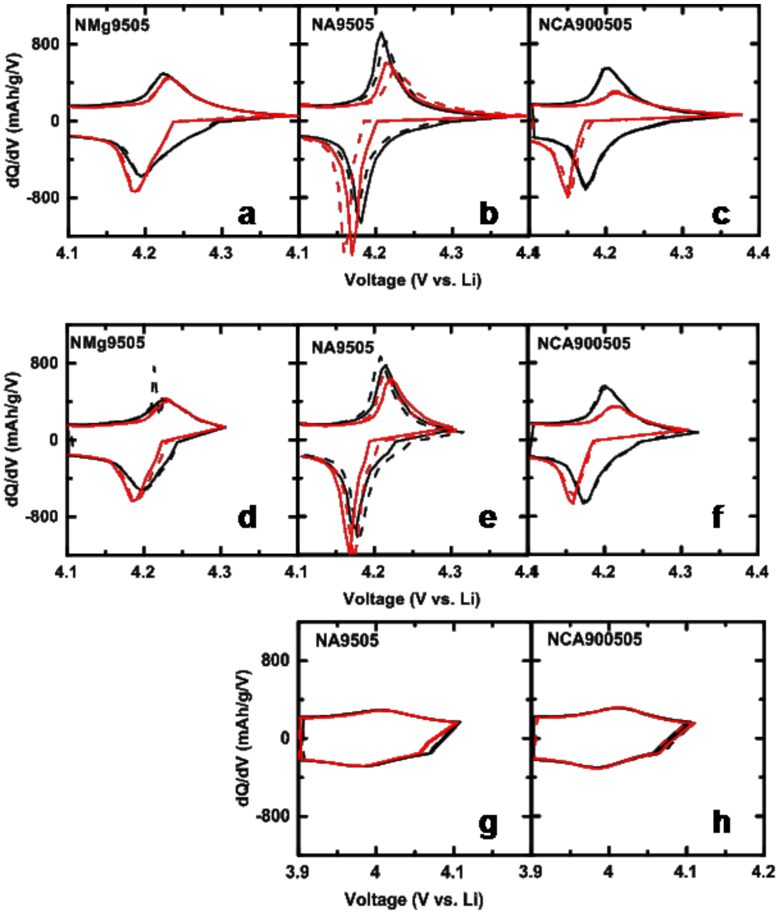

Figure 8.7 Expanded views of dQ/dV vs. V (a – h) of the 1st (black) and 50th (red) cycles for the data shown in Figure 8.6. Solid and dashed lines in the same color represent pair cells.

The analysis of the dQ/dV vs. V curves shows that the capacity loss observed in the half cells is mostly due to impedance. A question that needs to be answered is what caused the impedance growth? Impedance can be affected by electrolyte oxidation on existing surfaces,[20] surface impurities,[105] oxygen loss from the materials,[245,249] as well as structural fractures which can expose new surfaces to electrolyte.[130] Here, the comparison between NMg9505, NA9505 and NCA900505 shows that with the same UCV, the impedance developed in NMg9505 cells is always the least, which suggests that electrolyte oxidation on existing surfaces may not be the dominant factor causing impedance growth. In terms of surface impurities, Figure 8.8a shows a blow-up view of the 1st cycle voltage profiles for NMg9505, NA9505, and NCA900505 cells. N.V. Faenza et al. showed that the open circuit voltage and the voltage overshoot in the beginning of the 1st cycle are good indicators of cell impedance caused by surface impurities.[105] Figure 8.8a shows that NMg9505 and NA9505 cells have some small voltage overshoot in the beginning of the 1st cycle, while NCA900505 does not. This observation suggests that there is no obvious correlation between the surface impurities and the cell cycling performance at least at the minor levels of the impurities in these samples. Figure 8.5a shows that symbols in the region indicated by the red ellipse represent cells that have almost complete 4.2 V dQ/dV peaks, while cells in the region indicated by the blue ellipse only have partial or no 4.2 V dQ/dV peaks. Figures 8.4a-8.4c show that the biggest difference before and after the 4.2 V peak is the unit cell volume. This strongly suggests that the half-cell capacity fade and impedance growth is related to the unit cell volume change, which can cause particle cracking and reactions of electrolyte on fresh surfaces coupled with oxygen loss to the electrolyte.[249].

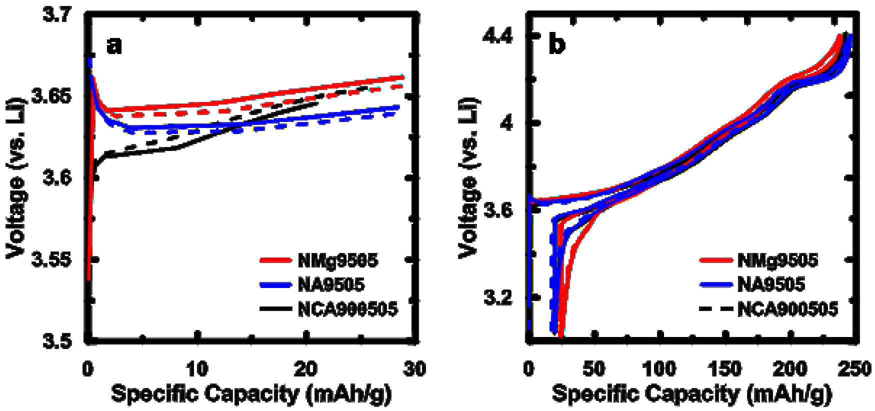

Figure 8.8 Expanded view of the 1st cycle voltage profiles for NMg9505, NA9505, and NCA900505 half cells (a). Solid and dashed curves represent pair cells. Full view of the voltage profile (b).

8.2.5 Universal Behavior of Ni-rich Positive Electrode Materials

Figure 8.5b suggests that the capacity retention trend is a universal behavior, which is not greatly affected by cathode composition or electrolyte choice. Figures 8.9a-8.9c show the a-axis lattice, c-axis lattice, and unit cell volume as a function of cell voltage, collected from in-situ XRD experiments in previous works and in Chapters 4 and 5.[31,32,250] Cells with higher Ni content experience greater c-axis lattice collapse and unit cell volume change when cycled to the same UCV. However, Figure 8.9d shows that when the normalized unit cell volume is plotted as a function of delithiation degree (x in $Li_{1-x}MO_2$), regardless of the Ni content which ranges from 50% to 95% and different cation substituents, all the materials show an almost identical trend of unit cell volume change. The onset of sharp unit cell volume change is virtually the same as the onset of the H2-H3 phase transition in LNO, which suggests that the unit cell volume contraction is an intrinsic property of LNO derivatives. Figure 8.9e shows each cell's capacity retention vs. the corresponding delithiation degree (x in $Li_{1-x}MO_2$) calculated based the

1st C/20 discharge capacity, and in the same graph, the normalized unit cell volume change profile of NCA900505 is plotted as a representative. Figure 8.9e shows that the profile of unit cell volume change follows the pattern of the capacity retention versus delivered capacity curve.

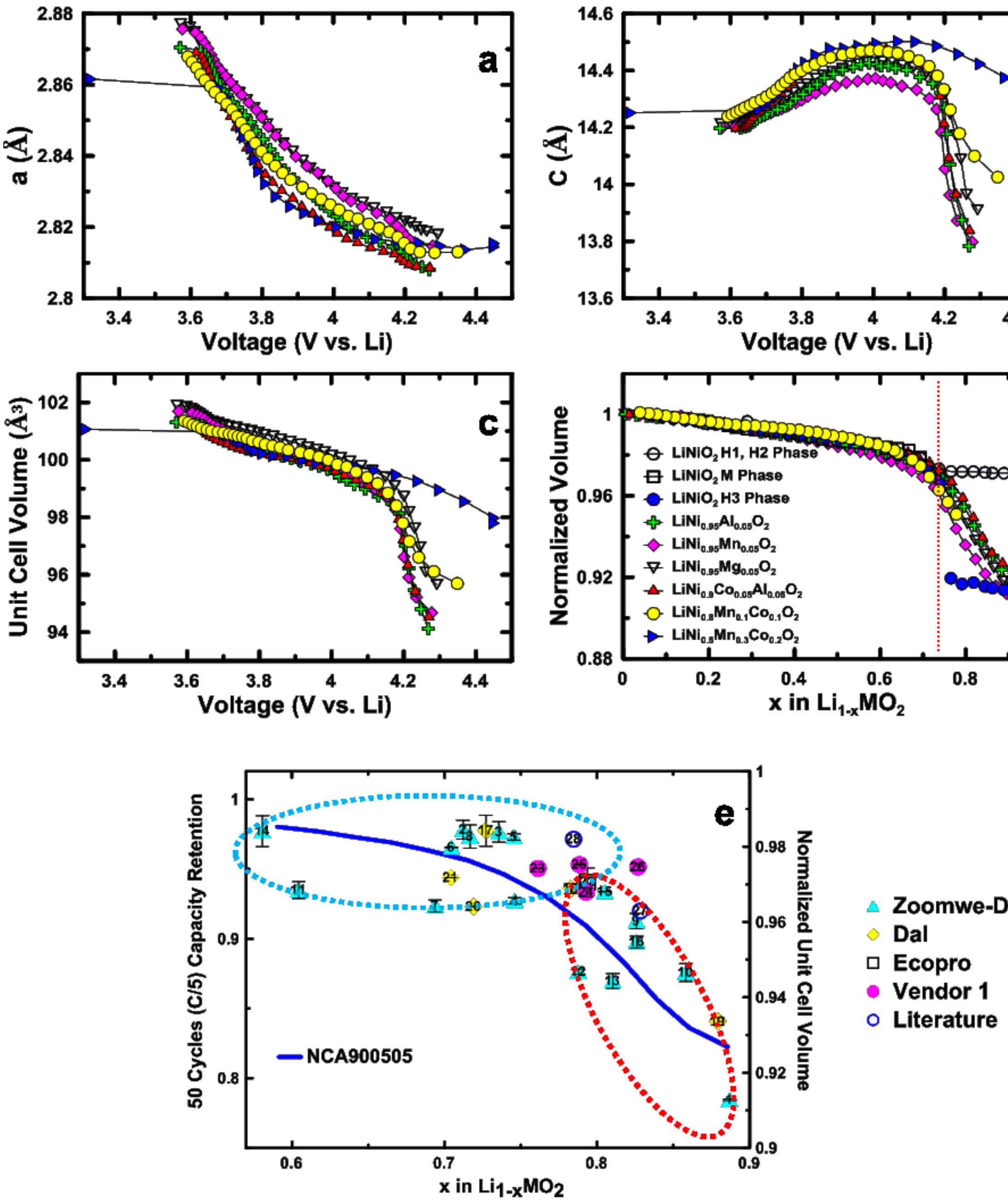

Figure 8.9 a-axis lattice parameter (a), c-axis lattice parameter (b), and unit cell volume (c) as a function of cell voltage for $LiNi_{0.95}Al_{0.05}O_2$, $LiNi_{0.95}Mn_{0.05}O_2$, $LiNi_{0.95}Mg_{0.05}O_2$, $LiNi_{0.9}Co_{0.05}Al_{0.05}O_2$, $LiNi_{0.8}Mn_{0.1}Co_{0.1}O_2$, and $LiNi_{0.5}Mn_{0.3}Co_{0.2}O_2$. Normalized unit cell volume (d) as a function of x in Li_xMO_2. Capacity retention after 50 cycles (C/5) as a function of x in $Li_{1-x}MO_2$ for cells listed in Table 8.1(e) .

It is tempting to speculate that the universal unit cell volume change is the mechanism behind the reduction of capacity retention with delivered capacity. When the cells are cycled with less capacity, the volume change of the unit cell falls into the blue region of Figure 8.5, and relatively good capacity retention can be achieved. Once the capacity delivered by the cathode is higher than a certain value, the red region in Figure 8.5 is entered where much greater anisotropic volume change is inevitably experienced by the electrode materials. Resulting from the more aggressive structural change during each cycle, cathode material degrades faster, and a much steeper capacity retention drop is expected. Figure 8.9e shows an outlier labeled as No.26. Table 8.1 shows that cells No.25 and No.26 were made with polycrystalline (PC) NMC811 electrodes provided by Vendor 1, and it is known by the authors that the PC-NMC811 cathode materials were coated with materials not disclosed by Vendor 1. Besides, cells No.10 made with $LiNi_{0.99}Mg_{0.01}O_2$ surprisingly show that the 1% Mg cation substitution can greatly improve the cycling stability. The role of Mg substitution is still debatable and it has been reported that Mg atoms, at low Mg content tend to stay in the Li layer and act as "pillars" to enhance structural stability.[160,225,251]

Figure 8.9e correlates cathode failure more to the inevitable unit cell volume contraction, but less to the choice of cathode composition. Therefore, an important route for moving to the top right of Figure 8.9e should be enhancing the structural stability of the material. Single crystal cathode materials represent a good approach to enhance particle integrity during cycling,[173] although the single crystal cathode materials in this study do not stand out. It is possible that an appropriate electrolyte system is required for the single crystal cathode to demonstrate its advantages.[174] Gradient core-shell materials as promoted by the research group of Y.K. Sun et al.[166,167] may also represent a path toward the right corner of Figure 8.9e. A surface with a high dopant content changing smoothly to a core of extremely Ni-rich material may be successful. As many efforts are being made to improve the performance of positive electrode materials, it is hoped that Figure 8.9e can help researchers make more sensible evaluations.

8.3 Conclusions

Based on half coin cell cycling of $LiNiO_2$ with different UCVs and LCVs, the H2-H3 phase transition was found to be a major cause of poor capacity retention. With cation substitutions, the derivatives of LNO, including NMC and NCA materials, can avoid this phase transition. However, the single phase unit cell contraction in the same composition range was found to be a universal behavior dependent on delithiation degree. The half coin cell cycling data collected from 26 different sets of cells showed that capacity retention worsens as accessible capacity increases, leading to an inevitable challenge for Ni-rich positive electrode materials. Most of the cells follow the trend in Figure 8.9e regardless of differences in cathode chemical composition, electrolyte, etc. By combining the capacity retention versus delivered capacity curve with the universal unit cell volume change, it is proposed that the anisotropic unit cell volume change is a contributing failure mechanism of Ni-rich positive electrode materials. This work is believed to be of value for researchers working to understand the intrinsic properties of Ni-rich cathode materials, and may help them make further effective improvements.

CHAPTER 9 CONCLUSIONS AND FUTURE WORK

9.1 Conclusions

Ni-rich positive electrode materials are widely used in EVs due to the high energy density and lower price. In this thesis, studies of Ni-rich positive electrode materials covering investigations of fundamental mechanism, synthesis methods, and failure analysis were included. The multiple phase transitions of $LiNiO_2$ and the effect of cation substitutions were systematically studied by in-situ XRD accompanied with other measurements. Single crystal NMC and NCA synthesis studies were conducted to find optimal conditions. With an extensive coin cell data set and in-situ XRD data, a universal failure mechanism for Ni-rich positive electrode materials was proposed.

Chapter 4 presented a study of $LiNiO_2$. The electrochemical and structural properties of Li_xNiO_2 were measured carefully. The multiple phase transitions during charge and discharge were clearly identified and analyzed with Rietveld and Le Bail refinements. A neutron diffraction measurement on distorted monoclinic Li_xNiO_2 showed that an ordering of Li and vacancies in alternating rows may not exist based on the Rietveld refinement results.

Based on the work in Chapter 4 and driven by the need to increase Ni content and eliminate Co, Chapter 5 presented a systematic study on the roles of different cation substituents in a series of $LiNi_{1-n}M_nO_2$ (M = Al, Mn, Mg, or Co) materials. In-situ XRD and dQ/dV vs. V studies showed that the multiple phase transitions in Li_xNiO_2 ($0 \leq x \leq 1$) during charge and discharge, thought to cause poor charge-discharge capacity retention, were suppressed in $Li_xNi_{0.95}M_{0.05}O_2$ (M = Al, Mn, or Mg, $0 \leq x \leq 1$), while 5% Co failed to suppress the phase transitions. Besides, the thermal stability measured by ARC and cycling performance tested with half coin cells showed that 5% Co did not bring any benefits. A mechanism for how substituents function in $LiNiO_2$ was proposed and showed good agreement with the experimental results. It was concluded that Co, commonly believed to be an essential dopant in Ni-rich materials, is actually not required.

Chapter 6 and Chapter 7 presented work on single crystal positive electrode material synthesis. Synthesis conditions for single crystal NMC622 were explored, the corresponding impacts on electrochemical properties were studied, and the advantages of single crystal positive electrode materials were discussed in Chapter 6. Chapter 7 introduced a two-step method for impurity-free single crystal NCA synthesis. Different from single crystal NMC, which is already commercially available, single crystal NCA synthesis is not mature in industry, and Li_5AlO_4 impurity formation is potentially a challenge. This work showed that the two-step synthesis method eliminated the impurity formation. The method can be adopted to synthesize other Al containing single crystal positive electrode materials as well.

Chapter 8 discussed an unavoidable challenge for Ni-rich positive electrode materials. From the work presented in the previous chapters and work beyond this thesis, a large amount of electrochemical and structural data for Ni-rich positive electrode materials having various compositions was collected. It was found that for Ni-rich positive electrode materials derived from LNO, including NMC and NCA materials, multiple phase transitions can be avoided. But similar to the unit cell contraction in the H2-H3 phase transition for LNO, the single phase unit cell contraction for Ni-rich positive electrode materials was found to be a universal behavior dependent on delithiation degree, not material composition. By combining the collected electrochemical data with the universal unit cell volume change, it was proposed that the anisotropic unit cell volume change is a contributing failure mechanism of Ni-rich positive electrode materials.

9.2 Future Work

Many aspects of Ni-rich positive electrode materials, including fundamental studies, novel material synthesis, and failure mechanism analysis, are investigated in this thesis, while many topics are worth further studies.

9.2.1 Studies of the Origin of Phase Transitions in Li_xNiO_2

Neutron diffraction measurements presented in Chapter 4 showed that in the monoclinic phase of Li_xNiO_2, there is no evidence of Li/vacancy ordering in alternative rows, which has been widely considered to be the driver of the hexagonal-monoclinic phase transition.[212,213] The electrochemical features in the dQ/dV vs. V curves of LNO during charge and discharge show a minimum in dQ/dV vs. V, which is a strong signature of a composition where Li atoms are ordered.[216] To figure out the origin of the multiple phase transitions in Li_xNiO_2, nuclear magnetic resonance (NMR), which is sensitive to Li ions and their local structure and dynamics,[252,253] is one method that can be potentially applied to learn about the behavior of Li ions in LNO in the future studies.

Although no super lattice diffraction peaks were found by neutron diffraction in Li_xNiO_2 at various states of charge (SOC), which indicates the absence of long-range ordering of Li atoms, short-range ordering is not ruled out. ^{7}Li has a nuclear spin of 3/2, and is accessible by NMR spectroscopy.[254] K. Märker et al.[255] conducted ex-situ solid-state NMR on NMC811 materials charged to different SOC. At about 75% SOC, it was found that the NMR spectra **cannot** be fit to a simple random solution model, and it was proposed that a Li/vacancy ordering exists at this SOC.[255] However, NMC811 remains a single phase during charge and discharge[256] because the Li ordering believed to be responsible for multiple phase transitions in LNO is disturbed greatly by Mn and Co substitutions. Potentially because of this, the study presented by K. Märker et al. did not show a direct and clear proof of the Li/vacancy ordering. Using the pure un-doped LNO, it is optimistic that ex-situ NMR measurements on LNO materials charged to different SOC can be helpful to study the behavior of Li ions in a better way.

9.2.2 Development of Co-free Single Crystal Positive Electrode Material

Chapter 5 demonstrated that Co is not required in Ni-rich positive electrode materials, Chapter 6 and Chapter 7 presented work on single crystal NMC and NCA synthesis, and Chapter 8 showed that there is an unavoidable challenge of Ni-rich positive electrode materials and single crystal could be a solution. With all the above mentioned work presented in this thesis, Co-free single crystal positive electrode material naturally becomes a promising candidate.

The choices of dopants to be used in LNO should be able to render structural stability, cycling stability, thermal stability, and low cost. Chapter 5 demonstrated experiments which showed that Al and Mg are good choices. Single crystal Al containing material synthesis has an issue of impurity formation, and Chapter 7 showed that the two-step lithiation method can be adopted. Mg is another possible choice and does not have the issue of impurity formation. Besides Mg and Al, some recent works by Y.K Sun's group show that a small amount of W doping is able to improve LNO greatly.[165,257,258]

Both Al and Mg have been shown to have fast inter-diffusion with Ni atoms during heat treatment,[259] and this fast inter-diffusion might make it possible to eliminate the co-precipitation precursor synthesis by using the solid-state synthesis without impairing homogeneous atomic mixing. Using appropriate Ni sources and dopant sources, and the exploration of optimal synthesis conditions is critical in the future studies.

9.2.3 Studies of Surface Modification

Applying coatings onto the surface of positive electrode materials has been used by industry to reduce side reactions between electrolyte and electrodes. However, there is a lack of in-depth understanding of how coating layers function.

Al_2O_3 is one of the most commonly used coating materials, and has been shown to be beneficial for cell performance.[175,176] Although widely used in industry and academia, Al_2O_3 is still mysterious in terms of how it works as a non-Li-ion conductor. The transport of Li ion through the coating layer needs to be understood.

Evaluation of coatings at the lab scale is other important aspect. University research groups are generally not capable of fabricating full pouch cells with synthesized or modified raw materials. This makes it necessary to develop feasible methods to evaluate the effects and quality of coatings. D. Xiong et al. used a "pouch bag" method to study the reactivity between electrodes and electrolyte.[126] This method can be adopted and combined with the pellet coin cell used in ARC measurements. The coated material can be charged to high SOC in pellet cells and recovered, and then sealed with electrolyte in a pouch bag. Further tests like high temperature storage can be performed to study the effects of coatings on reducing side reactions between positive electrodes and electrolyte. Pouch bag gas formation, electrolyte composition changes, and positive electrode material surface and interface evolution can be comprehensively studied by methods like gas chromatography and X-ray photoelectron spectroscopy.

9.2.4 Studies of Post Synthesis Processing

Washing-drying is a widely used post synthesis processing method to remove the surface base content on positive electrode materials in industry. A systematic investigation of how water changes the material and how it recovers by the subsequent drying/heating step is of great value especially for Ni-rich positive electrode materials that are very sensitive to moisture. [106,107]

Chapter 6 and work from literature have shown that washing can result in faster cell degradation in some cases. [111] This is potentially related to the ion exchange that happens to Ni-rich positive electrode materials upon exposure to water. The protons left in materials after ion-exchange could form HF with $LiPF_6$ in the electrolyte, and that is detrimental to cells. Thus the subsequent drying/heating process is critical to recover the washed material. Apart from ion exchange, dissolution of the transition metal ions is another possible ongoing process during water exposure.[260] So it is necessary to figure out how the surface and bulk of Ni-rich positive electrode material change during the washing process, and how to appropriately recover the washed materials with the drying/heating step.

9.2.5 Probe and Quantify Micro Cracks

As discussed in the previous chapters, the degradation of Ni-rich positive electrode materials is widely attributed to micro cracks. Cross-sectional SEM imaging is generally the method used to probe the cracks. However, it is destructive, and the analysis is generally on certain particles and not statistically convincing. To rigorously study the generation of micro cracks and correlate it with material and cell degradation, a more sensible method needs to be developed.

Computed tomography (CT) is a powerful and non-destructive method that can be potentially applied to study the micro cracks. D. P. Finegan et al.[261] performed an in-situ X-ray CT on a 160 mA h Li-ion pouch cell made with $LiCoO_2$ as positive electrode material. It showed that cracked $LiCoO_2$ can be detected when the cell is overcharged. From the CT data, the particle size distribution was extracted and could be correlated to the degree of cracking on a macro-scale instead of particle scale. It would be meaningful to conduct similar measurements on Ni-rich positive electrode materials at a full cell level and find correlations between the cracking and cell degradation.

9.2.6 Development of Ni-free Positive Electrode Materials

Similar to the need for eliminating Co in battery materials, the need for reducing Ni will emerge as more Ni sources get exploited and utilized to make Ni-rich positive electrode materials. Thus, it is reasonable to predict that eliminating or reducing Ni would be another target for positive electrode development in the future.

Li-rich layered oxide positive electrode materials, which are Mn-rich at the same time, are promising candidates as Mn is abundant, cheap, and less toxic. Li-rich layered oxide positive electrode material can be written as $Li[Li_xM_{1-x}]O_2$, and it can also be considered as a solid-solution of monoclinic Li_2MnO_3 and rhombohedral $LiMO_2$ ($(1-y)Li_2MnO_3 \cdot yLiMO_2$). The Li-rich material is able to deliver a reversible specific capacity of 280 mAh/g when the material is “activated” by being charged to high voltage. However, many aspects of Li-rich materials, such as the activation mechanism, voltage decay during cycling, and poor rate capability, still remain unclear and unresolved.[262–264] A systematic study of Li-rich materials, from basics to improvements, is important to undertake.

9.2.7 Studies on Precursor Synthesis with Raman Spectroscopy

Metal hydroxide precursor synthesis has critical effects on the quality of final positive electrode materials. For core-shell material synthesis, a dense shell with desired composition and thickness is important, and this is directly related to the quality of core-shell precursors. Raman spectroscopy is surface sensitive and is able to probe the short-range environment of metal cations. It would be beneficial to apply Raman spectroscopy in the co-precipitation process, and study the growth of the shell in-situ/ex-situ to explore the optimal conditions for shell preparation.

REFERENCES

1. D. Linden and T. B. Reddy, *Handbook of batteries third edition*, p. 35.1-35.94, (2002).

2. C. S. Yoon, D.-W. Jun, S.-T. Myung, and Y.-K. Sun, *ACS Energy Lett.*, **2**, 1150–1155 (2017).

3. M. Guilmard, L. Croguennec, D. Denux, and C. Delmas, *Chem. Mater.*, **15**, 4476–4483 (2003).

4. J. R. Dahn, E. W. Fuller, M. Obrovac, and U. von Sacken, *Solid State Ionics*, **69**, 265–270 (1994).

5. J. Morales, C. Pérez-Vicente, and J. L. Tirado, *J. Therm. Anal.*, **38**, 295–301 (1992).

6. Z. Lu, D. D. MacNeil, and J. R. Dahn, *Electrochem. Solid-State Lett.*, **4**, A200 (2001).

7. Https://electrek.co/2016/11/01/breakdown-raw-materials-tesla-batteries-possible-bottleneck/,.

8. H. Noh, S. Youn, C. Seung, and Y. Sun, *J. Power Sources*, **233**, 121–130 (2013).

9. H. Li, N. Zhang, J. Li, and J. R. Dahn, *J. Electrochem. Soc.*, **165**, A2985–A2993 (2018).

10. S. T. Myung, F. Maglia, K. J. Park, C. S. Yoon, P. Lamp, S. J. Kim, and Y. K. Sun, *ACS Energy Lett.*, **2**, 196–223 (2017).

11. C. Delmas, I. Saadoune, and A. Rougier, *J. Power Sources*, **44**, 595–602 (1993).

12. A. Ueda and T. Ohzuku, *J. Electrochem. Soc.*, **141**, 2010–2014 (1994).

13. J. Li, A. R. Cameron, H. Li, S. Glazier, D. Xiong, M. Chatzidakis, J. Allen, G. A. Botton, and J. R. Dahn, *J. Electrochem. Soc.*, **164**, A1534–A1544 (2017).

14. ISO 12405-1:2011 Electrically propelled road vehicles — Test specification for lithium-ion traction battery packs and systems — Part 1: High-power applications,.

15. D. H. Doughty and C. C. Crafts, *FreedomCAR :electrical energy storage system abuse test manual for electric and hybrid electric vehicle applications.*, Albuquerque, NM, and Livermore, CA (United States), (2006).

16. M. N. Obrovac and V. L. Chevrier, *Chem. Rev.*, **114**, 11444–11502 (2014).

17. Z. Ogumi and M. Inaba, *Bull. Chem. Soc. Jpn.*, **71**, 521–534 (1998).

18. C. Daniel and J. O. Besenhard, *Handbook of Battery Materials: Second Edition*, (2011).

19. K. Xu, *Chem. Rev.*, **104**, 4303–4417 (2004).

20. K. Xu, *Chem. Rev.*, **114**, 11503–11618 (2014).

21. J. B. Goodenough and Y. Kim, *J. Power Sources*, **196**, 6688–6694 (2011).

22. J. B. Goodenough and K. S. Park, *J. Am. Chem. Soc.*, **135**, 1167–1176 (2013).

23. T. Ohzuku and R. J. Brodd, *J. Power Sources*, **174**, 449–456 (2007).

24. F. Ding, W. Xu, X. Chen, J. Zhang, M. H. Engelhard, Y. Zhang, B. R. Johnson, J. V. Crum, T. A. Blake, X. Liu, and J.-G. Zhang, *J. Electrochem. Soc.*, **160**, A1894–A1901 (2013).

25. D. Aurbach, E. Zinigrad, H. Teller, and P. Dan, *J. Electrochem. Soc.*, **147**, 1274 (2002).

26. D. Lin, Y. Liu, and Y. Cui, *Nat. Nanotechnol.*, **12**, 194–206 (2017).

27. Jan N. Reimers and J. R. Dahn, *J. Electrochem. Soc.*, **139** (1992).

28. Z. Chen, Z. Lu, and J. R. Dahn, *J. Electrochem. Soc.*, **149**, A1604 (2002).

29. A. Van der Ven, M. Aydinol, G. Ceder, G. Kresse, and J. Hafner, *Phys. Rev. B - Condens. Matter Mater. Phys.*, **58**, 2975–2987 (1998).

30. A. Van der Ven, M. K. Aydinol, and G. Ceder, *J. Electrochem. Soc.*, **145**, 2149–2155 (1998).

31. R. Weber, C. R. Fell, J. R. Dahn, and S. Hy, *J. Electrochem. Soc.*, **164**, A2992–A2999 (2017).

32. H. Li, M. Cormier, N. Zhang, J. Inglis, J. Li, and J. R. Dahn, *J. Electrochem. Soc.*, **166**, A429–A439 (2019).

33. W. Li, H. Yaghoobnejad Asl, Q. Xie, and A. Manthiram, *J. Am. Chem. Soc.*, **141**,

5097–5101 (2019).

34. D. D. MacNeil, T. D. Hatchard, and J. R. Dahn, *J. Electrochem. Soc.*, **148**, A663–A667 (2001).

35. G. Amatucci and J.-M. Tarascon, *J. Electrochem. Soc.*, **150**, L9 (2003).

36. M. Wohlfahrt-Mehrens, C. Vogler, and J. Garche, in *Journal of Power Sources*,, vol. 127, p. 58–64 (2004).

37. J. Vetter, P. Novák, M. R. Wagner, C. Veit, K.-C. Möller, J. O. Besenhard, M. Winter, M. Wohlfahrt-Mehrens, C. Vogler, and A. Hammouche, *J. Power Sources*, **147**, 269–281 (2005).

38. A. Du Pasquier, A. Blyr, P. Courjal, D. Larcher, G. Amatucci, B. Gérand, and J. Tarascon, *J. Electrochem. Soc.*, **146**, 428–436 (1999).

39. A. Banerjee, Y. Shilina, B. Ziv, J. M. Ziegelbauer, S. Luski, D. Aurbach, and I. C. Halalay, *J. Electrochem. Soc.*, **164**, A6315–A6323 (2017).

40. Https://pulead.diytrade.com/sdp/2189030/4/pd-7066224/12285423-0/Lithium_Iron_Phosphate_LFP__P600A.html,.

41. C. Pillot, *The Rechargeable Battery Market and Main Trends 2016-2025*, (2018).

42. G. Pistoia, *Lithium batteries: New materials, developments and perspectives*, (1994).

43. M. S. Whittingham and R. R. Chianelli, *J. Chem. Educ.*, **57**, 569 (1980).

44. H. Shi, J. Barker, M. Y. Saïdi, R. Koksbang, and L. Morris, *J. Power Sources*, **68**, 291–295 (1997).

45. R. E. Franklin, *Proc. R. Soc. A*, **209**, 196–218 (1951).

46. H. Shi, J. N. Reimers, and J. R. Dahn, *J. Appl. Crystallogr.*, **26**, 827–836 (1993).

47. M. Yoshio, H. Wang, and K. Fukuda, *Angew. Chemie - Int. Ed.*, **42**, 4203–4206 (2003).

48. Y.-S. Park, T.-W. Lee, M.-S. Shin, S.-H. Lim, and S.-M. Lee, *J. Electrochem. Soc.*, **163**, A3078–A3086 (2016).

49. M. Yoshio, H. Wang, K. Fukuda, Y. Hara, and Y. Adachi, *J. Electrochem. Soc.*, **147**,

1245 (2002).

50. H. Nakamura, H. Komatsu, and M. Yoshio, *J. Power Sources*, **62**, 219–222 (1996).

51. D. W. Murphy, R. J. Cava, S. M. Zahurak, and A. Santoro, *Solid State Ionics*, **9–10**, 413–417 (1983).

52. K. M. Colbow, J. R. Dahn, and R. R. Haering, *J. Power Sources*, **26**, 397–402 (1989).

53. T. Ohzuku, *J. Electrochem. Soc.*, **142**, 1431 (1995).

54. R. Weber, A. J. Louli, K. P. Plucknett, and J. R. Dahn, *J. Electrochem. Soc.*, **166**, A1779–A1784 (2019).

55. J. Bareño, I. A. Shkrob, J. A. Gilbert, M. Klett, and D. P. Abraham, *J. Phys. Chem. C*, **121**, 20640–20649 (2017).

56. R. Weber, M. Genovese, A. J. Louli, S. Hames, C. Martin, I. G. Hill, and J. R. Dahn, *Nat. Energy*, **4**, 683–689 (2019).

57. N. Nitta, F. Wu, J. T. Lee, G. Yushin, X.-B. Cheng, R. Zhang, C.-Z. Zhao, F. Wei, J. J.-G. G. Zhang, Q. Zhang, Z. Li, J. Huang, B. Yann Liaw, V. Metzler, J. J.-G. G. Zhang, E. C. Evarts, J. Song, E. Sahadeo, M. Noked, et al., *J. Electrochem. Soc.*, **3**, 7207–7209 (2015).

58. J. Qian, B. D. Adams, J. Zheng, W. Xu, W. A. Henderson, J. Wang, M. E. Bowden, S. Xu, J. Hu, and J. G. Zhang, *Adv. Funct. Mater.*, **26**, 7094–7102 (2016).

59. T. T. Hagos, B. Thirumalraj, C. J. Huang, L. H. Abrha, T. M. Hagos, G. B. Berhe, H. K. Bezabh, J. Cherng, S. F. Chiu, W. N. Su, and B. J. Hwang, *ACS Appl. Mater. Interfaces*, **11**, 9955–9963 (2019).

60. M. S. Ding, K. Xu, S. S. Zhang, K. Amine, G. L. Henriksen, and T. R. Jow, *J. Electrochem. Soc.*, **148**, A1196 (2002).

61. K. Takata, *J. Electrochem. Soc.*, **132**, 126 (2006).

62. K. Xu, S. Zhang, T. R. Jow, W. Xu, and C. A. Angell, *Electrochem. Solid-State Lett.*, **5**, A26 (2002).

63. S. Shui Zhang, *Electrochem. commun.*, **8**, 1423–1428 (2006).

64. G. G. Eshetu, S. Grugeon, G. Gachot, D. Mathiron, M. Armand, and S. Laruelle, *Electrochim. Acta*, **102**, 133–141 (2013).

65. H. B. Han, S. S. Zhou, D. J. Zhang, S. W. Feng, L. F. Li, K. Liu, W. F. Feng, J. Nie, H. Li, X. J. Huang, M. Armand, and Z. Bin Zhou, *J. Power Sources*, **196**, 3623–3632 (2011).

66. A. Abouimrane, J. Ding, and I. J. Davidson, *J. Power Sources*, **189**, 693–696 (2009).

67. J. L. Nowinski, P. Lightfoot, and P. G. Bruce, *J. Mater. Chem.*, **4**, 1579 (2004).

68. M. Ue, A. Murakami, and S. Nakamura, *J. Electrochem. Soc.*, **149**, A1572 (2002).

69. M. Ue, *J. Electrochem. Soc.*, **144**, 2684 (2006).

70. Z.-B. Zhou, M. Takeda, T. Fujii, and M. Ue, *J. Electrochem. Soc.*, **152**, A351 (2005).

71. Z. Chen, J. Liu, K. A.-E. and solid-state Letters, and U. 2007, *Electrochem. Solid-State Lett.*, **10**, A45–A47 (2001).

72. D. P. Abraham, M. M. Furczon, S. H. Kang, D. W. Dees, and A. N. Jansen, *J. Power Sources*, **180**, 612–620 (2008).

73. I. A. Shkrob, Y. Zhu, T. W. Marin, and D. P. Abraham, *J. Phys. Chem. C*, **117**, 23750–23756 (2013).

74. D. Xiong, J. C. Burns, A. J. Smith, N. Sinha, and J. R. Dahn, *J. Electrochem. Soc.*, **158**, A1431 (2011).

75. H. Yamane, T. Inoue, M. Fujita, and M. Sano, *J. Power Sources*, **99**, 60–65 (2001).

76. L. Ma, L. Ellis, S. L. Glazier, X. Ma, Q. Liu, J. Li, and J. R. Dahn, *J. Electrochem. Soc.*, **165**, 891–899 (2018).

77. L. Ma, L. Ellis, S. L. Glazier, X. Ma, and J. R. Dahn, *J. Electrochem. Soc.*, **165**, 1718–1724 (2018).

78. D. Aurbach, K. Gamolsky, B. Markovsky, Y. Gofer, M. Schmidt, and U. Heider, *Electrochim. Acta*, **47**, 1423–1439 (2002).

79. A. L. Michan, B. S. Parimalam, M. Leskes, R. N. Kerber, T. Yoon, C. P. Grey, and B. L. Lucht, *Chem. Mater.*, **28**, 8149–8159 (2016).

80. C. C. Nguyen and B. L. Lucht, *J. Electrochem. Soc.*, **161**, A1933–A1938 (2014).

81. H. J. Noh, S. Youn, C. S. Yoon, and Y. K. Sun, *J. Power Sources*, **233**, 121–130 (2013).

82. J. Zheng, Y. Ye, T. Liu, Y. Xiao, C. Wang, F. Wang, and F. Pan, *Acc. Chem. Res.* (2019).

83. N. A. Chernova, M. Ma, J. Xiao, M. S. Whittingham, J. Breger, and C. P. Grey, *Chem. Mater.*, **19**, 4682–4693 (2007).

84. H. Arai, S. Okada, H. Ohtsuka, M. Ichimura, and J. Yamaki, *Solid State Ionics*, **80**, 261–269 (1995).

85. J. Morales, C. Pérez-Vicente, and J. L. Tirado, *Mater. Res. Bull.*, **25**, 623–630 (1990).

86. M. Bianchini, M. Roca-Ayats, P. Hartmann, T. Brezesinski, and J. Janek, *Angew. Chemie - Int. Ed.* (2019).

87. R. D. Shannon, *Acta Crystallogr. Sect. A*, **32**, 751–767 (1976).

88. A. Rougier, I. Saadoune, P. Gravereau, P. Willmann, and C. Delmas, *Solid State Ionics*, **90**, 83–90 (1996).

89. J. B. Goodenough, D. G. Wickham, and W. J. Croft, *J. Phys. Chem. Solids*, **5**, 107–116 (1958).

90. V. Berbenni, V. Massarotti, D. Capsoni, R. Riccardi, A. Marini, and E. Antolini, *Solid State Ionics*, **48**, 101–111 (1991).

91. J. Li, N. Zhang, H. Li, A. Liu, Y. Wang, S. Yin, H. Wu, and J. R. Dahn, *J. Electrochem. Soc.*, **165**, A3544–A3557 (2018).

92. N. Zhang, J. Li, H. Li, A. Liu, Q. Huang, L. Ma, Y. Li, and J. R. Dahn, *Chem. Mater.*, **30**, 8852–8860 (2018).

93. M. D. Radin, S. Hy, M. Sina, C. Fang, H. Liu, J. Vinckeviciute, M. Zhang, M. S. Whittingham, Y. S. Meng, and A. Van der Ven, *Adv. Energy Mater.*, **7**, 1–33 (2017).

94. W. R. McKinnon, in *Solid state electrochemistry*, (2009).

95. D. D. MacNeil, Z. Lu, and J. R. Dahn, *J. Electrochem. Soc.*, **149**, A1332–A1336

(2002).

96. G. Cherkashinin, M. Motzko, N. Schulz, T. Späth, and W. Jaegermann, *Chem. Mater.*, **27**, 2875–2887 (2015).

97. A. Deb, U. Bergmann, S. P. Cramer, and E. J. Cairns, *J. Appl. Phys.*, **97**, 113523 (2005).

98. H. A. JAHN and E. TELLER, in *Applied Group Theory*, (1968).

99. M. E. Arroyo y de Dompablo and G. Ceder, *Chem. Mater.*, **15**, 63–67 (2003).

100. M. E. Arroyo y de Dompablo and G. Ceder, *J. Power Sources*, **119**, 654–657 (2003).

101. F. Lin, Y. Liu, X. Yu, L. Cheng, A. Singer, O. G. Shpyrko, H. L. Xin, N. Tamura, C. Tian, T. C. Weng, X. Q. Yang, Y. S. Meng, D. Nordlund, W. Yang, and M. M. Doeff, *Chem. Rev.*, **117**, 13123–13186 (2017).

102. B. J. Hwang, Y. W. Tsai, D. Carlier, and G. Ceder, *Chem. Mater.*, **15**, 3676–3682 (2003).

103. C. Delmas, M. Ménétrier, L. Croguennec, I. Saadoune, A. Rougier, C. Pouillerie, G. Prado, M. Grüne, and L. Fournès, *Electrochim. Acta*, **45**, 243–253 (1999).

104. J. Paulsen and J. Kim, US 0054495 A1 (2014).

105. N. V. Faenza, L. Bruce, Z. W. Lebens-Higgins, I. Plitz, N. Pereira, L. F. J. Piper, and G. G. Amatucci, *J. Electrochem. Soc.*, **164**, A3727–A3741 (2017).

106. J. Sicklinger, M. Metzger, H. Beyer, D. Pritzl, and H. A. Gasteiger, *J. Electrochem. Soc.*, **166**, A2322–A2335 (2019).

107. R. Jung, R. Morasch, P. Karayaylali, K. Phillips, F. Maglia, C. Stinner, Y. Shao-Horn, and H. A. Gasteiger, *J. Electrochem. Soc.*, **165**, A132–A141 (2018).

108. R. Robert, C. Bunzli, E. J. Berg, and P. Novák, *Chem. Mater.*, **27**, 526–536 (2015).

109. Y. Kim, *J. Mater. Sci.*, **48**, 8547–8551 (2013).

110. Y. Bassi, A.S., Zhu, J.X., Lan, Q., Margaritis, A., Zheng, US 9.202,945 B2.

111. X. Xiong, Z. Wang, P. Yue, H. Guo, F. Wu, J. Wang, and X. Li, *J. Power Sources*, **222**, 318–325 (2013).

112. F. Kong, C. Liang, L. Wang, Y. Zheng, S. Perananthan, R. C. Longo, J. P. Ferraris, M. Kim, and K. Cho, *Adv. Energy Mater.* (2019).

113. F. Lin, I. M. Markus, D. Nordlund, T.-C. Weng, M. D. Asta, H. L. Xin, and M. M. Doeff, *Nat. Commun.*, **5**, 3529 (2014).

114. K. W. Nam, S. M. Bak, E. Hu, X. Yu, Y. Zhou, X. Wang, L. Wu, Y. Zhu, K. Y. Chung, and X. Q. Yang, *Adv. Funct. Mater.*, **23**, 1047–1063 (2013).

115. S. Hwang, W. Chang, S. M. Kim, D. Su, D. H. Kim, J. Y. Lee, K. Y. Chung, and E. A. Stach, *Chem. Mater.*, **26**, 1084–1092 (2014).

116. S. Hwang, S. M. Kim, S. M. Bak, K. Y. Chung, and W. Chang, *Chem. Mater.*, **27**, 6044–6052 (2015).

117. S. M. Bak, K. W. Nam, W. Chang, X. Yu, E. Hu, S. Hwang, E. A. Stach, K. B. Kim, K. Y. Chung, and X. Q. Yang, *Chem. Mater.* (2013).

118. Y. Wang, J. Jiang, and J. R. Dahn, *Electrochem. commun.*, **9**, 2534–2540 (2007).

119. I. Belharouak, W. Lu, D. Vissers, and K. Amine, *Electrochem. commun.* (2006).

120. Z. Wang, X. Huang, and L. Chen, *J. Electrochem. Soc.*, **151**, A1641–A1652 (2004).

121. Z. Wang, X. Huang, and L. Chen, *J. Electrochem. Soc.*, **150**, A199–A208 (2003).

122. D. Aurbach, B. Markovsky, G. Salitra, E. Markevich, Y. Talyossef, M. Koltypin, L. Nazar, B. Ellis, and D. Kovacheva, *J. Power Sources* (2007).

123. A. J. Smith, J. C. Burns, X. Zhao, D. Xiong, and J. R. Dahn, *J. Electrochem. Soc.*, **158**, S23 (2011).

124. A. J. Smith, J. C. Burns, S. Trussler, and J. R. Dahn, *J. Electrochem. Soc.*, **157**, A196 (2010).

125. A. J. Smith, J. C. Burns, D. Xiong, and J. R. Dahn, *J. Electrochem. Soc.*, **158**, A1136 (2011).

126. D. J. Xiong, L. D. Ellis, K. J. Nelson, T. Hynes, R. Petibon, and J. R. Dahn, *J. Electrochem. Soc.*, **163**, A3069–A3077 (2016).

127. D. J. Xiong, L. D. Ellis, R. Petibon, T. Hynes, Q. Q. Liu, and J. R. Dahn, *J.*

Electrochem. Soc., **164**, A340–A347 (2017).

128. J.-H. Kim, S. J. Kim, T. Yuk, J. Kim, C. S. Yoon, and Y.-K. Sun, *ACS Energy Lett.*, 3002–3007 (2018).

129. C. S. Yoon, H. H. Ryu, G. T. Park, J. H. Kim, K. H. Kim, and Y. K. Sun, *J. Mater. Chem. A*, **6**, 4126–4132 (2018).

130. H.-H. Ryu, K.-J. Park, C. S. Yoon, and Y.-K. Sun, *Chem. Mater.*, **30**, 1155–1163 (2018).

131. S. Muto, Y. Sasano, K. Tatsumi, T. Sasaki, K. Horibuchi, Y. Takeuchi, and Y. Ukyo, *J. Electrochem. Soc.*, **156**, A371 (2009).

132. Y. Makimura, S. Zheng, Y. Ikuhara, and Y. Ukyo, *J. Electrochem. Soc.*, **159**, A1070–A1073 (2012).

133. H. Zhang, F. Omenya, P. Yan, L. Luo, M. S. Whittingham, C. Wang, and G. Zhou, *ACS Energy Lett.*, **2**, 2607–2615 (2017).

134. H. Liu, M. Wolf, K. Karki, Y. S. Yu, E. A. Stach, J. Cabana, K. W. Chapman, and P. J. Chupas, *Nano Lett.*, **17**, 3452–3457 (2017).

135. H. H. Ryu, K. J. Park, C. S. Yoon, and Y. K. Sun, *Chem. Mater.*, **30**, 1155–1163 (2018).

136. D. D. MacNeil, D. Larcher, and J. R. Dahn, *J. Electrochem. Soc.*, **146**, 3596–3602 (1999).

137. D. D. MacNeil, Z. Lu, Z. Chen, and J. R. Dahn, *J. Power Sources*, **108**, 8–14 (2002).

138. A. W. Golubkov, S. Scheikl, R. Planteu, G. Voitic, H. Wiltsche, C. Stangl, G. Fauler, A. Thaler, and V. Hacker, *RSC Adv.*, **5**, 57171–57186 (2015).

139. A. Mauger and C. M. Julien, *Ionics (Kiel).*, **23**, 1933–1947 (2017).

140. K. Liu, Y. Liu, D. Lin, A. Pei, and Y. Cui, *Sci. Adv.*, **4**, eaas9820(1-11) (2018).

141. D. Ren, X. Liu, X. Feng, L. Lu, M. Ouyang, J. Li, and X. He, *Appl. Energy*, **228**, 633–644 (2018).

142. J. Xu, F. Lin, M. M. Doeff, and W. Tong, *J. Mater. Chem. A*, **5**, 874–901 (2017).

143. S. T. Myung, F. Maglia, K. J. Park, C. S. Yoon, P. Lamp, S. J. Kim, and Y. K. Sun, *ACS Energy Lett.*, **2**, 196–223 (2017).

144. J. R. Dahn, E. W. Fuller, M. Obrovac, and U. von Sacken, *Solid State Ionics*, **69**, 265–270 (1994).

145. M. Guilmard, L. Croguennec, and C. Delmas, *Chem. Mater.*, **15**, 4484–4493 (2003).

146. X. Yu, E. Hu, S. M. Bak, Y. N. Zhou, and X. Q. Yang, *Chinese Phys. B*, **25**, 018205(1–10) (2016).

147. Y. K. Sun, D. J. Lee, Y. J. Lee, Z. Chen, and S. T. Myung, *ACS Appl. Mater. Interfaces*, **5**, 11434–11440 (2013).

148. H. Konishi, M. Yoshikawa, T. Hirano, and K. Hidaka, *J. Power Sources*, **254**, 338–344 (2014).

149. S. M. Bak, E. Hu, Y. N. Zhou, X. Yu, S. D. Senanayake, S. J. Cho, K. B. Kim, K. Y. Chung, X. Q. Yang, and K. W. Nam, *ACS Appl. Mater. Interfaces*, **6**, 22594–22601 (2014).

150. C. Tian, F. Lin, and M. M. Doeff, *Acc. Chem. Res.*, **51**, 89–96 (2018).

151. S. M. Bak, K. W. Nam, W. Y. Chang, X. Yu, E. Hu, S. Y. Hwang, E. A. Stach, K. B. Kim, K. Y. Chung, and X. Q. Yang, *Chem. Mater.*, **25**, 337–351 (2013).

152. A. Benmayza, W. Lu, V. Ramani, and J. Prakash, *Electrochim. Acta*, **123**, 7–13 (2014).

153. H. Arai, S. Okada, Y. Sakurai, and J. Yamaki, *J. Electrochem. Soc.* , **144**, 3117–3125 (1997).

154. T. Ohzuku, A. Ueda, and M. Kouguchi, *J. Electrochem. Soc.*, **142**, 4033–4039 (1995).

155. M. Guilmard, A. Rougier, M. Grüne, L. Croguennec, and C. Delmas, *J. Power Sources*, **115**, 305–314 (2003).

156. U.-H. Kim, L.-Y. Kuo, P. Kaghazchi, C. S. Yoon, and Y.-K. Sun, *ACS Energy Lett.*, **4**, 576–582 (2019).

157. H. Kondo, Y. Takeuchi, T. Sasaki, S. Kawauchi, Y. Itou, O. Hiruta, C. Okuda, M. Yonemura, T. Kamiyama, and Y. Ukyo, *J. Power Sources*, **174**, 1131–1136 (2007).

158. S. Muto, K. Tatsumi, Y. Kojima, H. Oka, H. Kondo, K. Horibuchi, and Y. Ukyo, *J. Power Sources*, **205**, 449–455 (2012).

159. C. Pouillerie, F. Perton, P. Biensan, J. P. Pérès, M. Broussely, and C. Delmas, *J. Power Sources*, **96**, 293–302 (2001).

160. Q. Xie, W. Li, and A. Manthiram, *Chem. Mater.*, **31**, 938–946 (2019).

161. K. J. Park, H. G. Jung, L. Y. Kuo, P. Kaghazchi, C. S. Yoon, and Y. K. Sun, *Adv. Energy Mater.*, **8** (2018).

162. J. N. Reimers, E. Rossen, C. D. Jones, and J. R. Dahn, *Solid State Ionics*, **61**, 335–344 (1993).

163. M. Y. Song, S. N. Kwon, S. Do Yoon, and D. R. Mumm, *J. Appl. Electrochem.*, **39**, 807–814 (2009).

164. J. R. Mueller-Neuhaus, R. A. Dunlap, and J. R. Dahn, *J. Electrochem. Soc.*, **147**, 3598–3605 (2000).

165. U. H. Kim, D. W. Jun, K. J. Park, Q. Zhang, P. Kaghazchi, D. Aurbach, D. T. Major, G. Goobes, M. Dixit, N. Leifer, C. M. Wang, P. Yan, D. Ahn, K. H. Kim, C. S. Yoon, and Y. K. Sun, *Energy Environ. Sci.*, **11**, 1271–1279 (2018).

166. Y. K. Sun, S. T. Myung, B. C. Park, J. Prakash, I. Belharouak, and K. Amine, *Nat. Mater.*, **8**, 320–324 (2009).

167. S. T. Myung, H. J. Noh, S. J. Yoon, E. J. Lee, and Y. K. Sun, *J. Phys. Chem. Lett.*, **5**, 671–679 (2014).

168. J. K. Noh, S. Kim, H. Kim, W. Choi, W. Chang, D. Byun, B. W. Cho, and K. Y. Chung, *Sci. Rep.*, **4** (2014).

169. Y. K. Sun, S. T. Myung, M. H. Kim, J. Prakash, and K. Amine, *J. Am. Chem. Soc.*, **127**, 13411–13418 (2005).

170. J. Li, J. Camardese, R. Shunmugasundaram, S. Glazier, Z. Lu, and J. R. Dahn, *Chem.*

Mater., **27**, 3366–3377 (2015).

171. J. Camardese, J. Li, D. W. Abarbanel, A. T. B. Wright, and J. R. Dahn, *J. Electrochem. Soc.*, **162**, A269–A277 (2015).

172. C. S. Yoon, K. J. Park, U. H. Kim, K. H. Kang, H. H. Ryu, and Y. K. Sun, *Chem. Mater.*, **29**, 10436–10445 (2017).

173. J. Kim, H. Lee, H. Cha, M. Yoon, M. Park, and J. Cho, *Adv. Energy Mater.*, **1702028**, 1–25 (2017).

174. J. Li, A. R. Cameron, H. Li, S. Glazier, D. Xiong, M. Chatzidakis, J. Allen, G. A. Botton, and J. R. Dahn, *J. Electrochem. Soc.*, **164**, 1534–1544 (2017).

175. R. S. Arumugam, L. Ma, J. Li, X. Xia, J. M. Paulsen, and J. R. Dahn, *J. Electrochem. Soc.*, **163**, A2531–A2538 (2016).

176. D. S. Hall, R. Gauthier, A. Eldesoky, V. S. Murray, and J. R. Dahn, *ACS Appl. Mater. Interfaces*, **11**, 14095–14100 (2019).

177. D. Mohanty, K. Dahlberg, D. M. King, L. A. David, A. S. Sefat, D. L. Wood, C. Daniel, S. Dhar, V. Mahajan, M. Lee, and F. Albano, *Sci. Rep.*, **6**, 26532 (2016).

178. L. Zheng, C. Wei, M. D. L. Garayt, J. MacInnis, and M. N. Obrovac, *J. Electrochem. Soc.*, **166**, A2924–A2927 (2019).

179. L. Zheng, T. D. Hatchard, and M. N. Obrovac, *MRS Commun.*, **9**, 245–250 (2019).

180. H. Kim, M. G. Kim, H. Y. Jeong, H. Nam, and J. Cho, *Nano Lett.*, **15**, 2111–2119 (2015).

181. K. Min, C. Jung, D. S. Ko, K. Kim, J. Jang, K. Park, and E. Cho, *ACS Appl. Mater. Interfaces*, **10**, 20599–20610 (2018).

182. F. Zhou, X. Zhao, A. Van Bommel, A. W. Rowe, and J. R. Dahn, *Chem. Mater.*, **22**, 1015–1021 (2010).

183. A. Van Bommel and J. R. Dahn, *Chem. Mater.*, **21**, 1500–1503 (2009).

184. A. van Bommel and J. R. Dahn, *J. Electrochem. Soc.*, **156**, A362 (2009).

185. X. Luo, X. Wang, L. Liao, S. Gamboa, and P. J. Sebastian, *J. Power Sources*, **158**,

654–658 (2006).

186. K. S. Lee, S. T. Myung, J. S. Moon, and Y. K. Sun, *Electrochim. Acta*, **53**, 6033–6037 (2008).

187. A. Liu, N. Zhang, J. Li, T. Casagrande, C. Butcher, J. Martinez, A. Korinek, G. Botton, and J. R. Dahn, *J. Electrochem. Soc.*, **165**, A2781–A2791 (2018).

188. K. He, Z. Ruan, X. Teng, and Y. Zhu, *Mater. Res. Bull.*, **90**, 131–137 (2017).

189. J. Duan, C. Wu, Y. Cao, D. Huang, K. Du, Z. Peng, and G. Hu, *J. Alloys Compd.*, **695**, 91–99 (2017).

190. S. Yoon, C. W. Lee, Y. S. Bae, I. Hwang, Y.-K. Park, and J. H. Song, *Electrochem. Solid-State Lett.*, **12**, A211 (2009).

191. B. D. Cullity and S. R. Stock, *Prentice Hall* (2001).

192. C. J. H. B.A. Hunter, *Australian Nuclear Science and Technology of X-Ray and Neutron*, (1998).

193. F. H. Chung and D. K. Smith, *Industrial applications of x-ray diffraction*, (1999).

194. W. Zhou and Z. L. Wang, *Scanning microscopy for nanotechnology: Techniques and applications*, (2007).

195. P. Echlin, *Handbook of Sample Preparation for Scanning Electron Microscopy and X-Ray Microanalysis*, (2009).

196. R. F. Egerton, *Physical Principles of Electron Microscopy*, (2005).

197. T. Maitland and S. Sitzman, in *Scanning Microscopy for Nanotechnology*,, p. 41–75, Springer New York, New York, NY (2006).

198. H. K. Livingston, *J. Am. Chem. Soc.*, **66**, 569–573 (1944).

199. S. Brunauer, J. Skalny, and E. E. Bodor, *J. Colloid Interface Sci.*, **30**, 546–552 (1969).

200. G. Fagerlund, *Matériaux Constr.*, **6**, 239–245 (1973).

201. ISO [International Organization for Standardization], *Ref. number ISO*, **9277**, 30 pp. (2010).

202. K. Shizuka and K. Okahara, US8354191B2 (2013).

203. M. N. Richard and J. R. Dahn, *J. Electrochem. Soc.*, **146**, 2068–2077 (1999).

204. M. N. Richard and J. R. Dahn, *J. Electrochem. Soc.*, **146**, 2078 (1999).

205. D. D. MacNeil and J. R. Dahn, *J. Electrochem. Soc.*, **148**, A1205 (2001).

206. Y. Kobayashi, M. Tabuchi, H. Miyashiro, and N. Kuriyama, *J. Power Sources*, **364**, 156–162 (2017).

207. K. K. Lee, W. S. Yoon, K. B. Kim, K. Y. Lee, and S. T. Hong, *J. Power Sources*, **97**–**98**, 308–312 (2001).

208. A. Ueda and T. Ohzuku, *J. Electrochem. Soc.*, **141**, 2972 (1994).

209. W. Li, J. Reimers, and J. Dahn, *Solid State Ionics*, **67**, 123–130 (1993).

210. T. Ohzuku, A. Ueda, and M. Nagayama, *J. Electrochem. Soc.*, **140**, 1862 (1993).

211. E. McCalla, G. H. Carey, and J. R. Dahn, *Solid State Ionics*, **219**, 11–19 (2012).

212. C. Delmas, J. P. Pérès, A. Rougier, A. Demourgues, F. Weill, A. Chadwick, M. Broussely, F. Perton, P. Biensan, and P. Willmann, *J. Power Sources*, **68**, 120–125 (1997).

213. J. P. Peres, F. Weill, and C. Delmas, *Solid State Ionics*, **116**, 19–27 (1999).

214. J. Li, L. E. Downie, L. Ma, W. Qiu, and J. R. Dahn, *J. Electrochem. Soc.*, **162**, A1401–A1408 (2015).

215. M. Winter, *J. Electrochem. Soc.*, **145**, 428 (1998).

216. A. J. Berlinsky, W. G. Unruh, W. R. McKinnon, and R. R. Haering, *Solid State Commun.*, **31**, 135–138 (1979).

217. T. Morita, *Phys. A Stat. Mech. its Appl.*, **133**, 173–186 (1985).

218. A. Van Der Ven, J. C. Thomas, Q. Xu, B. Swoboda, and D. Morgan, *Phys. Rev. B - Condens. Matter Mater. Phys.*, **78**, 1–12 (2008).

219. A. Rougier, P. Gravereau, and C. Delmas, *J. Electrochem. Soc.*, **143**, 1168–1175 (1996).

220. J. Li, J. Harlow, N. Stakheiko, N. Zhang, J. Paulsen, and J. Dahn, *J. Electrochem. Soc.*, **165**, A2682–A2695 (2018).

221. E. H. Kisi and C. J. Howard, *Applications of Neutron Powder Diffraction*, (2009).

222. V. F. Sears, *Neutron News*, **3**, 26–37 (1992).

223. Y. Shao-Horn, S. Levasseur, F. Weill, and C. Delmas, *J. Electrochem. Soc.*, **150**, A366–A373 (2003).

224. E. Rossen, C. D. W. Jones, and J. R. Dahn, *Solid State Ionics*, **57**, 311–318 (1992).

225. C. C. Chang, J. Y. Kim, and P. N. Kumta, *J. Electrochem. Soc.*, **147**, 1722–1729 (2000).

226. and J. R. D. Jing Li, Ning Zhang, Hongyang Li, Aaron Liu, Yiqiao Wang, Shuo Yin, Haohan Wu, *J. Electrochem. Soc. 2018*.

227. M. Sathiya, G. Rousse, K. Ramesha, C. P. Laisa, H. Vezin, M. T. Sougrati, M. L. Doublet, D. Foix, D. Gonbeau, W. Walker, A. S. Prakash, M. Ben Hassine, L. Dupont, and J. M. Tarascon, *Nat. Mater.*, **12**, 827–835 (2013).

228. T. Kimijima, N. Zettsu, K. Yubuta, K. Hirata, K. Kami, and K. Teshima, *J. Mater. Chem. A*, **4**, 7289–7296 (2016).

229. Y. Kim, *ACS Appl. Mater. Interfaces*, **4**, 2329–2333 (2012).

230. J. Li, H. Li, W. Stone, R. Weber, S. Hy, and J. R. Dahn, *J. Electrochem. Soc.*, **164**, A3529–A3537 (2017).

231. L. Wang, B. Wu, D. Mu, X. Liu, Y. Peng, H. Xu, Q. Liu, L. Gai, and F. Wu, *J. Alloys Compd.*, **674**, 360–367 (2016).

232. H. Li, J. Li, X. Ma, and J. R. Dahn, *J. Electrochem. Soc.*, **165**, 1038–1045 (2018).

233. Z. Chen and J. R. Dahn, *Electrochim. Acta*, **49**, 1079–1090 (2004).

234. S. R. Culity, B.D. and Stock, *Elements of X-ray Diffraction*, 3 edition., Pearson, (2010).

235. J. Li, J. Camardese, S. Glazier, and J. R. Dahn, *Chem. Mater.*, **26**, 7059–7066 (2014).

236. E. Mccalla, A. W. Rowe, R. Shunmugasundaram, and J. R. Dahn, *Chem. Mater.*, **25**,

989–999 (2013).

237. M. S. Whittingham and W. M. S., *Chem. Rev.*, **104**, 4271–4301 (2004).

238. J. Kim, Y. Hong, K. S. Ryu, M. G. Kim, and J. Cho, *Electrochem. Solid-State Lett.*, **9**, A19 (2006).

239. B. Xiao and X. Sun, *Adv. Energy Mater.*, **8** (2018).

240. J. E. Harlow, X. Ma, J. Li, E. Logan, Y. Liu, N. Zhang, L. Ma, S. L. Glazier, M. M. E. Cormier, M. Genovese, S. Buteau, A. Cameron, J. E. Stark, and J. R. Dahn, *J. Electrochem. Soc.*, **166**, A3031–A3044 (2019).

241. Y. Liu, J. Harlow, and J. Dahn, *J. Electrochem. Soc.*, #JESP-19-3955.

242. S. Watanabe, M. Kinoshita, T. Hosokawa, K. Morigaki, and K. Nakura, *J. Power Sources*, **258**, 210–217 (2014).

243. H. Li, J. Li, N. Zaker, N. Zhang, G. A. Botton, and J. R. Dahn, *J. Electrochem. Soc.*, **166**, A1956–A1963 (2019).

244. J. Li, H. Li, W. Stone, S. Glazier, and J. R. Dahn, *J. Electrochem. Soc.*, **165**, A626–A635 (2018).

245. R. Jung, P. Strobl, F. Maglia, C. Stinner, and H. A. Gasteiger, *J. Electrochem. Soc.*, **165**, A2869–A2879 (2018).

246. H. Li, A. Liu, N. Zhang, Y. Wang, S. Yin, H. Wu, and J. R. Dahn, *Chem. Mater.*, **31**, 7574−7583 (2019).

247. J. H. Kim, K. J. Park, S. J. Kim, C. S. Yoon, and Y. K. Sun, *J. Mater. Chem. A*, **7**, 2694–2701 (2019).

248. H. H. Ryu, G. T. Park, C. S. Yoon, and Y. K. Sun, *Small*, **14** (2018).

249. R. Jung, M. Metzger, F. Maglia, C. Stinner, and H. A. Gasteiger, *J. Electrochem. Soc.*, **164**, A1361–A1377 (2017).

250. J. Li, L. E. Downie, L. Ma, W. Qiu, and J. R. Dahn, *J. Electrochem. Soc.*, **162**, A1401–A1408 (2015).

251. C. Pouillerie, L. Croguennec, P. Biensan, P. Willmann, and C. Delmas, *J.*

Electrochem. Soc., **147**, 2061–2069 (2000).

252. O. Pecher, J. Carretero-Gonzalez, K. J. Griffith, and C. P. Grey, *Chem. Mater.*, **29**, 213–242 (2017).

253. C. P. Grey and N. Dupré, *Chem. Rev.*, **104**, 4493–4512 (2004).

254. D. D. Laws, H. M. L. Bitter, and A. Jerschow, *Angew. Chemie - Int. Ed.*, **41**, 3096–3129 (2002).

255. K. Mä, P. J. Reeves, C. Xu, K. J. Griffith, and C. P. Grey, *Chem. Mater.*, **31**, 2545–2554 (2019).

256. J. Li, L. E. Downie, L. Ma, W. Qiu, and J. R. Dahn, *J. Electrochem. Soc.*, **162**, A1401–A1408 (2015).

257. H.-H. Ryu, G.-T. Park, C. S. Yoon, and Y.-K. Sun, *J. Mater. Chem. A*, **7**, 18580–18588 (2019).

258. G. T. Park, H. H. Ryu, N. Y. Park, C. S. Yoon, and Y. K. Sun, *J. Power Sources*, **442** (2019).

259. N. Zhang, N. Zaker, H. Li, A. Liu, J. Inglis, L. Jing, J. Li, G. A. Botton, and J. Dahn, *Chem. Mater.*, **Manuscript**.

260. J. C. Hunter, *J. Solid State Chem.*, **39**, 142–147 (1981).

261. D. P. Finegan, M. Scheel, J. B. Robinson, B. Tjaden, M. Di Michiel, G. Hinds, D. J. L. Brett, and P. R. Shearing, *Phys. Chem. Chem. Phys.*, **18**, 30912–30919 (2016).

262. J. L. Shi, D. D. Xiao, X. D. Zhang, Y. X. Yin, Y. G. Guo, L. Gu, and L. J. Wan, *Nano Res.*, **10**, 4201–4209 (2017).

263. S. Hy, H. Liu, M. Zhang, D. Qian, B. J. Hwang, and Y. S. Meng, *Energy Environ. Sci.*, **9**, 1931–1954 (2016).

264. P. Rozier and J. M. Tarascon, *J. Electrochem. Soc.*, **162**, A2490–A2499 (2015).

APPENDIX

COPYRIGHT PERMISSIONS

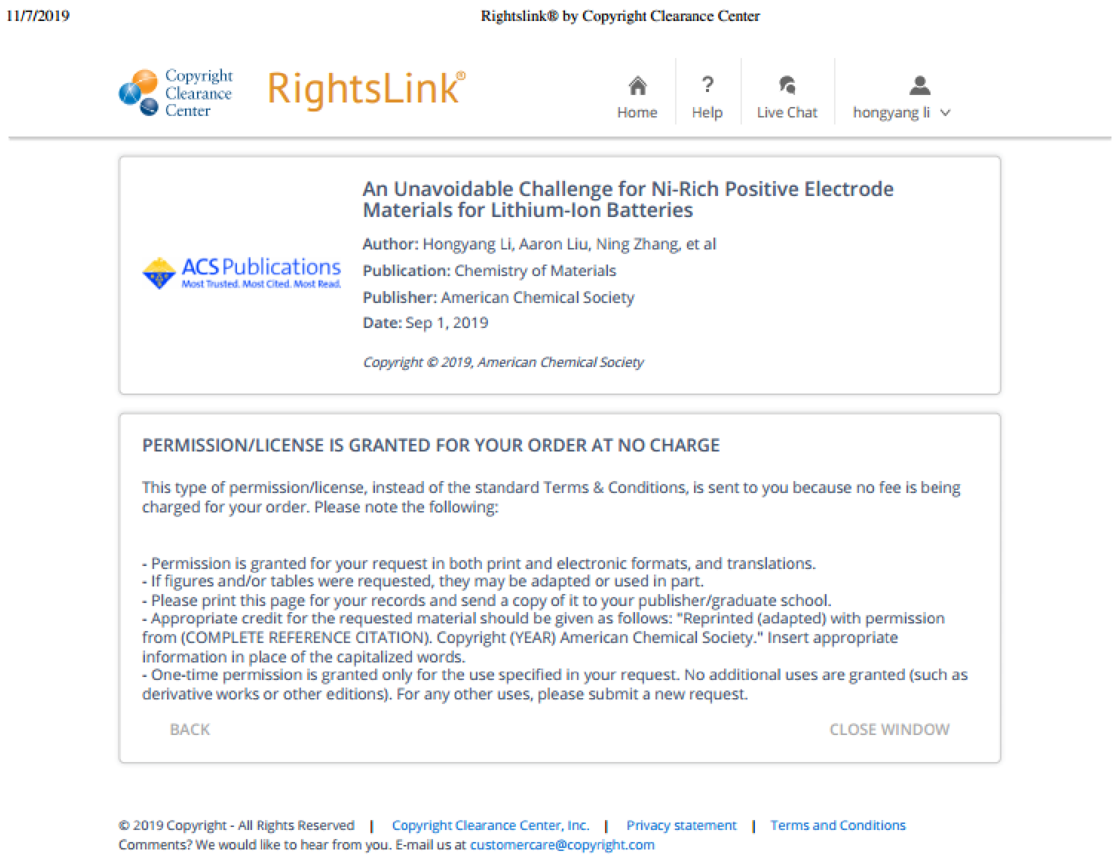

11/7/2019 Rightslink® by Copyright Clearance Center

An Unavoidable Challenge for Ni-Rich Positive Electrode Materials for Lithium-Ion Batteries

Author: Hongyang Li, Aaron Liu, Ning Zhang, et al

Publication: Chemistry of Materials

Publisher: American Chemical Society

Date: Sep 1, 2019

Copyright © 2019, American Chemical Society

PERMISSION/LICENSE IS GRANTED FOR YOUR ORDER AT NO CHARGE

This type of permission/license, instead of the standard Terms & Conditions, is sent to you because no fee is being charged for your order. Please note the following:

- Permission is granted for your request in both print and electronic formats, and translations.
- If figures and/or tables were requested, they may be adapted or used in part.
- Please print this page for your records and send a copy of it to your publisher/graduate school.
- Appropriate credit for the requested material should be given as follows: "Reprinted (adapted) with permission from (COMPLETE REFERENCE CITATION). Copyright (YEAR) American Chemical Society." Insert appropriate information in place of the capitalized words.
- One-time permission is granted only for the use specified in your request. No additional uses are granted (such as derivative works or other editions). For any other uses, please submit a new request.

© 2019 Copyright - All Rights Reserved | Copyright Clearance Center, Inc. | Privacy statement | Terms and Conditions

Comments? We would like to hear from you. E-mail us at customercare@copyright.com

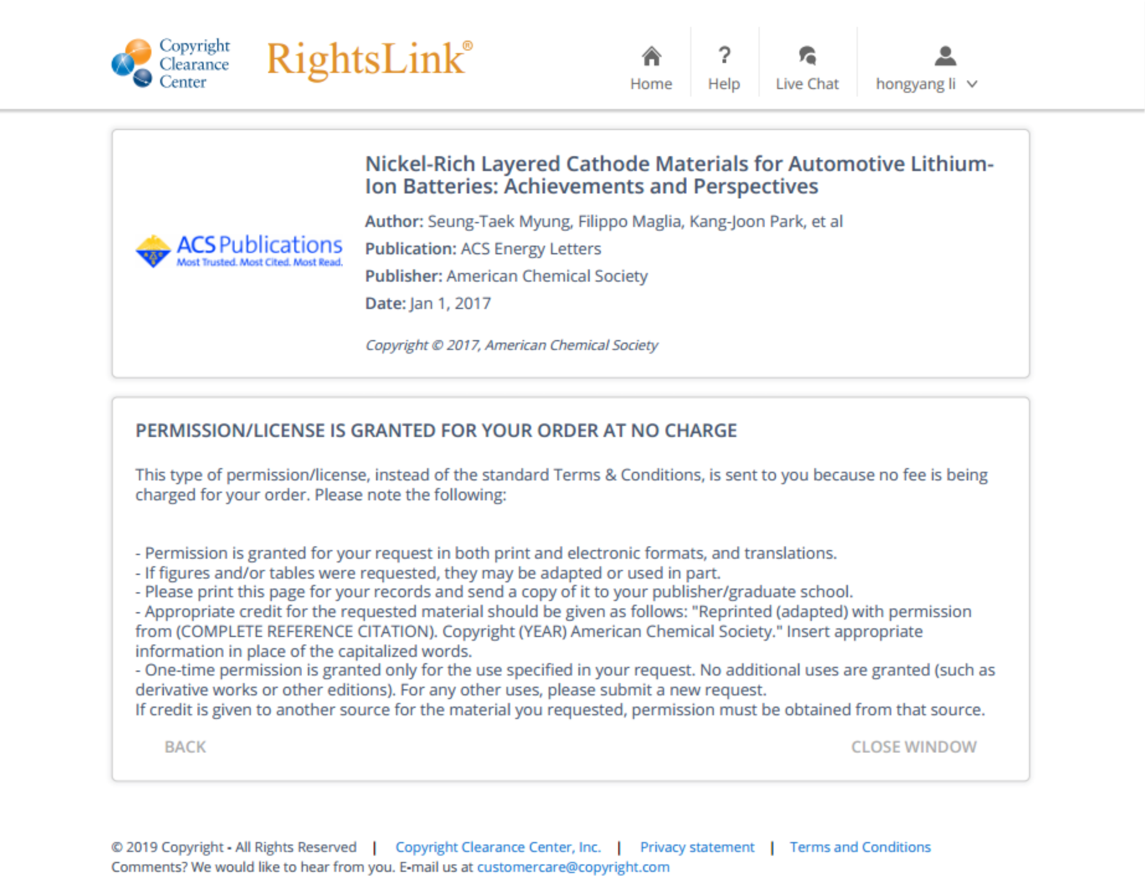

Nickel-Rich Layered Cathode Materials for Automotive Lithium-Ion Batteries: Achievements and Perspectives

Author: Seung-Taek Myung, Filippo Maglia, Kang-Joon Park, et al

Publication: ACS Energy Letters

Publisher: American Chemical Society

Date: Jan 1, 2017

Copyright © 2017, American Chemical Society

PERMISSION/LICENSE IS GRANTED FOR YOUR ORDER AT NO CHARGE

This type of permission/license, instead of the standard Terms & Conditions, is sent to you because no fee is being charged for your order. Please note the following:

- Permission is granted for your request in both print and electronic formats, and translations.
- If figures and/or tables were requested, they may be adapted or used in part.
- Please print this page for your records and send a copy of it to your publisher/graduate school.
- Appropriate credit for the requested material should be given as follows: "Reprinted (adapted) with permission from (COMPLETE REFERENCE CITATION). Copyright (YEAR) American Chemical Society." Insert appropriate information in place of the capitalized words.
- One-time permission is granted only for the use specified in your request. No additional uses are granted (such as derivative works or other editions). For any other uses, please submit a new request.

If credit is given to another source for the material you requested, permission must be obtained from that source.

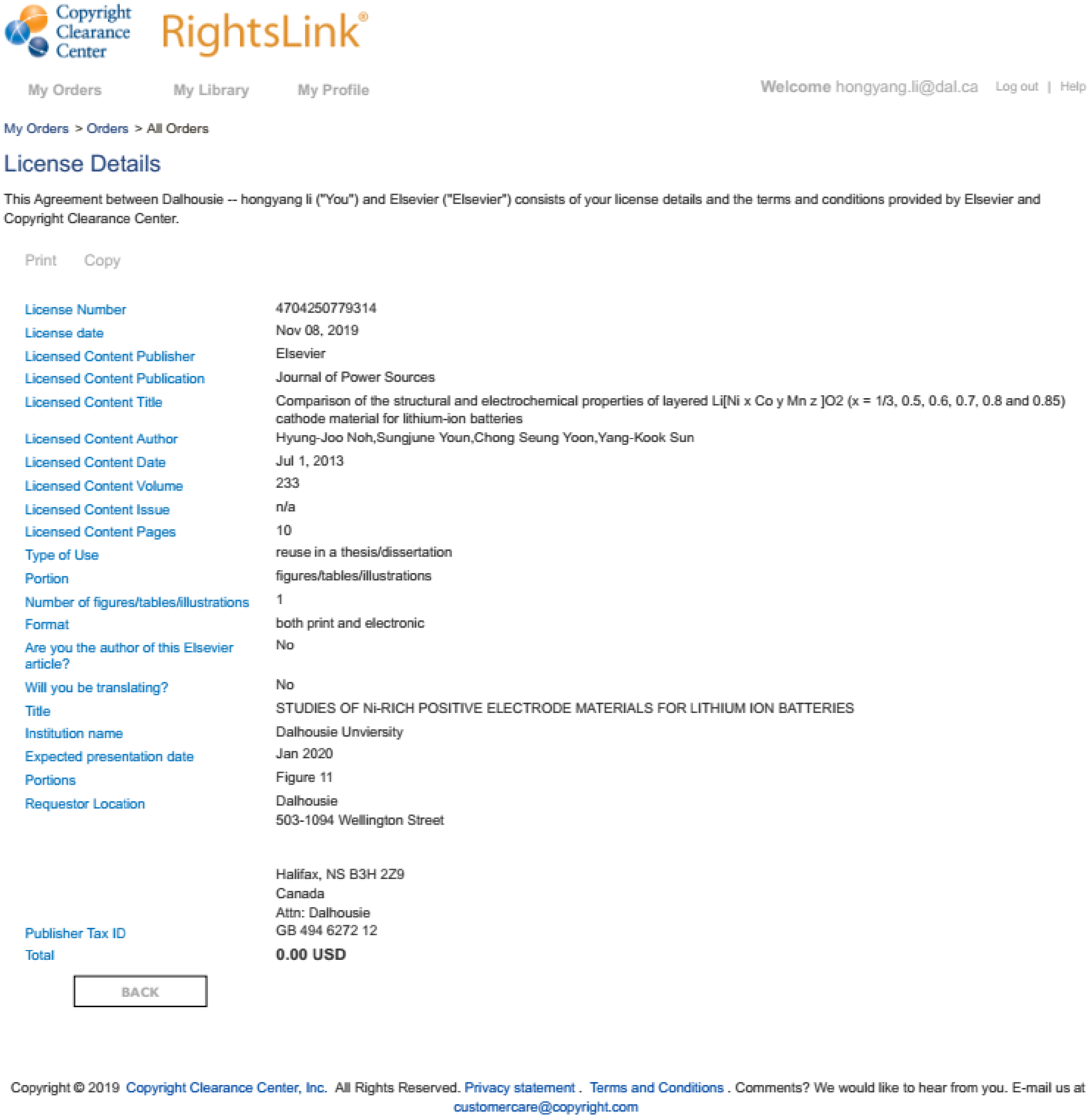

License Details

This Agreement between Dalhousie -- hongyang li ("You") and Elsevier ("Elsevier") consists of your license details and the terms and conditions provided by Elsevier and Copyright Clearance Center.

License Number	4704250779314
License date	Nov 08, 2019
Licensed Content Publisher	Elsevier
Licensed Content Publication	Journal of Power Sources
Licensed Content Title	Comparison of the structural and electrochemical properties of layered Li[Ni x Co y Mn z]O2 (x = 1/3, 0.5, 0.6, 0.7, 0.8 and 0.85) cathode material for lithium-ion batteries
Licensed Content Author	Hyung-Joo Noh,Sungjune Youn,Chong Seung Yoon,Yang-Kook Sun
Licensed Content Date	Jul 1, 2013
Licensed Content Volume	233
Licensed Content Issue	n/a
Licensed Content Pages	10
Type of Use	reuse in a thesis/dissertation
Portion	figures/tables/illustrations
Number of figures/tables/illustrations	1
Format	both print and electronic
Are you the author of this Elsevier article?	No
Will you be translating?	No
Title	STUDIES OF Ni-RICH POSITIVE ELECTRODE MATERIALS FOR LITHIUM ION BATTERIES
Institution name	Dalhousie Unviersity
Expected presentation date	Jan 2020
Portions	Figure 11
Requestor Location	Dalhousie 503-1094 Wellington Street Halifax, NS B3H 2Z9 Canada Attn: Dalhousie
Publisher Tax ID	GB 494 6272 12
Total	**0.00 USD**

Copyright Clearance Center Marketplace™

Royal Society of Chemistry - License Terms and Conditions

Order Date	08-Nov-2019
Order license ID	1002832-1
ISSN	2050-7496
Type of Use	Republish in a thesis/dissertation
Publisher	Royal Society of Chemistry
Portion	Image/photo/illustration

LICENSED CONTENT

Publication Title	Journal of materials chemistry. A, Materials for energy and sustainability	**Country**	United Kingdom of Great Britain and Northern Ireland
Author/Editor	Royal Society of Chemistry (Great Britain)	**Rightsholder**	Royal Society of Chemistry
		Publication Type	e-Journal
Date	01/01/2013	**URL**	http://pubs.rsc.org/en/journals/journalissues/ta
Language	English		

REQUEST DETAILS

Portion Type	Image/photo/illustration	**Distribution**	Worldwide
Number of images / photos / illustrations	1	**Translation**	Original language of publication
Format (select all that apply)	Electronic	**Copies for the disabled?**	No
		Minor editing privileges?	No
Who will republish the content?	Academic institution	**Incidental promotional use?**	No
Duration of Use	Life of current edition	**Currency**	CAD
Lifetime Unit Quantity	Up to 999		
Rights Requested	Main product		

NEW WORK DETAILS

Title	STUDIES OF Ni-RICH POSITIVE ELECTRODE MATERIALS FOR LITHIUM ION BATTERIES	**Institution name**	Dalhousie University
		Expected presentation date	2020-01-01
Instructor name	Hongyang Li		

ADDITIONAL DETAILS

Order reference number	N/A	**The requesting person / organization to appear on the license**	Hongyang Li

REUSE CONTENT DETAILS

Title, description or numeric reference of the portion(s)	Figure 2d
Editor of portion(s)	N/A
Volume of serial or monograph	N/A
Page or page range of portion	2696

Title of the article/chapter the portion is from	A method of increasing the energy density of layered Ni-rich Li[Ni1−2xCoxMnx]O2 cathodes (x = 0.05, 0.1, 0.2)
Author of portion(s)	Jae-Hyung Kim, Kang-Joon Park, Suk Jun Kim, Chong S. Yoon, and Yang-Kook Sun
Issue, if republishing an article from a serial	N/A
Publication date of portion	2019-01-07

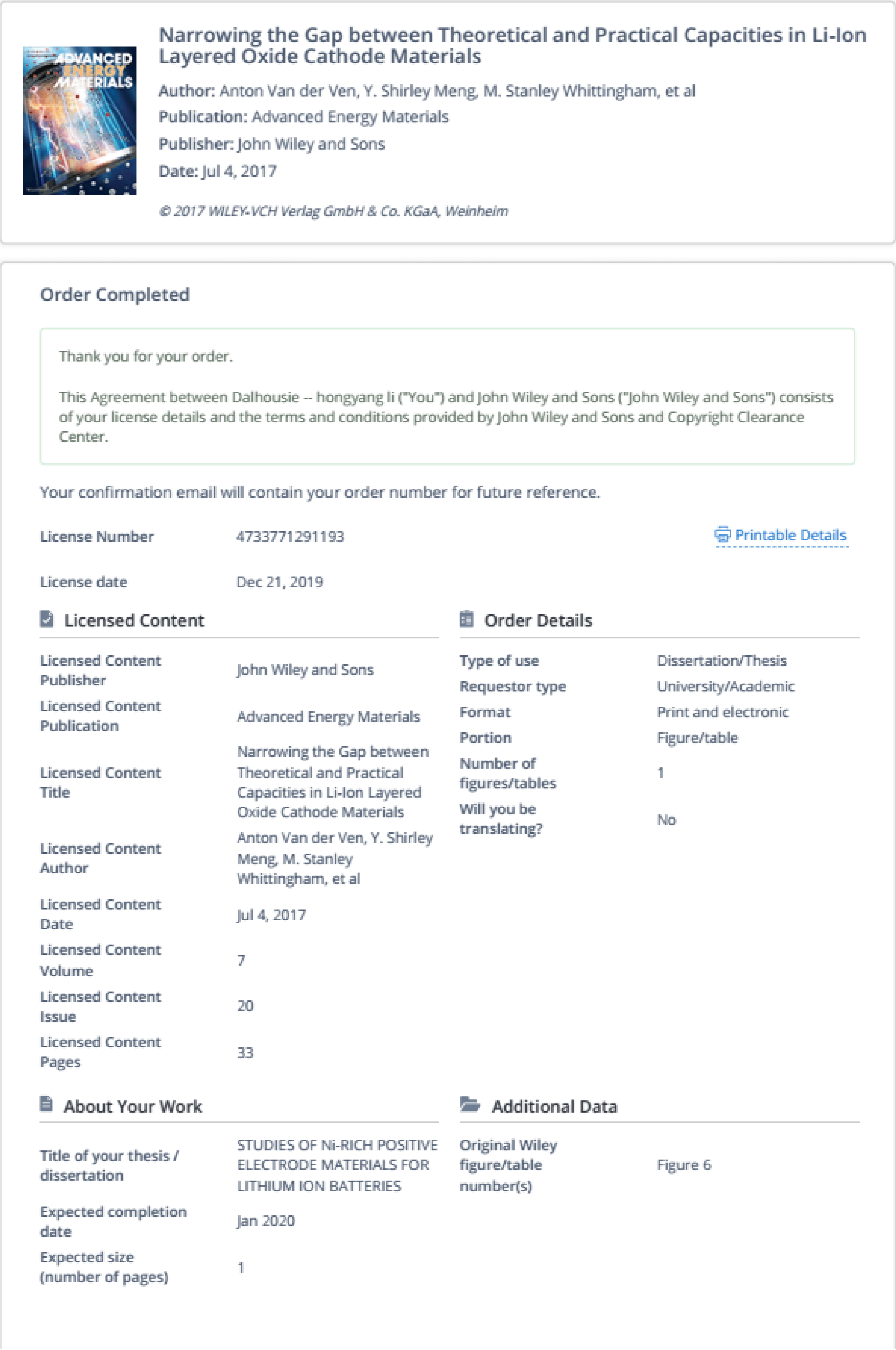

Narrowing the Gap between Theoretical and Practical Capacities in Li-Ion Layered Oxide Cathode Materials

Author: Anton Van der Ven, Y. Shirley Meng, M. Stanley Whittingham, et al
Publication: Advanced Energy Materials
Publisher: John Wiley and Sons
Date: Jul 4, 2017

© 2017 WILEY-VCH Verlag GmbH & Co. KGaA, Weinheim

Order Completed

Thank you for your order.

This Agreement between Dalhousie -- hongyang li ("You") and John Wiley and Sons ("John Wiley and Sons") consists of your license details and the terms and conditions provided by John Wiley and Sons and Copyright Clearance Center.

Your confirmation email will contain your order number for future reference.

License Number	4733771291193
License date	Dec 21, 2019

Licensed Content

Licensed Content Publisher	John Wiley and Sons
Licensed Content Publication	Advanced Energy Materials
Licensed Content Title	Narrowing the Gap between Theoretical and Practical Capacities in Li-Ion Layered Oxide Cathode Materials
Licensed Content Author	Anton Van der Ven, Y. Shirley Meng, M. Stanley Whittingham, et al
Licensed Content Date	Jul 4, 2017
Licensed Content Volume	7
Licensed Content Issue	20
Licensed Content Pages	33

Order Details

Type of use	Dissertation/Thesis
Requestor type	University/Academic
Format	Print and electronic
Portion	Figure/table
Number of figures/tables	1
Will you be translating?	No

About Your Work

Title of your thesis / dissertation	STUDIES OF Ni-RICH POSITIVE ELECTRODE MATERIALS FOR LITHIUM ION BATTERIES
Expected completion date	Jan 2020
Expected size (number of pages)	1

Additional Data

Original Wiley figure/table number(s)	Figure 6

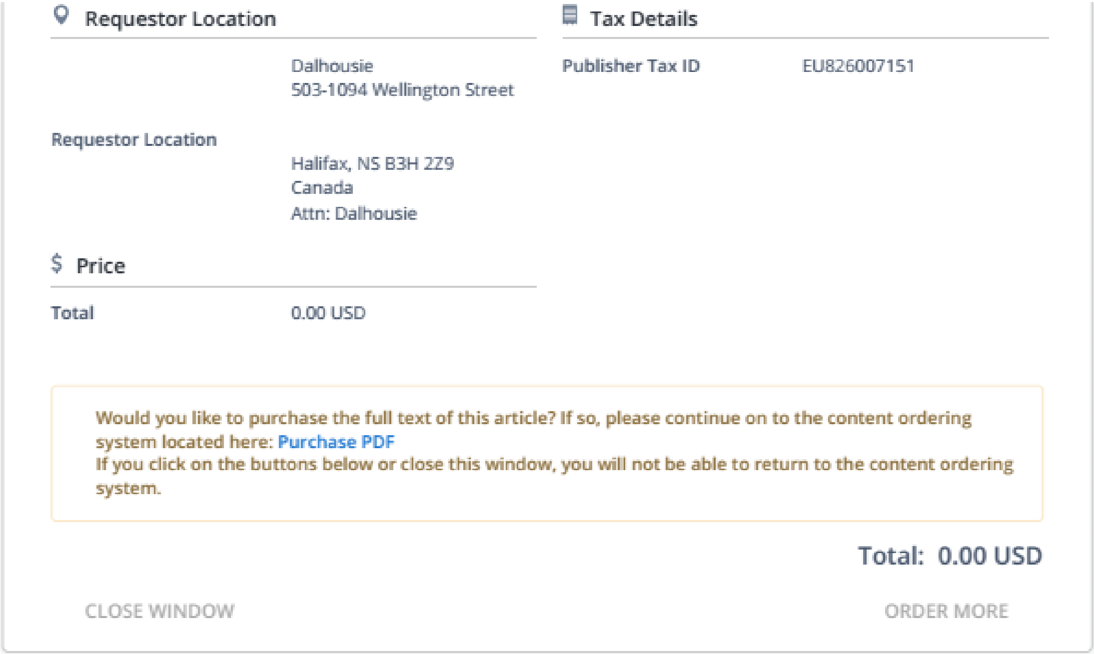

Requestor Location

Requestor Location	Dalhousie 503-1094 Wellington Street Halifax, NS B3H 2Z9 Canada Attn: Dalhousie

Tax Details

Publisher Tax ID	EU826007151

Price

Total	0.00 USD

Would you like to purchase the full text of this article? If so, please continue on to the content ordering system located here: Purchase PDF
If you click on the buttons below or close this window, you will not be able to return to the content ordering system.

Total: 0.00 USD

American Physical Society
Reuse and Permissions License

20-Dec-2019

This license agreement between the American Physical Society ("APS") and Hongyang Li ("You") consists of your license details and the terms and conditions provided by the American Physical Society and SciPris.

Licensed Content Information

License Number:	**RNP/19/DEC/021397**
License date:	20-Dec-2019
DOI:	10.1103/PhysRevB.78.104306
Title:	Nondilute diffusion from first principles: Li diffusion in `${\text{Li}}_{x}{\text{TiS}}_{2}$`
Author:	Anton Van der Ven et al.
Publication:	Physical Review B
Publisher:	American Physical Society
Cost:	USD $ 0.00

Request Details

Does your reuse require significant modifications: No

Specify intended distribution locations:	Worldwide
Reuse Category:	Reuse in a thesis/dissertation
Requestor Type:	Student
Items for Reuse:	Figures/Tables
Number of Figure/Tables:	1
Figure/Tables Details:	Figure 1b and figure 1c
Format for Reuse:	Electronic and Print
Total number of print copies:	Up to 1000

Information about New Publication:

University/Publisher:	Dalhousie University
Title of dissertation/thesis:	STUDIES OF Ni-RICH POSITIVE ELECTRODE MATERIALS FOR LITHIUM ION BATTERIES
Author(s):	Hongyang Li
Expected completion date:	Jan. 2020

License Requestor Information

Name:	Hongyang Li
Affiliation:	Individual
Email Id:	hongyangli@g.ucla.edu
Country:	Canada